2002

Symmetry-breaking transitions in RECuAs[subscript 2-x]P[subscript x] (RE=Sm, Gd, Ho and Er)

Yurij Mozharivskyj
Iowa State University

INFORMATION TO USERS

This manuscript has been reproduced from the microfilm master. UMI films the text directly from the original or copy submitted. Thus, some thesis and dissertation copies are in typewriter face, while others may be from any type of computer printer.

The quality of this reproduction is dependent upon the quality of the copy submitted. Broken or indistinct print, colored or poor quality illustrations and photographs, print bleedthrough, substandard margins, and improper alignment can adversely affect reproduction.

In the unlikely event that the author did not send UMI a complete manuscript and there are missing pages, these will be noted. Also, if unauthorized copyright material had to be removed, a note will indicate the deletion.

Oversize materials (e.g., maps, drawings, charts) are reproduced by sectioning the original, beginning at the upper left-hand corner and continuing from left to right in equal sections with small overlaps.

Photographs included in the original manuscript have been reproduced xerographically in this copy. Higher quality 6" x 9" black and white photographic prints are available for any photographs or illustrations appearing in this copy for an additional charge. Contact UMI directly to order.

ProQuest Information and Learning
300 North Zeeb Road, Ann Arbor, MI 48106-1346 USA
800-521-0600

Symmetry-breaking transitions in RECuAs$_{2-x}$P$_x$ (RE = Sm, Gd, Ho and Er)

by

Yurij Mozharivskyj

A dissertation submitted to the graduate faculty

in partial fulfillment of the requirements for the degree of

DOCTOR OF PHILOSOPHY

Major: Physical Chemistry

Program of Study Committee:
Hugo F. Franzen, Major Professor
Mark S. Gordon
Gerald J. Small
Gordon J. Miller
Vitalij K. Pecharsky

Iowa State University

Ames, Iowa

2002

UMI Number: 3051488

UMI Microform 3051488

ProQuest Information and Learning Company
300 North Zeeb Road
P.O. Box 1346
Ann Arbor, MI 48106-1346

Iowa State University

This is to certify that the doctoral dissertation of

Yurij Mozharivskyj

has met the dissertation requirements of Iowa State University

Signature was redacted for privacy.

Major Professor

Signature was redacted for privacy.

For the Major Program

TABLE OF CONTENTS

CHAPTER 1. GENERAL INTRODUCTION

Gibbs Free Energy

As is well known to chemists the change in Gibbs free energy accompanying a process determines whether the process is spontaneous as considered ($\Delta G < 0$), spontaneous in the opposite direction ($\Delta G > 0$) or reversible ($\Delta G = 0$). Since $\Delta G = \Delta H - T\Delta S$ and the principal temperature dependence resides in the term T multiplying the entropy change, it follows that at $T < \Delta H/\Delta S$ the process is spontaneous in the direction that lowers the enthalpy, while at $T > \Delta H/\Delta S$ the process is spontaneous in the direction that increases the entropy. In general the degeneracies of the states of any type, although electronic and vibrational states are particularly relevant in this context, are higher in higher symmetry solids and since higher degeneracy means higher entropy, it can be concluded that the high temperature form of a solid has high symmetry, and therefore high degeneracy and entropy, while the low temperature form has broken, or lower, symmetry and lower energy. It can be said that symmetry is generally broken at low temperatures as the result of a lowering of the electronic or vibrational energy, a lowering that is accompanied by a decrease in the degeneracies of the states accessible to the system.

For second-order phase transitions (continuous symmetry-breaking transitions) these conclusions are also valid in spite of the fact that ΔH and ΔS pass through zero at the transition point. In this case a single Gibbs free energy surface at high temperature splits into a continuous set of bounded surfaces at low temperatures (Figure 1 shows a schematic representation of the intersection of the surfaces with a constant pressure plane). The slopes of the curves are the negative of the entropies of the respective forms of the solid, and since the slopes of the lower curves are necessarily less negative than those above them, the lowest curve (the stable phase below the transition point)

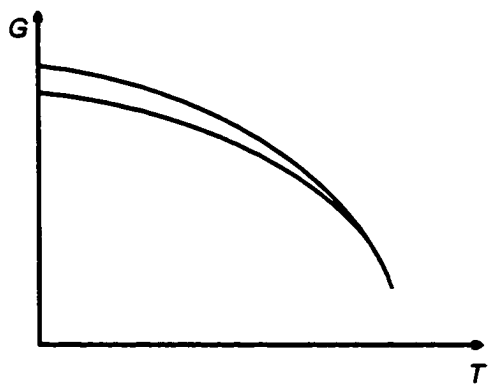

Figure 1. G versus T for a second-order phase transition.
The low-temperature phase has lower symmetry.

represents the phase of lowest entropy. Since this low entropy phase is entropically unstable with respect to those with higher G, this stable phase must be enthalpically (energetically) stable relative to the phases of higher Gibbs free energy. Thus whether two phases are related by a first- or a second-order transition, the high temperature form is entropically stabilized and the low temperature form is energetically stabilized.

It follows that in principle a point of high degeneracy in the Brillouin zone is a point of instability with respect to symmetry breaking at low temperature, and if the phase can be studied at sufficiently low temperature some form of symmetry breaking will occur to lower the degeneracy. This generalization provides the motivation for examining high symmetry solids in detail. The studies reported here used X-ray diffraction as the principal tool for studying symmetry breaking in a group of solids, the $RECuX_2$ compounds with RE = a rare-earth metal and X = P or As, or a mixture of these elements. These compounds have as their parent symmetry the space group $P4/nmm$ with a and b dimensionally and structurally distinct from c. Under this condition the space group of this structure does not result from the breaking of cubic symmetry, and the space group is a maximal subgroup. There are points of high symmetry with double degeneracy in the small representation which, as discussed above, provide instability with respect to symmetry lowering. These points can be considered in terms of the symmetry of the square nets produced in the *ab* plane.

Gibbs Free Energy and Square Layers of Main Group Elements

Structures with the square nets of main group elements offer a unique opportunity to study effects of both the energetic and entropy factors on crystal structures. Square layers generate energy bands that cross along some symmetry lines in reciprocal space (see a band structure of P square layer in Figure 2**a**). If the electron count is right, the Fermi level resides at the crossing. The presence of degenerate states at the Fermi level in solids is analogous to the presence of degenerate half-occupied molecular orbitals (MO) in molecules, which always leads to molecular distortions unless the molecule is linear. While such a molecular instability is known as a *Jahn-Teller instability*[1], the structural instability with respect to symmetry breaking in solids is referred to as a *Peierls instability*[2] or a *charge density wave*[3]. As with molecules, Peierls instabilities lead to large couplings of the vibrational and electronic motions. There is at least one normal mode that breaks the degeneracy and lowers the symmetry of the solid and its electronic energy through opening a band gap (see the band structure of the P layer of $ErCuP_2$ in Figure 2**b**).

As discussed above, when such a distortion occurs spontaneously ($\Delta G < 0$), it lowers the energy of the solid. The resulting structure of lower symmetry has a lower entropy ($\Delta S < 0$) and is

stable at low temperatures. Calcium aluminide $CaAl_4$ with the tetragonal $BaAl_4$ structure containing square Al nets exhibits this type of distortion[4]. Below 170°C, $CaAl_4$ undergoes a continuous symmetry-breaking transition (*I*4/*mmm* → *C*2/*m*) that opens a band gap, which provides the energy lowering in the low-symmetry structure. The high-symmetry structure of $CaAl_4$ is restored upon heating above 170°C.

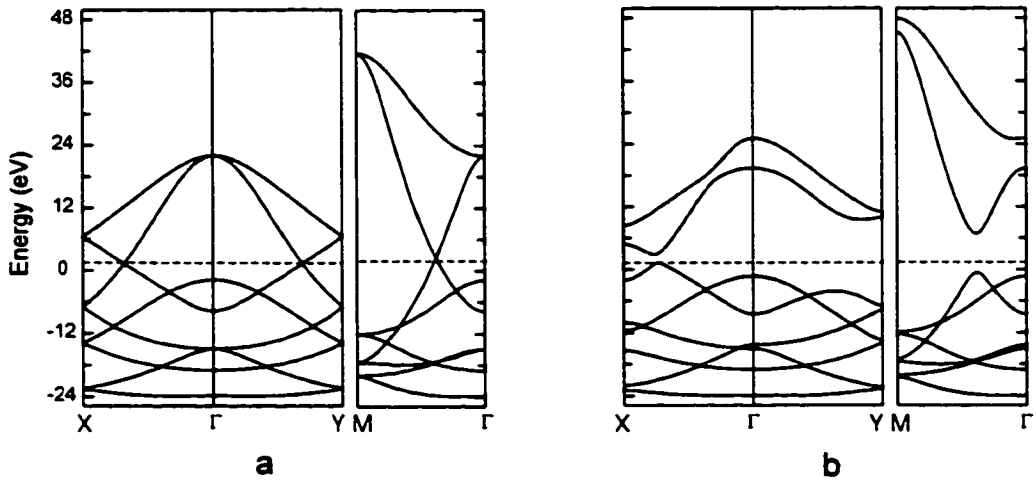

Figure 2. Band structures of (a) the P square layer and of (b) the distorted P net in $ErCuP_2$. The dashed lines represent the Fermi level.

Phases with the tetragonal $HfCuSi_2$-type structure contain square layers some of which are formed by main group elements and can be subject to Peierls distortions. Rare-earth copper phosphides were previously found to adopt the $HfCuSi_2$ structure[5-7]. In these compounds, p_x and p_y bands from phosphorus do not overlap with the other bands, they are highly dispersed, half occupied and cross at the Fermi level; an ideal situation for a Peierls-type distortion and lowering electronic energy through opening a band gap. Thus, electronically-driven symmetry-breaking transitions can be expected to occur at low temperatures.

Lowering of the electronic energy is only one of the mechanisms for decreasing the enthalpy of a solid. Transitions to low-symmetry structures can be also driven by changes in Coulomb interactions, which are strongly dependent on interatomic distances and atomic radii (their ratio is one of the indicators of packing efficiency). Thus, atomic substitution that changes the packing efficiency can be a factor determining the strength of Coulomb interactions and the crystal structure of a substituted compound. In addition, new atoms in the structure can produce more disperse bands and thus, can lead to a larger electronic energy gain upon opening a band gap. From this perspective, the rare-earth copper arsenides, phosphides and mixed arsenophosphides with the $HfCuSi_2$-type structure

offer an opportunity to examine the role of different energetic and entropic contributions to the stabilities of distorted crystal structures. Gradual substitution of As atoms by smaller P atoms (RECuAs$_{2-x}$P$_x$ compositions) can be seen as a fine-tuning of the electron and Coulomb interactions that allows the control of structures and yields a deeper insight into symmetry-breaking forces in the solid state.

Structural transformations driven either energetically or entropically can occur in two different ways. The next sections explain differences between the two transformation types and develop the tools necessary to determine the nature of these structural transformations.

First- and Second-Order Structural Transitions

Transitions between different crystal modifications usually take place via abrupt reconstruction of the crystal lattice, and the structure of a solid undergoes a discontinuous change. For these transitions the *first derivatives* of the Gibbs free energy with respect to the *intensive* variables (the derivatives are V, S, etc.) are discontinuous at the transition point, and these transitions are called *first-order*. However, besides such discontinuous transitions, another type of transition involving a change in symmetry is possible, namely one in which the arrangement of the atoms in a crystal changes continuously breaking the symmetry at a certain transition temperature, pressure or composition. In this case the first derivatives of the Gibbs free energy are continuous at the transition point, but the *second derivatives* (c_p, χ, etc.) have singularities (discontinuities or divergences) at the transition point, and the transitions are known as *second-order*. Such second-order structural transitions can occur via continuous displacement of atoms or via continuous changes in the ordering in the crystal or via a combination of both. An example of displacive transitions is the NiAs-type to MnP-type phase transition in which atomic positions change continuously away from high-symmetry positions ($P6_3/mmc \rightarrow Pcmn$) with decreasing temperature[8]. The β - β' ($Im\bar{3}m \rightarrow Pm\bar{3}m$) brass distortion is a classical example of a pure order-disorder transition in which Zn and Cu atoms interchange their positions with increasing temperature[9]. An example of the third type, the combination of displacive and order-disorder, is the NbN$_{1-x}$ distortion from the cubic NaCl-type structure to the tetragonal NbN$_{1-x}$-type structure[10,11].

In a first-order transition, two structures coexist at the transition point. The reason is that the first-order transition occurs at a point at which the chemical potentials or Gibbs free energies of the two structures are equal. Yet it is an ordinary point for each of the functions G_1 and G_2 and each function on either side of the transition point corresponds to some equilibrium (though metastable with respect to transition for the structure with larger G) state of the solid. For a second-order phase

transition, if one formally considers the chemical potential of either phase beyond the transition point, the potential corresponds to no equilibrium state, i.e., to no minimum of G (in the next section we will see that the chemical potential of the more symmetrical phase corresponds even to a maximum beyond the transition point).

Due to this characteristic feature the superheating or supercooling in second-order displasive transitions is impossible (both are possible for first-order transitions). The high-symmetry structure in this case cannot exist beyond the transition point, except for the very short time required to establish the equilibrium configuration of the atoms. However, for order-disorder transitions requiring diffusion this time can be very long, especially at low temperatures.

Landau Theory

Gibbs Free Energy of Second-Order Phase Transition

Landau theory deals with second-order phase transitions[12-14]. At every stage of the transition one can introduce a quantitative *order parameter* η that determines the extent to which the atomic configuration in the less symmetrical phase departs from the configuration in a more symmetrical phase. The order parameter vanishes at the transition to the high-symmetry structure and has non-zero positive or negative values for the low-symmetry structure. For a displacive transition the order parameter can be taken as the length of the vector giving the displacement of atoms from their ideal position in the high-symmetry structure.

Since the order parameter changes continuously, it can take arbitrarily small values near the transition point. Therefore, the Gibbs free energy of the solid can be expanded as a series in powers of η:

$$G = G^{\circ} + \alpha\eta + A\eta^2 + B\eta^3 + C\eta^4 + \cdots, \qquad (9)$$

where G° is the Gibbs free energy of the high-symmetry structure, α, A, B, C, $\cdots$ are coefficients that depend on the specific thermodynamic state. It is customary and usually sufficient to consider terms only up to the forth power of η (a case when the sixth power of η is important is presented below).

Thermodynamic and group-theoretical analyses require $\alpha \equiv 0$ in order for the Gibbs free energy to be at minimum with respect to η. For a transition to be continuous the third-order term must vanish ($B \equiv 0$ as a result of the symmetry properties of the crystal), the forth-order term must be positive ($C > 0$) and the second-order term must change sign at the transition point:

$A > 0$ when the high-symmetry structure is stable (Figure 3**a**),

$A < 0$ when the low-symmetry structure is stable (Figure 3**b**).

If the third-order term appears in G, there are two minima in this G (one at $\eta = 0$ and one at η or $-\eta \neq 0$) and there is a state at which the two structures coexist (Figure 4).

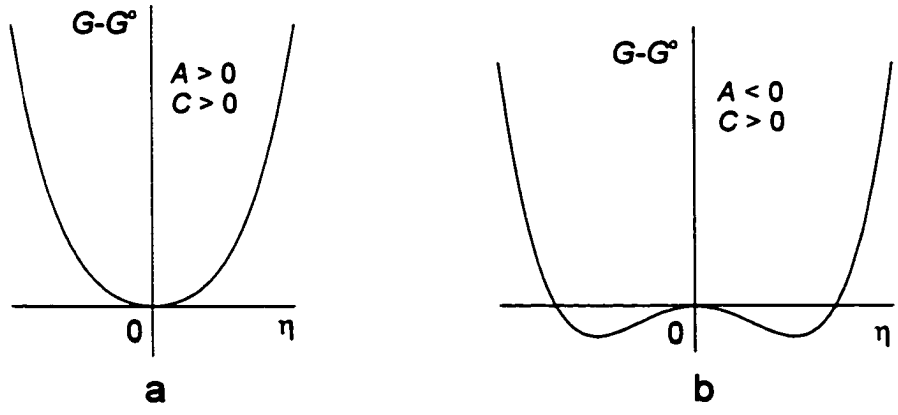

Figure 3. (a) High-symmetry structure is stable. (b) Low-symmetry structure is stable.

Group Theory and Landau Conditions

The question of whether a transition can actually take place by means of a second-order transition is answered by group theory. The particle density ρ (e.g., a function that gives the time averaged probability distribution of the atoms in the crystal) can be expanded as a linear combination of the functions ϕ that are basis functions for the irreducible representations of the space group of the high-symmetry structure (i.e., $c_i^{(n)}$ can be found using projection operators):

$$\rho = \sum_n \sum_i c_i^{(n)} \phi_i^{(n)}, \tag{10}$$

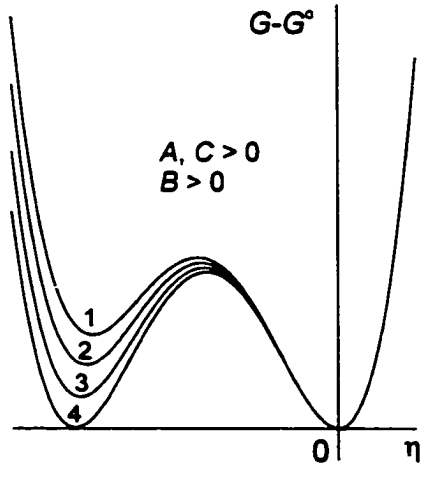

Figure 4. Gibbs free energy for different thermodynamic states of the crystal. In state 4 the undistorted and distorted structures are in equilibrium.

where the first summation is over the irreducible representations and the second is over the basis functions of the irreducible representations. The basis function of the totally symmetrical representation has the full symmetry $\mathcal{G}^o$ of the high-symmetry structure, while the symmetry of the rest of the functions $\delta\rho$ is lower:

$$\rho = \rho^o + \delta\rho; \qquad \delta\rho = \sum_n{}' \sum_i c_i^{(n)} \phi_i^{(n)}, \tag{11}$$

Now the first summation does not include the totally symmetrical representation. The function $\delta\rho$ has lower symmetry than $\mathcal{G}^o$ because if $\delta\rho$ remains invariant under some transformations of $\mathcal{G}^o$, it certainly does not under all of them. Thus the symmetry of the distorted structure resulting from a second-order transition is determined by the symmetry of $\delta\rho$ and, obviously, it is a *subgroup of the space group* of the high-symmetry structure.

For the crystal to have symmetry $\mathcal{G}^o$ ($\rho = \rho^o$) at the transition point, it is necessary that $\delta\rho$ and thus the coefficients $c_i^{(n)}$ in Equation 11 vary and they vanish at the transition point. Continuity in $c_i^{(n)}$ allows a Taylor expansion of the Gibbs free energy in $c_i^{(n)}$. Since the structure is invariant under all transformations of the group $\mathcal{G}^o$, so too is the Gibbs free energy. Hence, the terms in $c_i^{(n)}$'s in G must be invariant combinations of $c_i^{(n)}$. No linear invariants can be constructed from quantities $c_i^{(n)}$, which transform according to an irreducible representation of the group (the only exception is a one-dimensional totally symmetric representation, but this representation corresponds to the full symmetry $\mathcal{G}^o$ and no transition). The quadratic terms of $c_i^{(n)}$ can be always reduced to a sum of squares $\sum c_i^{(n)\,2}$ (or sum $\sum c_i^{(n)} c_i^{(n)\,*}$ if c_i is complex), and the expansion of G begins with the terms

$$G = G^o + \sum_n{}' A^{(n)} \sum_i c_i^{(n)\,2} + \cdots. \tag{12}$$

In the high-symmetry structure the coefficients $A^{(n)}$ must be positive to yield a minimum in G for all $c_i^{(n)} = 0$. Symmetry of the crystal can change if one of the coefficients $A^{(j)}$ becomes negative, hence at the transition point that coefficient must vanish. (Two of the coefficients $A^{(n)}$ can vanish simultaneously at an isolated point, which would be the intersection of two second-order transition lines). The rest of the coefficients $A^{(n)}$ remain positive near the transition point and the corresponding $c_i^{(n)}$ still equal 0. The irreducible representation to which the coefficient $A^{(j)}$ belongs determines the symmetry of the distorted structure through the following equations:

$$\rho = \rho^o + \delta\rho; \qquad \delta\rho = \sum_i c_i^{(j)} \phi_i^{(j)} = \sum_i c_i \phi_i, \tag{13}$$

Now the summation is only over the basis functions of one irreducible representation. Thus, we derived an important criterion for a second-order transition, namely, a second-order transition, unless it is restricted to an isolated point, must correspond to a *single irreducible representation*.

Since the order parameter η represents the extent of the distortion, it is useful to relate c_i to η in the following way:

$$\eta^2 = \sum_i c_i^2 \text{ (or } \sum_i c_i c_i^*); \qquad c_i = \eta \gamma_i, \tag{14}$$

$$\text{so that } \sum_i \gamma_i^2 = \frac{1}{\eta^2} \sum_i c_i^2 = 1. \tag{15}$$

The expansion of G can now be written as:

$$G = G^o + A\eta^2 + \eta^3 \sum_\alpha B_\alpha f_\alpha^{(3)}(\gamma_i) + \eta^4 \sum_\alpha C_\alpha f_\alpha^{(4)}(\gamma_i) + \cdots, \tag{16}$$

where $f_\alpha^{(3)}(\gamma_i)$ and $f_\alpha^{(4)}(\gamma_i)$ are invariants of third, fourth, etc. order constructed from γ_i, B_α and C_α are coefficients that multiply the invariants, and the summations are over different invariants. As mentioned above, for a transition to be continuous (second-order) the *third-order invariants must vanish* due to the symmetry transformations of $\mathcal{G}^o$. Often this condition is met only for some but not for all irreducible representations of the space group.

The combinations of the coefficients γ_i that determine the symmetry of the stable distorted structure are found through minimizing the Gibbs free energy (Equation 16 without the third-order terms). If an irreducible representation, to which a second-order transition corresponds, is one dimensional, there is only one basis function with $\gamma = 1$ and one does not need minimize G with respect to γ.

Lifshitz Condition

Transitions in solids are characterized by a wave vector $\boldsymbol{k}$, which determines the new smallest periodicity along this vector. The Gibbs free energy as a function of $\boldsymbol{k}$ must correspond to a minimum, for otherwise the structure will be unstable to continuous changes $\delta\boldsymbol{k}$ in periodicity and development of an incommensurate structure. If the Gibbs free energy is expanded about $\boldsymbol{k}$

$$G(\boldsymbol{k}+\delta\boldsymbol{k}) = G(\boldsymbol{k}) + \alpha \cdot \delta\boldsymbol{k} + \ldots, \tag{17}$$

it becomes obvious that the coefficient α must vanish to yield a minimum in $G(\boldsymbol{k})$ and a stable solution for a specific wave-vector $\boldsymbol{k}$. This fourth condition of Landau theory is known as a *Lifshitz*

condition. The criterion $\alpha \equiv 0$ is met when the group $\mathcal{g}(\boldsymbol{k})$ of the wave vector contains operations that eliminate the possibility of an invariant vector (the simplest case is presence of an inversion axis or inversion in $\mathcal{g}(\boldsymbol{k})$).

A transition, in which the minimum in the Gibbs free energy is not locked by the symmetry at $\boldsymbol{k}$, can still occur as a second-order phase transition, but the low-symmetry structure is now, except at isolated points, an incommensurate structure and can not be described in a space group in three dimensions.

Sixth-Order Term

Even if all criteria of Landau theory are met, a transition can still occur as a first-order one. To understand this possibility it is necessary to consider terms to the 6th order (the 5th and higher odd order invariants do not exist):

$$G = G^{o} + A\eta^{2} + C\eta^{4} + E\eta^{6} + \cdots. \qquad (18)$$

Now, if A, $E > 0$ and $C < 0$ there are three minima in G (Figure 5), and the behavior of G is similar to that when $B \neq 0$. Under these circumstances a change in one or more of the intensive parameters of a solid can yield a state (one with $\eta = 0$ and the other with $\eta \neq 0$) at which two structures are at equilibrium.

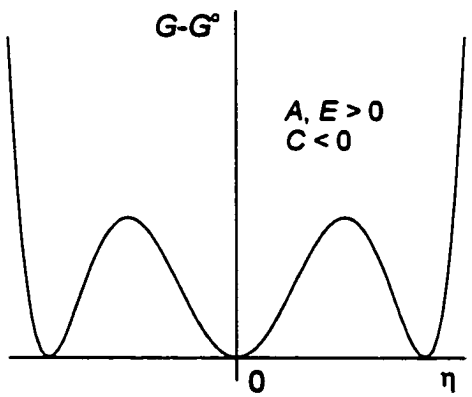

Figure 5. Undistorted and distorted structures are in equilibrium.

Dissertation Organization

The dissertation includes nine chapters, with chapters 3-8 being separate papers that have been published, are in print, have been submitted or will be submitted. Chapter 2 is of the theoretical nature and employs Landau theory to derive space groups that can arise continuously (during second-

order phase transitions) from the *P4/nmm* space group at the Γ symmetry point. Chapters 3-6 present experimental results and theoretical interpretations of these results for the $GdCuAs_{2-x}P_x$, $HoCuAs_{2-x}P_x$, $ErCuAs_{2-x}P_x$ and $SmCu_{1+\delta}As_{2-x}P_x$ series. Chapter 7 explains the distortions of the P nets in $ErCuP_2$ and $SmCu_{1.15}P_2$ and Chapter 8 studies the forces that are important in the *P4/nmm→Pmmn* continuous symmetry-breaking transitions. Chapter 9 is the concluding chapter, which summarizes the obtained results and discusses the stability of the rare-earth copper phosphides, arsenides and arsenophosphides.

Appendices A-D are published papers that present my work on different intermetallic compounds ($Cu_{47}Si_{91}P_{144}$, $Y_5Ni_xSb_{3-x}$, RE_5M_2X) which, although not directly related to the $RECuAs_{2-x}P_x$ phases, were investigated during my dissertation research.

Solid state experimental and theoretical techniques used during the studies are described in the papers presented in this dissertation.

References

(1) Jahn, H. A.; E, T. *Proc. Roy. Soc. A* **1937**, *161*, 220.

(2) Peierls, R. E. *Quantum Theory of Solids*; Oxford University Press: London, 1955.

(3) Albright, T. A.; Burdett, J. K.; Whangbo, M.-H. *Orbital Interactions in Chemistry*; Wiley: New York, 1985.

(4) Miller, G. J.; Li, F.; Franzen, H. F. *J. Am. Chem. Soc.* **1993**, *115*, 3739-3745.

(5) Chykhrij, S. I.; Kuz'ma, Y. B.; Oryshchyn, S. V. *Dopov. Akad. Nauk Ukr. RSR, Ser. B* **1989**, *3*, 63.

(6) Chikhrii, S. I. *Zh. Neorg. Khim.* **1990**, *35*, 1656-1658.

(7) Kuz'ma, Y.; Chykhrij, S. In *Handb. Phys. Chem. Rare Earths*; Gschneider, K. A., Jr., Eyring, L., Eds.; Elsevier: Amsterdam, 1996; Vol. 23, pp 285-434.

(8) Franzen, H. F.; Haas, C.; Jellinek, F. *Phys. Rev. B* **1974**, *10*, 1248-1251.

(9) Beck, L. H.; Smith, C. S. *J. Metals* **1952**, *4*, 1079-1083.

(10) Franzen, H. F.; Kim, S. J. *High Temp. Sci.* **1990**, *26*, 87-93.

(11) Kim, S. J.; Franzen, H. F. *J. Less-Common Met.* **1988**, *143*, 339-343.

(12) Landau, L. D.; Lifshits, E. M. *Statistical Physics*; Pergamon Press: London, 1958; Vol. 5.

(13) Franzen, H. F. *Chem. Mater.* **1990**, *2*, 486-491.

(14) Franzen, H. F. *Physical Chemistry of Solids*; World Scientific: Singapore, 1994.

CHAPTER 2. SPACE GROUPS ARISING CONTINUOUSLY FROM DISTORTIONS OF SQUARE NETS IN THE $HfCuSi_2$-TYPE STRUCTURES AT THE Γ POINT

Irreducible Representations at the Γ Point.

As was mentioned in the introduction, $HfCuSi_2$-type structures (*P4/nmm* space group) with square layers of main group elements often exhibit Peierls-type instabilities and undergo symmetry-breaking transitions lowering the electronic energy of crystals. Distortions of the $HfCuSi_2$-type structures can be also driven by Coulomb interactions. Obviously the spectrum of all possible distorted structures is very large, they can correspond to different wave vectors $\boldsymbol{k}$ and they can result from either first- or second-order transitions. This chapter will focus only on second-order transitions which occur with no loss in the translation symmetry, i.e., no superstructure is created during the transitions. Derivation of the resulting symmetries will proceed through the following steps:

1) determination of the wave vector ($\boldsymbol{k}$) of the transition;
2) finding irreducible representations of the space group for the wave vector $\boldsymbol{k}$;
3) checking whether any third-order invariants exist in the Gibbs free energy expansion G for a specific irreducible representation;
4) finding stable structures through minimizing G with respect to γ_i (if necessary);
5) checking the Lifshitz condition.

The wave vector ($\boldsymbol{k}$) of the transition is determined through the fact that any lost translations (vectors $\boldsymbol{T}_i$) yield nonintegral values for $\boldsymbol{k}\cdot\boldsymbol{T}_i/2\pi$. Since no translation is lost in the transitions of interest, the $\boldsymbol{k}$ vector for all the transitions is $\boldsymbol{k} = 0$ and it corresponds to the Γ symmetry point in reciprocal space.

All symmetry operations of the *P4/nmm* space group (rotational operations are given in Table 1) transform the vector $\boldsymbol{k} = 0$ into itself, therefore the group $\mathcal{G}(\boldsymbol{k})$ of the wave vector is the space group itself. Since irreducible representations of $\mathcal{G}(\boldsymbol{k})$ are identical to those of the factor group $\mathcal{G}(\boldsymbol{k}) / \mathcal{T}(\boldsymbol{k})$ and for $\boldsymbol{k} = 0$ $\mathcal{G}(\boldsymbol{k})/\mathcal{T}(\boldsymbol{k}) = \mathcal{G}/\mathcal{T}$ which is isomorphous with D_{4h}, it follows that the group $\mathcal{G}(\boldsymbol{k})$ is isomorphous with the point group D_{4h} and thus the irreducible representations of D_{4h} can be used to analyze the possible second-order phase transitions ($\mathcal{T}$ is a translational subgroup). There are eight one-dimensional and two two-dimensional representations (Table 2). We will analyze the one-dimensional representations first.

Table 1. Rotational Symmetry Operations of the *P4/nmm* Space Group

$\epsilon \mid 0$	$C_{4z} \mid \frac{1}{2}(\boldsymbol{a}+\boldsymbol{b})$	$C_{4z}^3 \mid \frac{1}{2}(\boldsymbol{a}+\boldsymbol{b})$	$C_{2z} \mid \frac{1}{2}(\boldsymbol{a}+\boldsymbol{b})$	$C_{2x} \mid \frac{1}{2}\boldsymbol{a}$	$C_{2y} \mid \frac{1}{2}\boldsymbol{b}$	$C_{2(x+y)} \mid \frac{1}{2}(\boldsymbol{a}+\boldsymbol{b})$	$C_{2(x-y)} \mid 0$
$i \mid 0$	$\bar{C}_{4z} \mid \frac{1}{2}(\boldsymbol{a}-\boldsymbol{b})$	$\bar{C}_{4z}^3 \mid \frac{1}{2}(\boldsymbol{a}-\boldsymbol{b})$	$\sigma_z \mid \frac{1}{2}(\boldsymbol{a}+\boldsymbol{b})$	$\sigma_x \mid \frac{1}{2}\boldsymbol{a}$	$\sigma_y \mid \frac{1}{2}\boldsymbol{b}$	$\sigma_{x+y} \mid \frac{1}{2}(\boldsymbol{a}+\boldsymbol{b})$	$\sigma_{x-y} \mid 0$

Table 2. Irreducible Representations of D_{4h} *

g	ϵ	C_{4z}, C_{4z}^3	C_{2z}	C_{2x}, C_{2y}	$C_{2(x+y)}$, $C_{2(x-y)}$	i	$\bar{C}_{4z}$, $\bar{C}_{4z}^3$	σ_z	σ_x, σ_y	σ_{x+y}, σ_{x-y}
A_{1g}	1	1	1	1	1	1	1	1	1	1
A_{2g}	1	1	1	-1	-1	1	1	1	-1	-1
B_{1g}	1	-1	1	1	-1	1	-1	1	1	-1
B_{2g}	1	-1	1	-1	1	1	-1	1	-1	1
E_g	2	0	-2	0	0	2	0	-2	0	0
A_{1u}	1	1	1	1	1	-1	-1	-1	-1	-1
A_{2u}	1	1	1	-1	-1	-1	-1	-1	1	1
B_{1u}	1	-1	1	1	-1	-1	1	-1	-1	1
B_{1u}	1	-1	1	-1	1	-1	1	-1	1	-1
E_u	2	0	-2	0	0	-2	0	2	0	0

* for *P4/nmm* at Γ the symmetry operations include translations as given in Table 1.

Space Groups Arising Continuously from 1D Irreducible Representations of *P4/nmm* at Γ

The third consideration of the Landau theory is to determine whether any third-order invariant can be formed from the basis functions, i.e., whether any $f_\alpha^{(3)}(\gamma_i)$ invariants exist in Equation 16. As we discussed above, the totally symmetric representation corresponds to no change in symmetry (no transition) and therefore it is of no interest. In the rest of the 1D representations half of the symmetry operations take the basis function into its negative, thus γ^3 is transformed into $-\gamma^3$ and thus there are no third-order invariants ($B \equiv 0$ as a result of the symmetry properties). Since the representations are one-dimensional, there is only one independent coefficient γ in Equation 16, which must equal 1 according to Equation 15, and thus minimization of the Gibbs free energy with respect to γ is unnecessary.

The group $\mathcal{G}(\boldsymbol{k})$ contains an inversion center, thus all the one-dimensional irreducible representations meet the Lifshitz criterion. The resulting space groups are determined from

transformation properties of the particle density in Equation 13. The irreducible representations of interest lead to a loss of all symmetry operations with character –1, which follows from the fact that the particle density function $\rho = \rho^{o} + \eta\phi$ must remain invariant under all symmetry operations. According to Landau theory these representations lead to a halving of the number of the rotational symmetry elements, and thus to space groups with eight essential symmetry elements. The one-dimensional irreducible representations, the resulting space groups and the new lattice vectors $\boldsymbol{a}'$, $\boldsymbol{b}'$, $\boldsymbol{c}'$ with respect to the old ones $\boldsymbol{a}$, $\boldsymbol{b}$, $\boldsymbol{c}$ are given in Table 3.

Table 3. Space Groups Arising Continuously from the 1D Irreducible Representations at the Γ Point from the *P4/nmm* Space Group

Space group	Lattice vectors	Space group	Lattice vectors
$A_{2g} \rightarrow P4/n$	$\boldsymbol{a}' = \boldsymbol{a}$, $\boldsymbol{b}' = \boldsymbol{b}$, $\boldsymbol{c}' = \boldsymbol{c}$	$A_{2u} \rightarrow P4mm$	$\boldsymbol{a}' = \boldsymbol{a}$, $\boldsymbol{b}' = \boldsymbol{b}$, $\boldsymbol{c}' = \boldsymbol{c}$
$B_{1g} \rightarrow Pmmn$	$\boldsymbol{a}' = \boldsymbol{a}$, $\boldsymbol{b}' = \boldsymbol{b}$, $\boldsymbol{c}' = \boldsymbol{c}$	$B_{1u} \rightarrow P\bar{4}2_1m$	$\boldsymbol{a}' = \boldsymbol{a}$, $\boldsymbol{b}' = \boldsymbol{b}$, $\boldsymbol{c}' = \boldsymbol{c}$
$B_{2g} \rightarrow Cmma$	$\boldsymbol{a}' = \boldsymbol{a} + \boldsymbol{b}$, $\boldsymbol{b}' = -\boldsymbol{a} + \boldsymbol{b}$, $\boldsymbol{c}' = \boldsymbol{c}$	$B_{1u} \rightarrow P\bar{4}m2$	$\boldsymbol{a}' = \boldsymbol{a}$, $\boldsymbol{b}' = \boldsymbol{b}$, $\boldsymbol{c}' = \boldsymbol{c}$
$A_{1u} \rightarrow P42_12$	$\boldsymbol{a}' = \boldsymbol{a}$, $\boldsymbol{b}' = \boldsymbol{b}$, $\boldsymbol{c}' = \boldsymbol{c}$		

Space Groups Arising Continuously from 2D Irreducible Representations of *P4/nmm* at Γ

Invariance of the third-order terms $(b_1\gamma_1^3 + b_2\gamma_2^3 + b_3\gamma_1\gamma_2^2 + b_4\gamma_1^2\gamma_2)$ formed from the basis functions ϕ_1, ϕ_2 of the 2D irreducible representations E_g and E_u can be checked by applying the transformation matrices which are given in Table 4. In both cases the operation C_{2x} takes ϕ_1 and ϕ_2 into $-\phi_1$ and $-\phi_2$ and thus no third-order combinations can be made from the basis functions.

The possible fourth-order polynomials in the expansion of the Gibbs free energy are

$$c_1\gamma_1^4 + c_2\gamma_2^4 + c_3\gamma_1\gamma_2^3 + c_4\gamma_1^3\gamma_2 + c_5\gamma_1^2\gamma_2^2. \qquad (19)$$

The operation C_{2x} transforms $c_3\gamma_1\gamma_2^3$ and $c_4\gamma_1^3\gamma_2$ into $-c_3\gamma_1\gamma_2^3$ and $-c_4\gamma_1^3\gamma_2$, thus $c_3 = c_4 = 0$. The last term in Equation 19 is invariant under all transformations and the first two terms are invariant provided $c_1 = c_2$. So, the Gibbs free energy is

$$G = G^{o} + A\eta^2 + c_1(\gamma_1^4 + \gamma_2^4)\eta^4 + c_5\gamma_1^2\gamma_2^2\eta^4 + \cdots \qquad (20)$$

Table 4. 2D Irreducible Representations of D_{4h} (and of $P4/nmm$ at Γ) in the Matrix Form

	ϵ	C_{4z}	C_{4z}^3	C_{2z}	C_{2x}	C_{2y}	$C_{2(x+y)}$	$C_{2(x-y)}$
E_g	$\begin{pmatrix}1&0\\0&1\end{pmatrix}$	$\begin{pmatrix}0&-1\\1&0\end{pmatrix}$	$\begin{pmatrix}0&1\\-1&0\end{pmatrix}$	$\begin{pmatrix}-1&0\\0&-1\end{pmatrix}$	$\begin{pmatrix}1&0\\0&-1\end{pmatrix}$	$\begin{pmatrix}-1&0\\0&1\end{pmatrix}$	$\begin{pmatrix}0&1\\1&0\end{pmatrix}$	$\begin{pmatrix}0&-1\\-1&0\end{pmatrix}$
E_u	$\begin{pmatrix}1&0\\0&1\end{pmatrix}$	$\begin{pmatrix}0&-1\\1&0\end{pmatrix}$	$\begin{pmatrix}0&1\\-1&0\end{pmatrix}$	$\begin{pmatrix}-1&0\\0&-1\end{pmatrix}$	$\begin{pmatrix}1&0\\0&-1\end{pmatrix}$	$\begin{pmatrix}-1&0\\0&1\end{pmatrix}$	$\begin{pmatrix}0&1\\1&0\end{pmatrix}$	$\begin{pmatrix}0&-1\\-1&0\end{pmatrix}$
	i	$\bar{C}_{4z}$	$\bar{C}_{4z}^3$	σ_z	σ_x	σ_y	σ_{x+y}	σ_{x-y}
E_g	$\begin{pmatrix}1&0\\0&1\end{pmatrix}$	$\begin{pmatrix}0&-1\\1&0\end{pmatrix}$	$\begin{pmatrix}0&1\\-1&0\end{pmatrix}$	$\begin{pmatrix}-1&0\\0&-1\end{pmatrix}$	$\begin{pmatrix}1&0\\0&-1\end{pmatrix}$	$\begin{pmatrix}-1&0\\0&1\end{pmatrix}$	$\begin{pmatrix}0&1\\1&0\end{pmatrix}$	$\begin{pmatrix}0&-1\\-1&0\end{pmatrix}$
E_u	$\begin{pmatrix}-1&0\\0&-1\end{pmatrix}$	$\begin{pmatrix}0&1\\-1&0\end{pmatrix}$	$\begin{pmatrix}0&-1\\1&0\end{pmatrix}$	$\begin{pmatrix}1&0\\0&1\end{pmatrix}$	$\begin{pmatrix}-1&0\\0&1\end{pmatrix}$	$\begin{pmatrix}1&0\\0&-1\end{pmatrix}$	$\begin{pmatrix}0&-1\\-1&0\end{pmatrix}$	$\begin{pmatrix}0&1\\1&0\end{pmatrix}$

The last equation can be simplified by noting that

$$(\gamma_1^2+\gamma_2^2)^2=\gamma_1^4+2\gamma_1^2\gamma_2^2+\gamma_2^4=1 \text{ and } \gamma_1^4+\gamma_2^4=1-2\gamma_1^2\gamma_2^2.$$

Thus the first polynomial can be eliminated:

$$G=G^o+A\eta^2+c_1\eta^4+(c_5-2c_1)\gamma_1^2\gamma_2^2\eta^4=G^o+A\eta^2+c_1\eta^4+c\gamma_1^2\gamma_2^2\eta^4 \qquad (21)$$

The extrema in G (Equation 21) relative to γ_1 and γ_2 subject to $\gamma_1^2+\gamma_2^2=1$ can be found using Lagrange's method of undetermined multipliers (λ = the undetermined multiplier):

$$\frac{\partial[c\gamma_1^2\gamma_2^2+\lambda(\gamma_1^2+\gamma_2^2)]}{\partial\gamma_i}=2c\frac{\gamma_1^2\gamma_2^2}{\gamma_i}+2\lambda\gamma_i=0. \qquad (22)$$

The two trivial solutions to Equations 22 and $\gamma_1^2+\gamma_2^2=1$ are $\gamma_1=0$, $|\gamma_2|=1$ and $|\gamma_1|=1$, $\gamma_2=0$. These solutions are equivalent since the two basis functions have the same thermodynamic properties. We also seek the solutions for which $\gamma_i\neq 0$. In this case

$$2c\gamma_1\gamma_2^2+2\lambda\gamma_1=0, \quad \text{or} \quad 2c\gamma_1^2\gamma_2^2=-2\lambda\gamma_1^2, \text{ and}$$

$$2c\gamma_1^2\gamma_2+2\lambda\gamma_2=0, \quad \text{or} \quad 2c\gamma_1^2\gamma_2^2=-2\lambda\gamma_2^2,$$

which gives $\gamma_1^2=\gamma_2^2$. And since $\gamma_1^2+\gamma_2^2=1$, it follows that $|\gamma_1|=|\gamma_2|=1/\sqrt{2}$.

So, there are two distinct solutions:

1. $|\gamma_1|=1$, $\gamma_2=0$ and $G=G^o+A\eta^2+c_1\eta^4$, (23)

2. $|\gamma_1|=|\gamma_2|=1/\sqrt{2}$ and $G=G^o+A\eta^2+(c_1+1/4c)\eta^4$. (24)

The second solution corresponds to a minimum in G if $c < 0$, otherwise it is a maximum (if $c = 0$ the two solutions have the same Gibbs free energy).

For the two-dimensional irreducible representations the particle density functions are

$\rho = \rho^{\circ} + \eta\phi_1$ for solution 1,

$\rho = \rho^{\circ} + 1/\sqrt{2}\eta(\phi_1 + \phi_2)$ for solution 2.

Transformation properties of these density functions under the symmetry operations of *P4/nmm* (application of the matrices from Table 4) yield space groups and lattice vectors of the distorted structures (Table 5).

Table 5. Space Groups Arising Continuously from the 2D Irreducible Representations at the Γ Point from the *P4/nmm* Space Group

Particle function	Space group	Lattice vectors
$\rho = \rho^{\circ} + \eta\phi_1$	$E_g \rightarrow P2_1/m$	$\boldsymbol{a}' = \boldsymbol{c}$, $\boldsymbol{b}' = \boldsymbol{a}$, $\boldsymbol{c}' = \boldsymbol{b}$
	$E_u \rightarrow Pmn2_1$	$\boldsymbol{a}' = \boldsymbol{b}$, $\boldsymbol{b}' = \boldsymbol{c}$, $\boldsymbol{c}' = \boldsymbol{a}$
$\rho = \rho^{\circ} + 1/\sqrt{2}\eta(\phi_1 + \phi_2)$	$E_g \rightarrow C2/m$	$\boldsymbol{a}' = \boldsymbol{a} - \boldsymbol{b}$, $\boldsymbol{b}' = \boldsymbol{a} + \boldsymbol{b}$, $\boldsymbol{c}' = \boldsymbol{c}$
	$E_u \rightarrow Amm2$	$\boldsymbol{a}' = \boldsymbol{c}$, $\boldsymbol{b}' = \boldsymbol{a} - \boldsymbol{b}$, $\boldsymbol{c}' = \boldsymbol{a} + \boldsymbol{b}$

The structures with the space groups $P2_1/m$ and $Pmn2_1$ can form in two different ways, which follows from the fact that the remaining two-fold screw axis can be the axis along the x direction (the $|\gamma_1| = 1$, $\gamma_2 = 0$ solution) or the axis along the y axis (the $\gamma_1 = 0$, $|\gamma_2| = 1$ solution) of the tetragonal cell. Thus, there are possibilities for twinning of the underlying sublattice, i.e., for the development of domains with different orientations.

Since each of the irreducible representations E_g and E_u corresponds to two different 1*D* irreducible representation along the x and y axes and to a single 2D irreducible representation along the z axis, it follows that the representations E_g and E_u meet the Lifshitz criterion and that the corresponding transitions can be second-order ones.

CHAPTER 3. SYMMETRY-BREAKING TRANSITIONS FROM $GdCuAs_2$ THROUGH $GdCuAs_{1.15}P_{0.85}$ TO $GdCuP_{2.20}$: CRYSTAL STRUCTURE, APPLICATION OF LANDAU THEORY, BONDING, MAGNETIC AND ELECTRICAL PROPERTIES

A paper published in Journal of Solid State Chemistry
J. Solid State Chem. **155**, 259 (2000)

Yurij Mozharivskyj[a], Dariusz Kaczorowski[b] and Hugo F. Franzen[a]
[a]*Department of Chemistry and Ames Laboratory of US DOE, Spedding Hall, Iowa State University, Ames, Iowa 50011, USA*
[b]*W. Trzebiatowski Institute of Low Temperature and Structure Research, Polish Academy of Sciences, P.O. Box, 50-950 Wroclaw, Poland*

Abstract

The crystal structures of $GdCuAs_2$, $GdCuAs_{1.15}P_{0.85}$ and $GdCuP_{2.20}$ have been investigated by the single crystal and powder methods. While $GdCuAs_2$ (*P4/nmm*) retains the tetragonal $HfCuSi_2$ structure (M. Brylak, M.H. Möller and W. Jeitschko, *J. Solid State Chem.* **115**, 305 (1995)), $GdCuAs_{1.15}P_{0.85}$ (*Pmmn*, a = 3.849(1), b = 3.850(1), c = 9.871(3) Å) and $GdCuP_{2.20}$ (*Pmm2*, a = 5.3747(9), b = 5.3830(9), c = 9.7376(16) Å) undergo orthorhombic distortions. The changes are significant in $GdCuP_{2.20}$: P dimers are formed in the P layer along the a direction and there is an additional (but deficient) P site on one side of the layer that links the dimers.

The $GdCuAs_{1.15}P_{0.85}$ structure was predicted by the Landau theory. According to this theory the transition from $GdCuAs_2$ to $GdCuAs_{1.15}P_{0.85}$ can be a continuous one, the transition from $GdCuAs_{1.15}P_{0.85}$ to $GdCuP_{2.20}$ is a first-order one. The transition to $GdCuP_{2.20}$ occurs with twin formation.

The electronic structure and bonding are analyzed by the extended Hückel tight-binding method. The conductivity and magnetic measurements for the arsenide and phosphide are reported.

1. Introduction

Intermetallic compounds with 2D square nets of the main group elements are of theoretical and experimental interest to researchers. They show a structural variety in the form of unit cell

distortions and help in the understanding of the driving forces of symmetry-breaking in the solid state. Some of them have partially filled bands and an innate tendency to lower their energy by opening a band gap at the Fermi level (1-2); as a result, a metal-to-semiconductor transition is observed. The electronic instabilities and the resulting distortions are usually referred to as "Peierls", and they are the solid state analogues of the molecular Jahn-Teller distortions (3). The presence of the degenerate half-filled states necessitates a large coupling of the vibrational and electronic motions. There is at least one normal mode that will break the degeneracy and lower the energy of the system and, of course, its symmetry. The GdPS (4) and CeAsS (5) structures (members of the *MAB* series) are examples of a 2*D* Peierls instability, where the layers of P and As atoms distort to form cis-trans or zigzag chains, respectively. The electronic structure of the phases was calculated, and the distortion was traced to a band crossing at the Fermi level (6). The deformations are driven by the formation of an energy gap at the Fermi level and result in semiconducting properties. It was suggested that the relative electronegativity of the *M* and *A* atoms dictates whether the distorted or undistorted structure is preferred: a prerequisite for the distortion to occur is a separation of the valence band and metal *d* block (6). The general distortion type square net → zigzag chain can also be found in other phases containing 4^4 nets of the main group atoms, e.g., a distortion from the $ZrSi_2$ to $CaSb_2$ type structures for $YbSb_2$ (7) and $EuSb_2$ (8).

If the Peierls instabilities are important in the 1*D* and 2*D* compounds, an *s-p* mixing and next-nearest-neighbor interaction become more important in determining structures with 3*D* nets. Black phosphorus (orthorombic), As, Sb and Bi (rombohedral) have layered structures in which each atom has three short bonds in the layer and relatively long contacts with the atoms in the neighboring layer (9-10). Their structures have been traditionally interpreted as the ones resulting from the Peierls instability inherent in a simple cubic phase with half-filled *p* bands (11-13). Seo and Hoffmann have shown that the calculated Fermi surface for cubic P is not nested, and argued strongly that the structural distortion in black phosphorus has little to do with the Peierls instability (14). They suggested that by forming a non-bonding lone pair band the *s-p* mixing stabilizes the local distorted geometry in black phosphorus. The *s-p* mixing, as well as the distortion, should decrease down the group due to the *s*-orbital contraction (14), which is observed for P, As, Sb and Bi. The reverse order of the distortion is predicted from consideration of the Peierls instability. However, in 2*D* compounds the distortions are mainly associated with a Peierls instability, although there is always some *s-p* mixing and the Fermi surface may exhibit no nesting. The concept of the hidden 1*D* Fermi surfaces was developed. According to this approach, nesting associated with hidden surfaces is responsible for the observed symmetry-breaking processes (15-16).

Among the compounds with 2D nets of main group elements there are the ATB_2 (A = Ca, Sr, Ba; T = Zn, Cd, Mn; B = Sb, Bi (17-21)) phases that are formed of AlB_4-type TB layers and 4^4 nets of Sb or Bi with A atoms intercalated in between. The bands formed mainly by the B p_x and p_y orbitals are quite dispersed and crossed along Γ-X, Γ-Y and Γ-M symmetry lines in the Brillouin zone (BZ). There is an s-p mixing, but the major contribution at the Fermi level comes from the p orbitals. If the number of electrons and electronegativity of a T element are favorable, there will be no overlap of the p_x and p_y bands with other bands and the Fermi level will lie at or near the crossing: an ideal situation for a symmetry lowering and a gap opening. These prerequisites are met in $SrZnSb_2$, where Sb zigzag chains are formed (19).

The $RECuX_2$ (RE is a rare earth element, X = P, As, Sb) compounds with the $HfCuSi_2$ structure are also good candidates for a Peierls instability and consequent distortions. Like the ATB_2 phases they have two kinds of the X atoms: one half (X_1) forms the CuX layer, the other half (X_2) builds the square net. Assigning the charges gives the $RE^{+3}Cu^{+1}X_1^{-3}X_2^{-1}$ formula, *i.e.* six electrons for X_2 . The X_2 s and p_z bands can be seen as fully occupied, on the other hand, the X_2 p_x and p_y bands are quite disperse, half-occupied and ready for distortion. But a distortion was not observed. $RECuSb_2$ (22), $RECuAs_2$ (RE = Y, La-Lu except Pm and Eu (23)), $RECu_{1+x}P_{2-x}$ (RE = Gd-Er (24)), $CeCu_{1.09}P_{1.87}$ (a filled $SrZnBi_2$ structure (25)) and $SmCuP_2$ ($SrZnBi_2$ type (26)) were reported to have tetragonal symmetry and an ideal square net of the main group elements. Further single crystal studies on the arsenides showed some additional Cu sites in the structures and in one case a doubling of the c parameter: $LaCu_{1.23(1)}As_2$ adopts a stuffed variant of the $SrZnBi_2$ type, while $CeCu_{1.10(1)}As_2$ and $PrCu_{1.09(1)}As_2$ crystallized with a stuffed version of the $HfCuSi_2$ type (27). The additional Cu atoms enter into the structures on both sides of the still ideal, square As net, occupying the apexes of the square pyramids. During the investigation of the Ho-Cu-P system splitting of some peaks for $HoCu_{1+x}P_{2-x}$ was observed, however the structure was not determined (28). It was an indication of a possible distortion of the tetragonal cell and this structural change could be triggered by a symmetry-breaking process in the P net. We looked more closely into $RECuAs_2$ and $RECuP_2$ and observed a peak splitting also for Gd, Er phosphides. The corresponding Gd, Ho and Er arsenides were found to have the tetragonal $HfCuSi_2$ structures.

We focused our research on $GdCuP_2$ and saw interesting structural changes on going from the arsenide to the phosphide. The Guinier powder pattern of the phosphide could be originally indexed in sp. group $P2/n$ with a=3.7892(6), b=9.751(1), c=3.7904(5) Å and β=90.631(9)° (29). According to the Landau theory, a continuous symmetry-breaking transition from a tetragonal cell of $GdCuAs_2$ (23) to a monoclinic cell of $GdCuP_2$, maintaining the same principle axis direction, is stepwise through

orthorhombic symmetry. The orthorhombic cell with sp. group *Pmmn* has been experimentally found for a mixed $GdCuAs_{1.15}P_{0.85}$ arsenophosphide. However, the pure phosphide turned out to have an additional but deficient P site and a larger orthorhombic cell (30). Twinning of the phosphide crystals, which results from the symmetry-breaking process, was observed during the X-ray work. Here we report the structures, magnetic and electrical properties of $GdCuX_2$ (*X* is P, As or both) and analyze the observed distortions.

2. Experimental

2.1. Synthesis

The starting materials were powdered gadolinium (99.9%, Alfa Aesar), copper (99.5%, Alfa Aesar), amorphous red phosphorus (99%, Alfa Aesar) and arsenic (99.99%, Alfa Aesar). Weighing and handling of the samples were performed in an Ar-filled glove box. The powders with a total mass of 0.5-1.0g were intimately mixed, pressed to a pellet under a pressure of 2000 kg using a 10-mm dial tool, and sealed in evacuated silica tubes. For the X-ray powder analysis the samples with compositions $GdCuAs_xP_{2-x}$ (x = 0, 0.33, 0.67, 1.00, 1.33, 1.67, 2.00) were heated at the rate of 20°C/h to 600°C, kept at this temperature for 48 hours and furnace cooled. The samples were ground, pressed, sealed, heated at 40°C/h to 800°C, kept at 800°C for 3 days and cooled. The second step was repeated once more with the heat treatment period being increased to 7 days. After each step the Guinier powder patterns were taken to check for samples homogeneity.

Single crystals of $GdCuAs_2$, $GdCuAs_{1.15}P_{0.85}$ and $GdCuP_{2.20}$ were obtained by the iodine gas transport technique in a zone furnace: length of the silica tubes was ~200mm, inner diameter 10mm, the pellets were placed at the hot end at 900°C, the temperature of the cold end was 800°C. The initial compositions and iodine concentrations were $GdCuAs_2$ and 0.8 mg/cm^3, GdCuAsP and 0.45 mg/cm^3, $GdCuP_2$ and 1.0 mg/cm^3. The samples were heated at 20°C/h, kept for 2 weeks and then furnace cooled. Air stable single crystals as shiny square plates were obtained at the cold end of the tubes.

For the energy dispersive spectroscopy (EDS) analysis single crystals of CuP_2 were prepared by the above described gas transport method.

2.2. X-ray Analysis

The powder patterns of the samples with Si as an internal standard were recorded using Guinier cameras (Enraf Nonius, $CuK_{\alpha 1}$), and the exposed and developed films were laser scanned to obtained peak positions. The lattice parameters (Table 1) were derived by the least-square method using the CSD program package (31). Peak splitting was observed for the arsenophosphides and the

Table 1. Powder Lattice Parameters for $GdCuX_2$

Composition.	Sp. Group	*a*, Å	*b*, Å	*c*, Å	*b/a*	*V*, Å^3
$GdCuAs_2$	*P4/nmm*	3.9112(9)	3.9112(9)	9.930(3)	1.0000	152.9
$GdCuAs_{1.67}P_{0.33}$	*Pmmn*	3.883(2)	3.890(2)	9.908(4)	1.0018	149.7
$GdCuAs_{1.33}P_{0.67}$	*Pmmn*	3.850(2)	3.867(2)	9.888(4)	1.0044	147.2
GdCuAsP	*Pmmn*	3.8314(8)	3.8443(8)	9.8613(9)	1.0034	145.2
$GdCuAs_{0.67}P_{1.33}$	*Pmmn*	3.8072(9)	3.8278(9)	9.843(2)	1.0054	143.4
$GdCuAs_{0.33}P_{1.67}$	*Pmmn*	3.793(1)	3.812(1)	9.822(2)	1.0050	142.0
$GdCuP_{2.16}$[a]	*Pmm2*[b]	5.3284(1)	5.3868(1)	9.7487(3)	1.0110	139.9

[a] Composition from the Rietveld refinement.

[b] not a superstructure of $GdCuAs_{0.33}P_{1.67}$.

phosphide, but different peaks were split in two cases. The phosphide has the most intense and some smaller peaks well split, which is seen even on the diffractogram (Fig. 1), on the other hand, the mixed compounds have other peaks split and this splitting can be seen only on Guinier patterns. The powder patterns (Fig. 1) were also taken at the Siemens D5000 ($GdCuAs_2$, $CuK_{\alpha 1}$) and Scintag (GdCuPAs and $GdCuP_2$, solid state cooled detector, $CuK_{\alpha 1}$ and $CuK_{\alpha 2}$) diffractometers. The pattern of $GdCuAs_2$ was well indexed in the *P4/nmm* sp. group, and that of the phosphide was indexed, initially, in the *P2/n* sp. group with a=3.7892(6), b=9.751(1), c=3.7904(5) Å and β=90.631(9)°. From the Landau theory a mixed arsenophosphide with the *Pmmn* sp. group was predicted, and the observed reflections of the synthesized $GdCuAs_{2-x}P_x$ phases were found to correspond to this group (29).

Single crystal methods were used to confirm the indexing results and to refine the atomic parameters. Crystals in the form of the square plates, obtained by the gas transport technique from the $GdCuAs_2$, GdCuAsP and $GdCuP_2$ samples, were checked by the Laue method. Crystals of the arsenide and arsenophosphide were not twinned, their data sets were collected and structures easily refined (Table 2, 3, 5), using the SHELXTL program (32). Only the peaks relevant to the *Pmmn* sp. group and presented lattice parameters were observed on the two-dimensional CCD detector for the arsenophosphide. Statistical mixtures of P and As were found on both sites and the composition was refined to $GdCuAs_{1.15}P_{0.85}$.

Although all exammed single crystals of the phopshide looked ideal under the microscope, they were twins under X-rays. Analysis of the Laue pictures indicated that the plane of twinning was 010 (*b* is the largest axis, original monoclinic setting). Rotation around *b* gave 9.76 Å, rotation along the diagonal in the *ac* plane gave 5.35 Å, but rotation along *a* showed weak superstructure reflections,

doubling the current monoclinic *a* parameter. Further investigation was done on a Siemens SMART diffractometer with a CCD detector. Indexing of the reflections resulted in an orthorhombic unit cell with a=5.3747(9), b=5.3830(9) and c=9.7375(16) Å. In this case the relationship between the monoclinic and larger orthorhombic cells for the phosphide is obvious: $\boldsymbol{b}_{mon} = \boldsymbol{c}_{ort}$, $\boldsymbol{a}_{mon} = ½ (\boldsymbol{a}_{ort}+\boldsymbol{b}_{ort})$, $\boldsymbol{c}_{mon} = ½ (\boldsymbol{a}_{ort} - \boldsymbol{b}_{ort})$ and $\beta_{mon} = \angle(\boldsymbol{ab}_{ort})$.

The structure of the phosphide was solved in sp. group *Pmm*2 (Table 2). During the refinement (SHELXTL program, (32)) a significant residual electron density was observed on one

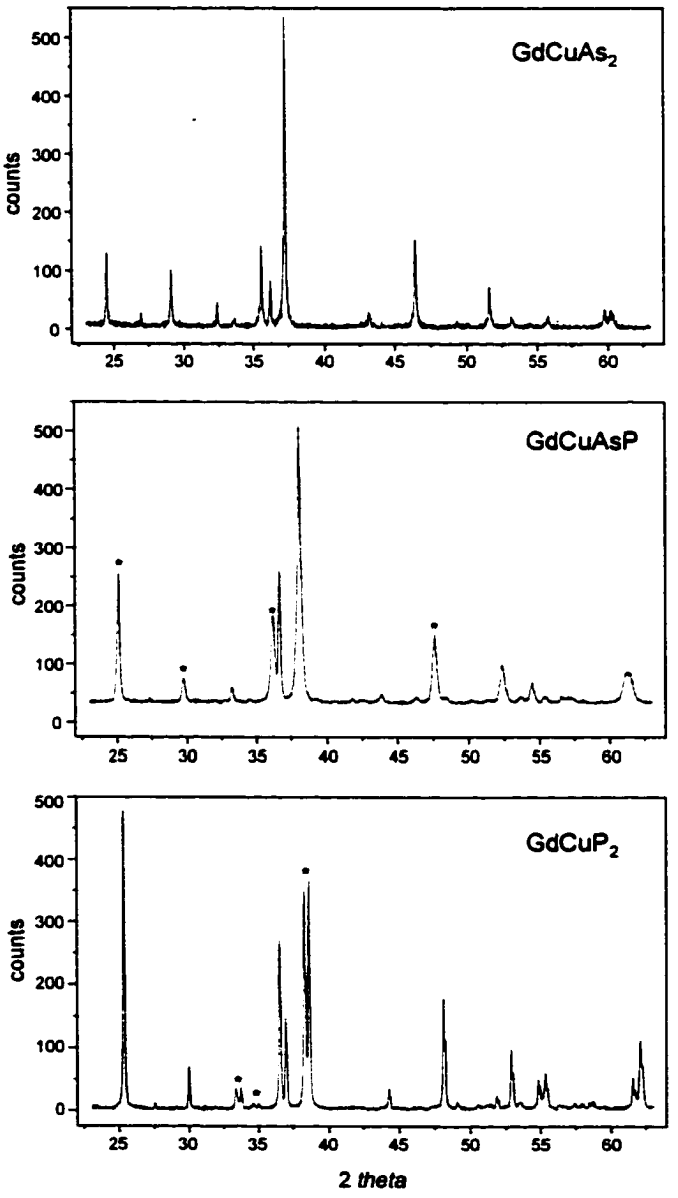

Figure 1. Powder patterns of $GdCuAs_2$, GdCuAsP and $GdCuP_2$ (all are the samples initial compositions). Asterisks indicate splitting of the low angle peaks.

side of the P net. On the basis of the interatomic distances the site was assigned to additional P atoms in the structure (P6 in Table 4, 6) and this resulted in the $GdCuP_{2.20}$ composition, which was later confirmed by an EDS analysis. The refinement was successful with the twinning rule:

$$\begin{pmatrix} 0 & 1 & 0 \\ 1 & 0 & 0 \\ 0 & 0 & -1 \end{pmatrix} \begin{pmatrix} a \\ b \\ c \end{pmatrix} = \begin{pmatrix} a' \\ b' \\ c' \end{pmatrix}$$

Table 2. Crystal Data and Structure Refinements (T=293(2) K, Mo$K\alpha$ - Radiation, Graphite Monochromator, the Refinement Method was Full-Matrix Least-Squares on F^2)

Empirical formula	$GdCuAs_2$	$GdCuAs_{1.15}P_{0.85}$	$GdCuP_{2.20}$
Space group	*P4/nmm* (No.129)	*Pmmn* (No.59)	*Pmm2* (No.25)
Unit cell dimensions, Å	a = 3.917(1)	a = 3.8468(10)	a = 5.3747(9)
	c = 9.939(1)	b = 3.8497(11)	b = 5.3830(9)
		c = 9.871(3)	c = 9.7375(16)
Z	2	2	4
Density (calculated)	8.072 g/cm^3	7.572 g/cm^3	6.825 g/cm^3
Diffractometer	Siemens P4	Siemens SMART	Siemens SMART
2θ range	4.10 to 53.50°	4.12 to 57.84°	4.18 to 56.88°
Index ranges	$-1 \le h \le 5$,	$-5 \le h \le 4$,	$-7 \le h \le 7$,
	$-5 \le k \le 5$, $-12 \le l \le 12$	$-4 \le k \le 5$,$-12 \le l \le 10$	$-6 \le k \le 7$,$-12 \le l \le 12$
Reflections collected	900 [$R\sigma$ = 0.0319]	919 [$R\sigma$ = 0.0362]	2506 [$R\sigma$ = 0.0328]
Abs. Correction / Program	empirical from ψ-scan	empirical / SADABS	empirical / SADABS
Independent reflections	127 [*Rint* = 0.0696]	228 [*Rint* = 0.0526]	794 [*Rint* = 0.0444]
Reflections with $I>2\sigma(I)$	125	208	723
Completeness to max 2θ	100.0 %	89.8 %	95.4 %
Data / restraints / par.	127 / 0 / 12	228 / 0 / 20	794 / 1 / 47
Goodness-of-fit on F^2	1.334	1.027	1.165
Final R indices [$I>2\sigma(I)$]	R_1 = 0.0257,	R_1 = 0.0201,	R_1 = 0.0359,
	wR_2 = 0.0590	wR_2 = 0.0453	wR_2 = 0.0983
R indices (all data)	R_1 = 0.0265,	R_1 = 0.0241,	R_1 = 0.0395,
	wR_2 = 0.0593	wR_2 = 0.0465	wR_2 = 0.1003
Extinction coefficient	0.038(3)	0.0087(14)	0.0096(6)
Largest diff. peak / hole	1.468 / –2.289 e./Å^3	0.875 / –1.103 e./Å^3	2.921 / –2.514 e./Å^3

$Rint = \Sigma|Fo^2-Fo^2mean|/\Sigma Fo^2$.
$R\sigma = \Sigma\sigma Fo^2/\Sigma Fo^2$.
$R_1 = \Sigma||Fo|-|Fc||/\Sigma|Fo|$.
$R_w = (\Sigma w\times(Fo^2-Fc^2)^2 / \Sigma w\times(Fo^2)^2)^{1/2}$, $w = 1/(\sigma^2(Fo^2)+(a\times P)^2+b\times P)$.
$GoF = (\Sigma w\times(Fo^2-Fc^2)^2 / (n-p))^{1/2}$ with $w = 1/(\sigma^2(Fo^2)+(a\times P)^2+b\times P)$, n is the number of observed reflections, p is number of parameters refined.

The relative arrangement of the atoms, except for P6, in the $GdCuP_{2.20}$ structure was similar to those of $GdCuAs_2$ and $GdCuAs_{1.15}P_{0.85}$. In the process of the refinement of the P1-P4 sites, which are located in the CuP layer and result from one atomic site in the parent $HfCuSi_2$ structure, had very close isotropic displacement factors (U_{eq}) and correlated z parameters. In the final steps all their U_{eq}'s were kept the same, and the z coordinates of P4 and P5 were related to z's of P1 and P2 by ($1-z_{P1,P2}$) with z's of P1 and P2 being equal. The refinement with these constraints was more stable and converged to R=0.0359. This indicated that the CuP block of the structure is very rigid and undergoes very small distortions in $GdCuP_{2.20}$.

Table 3. Atomic and Equivalent Isotropic Displacement Parameters (U_{eq}, Å^2) for $GdCuAs_2$ (Space Group *P4/nmm*, $HfCuSi_2$ Type) and $GdCuAs_{1.15}P_{0.85}$ (Space Group *Pmm*2)

	$GdCuAs_2$					$GdCuAs_{1.15}P_{0.85}$				
Atom		x	y	z	U_{eq}		x	x	z	U_{eq}
Gd	2*c*	¼	¼	0.23844(8)	0.0083(4)	2*a*	¼	¼	0.24108(4)	0.0159(3)
Cu	2*b*	¾	¼	1/2	0.0117(6)	2*b*	¼	¾	0.49989(12)	0.0192(3)
*X*1[a]	2*c*	¼	¼	0.65810(18)	0.0091(6)	2*a*	¼	¼	0.65545(16)	0.0172(6)
X2[b]	2*a*	¾	¼	0	0.0142(6)	2*b*	¼	¾	0.00005(11)	0.0256(5)

[a] *X*1 = 32.8(8)%As + 67.2(8)%P for $GdCuAs_{1.15}P_{0.85}$.
[b] *X*2 = 82.1(6)%As + 17.9(6)%P for $GdCuAs_{1.15}P_{0.85}$.

Table 4. Atomic and Equivalent Isotropic Displacement Parameters (U_{eq}, Å^2) for $GdCuP_{2.20}$ (Space Group *Pmm*2)

Atom		x	y	z	U_{eq}
Gd1	1*b*	0	1/2	0.2361(2)	0.011(1)
Gd2	1*c*	1/2	0	0.2459(2)	0.008(1)
Gd3	1*d*	1/2	1/2	0.7587(1)	0.007(1)
Gd4	1*a*	0	0	0.7756(2)	0.010(1)
Cu	4*i*	0.2480(2)	0.2506(5)	0.5026(5)	0.010(1)
P1	1*b*	0	1/2	0.6546(3)	0.008(1)
P2	1*c*	1/2	0	0.6546(3)	0.008(1)
P3	1*d*	1/2	1/2	0.3454(3)	0.008(1)
P4	1*a*	0	0	0.3454(3)	0.008(1)
P5	4*i*	0.2890(6)	0.2453(16)	0.0049(12)	0.018(1)
P6[a]	1*a*	0	0	0.1074(11)	0.024(3)

[a] Occupancy is 78(3)%.

Table 5. Interatomic Distances (Å) in $GdCuAs_2$ and $GdCuAs_{1.15}P_{0.85}$

Atoms	$GdCuAs_2$	$GdCuAs_{1.15}P_{0.85}$	Atoms	$GdCuAs_2$	$GdCuAs_{1.15}P_{0.85}$
Gd – 4*X*1	2.9545(9)	2.9065(7)	4*X*1 – 4Cu	2.5109(12)	2Cu at 2.4598(13)
4*X*2	3.0745(7)	3.0601(11)			2Cu at 2.4622(13)
4Cu	3.2548(8)	2Cu at 3.1986(12)	4Gd	2.9545(9)	2.9065(7)
		2Cu at 3.1995(12)			
			*X*2 – 4*X*2	2.7697(7)	2.7211(5)
Cu – 4*X*1	2.5109(12)	2*X*1 at 2.4598(13)	4Gd	3.0745(7)	3.0601(11)
		2*X*1 at 2.4622(13)			
4Cu	2.7697(7)	2.7211(5)			

X is As for $GdCuAs_2$ and As/P for $GdCuAs_{1.15}P_{0.85}$.

Table 6. Selected Interatomic Distances (Å) in $GdCuP_{2.20}$

Atoms	Distances	Atoms	Distances	Atoms	Distances
Gd1 – 2P3	2.8904(12)	Gd3 – 2P2	2.8721(11)	Cu – P2	2.403(4)
2P4	2.8943(12)	2P1	2.8760(11)	P1	2.418(4)
2P6	2.969(5)	4P5	2.985(10)	P4	2.437(4)
4P5	3.059(9)	4Cu	3.140(4)	P3	2.446(4)
4Cu	3.211(4)			Cu	2.666(2)
		Gd4 – 2P1	2.9342(12)	Cu	2.686(6)
Gd2 – 2P4	2.8564(11)	2P2	2.9380(12)	Cu	2.697(6)
2P3	2.8603(11)	4P5	3.023(10)	Cu	2.709(2)
4P5	2.922(10)	2P6	3.231(10)		
2P6	3.007(5)	4Cu	3.266(4)	P5 – P5	2.268(7)
4Cu	3.146(4)			P6	2.270(9)
				P5	2.641(17)
				P5	2.742(17)
				P5	3.106(7)
				P6 – 4P5	2.270(9)

On the other hand the P5 atoms showed significant shifts in the *a* direction from the ideal square lattice sites, but changes along *b* and *c* were small (Table 4). The twinning in the *ab* plane with *a* and *b* axes superimposed (this is discussed later) plus the large shifts along *a* obscured the electron density map in the P5 net and did not allow satisfactory refinement of the *y* and *z* parameters of P5. Nevertheless the distortion of the P5 net and the formation of the phosphorus dimers was obvious in $GdCuP_{2.20}$.

The structure of the phosphide was also refined by the full-profile Rietveld technique (Fig. 2), using the CSD package (31). The atomic parameters were close to those from the single crystal data, the composition changed a little to $GdCuP_{2.16}$. The formula $GdCuP_{2.20}$, based on the refinement of the single crystal data, is used further since the band structure calculations and structure analysis are based on the single crystal results.

2.3. EDS Analysis

EDS quantitative elemental analysis of phosphide crystals was performed on a JEOL 840A scanning electron microscope, equipped with a IXRF Systems Iridium X-ray analyzer. Single crystals of CuP_2, prepared by the gas transport technique, were used as standards to determine the Cu/P ratio in the gadolinium copper phosphide. The lattice parameters of CuP_2 crystals were checked on a single crystal diffractometer. A data set for one crystal was collected and the structure was refined to check the composition. No oxygen was observed in the crystals of CuP_2 and the gadolinium copper phosphides. The analysis of the three crystals (one is shown in Fig. 6) gave the P/Cu ratio of 2.32, 2.08, 2.11, which proved an additional P (not Cu or O) site in the structure. The mean (2.17) of these measurements was close to the results of the single crystal refinement ($GdCuP_{2.20}$).

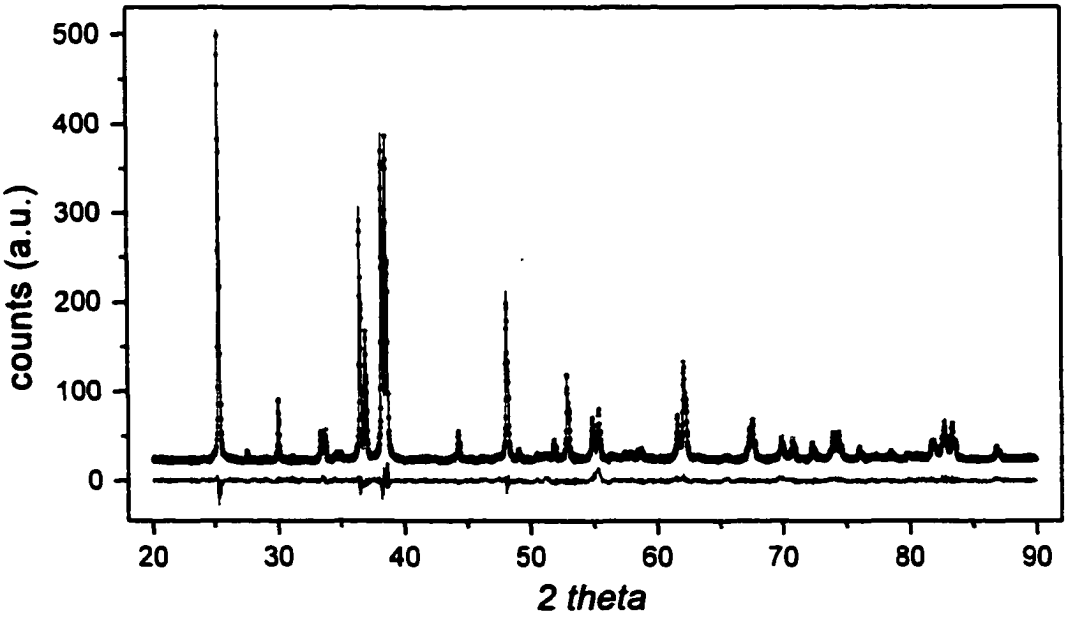

Figure 2. Observed (circles) and calculated (solid line) profiles and difference between them for the gadolinium copper phosphide.

2.4. Electric and Magnetic Measurements

Conductivities were measured on powders of the arsenide and a single crystal of the phosphide with a computer automated setup, using a standard DC two probe method. Electrode connections were made with the use of 50 μm silver wires and indium solder. Samples were cooled in a He flow cryostate. The temperature was measured with a LakeShore DT 470 silicon diode temperature sensor located close to the crystal. Resistivities were measured between 285K and 4K in increments of 2K. No indication of thermal hysteresis was observed, showing good temperature equilibrium throughout the measurement cycle.

Magnetic measurements were performed on powder of the arsenide and on powder and a single crystal of the phosphide in the temperature range 1.7-300 K and in applied magnetic fields up to 50 kOe employing a Quantum Design MPMS-5 SQUID magnetometer. Antiferromagnetic ordering at low temperatures is observed for both compounds.

2.5. Band Structure Calculations

Band structure calculations were performed by the extended Hückel tight binding (EHTB) method (33). Lattice and atomic parameters from the single crystal refinements of $GdCuAs_2$, $GdCuAs_{1.15}P_{0.85}$ and $GdCuP_{2.20}$ were used in the calculations. For the COOP analysis the X^{1-} and $Cu_2X_2^{2-}$ layers in $GdCuAs_{1.15}P_{0.85}$ were assumed to be occupied only by As and P, respectively. The additional P6 site in $GdCuP_{2.20}$ was considered fully occupied (the resulting composition was $GdCuP_{2.25}$), but later the electron number was taken as that for the real composition in order to have the right position of the Fermi level. The orbital energies and coefficients for the Slater-type orbitals were taken from (34). The parameters for Gd and Cu were refined by the alternating charge iteration technique, while the As and P parameters were kept constant (Table 7).

3. Results and Discussion

3.1. Structure Description

We observed no distortions of the tetragonal $GdCuAs_2$ structure (*P4/nmm* sp. group, $HfCuSi_2$ type), and its powder lattice parameters (Table 1) agreed well with the reported ones: a=3.9105(4) and c=9.929(2) Å (23). The mixed arsenophosphides adopt a previously unknown orthorhombic distorted version of the $HfCuSi_2$ structure with sp. group *Pmmn* (Fig.3). In the refined structure of $GdCuAs_{1.15}P_{0.85}$ both sites are statistically occupied and this can be assumed for the rest of the arsenophosphides. The unit cell volume (Fig. 4) decreases monotonically with the P content but the distortion has an opposite trend (Fig. 4).

Table 7. Parameters for the Extended Hückel Tight-Binding Calculations

Atom	Orbital	H_{ii}, eV, $GdCuAs_2$	H_{ii}, eV, $GdCuAs_{1.15}P_{0.85}$[a]	H_{ii}, eV, $GdCuP_{2.20}$[b]	ξ_1	c_1[c]	ξ_2	c_2[c]
Gd	6s	-7.61	-7.62	-7.14	1.369	1.00		
Gd	6p	-5.03	-5.04	-4.62	1.369	1.00		
Gd	5d	-8.05	-8.07	-7.45	2.747	0.7184	1.267	0.4447
Cu	4s	-9.46	-9.16	-8.46	2.20	1.00		
Cu	4p	-5.30	-5.07	-4.53	2.20	1.00		
Cu	3d	-14.55	-14.10	-12.97	5.95	0.5933	2.30	0.5744
As	4s	-16.22	-16.22		2.23	1.00		
As	4p	-12.16	-12.16		1.89	1.00		
P	3p		-18.60	-18.60	1.75	1.00		
P	3p		-14.00	-14.00	1.30	1.00		

[a] The composition GdCuAsP with As on the $X1$ site and P on the $X2$ site was taken for calculations.
[b] The P6 site was assumed to be fully occupied, that gave $GdCuP_{2.25}$ for the calculations.
[c] Coefficients used in the double-zeta Slater-type orbitals.

$GdCuP_{2.20}$ has an orthorhombic cell with twice the cell volume of $GdCuAs_{1.15}P_{0.85}$ (Fig. 3). As mentioned before, the CuP layer is rigid and therefore undergoes only small distortions. Each Cu atom has four P atoms at 2.403-2.446 Å (Table 4), and the bond variations can be attributed to the symmetry lowering. This kind of building block, composed of a transition metal tetrahedrally

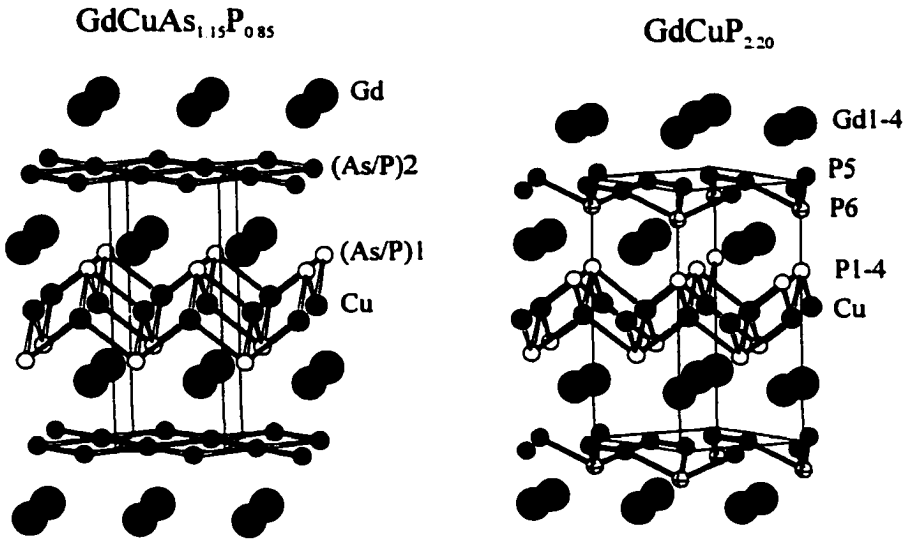

Figure 3. Structures of $GdCuAs_{1.15}P_{0.85}$ and $GdCuP_{2.20}$

coordinated by a main group element, can be found in many parent structures, e.g., $BaAl_4$, $ThCr_2Si_2$, $CaBe_2Ge_2$ and $HfCuSi_2$, with a large number of representatives among ternary phases.

The P layer undergoes a severe distortion in the *a* direction, resulting in P5-P5 dimer formation with short bonds of 2.268(7) Å and large distances of 3.106(7) Å between the dimers (Fig. 5). Shifts along the *b* axis are small and do not lead to a strong bond formation in that direction. Dimers are linked with each other along *a* by the additional phosphorus atoms (P6) on one side of the P5 layer. This additional phosphorus site stabilizes dimers by not allowing bond formation along the *b* axis. Energetics of the distortion and bond formation are discussed below. The P-P distances of 2.268 Å in the dimers are close to the single bond distances of 2.22-2.25 Å in the layers of the black phosphorus (9a). The P5-P6 distances (δ) of 2.271 Å (Fig. 5) are a little larger but also close to those in black phosphorus.

The P5-P5 and P5-P6 bonds are similar to the ones found in the rare-earth phosphides with relatively high amounts of phosphorus. In CeP_2 (35) and LaP_2 (36) phosphorus atoms are joined into fragments of the zigzag chains of 4 or 3 and 5 atoms with $\delta_{P\text{-}P}$ = 2.404-2.453 Å and $\delta_{P\text{-}P}$ = 2.197-2.314 Å, respectively. In LaP_5 (37) and LaP_7 (38) phosphorus forms a layer and a 3*D* framework with $\delta_{P\text{-}P}$ = 2.167-2.216 Å and $\delta_{P\text{-}P}$ = 2.1072-2.246 Å. However, the structural pattern of P atoms, as found in the structure of $GdCuP_{2.20}$, was not observed in any binary or other ternary phases.

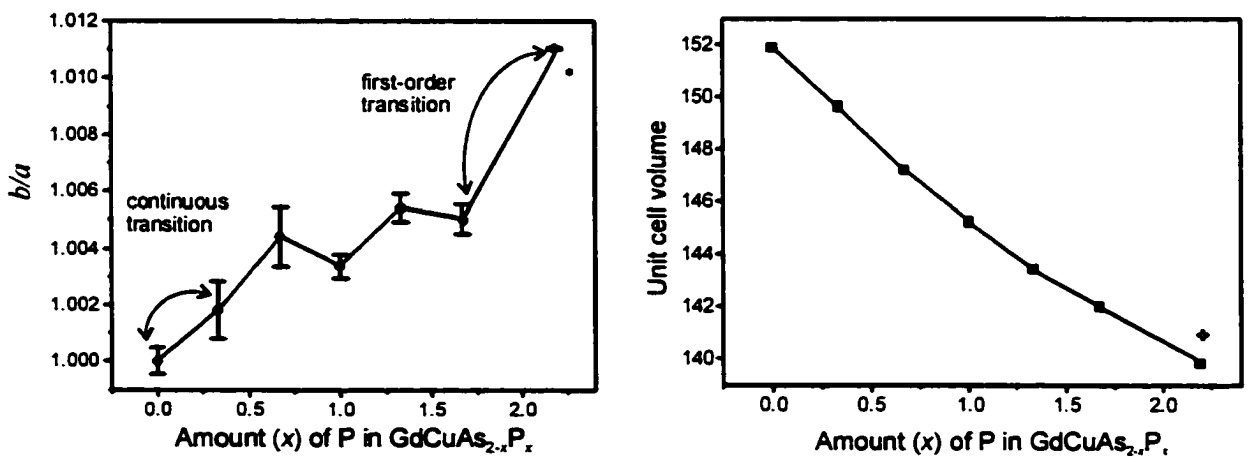

Figure 4. *b/a* ratio (left) and unit cell volume (right) versus phosphorus amounts. *Composition of the phosphide is $GdCuP_{2.16}$ (Rietveld refinement). ♦½ $V_{unit\ cell}$ of $GdCuP_{2.16}$.

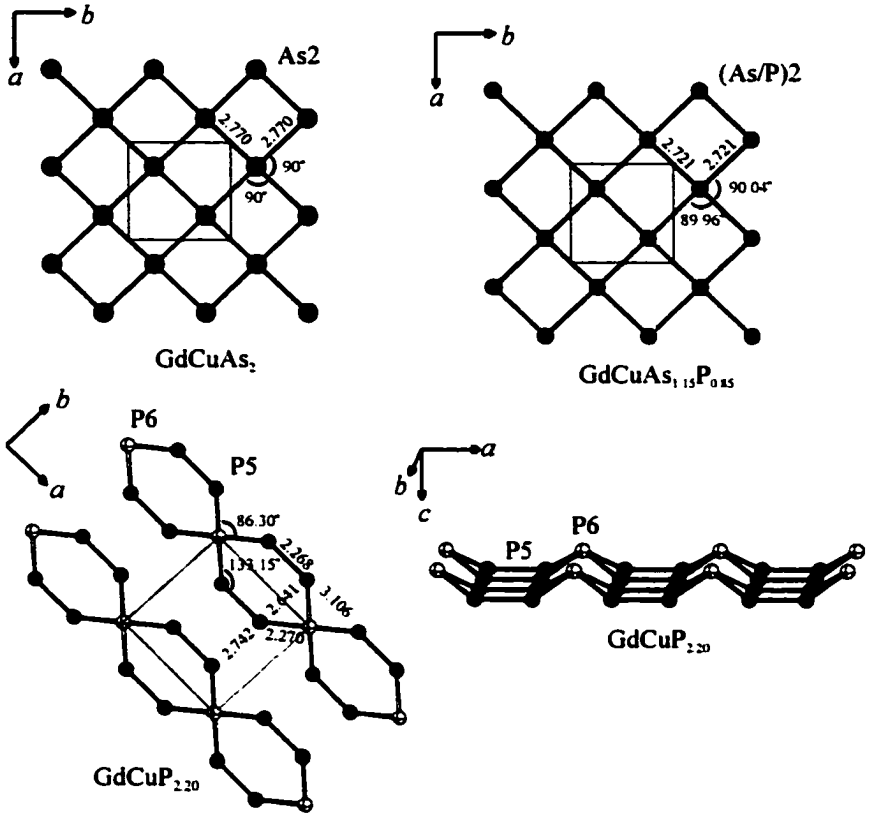

Figure 5. As, As/P and P layers in $GdCuAs_2$, $GdCuAs_{1.15}P_{0.85}$ and $GdCuP_{2.20}$.

3.2. Symmetry-Breaking Transitions and Landau Theory

When questions arise about the nature of phase transitions and correctness of a structure, researchers resort to the Landau theory (39-41) for answers. The theory can provide a structural model for one of the phases during a continuous symmetry-breaking process as it did for the low temperature modification of $CaAl_4$ (42). But its main benefit is that it provides symmetry constraints in cases of symmetry-breaking transitions.

Application of the Landau theory helped us to predict a new structure despite the fact that the initial structure of the phosphide was incorrect. From the powder data the structure of the phopshide was believed to be monoclinic with sp. group *P2/n*. Similarities in the powder patterns of the phosphide and arsenide indicated that the symmetry-breaking transition from the arsenide to the phosphide might be continuous (29). From the Landau theory such a continuos transition from a tetragonal cell of the arsenide to a monoclinic cell of the phosphide, maintaining the same principle axis direction must be stepwise through orthorhombic symmetry. Accordingly the orthorhombic cell with sp. group *Pmmn* was considered and it was experimentally confirmed for arsenophosphides

($GdCuAs_{1.15}P_{0.85}$ structure). However, the phosphide turned out to have a larger orthorhombic unit cell and an additional P site.

3.2.1. Transition from $GdCuAs_2$ to $GdCuAs_{1.15}P_{0.85}$

The first consideration in the Landau theory is the determination of a wave vector $\boldsymbol{k}$ (or set of equivalent wave vectors in a star), corresponding to the distortion in the sense that any lost translation (vectors $\boldsymbol{T}_i$) yield nonintegral values for $\boldsymbol{k}\cdot\boldsymbol{T}_i/2\pi$. Since there is no superstructure created by the distortion from tetragonal $GdCuAs_2$ to orthorhombic $GdCuAs_{1.15}P_{0.85}$, the $\boldsymbol{k}$ vector of the distortion is $\boldsymbol{k} = 0$. The second step is to find an irreducible representation corresponding to the $\boldsymbol{k}$ vector of the interest. Since the wave vector under consideration is $\boldsymbol{k} = 0$, the irreducible representations are isomorphous with those of the point group D_{4h} for $GdCuAs_2$.

There are eight one- and two two-dimensional such representations. The two-dimensional representations would result in 4 symmetry elements, corresponding to a monoclinic subgroup, and are not of interest. All, except the totally symmetric, one-dimensional representations result in a loss of all symmetry operations with character −1, and they lead according to Landau theory to a halving of the number of the rotational symmetry elements, and thus to space groups with eight essential symmetry elements. Four of the seven subgroups have orthorhombic unit cell, but only two (from the B_{1g} and B_{2g} representations) preserved the horizontal plane and inversion center. The space group ***Pmmn***, corresponding to B_{1g} (Table 8), is the one found experimentally in $GdCuAs_{1.15}P_{0.85}$.

The third consideration of Landau theory is to determine whether any third–order symmetry combination of basis vectors is invariant under all symmetry operations of the group. If such a third–order invariant exists, then a third-order term appears in the Gibbs free energy expansion in the order parameter η, and the transition must be discontinuous (40-41). In case of a one-dimensional irreducible representation the particle density, ρ, can be expressed in terms of that of symmetrical form, ρ^0, and one basic function, ϕ:

$$\rho = \rho^0 + \eta\phi$$

This function is symmetric to one half and antisymmetric to the other half of symmetry elements in B_{1g} (see Table 8), e.g., C_2^z takes ϕ into itself, but C_4^z transfroms ϕ into $-\phi$. Thus no third-order invariant combination can be formed from a basis function for this irreducible representation. It follows that ***P4/nmm*** $\rightarrow$ ***Pmmn*** with $\boldsymbol{a}_{ort} = \boldsymbol{a}_{tet}$, $\boldsymbol{b}_{ort} = \boldsymbol{b}_{tet}$ and $\boldsymbol{c}_{ort} = \boldsymbol{c}_{tet}$ meets the Landau conditions for a second-order phase transition.

Finally, in order for a second order transition from $GdCuAs_2$ to $GdCuAs_{1.15}P_{0.85}$ to be allowed the Lifshitz criterion must be met. This criterion is used to determine whether a minimum in the

Gibbs free energy as a function of wave vectors is fixed by symmetry at the reciprocal space point to which the transition corresponds. In the case under consideration inversion is in the point group of the wave vector and thus this point meets the Lifshitz condition.

3.2.2. Transition from $GdCuAs_{1.15}P_{0.85}$ to $GdCuP_{2.20}$

The transition from $GdCuAs_{1.15}P_{0.85}$ (sp. group *Pmmn*) to $GdCuP_{2.20}$ (sp. group *Pmm2*) is between two different subgroups of the parent *P4/nmm* symmetry of the $GdCuAs_2$ structure. The *a* and *b* directions in the arsenophosphide and phosphide correspond to *a* and *b* of *P4/nmm* for $GdCuAs_{1.15}P_{0.85}$ and to the face diagonals of *P4/nmm* for $GdCuP_{2.20}$, respectively. Thus, the phases are not in a group-subgroup relatonship, therefore, this is a first-order transition.

3.2.3. Twinning of Phopshide Crystals

During the X-ray studies all tested crystals of the phosphide were twins although they looked ideal under the microscope (Fig. 6). The twinning plane was 001 with the *a* and *b* axes of the twin parts being superimposed. Since the largest shifts are in the P layer of $GdCuP_{2.20}$, divergence of the distortion directions results in twin formation. In the (As/P)2 layer of $GdCuAs_{1.15}P_{0.85}$ each atom has four neighbors at 2.721 Å (Fig. 5), in the P5 layer of $GdCuP_{2.20}$ dimers with P-P distance of 2.269 Å are formed (Fig. 5). There are two ways in going from the (As/P)2-type layer to the real P5 layer of $GdCuP_{2.20}$: one is to form dimers along *a*, the other is along *b*. At the initial stage of crystal growth, when the lattice is not well defined, these two ways will not differ in energy with respect to the already formed lattice and are equally probable at the temperature of the experiment. So, one twin will have dimers along *a*, the other will have them along *b* (the *b* axis for the second twin will be its *a* axis). That is what is experimentally found for $GdCuP_{2.20}$ (Fig. 6).

Figure 6. A twin crystal of the phosphide and the twinning rule.

3.3. Electronic Structure and Bonding in $GdCuP_{2.20}$

As mentioned in the introduction, symmetry-breaking transitions involving 2*D* nets are the result of the instabilities that lead to energy lowering. Without the P6 site, the structure of $GdCuP_{2.20}$ would fit ideally into the classical 2*D* Peierls distortion case and probably would undergo a change similar to that in $SrZnSb_2$ (19). However, the situation is different: instead of cis-trans or zigzag chains the P5-P5 dimers are formed and the dimers are joined by the P6 atoms in the *a* direction to produce double chains (Fig. 5). To understand this unusual geometry we will break the distortion process into two steps. At the beginning we will analyze the instability of the P5 square net, and then we will try to explain the role of P6 atoms.

We start with an electron count in the hypothetical tetragonal structure of $GdCuP_2$ ($x = y =$ 0.25 for P5) with no additional P6 sites. The Gd1-Gd4 atoms have no short metal-metal bonds (Table 5) and therefore may be counted as Gd^{3+} in agreement with the results of the magnetic susceptibility measurements. The P1-P4 atoms have no close anion neighbors and can be safely assumed to be P^{3-}. The shortest Cu-Gd and Cu-Cu distances are 3.140–3.266 and 2.666–2.709 Å in the real structure, this is typical for Cu^+ (d^{10}) as it is mostly found in pnictide and chalocogenide systems. Based on the above oxidation state assignments the electronic structure can be described as $(Gd(1\text{-}4)^{3+})(Cu^{3+})(P(1\text{-}4)^{3-})(P(5)^-)$.

Since the energies of P *s* orbitals are low and the p_z orbitals do not ovelap much in the *xy* plane, the *s* and p_z bands of P5 will lie below the Fermi level and will be fully occupied. So far, we neglect an *s-p* mixing. There are four P5 atoms in the unit cell and therefore four types of molecular orbitals ($\sigma\pi$ and $\sigma\pi^*$ bonding, $\sigma^*\pi$ and $\sigma^*\pi^*$ antibonding) can be formed of the remaining half-filled p_x and p_y atomic orbitals (Fig. 7). Each MO generates a band and the evolution of the bands along Γ-*X* is presented in Fig. 8a. The $p_x\sigma\pi^*$ and $p_x\sigma^*\pi$ bands cross and the same will be observed for $p_y\sigma\pi^*$ and $p_y\sigma^*\pi$ bands along Γ-*Y*. The Fermi level resides at the crossing: the ideal situation for a Peierls instability and a distortion.

Distortion from the tetragonal unit cell to the observed orthorhombic one, while retaining $x =$ $y = 0.25$ for P5, will break only the degeneracy of the p_x and p_y bands, but the crossing will remain (Fig. 8b). The shifts along the *a* direction, resulting in dimer formation, will pull down the bonding $p_x\sigma\pi$ and $p_x\sigma\pi^*$ states and push up the antibonding $p_x\sigma^*\pi$ and $p_x\sigma^*\pi^*$ ones, thus leading to an energy gain and a gap opening along Γ-*X* (Fig. 8c). Along Γ-*Y* the crossing of the $p_y\sigma\pi^*$ and $p_y\sigma^*\pi$ bands still remains. Now we use a localized picture and grasp the role of the additional P6 sites in $GdCuP_{2.20}$. If the p_x orbitals of P5 form bonds in the dimers, the half-occupied p_y orbitals of P5 are not much involved in the bonding. Upon introducing P6 into the structure, the atomic orbitals of P6 will

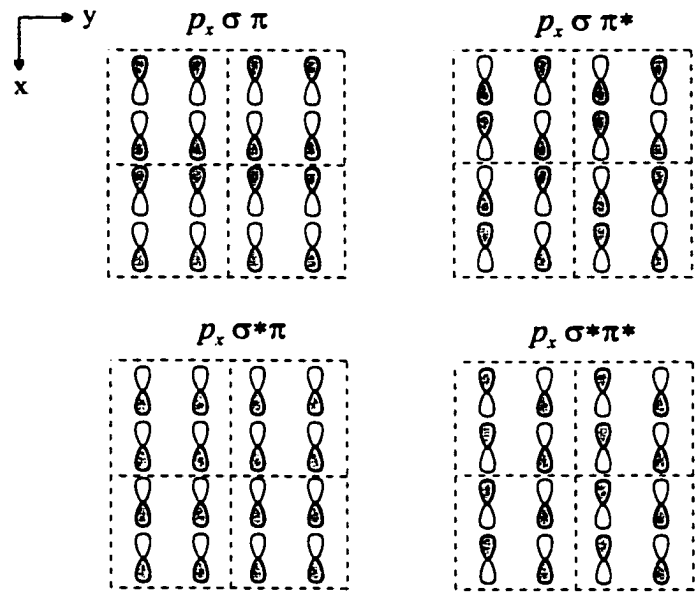

Figure 7. Molecular orbitals (MO's) from the p_x orbitals of the P5 atoms.

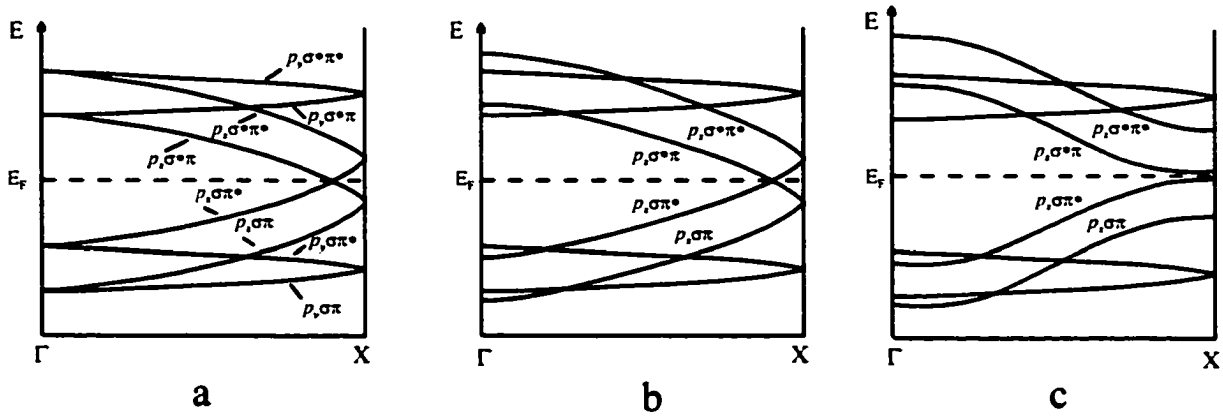

Figure 8. Schematic band structures of the P5 layers (only p_x and p_y bands are shown) along Γ-X: (a) the P5 layer is square; (b) after an orthorhombic distortion ($a < b$) like that in $GdCuAs_{1.15}P_{0.85}$; (c) phosphorus dimers are formed. The dashed line represents the Fermi level.

interact with the p_y orbitals of P5. To see the energy gain MO's are constructed from the $\sigma\pi$, $\sigma\pi^*$, $\sigma^*\pi$ and $\sigma^*\pi^*$ combinations of the P5 p_y orbitals and the P6 s and p orbitals. At the Γ point the symmetry allowed overlaps are only those between $p_y\sigma\pi$ and s and p_z, $p_y\sigma\pi^*$ and p_x, $p_y\sigma^*\pi$ orbitals of P5 and p_y orbitals of P6 (Fig. 9). As a consequence of bond formation, the resulting bonding MO's have lower energies than the original orbitals, the opposite is true for the antibonding MO's. The nine electrons occupy the lowest five MO's, with the HOMO being higher than the p orbitals of P6 and antibonding (Fig. 9). Filling of the antibonding HOMO with one electron is costly in energy and,

probably this is the reason for partial occupancy of P6. In total, the change in energy is favorable and leads to an energy gain upon formation of the bands from the described MO's. The presented process of the bond formation is simplified, in reality the P6 orbitals will interact not only with the p_y but also with the s, p_x and p_z orbitals of P5. Figure 10 shows the calculated band structure of the $[(P5)_4P6]^{4-}$ layer of $GdCuP_{2.20}$. Although there are both s-p mixing and additional interactions, the character of the bands at the Fermi level can be now understood. The complete band structure of $GdCuP_{2.20}$ is complicated, but the bands at the Fermi level are formed mainly by the P5 and P6 orbitals and their character is similar to that of the bands in Fig. 9. The complete band structure is not presented since it does not contribute much to the further understanding of the distortion process.

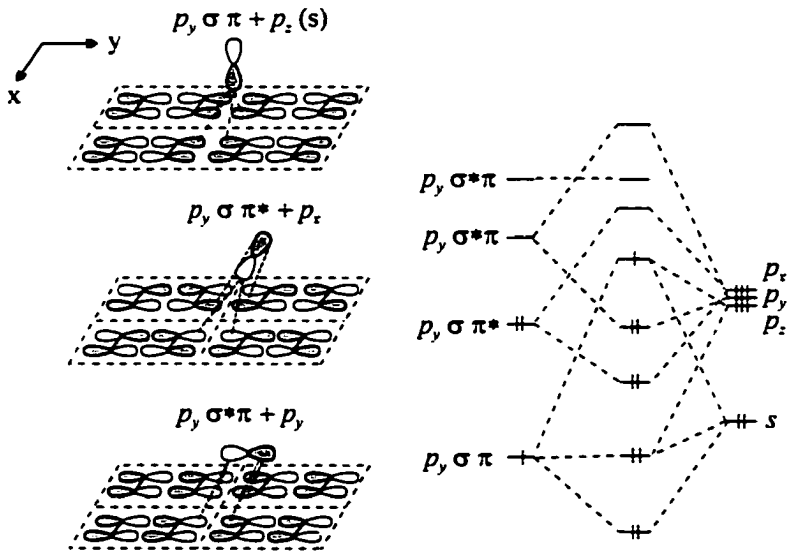

Figure 9. MOs formed from p_y orbitals of P5 and s and p orbitals of P6 (left); schematic energy diagram of the obtained MOs (right).

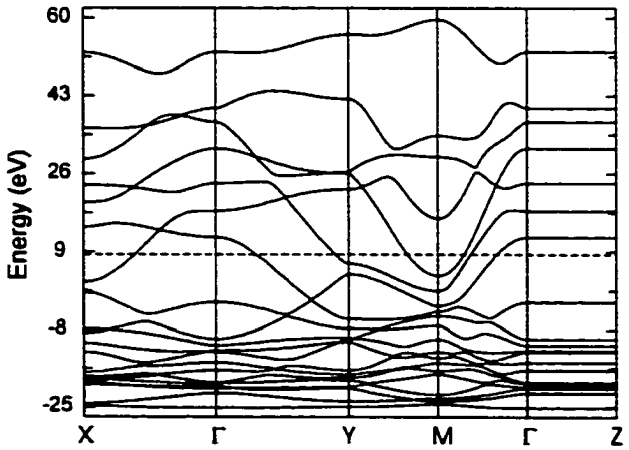

Figure 10. Calculated band structure of the $[(P5)_4P6]^{4-}$ layer of the phosphide. The position of the Fermi level corresponds to the 78% occupancy of the P6 site.

3.4. Electronic Structure and Bonding in $GdCuAs_2$ and $GdCuAs_{1.15}P_{0.85}$

The schematic band structures in Fig. 8a and 8b describe also the As^{1-} and $(As/P)^{1-}$ layers in $GdCuAs_2$ and $GdCuAs_{1.15}P_{0.85}$, respectively. The Fermi level is at the crossing, but no distortions, lifting the degeneracy, are observed (see also the calculated band structure of $GdCuAs_2$ in Fig. 11). One reason for this could be that the formation of the localized single bonds from delocalized ones in the square net is energetically more favorable for P than for As. The enthalpies for dissociation of the P-P and As-As single bonds can serve as qualitative (but crude) indicators of the process. They can be calculated from the enthalpies of the reactions $\frac{1}{4} X_4$ (g) = $\frac{1}{2} X_2$(g) and $\frac{1}{2} X_2$(g) = X(g) in the gaseous form (43):

$\frac{1}{4} P_4(g) = P(g)$ $\quad\quad$ $\Delta H^o = 72.1(2)$ kcal/mol

$\frac{1}{4} As_4(g) = As(g)$ $\quad\quad$ $\Delta H^o = 62.0(18)$ kcal/mol

The other reason may be the same as for the series of P, As, Sb and Bi with a decreasing magnitude of distortion (14). If so, the *s-p* mixing contributes to a distortion largely in $GdCuP_{2.20}$, less in $GdCuAs_{1.15}P_{0.85}$ and has no effect in $GdCuAs_2$.

A discussion of the partial As/P occupancies in the $GdCuAs_{1.15}P_{0.85}$ structure, in which arsenic dominates in the distorted X^{1-} layer while the phosphorus atoms are mainly in the $Cu_2X_2^{+}$ block (Table 3) follows. From the geometric point of view the larger As atoms (r = 1.25 Å for the gray modification) will enter into the slightly distorted square X^{1-} net with the closest neighbors at 2.721 Å. The smaller P atoms (r = 1.11 Å for the white modification) will prefer the compact $Cu_2X_2^{+}$ layer.

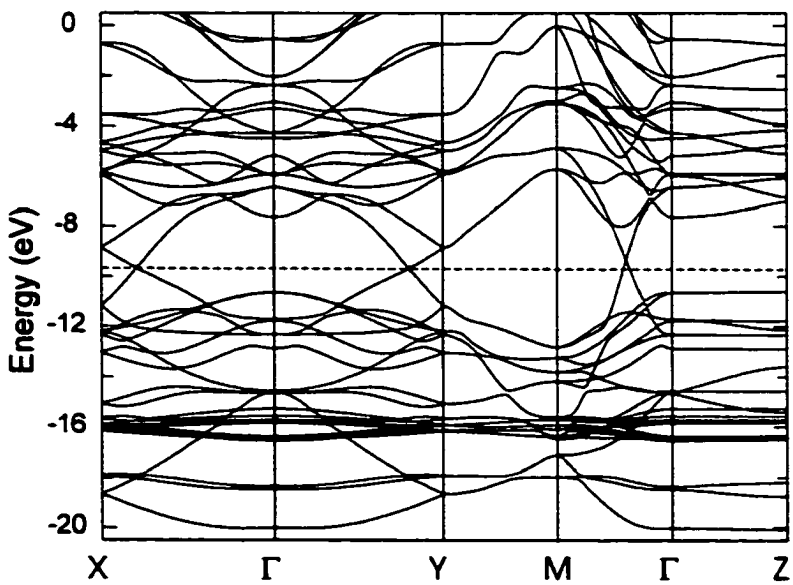

Figure 11. Band structure of $GdCuAs_2$

The same conclusion will follow from the analysis of the band structure. Since due to the *s-p* mixing the states of the X^{1-} net are antibonding at the Fermi level (Fig. 12), the less electronegative element (As here) with the less disperse bands will be a better choice for the net. This stability conclusion is based on the fact that when the orbitals overlap, the antibonding combinations are more antibonding than the bonding ones are bonding. Filling the antibonding combinations, filling the tops of widely dispersed bands, is costly in energy. However, the opposite is true for the $Cu_2X_2^{+}$ layer. Now, the states at the Fermi level are bonding (Fig. 12) and the more electronegative element (P here) will give greater stabilization energy.

If both the geometric and energetic factors favor separation of the P and As toms in the $GdCuAs_{1.15}P_{0.85}$ structure, the question may be asked why the As/P mixtures exist at all. The answer comes from the entropy part in the Gibbs free energy. According to statistical mechanics the entropy for the completely random solid solution would be:

$$\Delta S/R = -2(x_{As}\ln x_{As} + x_P \ln x_P) = 1.36,$$

which yields a stabilizing contribution of 1.36x1073x8.314 = 12,132 J/mol to the Gibbs free energy at 1073K, the temperature of the cold zone.

3.5. Electrical Conductivity and Magnetic Susceptibility

From the band structure calculations $GdCuAs_2$ and $GdCuP_{2.20}$ are expected to be metallic. Two-probe resistivity measurements reveal that the arsenide and phosphide show metallic behavior

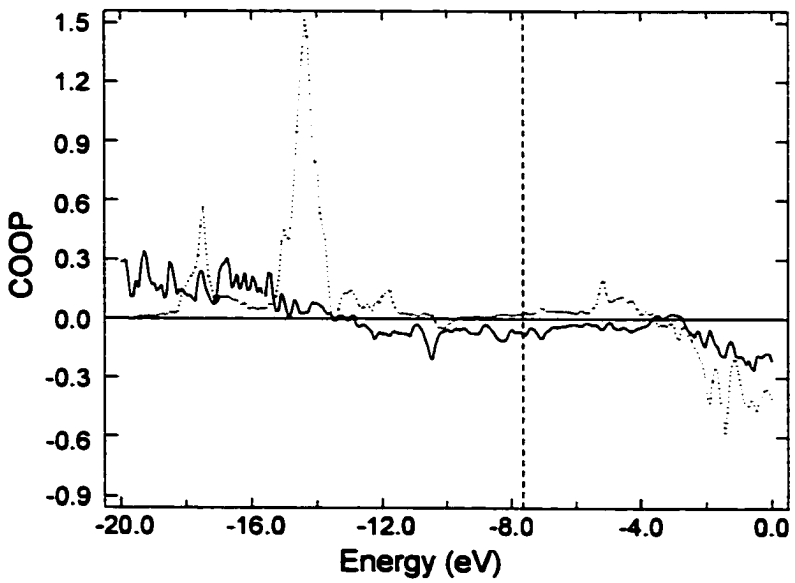

Figure 12. COOP curves for GdCuAsP. The *X*1 and *X*2 positions are assumed to be occupied by P and As atoms, respectively. Interactions in the upper part are bonding in the lower part antibonding. Solid line is As-As interactions, dotted is Cu-P interaction.

throughout the temperature range 4 - 285 K (Fig. 13). The specific resistivities could not be determined since the resistivities of the contacts in the two probe technique could not been measured exactly. The resistivities decrease monotonically by about 50% for arsenide and 60% for phosphide to 4K. Small resistivity anomalies are observed in the temperature range of the antiferromagnetic ordering; the temperatures of the resistivity increase, detected in the cooling and heating cycles, agree well with the magnetic data. No hysteresis was observed. The anomalies are typically attributed to increased spin-flip scattering in the critical temperature range.

The temperature dependencies of the inverse molar magnetic susceptibility of $GdCuAs_2$ and the phosphide are presented in Figs. 14a and 14b, respectively. The composition of the phosphide is

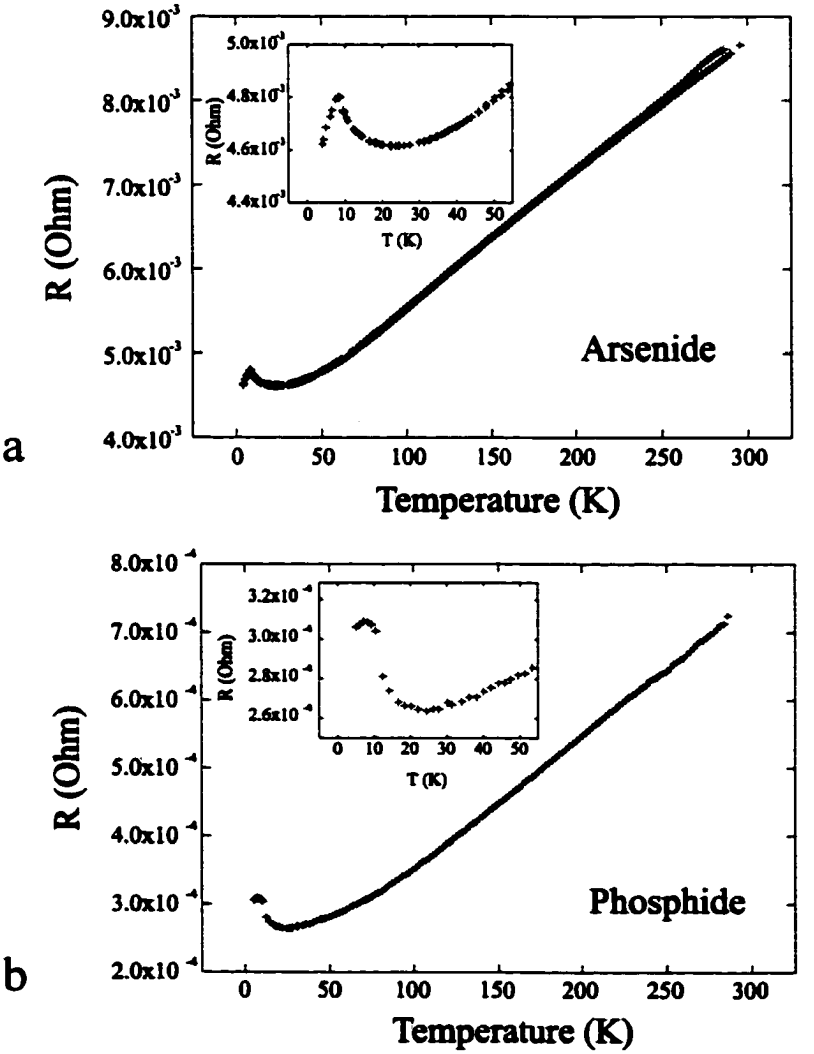

Figure 13. Resistance versus temperature curves for arsenide powder (a) and a phosphide single crystal (b).

not given since it may be different for powder and a single crystal. For both compounds the susceptibility above 50 K follows the Curie-Weiss (CW) law well. The CW parameters found by a least-square fitting procedure are as follows: θ_p = -1 K, μ_{eff} = 7.74 μ_B and θ_p = -5 K, μ_{eff} = 7.87 μ_B for the powder and single crystal of the phosphide and θ_p = -4 K and μ_{eff} = 7.96 μ_B for the arsenide. It is worth to noting that the experimental values of the effective magnetic moment are very close to the value expected for a free Gd^{3+} ion with the $4f^7$ electronic configuration ($g\sqrt{J(J+1)} = 7.94$). Slight deviations of χ^{-1}(T) from a straight-line behaviour, observed for both ternaries below 50 K, presumably result from crystal field interactions.

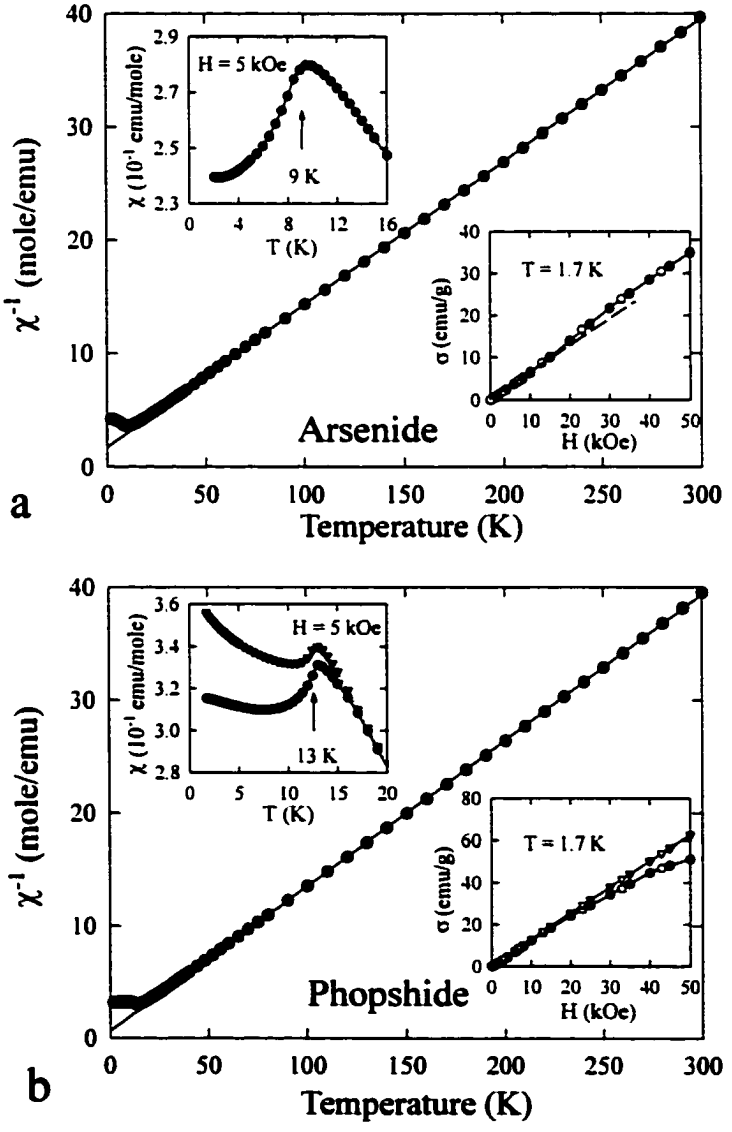

Figure 14. Magnetic susceptibility for arsenide powder (a) and a single crystal (triangles) and powder (dots) of the phosphide (b).

As is apparent from the upper insets to Figs. 14a and 14b, showing the behavior of $\chi(T)$ at low temperatures, the arsenide and phosphide order antiferromagnetically below 9 and 13 K, respectively. An antiferromagnetic nature of the ground state in the two compounds studied is corroborated by characteristic field variations of the magnetisation (see the lower insets to Figs. 14a and 14b), which exhibit metamagnetic-like transitions in a field of about 5 kOe.

4. Conclusions

The Landau theory was used for the analysis of the symmetry-breaking transitions. It showed that the transition from $GdCuAs_2$ to $GdCuAs_{1.15}P_{0.85}$ can be a continuous one, the transition from $GdCuAs_{1.15}P_{0.85}$ to $GdCuP_{2.20}$ is a first-order one. The $GdCuAs_{1.15}P_{0.85}$ structure (*Pmmn* sp. group) was predicted by the Landau theory.

The transitions are triggered by the innate instability of a square *2D* net with partially filled bands. Only a small orthorhombic distortion is found for the (As/P) layer in $GdCuAs_{1.15}P_{0.85}$. In $GdCuP_2$ P dimers are formed along the *a* direction, these dimers are linked by the additional P atoms (P6). The additional P site has stabilizing effect on the dimers by minimizing the distortion along *b* and by preventing, in this way, the formation of the zigzag or other types of chains. Although in the $GdCuAs_{1.15}P_{0.85}$ structure both the geometric and energetic factors favor separation of the P and As atoms, the statistical As/P mixtures exist due to the entropy contribution to the Gibbs free energy.

Acknowledgements

This research was supported by the Office of the Basic Energy Sciences, Materials Sciences Division, US Department of Energy, DOE. The Ames Laboratory is operated for DOE by Iowa State University under contract No. W-7405-Eng-82.

Part of the work was done at the group of Prof. W. Tremel, Johannes Gutenberg University, Mainz, Germany, while Yurij Mozharivskyj was a DAAD scholar.

Special thanks to Dr. Sasha Pecharsky for collecting powder diffraction data and to Dr. Dong-Kyun Seo for his help and discussion during the band structure calculations.

References

1. R.E. Peierls, "Quantum Theory of Solids". Oxford University Press, London, 1955.

2. T.A. Albright, J.K. Burdett and M.-H. Whangbo, "Orbital Interactions in Chemistry". Wiley, New York, 1985.

3. H.A. Jahn, E. Teller, *Proc Roy. Soc.* **A 161**, 220 (1937).

4. F. Hulliger, R. Schmelczer, D. Schwarzenbach, *J. Solid State Chem.* **21**, 371 (1977).

5. (a) G. Sfez and C. Adolphe, *C. Bull. Soc. Fr. Mineral. Kristallogr.* **95**, 553 (1972). (b) R. Ceolin, N. Rodier and P. Khodadad, *J. Less-Common Met.* **53**, 137 (1977).

6. W. Tremel and R. Hoffmann, *J. Am. Chem. Soc.* **109**, 124 (1987).

7. (a) R. Wang, R. Bodnar and H. Steinfink, *Inorg. Chem., Washington D.C.* **5 (8)**, 1468 (1966). (b) R.E. Bodnar and H. Steinfink, *Inorg. Chem., Washington D.C.* **6 (2)**, 327 (1967).

8. (a) F. Hulliger and R. Schmelczer, *J. Solid State Chem.* **26**, 389 (1978). (b) M. Wittmann, W. Schmettow, D. Sommer, W. Bauhofer and H.G. von Schnering, *Solid Compounds of Transition Metals VI, International Conf., Stuttgart, 1979*, 217 (1979).

9. (a) A. Brown and S. Rundqvist, *Acta Crystallogr.* **19**, 684 (1965). (b) D. Schiferl and C.S. Barrett, *J. Appl. Crystallogr.* **2**, 30 (1969). (c) C.S. Barrett and P. Cucka, *Acta Crystallogr.* **16**, 451 (1963). (d) C.S. Barrett and P. Cucka, *Acta Crystallogr.* **15**, 865 (1962).

10. U. Müller, "Inorganic Structural Chemistry", Wiley, Chichester, England, 1993.

11. J.K. Burdett and S. Lee, *J. Am. Chem. Soc.* **105**, 1079 (1983).

12. P.B. Littlewood, *J. Phys. C* **13**, 4855 (1980).

13. P.B. Littlewood, *CRC Crit. Rev. Solid State Mater. Sci.* **11**, 229 (1980).

14. D.-K. Seo and R. Hoffmann, *J. Solid State Chem.* **147**, 26-37 (1999).

15. E. Canadell and M.-H. Whangbo, *Chem. Rev.* **91**, 1034 (1991).

16. M.-H. Whangbo and E. Canadell, *J. Am. Chem. Soc.* **114**, 9687 (1992).

17. G. Gordier, B. Eisenmann and H.Z. Schäfer, *Z. Anorg. Allg. Chem.* **426**, 205 (1976).

18. G. Gordier and H.Z. Schäfer, *Z. Naturforsch.* **32b**, 383 (1977).

19. E. Brechtel, G. Gordier and H.Z. Schäfer, *Z. Naturforsch.* **34b**, 251 (1979).

20. E. Brechtel, G. Gordier and H.Z. Schäfer, *Z. Naturforsch.* **35b**, 1 (1980).

21. G. Gordier, H.Z. Schäfer and P. Woll, *Z. Naturforsch.* **40b**, 383 (1985).

22. O. Sologub, K. Hiebl, P. Rogl, H. Noël and O. Bodak, *J. Alloys Compd.* **210**, 153 (1994).

23. M. Brylak, M.H. Möller and W. Jeitschko, *J. Solid State Chem.* **115**, 305 (1995).

24. S.I. Chykhrij, Yu.B. Kuz'ma and S.V. Oryshchyn, *Dopov. Akad. Nauk Ukr. RSR, Ser. B*, **3**, 63 (1989).

25. S.I. Chykhrij, G.V. Loukashouk, S.V. Oryshchyn and Yu.B. Kuz'ma, *J. Alloys Compd.* **248**, 224 (1997).

26. S.I. Chykhrij, Yu.B. Kuz'ma, S.V. Oryshchyn, B.V. Khabursky and V.S. Fundamenskii, *Dopov. Akad. Nauk Ukr. RSR, Ser. B*, **9**, 49 (1990).

27. M. Wang, R. McDonald and A. Mar, *J. Solid State Chem.* **147**, 140 (1999).

28. Yu.B. Kuz'ma, Yu.A. Mozharivskyj, and O.N. Panas, *Inorg. Mater.* **34**, 7 (1998).

29. Yu. Mozharivskyj, O. Lang, D. Kaczorowski and H.F. Franzen, *1999 Midwest High Temperature Solid State Conf.*, June 10-12, 1999, Ames, Iowa.

30. Yu. Mozharivskyj and H.F. Franzen, *210th. ACS National Meet.*, March 26-30, 2000, San Francisco, California.

31. L.G. Akselrud, Yu.M. Grin and P.Yu. Zavalij, CSD - universal program package for single crystal and powder data treatment, *Proc.12th European Crystallographic Meet., Moscow, August 20-28, 1989*, Academy of Sciences, Moscow, USSR, *Kristallographiya, Suppl.*, **155**, 2-3 (1989).

32. *SHELXTL*, Bruker Analytical X-Ray Systems, Madison, USA 1997.

33. J. Ren, W. Liang and M.-H. Whangbo, *Crystal and Electronic Structure Analyser (CAESAR)*, North Carolina State University, Raleigh, NC, 1998.

34. S. Alvarez, *Table of Parameters for Extended Hückel Calculations*, Barcelona 1987.

35. (a) E. Hassler, T. Johnson and S. Rundqvist, *Acta Chem. Scand. Ser. A* **27**, 123 (1974). (b) Yu. Kuz'ma, S. Chykhrij, *in* "Handbook on the Physics and Chemistry of Rare Earths", K.A. Gscheidner, Jr. and L.R. Eyring, Vol. 23, p. 302. Elsevier, Amsterdam, 1996.

36. H.G. von Schnering, W. Wichelhaus and N.M.Schulze, *Z. Anorg. Allg.Chem.* **412**, 193 (1975).

37. W. Wichelhaus and H.G. von Schnering, *Z. Anorg. Allg.Chem.* **419**, 77 (1976).

38. W. Wichelhaus and H.G. von Schnering, *Naturwissenschaften*, **62**, 180 (1975).

39. L.D. Landau and E.M. Lifshitz, "Statistical Physics", Vol. 5, Permagon Press, London, 1958.

40. H.F. Franzen, *Chem. Mater.* **2**, 486 (1990).

41. H.F. Franzen, "Basic Principles of Symmetry and Stability of Crystalline Solids", World Scientific, Singapore, 1994.

42. G.J. Miller, F. Li and H.F. Franzen, *J. Am. Chem. Soc.* **115 (No. 9)**, 3739 (1993).

43. P. Hultgern , P. D. Desai, D.T. Hawkins, M. Gleiser, K.K. Kelley and D.D. Wagman, "Selected Values of the Thermodynamic Properties of the Elements", American Society for Metals, Metals Park , Ohio, 1973.

CHAPTER 4. TESTING THERMAL STABILILTY OF ORTHORHOMBIC $GdCuP_{2.16}$ STRUCTURE

A paper accepted for publication in Journal of Alloys and Compounds

Yurij Mozharivskyj[a], Vitalij K. Pecharsky[b] and Hugo F. Franzen[a]

[a]*Department of Chemistry,* [b]*Department of Materials Sciences and Ames Laboratory of US DOE, Iowa State University, Ames, Iowa 50011, USA*

Abstract

Thermal stability with respect to a structural transformation and the crystal structure of the orthorhombic gadolinium copper phosphide $GdCuP_{2.16}$ was investigated using powder diffraction techniques. The structure was refined from the data collected at room temperature to yield *Pmm*2 space group, a = 5.3284(1), b = 5.3868(1) and c = 9.7486(2) Å. The refinement results agree well with the single crystal results (Y. Mozharivskyj, D. Kaczorowski, and H. F. Franzen, *J. Solid State Chem.* **155**, 259-272 (2000)). Although the phosphide preserves the orthorhombic crystal structure up to 700°C, the thermal expansion along the a axis becomes larger than those along b and c axes above 500°C, indicating that a structural transformation is likely to occur at higher temperatures.

Keywords: gadolinium copper phosphide, crystal structure, structural stability.

1. Introduction

The $GdCuAs_{2-x}P_x$ series, reported recently [1], shows interesting symmetry-breaking transitions and crystal structures as a function of composition. Substitution of phosphorus for arsenic leads to a *P4/nmm* to *Pmmn* transformation followed by a second one from *Pmmn* to *Pmm*2 (Figure 1). According to Landau theory, the first transition can be continuous but the second transition is a first-order one. The orthorhombic structures (*Pmmn*) of the arsenophosphides $GdCuAs_{1.67}P_{0.33}$ through $GdCuAs_{0.33}P_{1.67}$ are adaptations to smaller P atoms and they are stabilized by the Coulomb interactions [2], on the contrary, the structure of the phosphide $GdCuP_{2.16}$ (*Pmm*2) is a consequence of the Peierls instability of the P square net [1]. In both cases the low-symmetry structures are energetically stabilized (through gains in the electrostatic or electronic energies), and probably they are stable only at low temperatures. The reverse structural transitions *Pmm*2 → *Pmmn* and *Pmmn* →

P4/nmm or even *Pmm2* → *P4/nmm* will increase the entropy of the phases ($\Delta S > 0$ in each case, since the higher symmetry structures have larger phonon densities [3]), and therefore if they occur, they will do so with increasing temperature.

The gadolinium copper phosphide $GdCuP_{2.16}$, the powder pattern of which shows a noticeable peak splitting, is suitable to investigate the possibility of a structural transition at high temperatures, and the results obtained are reported below. Since the peak splitting for the orthorhombic arsenophosphides (*Pmmn*) is very fine and is seen on a Guinier film but not on a diffraction pattern recorded on a conventional high-resolution θ-2θ diffractometer, the techniques we used did not provide enough resolution to trace structural transformations. Therefore the data for the arsenophosphides are not presented here.

2. Experimental

2.1. Synthesis

The starting materials were powdered gadolinium (99.9%, Alfa Aesar), copper (99.5%, Alfa Aesar) and amorphous red phosphorus (99%, Alfa Aesar). Weighing and handling of the sample with the initial composition $GdCuP_2$ were performed in an Ar-filled glove box. The powders with a total mass of 1.0g were thoroughly mixed, pressed into a pellet under 3000 kg using a 10-mm dial tool, and sealed in an evacuated silica tube. The sample was heated at the rate of 20°C/h to 600°C, kept at this temperature for 48 hours and cooled by switching off the furnace. The sample was ground, pressed, sealed, heated at 40°C/h to 800°C, kept at 800°C for 5 days and cooled. The second step was repeated once more with the heat treatment period being increased to 7 days.

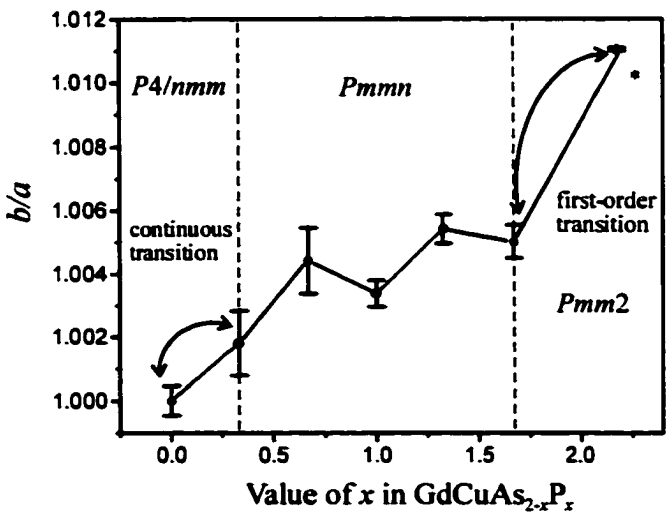

Figure 1. *b/a* ratio versus phosphorus concentration in $GdCuAs_{2-x}P_x$. * Composition of the phosphide is $GdCuP_{2.16}$ as determined from Rietveld refinement.

2.2. X-ray Analysis

The gadolinium copper phosphide sample was characterized using X-ray powder diffraction (Scintag diffractometer, solid state cooled detector, CuK_α, 25°C and Rigaku diffractometer, rotating anode, MoK_α, 25-700°C, 700°C was the upper temperature limit of the instrument). The temperature dependent lattice parameters (Table 1) were derived by the least-squares method using the CSD program package [4]. The structure of the phosphide was refined by the full-profile Rietveld technique (Figure 2, Table 2), using the CSD package, the atomic parameters from the single crystal refinement [1] were taken as an initial set. The refined parameters (Table 3) were close to those from the single crystal data, and the overall chemical compositions were similar ($GdCuP_{2.16}$ for the powder and $GdCuP_{2.20}$ for the single crystal). The structure contains an additional but partially occupied P6 site that results in the $GdCuP_{2.16}$ composition, which is different from the composition $GdCuP_2$ used for the synthesis.

Table 1. Lattice Parameters for $GdCuP_{2.16}$ as a Function of Temperature

T (°C)	*a*, Å	*b*, Å	*c*, Å	*b/a*	*V*, Å^3
25	5.3286(2)	5.3879(2)	9.7481(4)	1.01113(5)	279.87(3)
100	5.3320(2)	5.3912(2)	9.7550(4)	1.01110(5)	280.42(3)
200	5.3369(2)	5.3967(2)	9.7641(4)	1.01121(5)	281.23(4)
300	5.3423(2)	5.4023(2)	9.7740(4)	1.01123(5)	282.08(4)
400	5.3477(2)	5.4079(2)	9.7844(4)	1.01126(5)	282.96(4)
500	5.3551(2)	5.4142(2)	9.7963(4)	1.01104(5)	284.03(4)
600	5.3626(2)	5.4199(2)	9.8055(5)	1.01069(5)	285.00(4)
700	5.3798(3)	5.4239(3)	9.8144(6)	1.00820(5)	286.38(5)

Table 2. Data Collection and Least-Squares Refinement Results for $GdCuP_{2.16}$ at 25°C

Lattice parameters*, Å	$a = 5.3284(1)$
	$b = 5.3868(1)$
	$c = 9.7486(2)$
Diffractometer	Scintag
Wavelengths	Cu$K_{\alpha 1}$ and Cu$K_{\alpha 2}$
2θ range and step	20°-90°, 0.02°
$R_B = \Sigma \lvert I_o - kI_c \rvert / \Sigma I_o$	0.0835
$R_P = \Sigma \lvert y_{oi} - ky_{ci} \rvert / \Sigma y_{oi}$	0.1392

* The lattice parameters determined from the diffraction data collected using different wavelengths are slightly different and the CuK_α data should be considered more accurate.

Table 3. Atomic and Isotropic Thermal Displacement parameters for $GdCuP_{2.16}$ at 25°C

Atom		x	y	z	U_{eq}x100
Gd1	1*b*	0	1/2	0.2374(7)	0.22(3)
Gd2	1*c*	1/2	0	0.2325(7)	0.15(3)
Gd3	1*d*	1/2	1/2	0.7557(6)	0.20(3)
Gd4	1*a*	0	0	0.7688(6)	0.26(3)
Cu	4*i*	0.2580(8)	0.2548(9)	0.5007(9)	0.46(2)
P1	1*b*	0	1/2	0.6572(9)	0.61(3)
P2	1*c*	1/2	0	0.6564(9)	0.59(3)
P3	1*d*	1/2	1/2	0.3437(9)	0.56(3)
P4	1*a*	0	0	0.3427(9)	0.65(3)
P5	4*i*	0.2805(8)	0.2353(9)	-0.0017(10)	0.61(3)
P6[a]	1*a*	0	0	0.1174(9)	0.84(3)

[a] Occupancy is 65(2)%

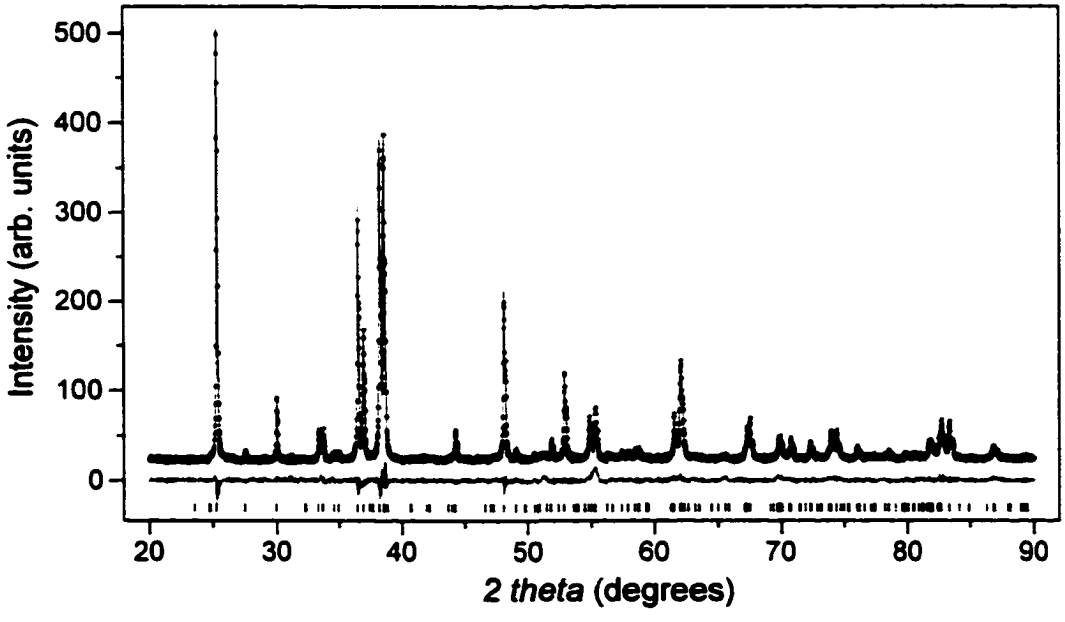

Figure 2. Observed (circles) and calculated (solid line) X-ray powder diffraction profiles and difference between them for the gadolinium copper phosphide (CuK_α radiation, 25°C). Vertical bars at the bottom of the plot indicate the calculated positions of the Bragg peaks.

3. Results and Discussion

3.1. Thermal Stability of the Orthorhombic $GdCuP_{2.16}$ Structure

As seen from the high-temperature diffraction data (Table 1), the phosphide retains its orthorhombic structure up to 700°C. Figure 3 presents experimental profiles for three temperatures and the insert shows 2θ changes for the 022 and 202 Bragg peaks at the temperature limits (the third

peak in the insert comes from Mo$K_{\alpha 2}$). Splitting of the 022 and 202 peaks is due to the difference between the *a* and *b* parameters. These peaks would merge if the $GdCuP_{2.16}$ structure transformed into the orthorhombic $GdCuAs_{1.15}P_{0.85}$-type structure (*Pmmn* space group, the 022 and 202 peaks would give the 112 peak) or into the tetragonal $HfCuSi_2$-type (*P4/nmm* space group).

Plots in Figures 4**a**, **b** and **c** indicate that up to 500°C the changes in the lattice parameters are due to the thermal expansion of the lattice. The relative changes in *a*, *b* and *c* (Figure 4**b**) are similar in the 25-500°C range, so the crystal expands nearly isotropicly between 25°C and 500°C. At 600°C and especially at 700°C the increase in *a* becomes larger than those in *b* and *c*, but the *a* parameter remains smaller than the *b* parameter and no structural transformation occurs below 700°C. Based on the observed onset of the anisotropic temperature dependence of the thermal expansion, it is likely that at a higher temperature the phosphide $GdCuP_{2.16}$ undergoes a structural transition, which can be *Pmm*2 → *Pmmn* or *Pmm*2 → *P4/nmm* or to a different space group.

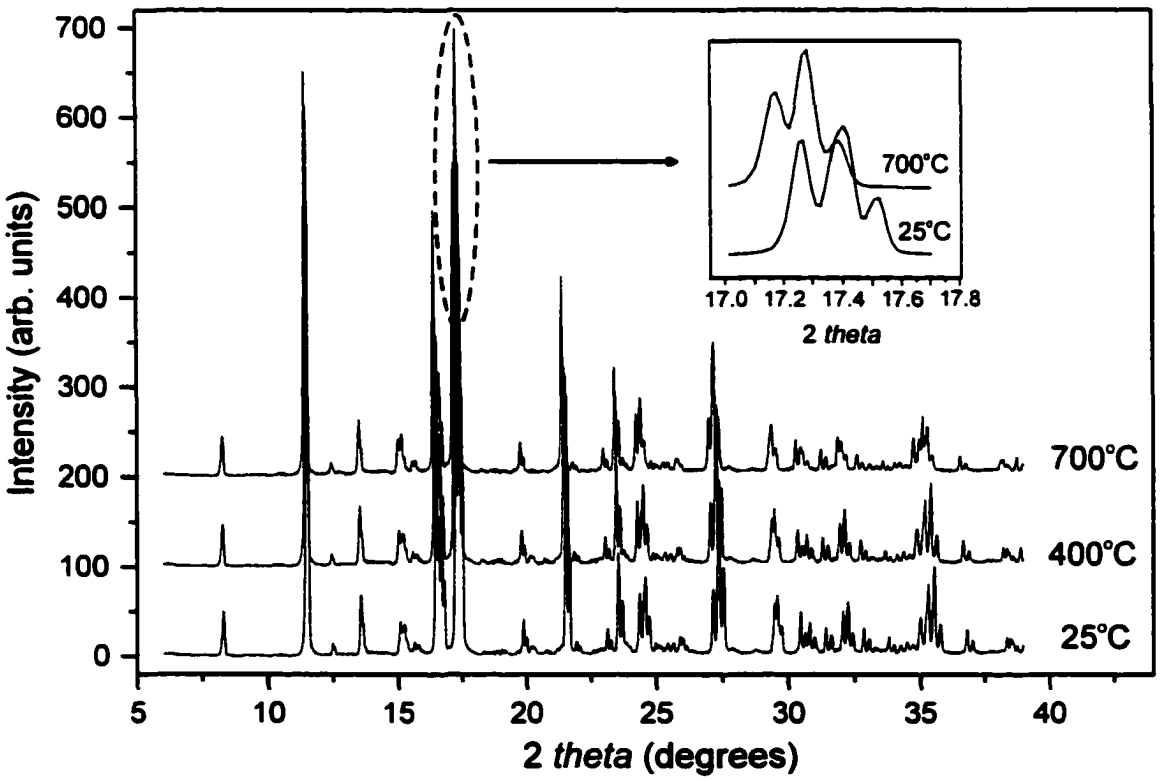

Figure 3. X-ray diffraction patterns of orthorhombic $GdCuP_{2.16}$ at three different temperatures (MoK_α radiation). The insert shows positions of the 022 and 202 Bragg peaks as a function of temperature.

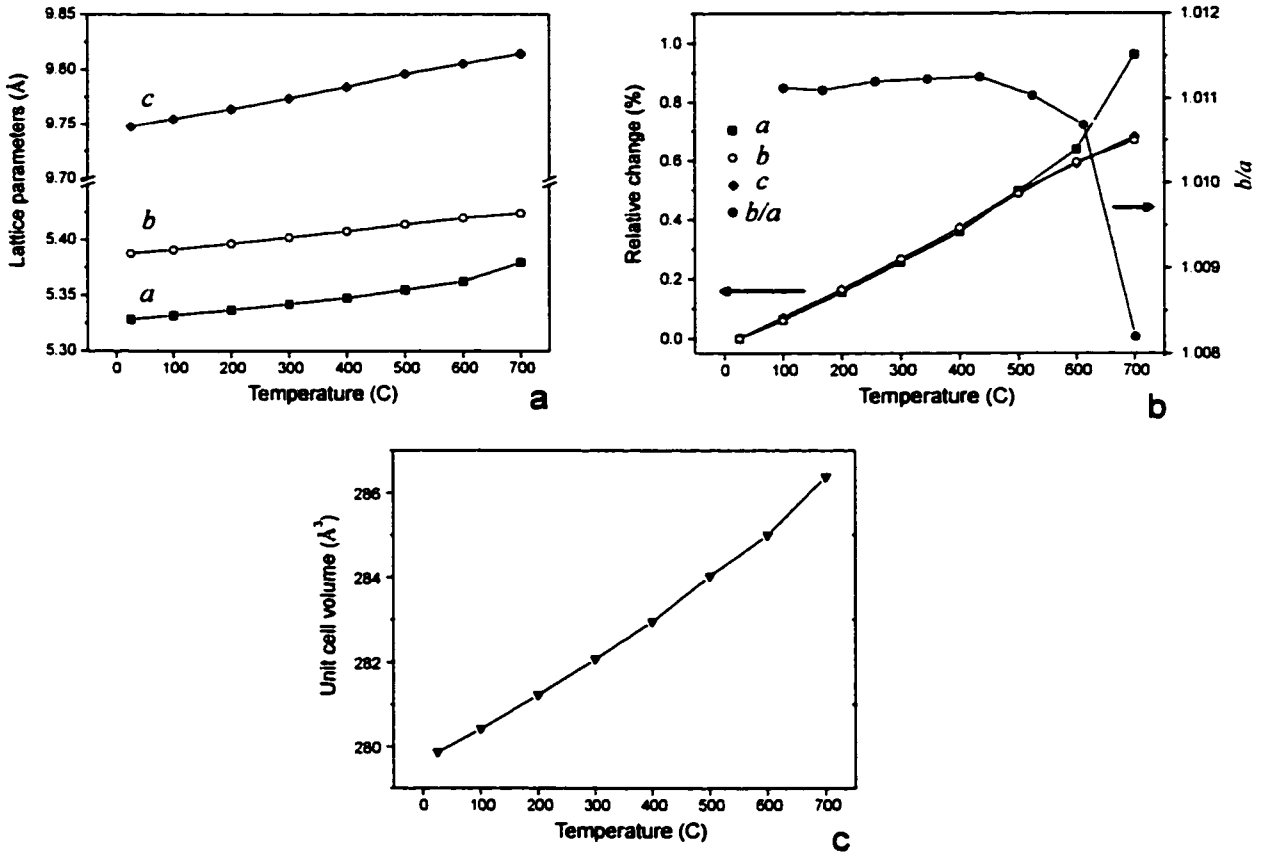

Figure 4. Absolute (**a**, **c**) and relative (**b**) changes of the lattice parameters of $GdCuP_{2.16}$ with temperature.

3.2. Crystal Structure Description

The structure of $GdCuP_{2.16}$ (Figure 5) is a distorted and partially filled variant of the $HfCuSi_2$ structure [5]. The structure can be viewed to consist of CuP blocks, in which the Cu atoms are tetrahedrally coordinated by the P1-4 atoms, of the Gd1-4 nets and P5P6 layers.

When compared to the $HfCuSi_2$ structure, the largest changes occur in the P layer, where P dimers are formed (Figure 6). The formation of phosphorus dimers along the *a* axis results form a Peierls instability of the square phosphorus net, which opens a band gap along the corresponding direction in the reciprocal space and lowers the electronic energy of the structure. These dimers are linked through additional P6 atoms that prevent formation of the short P5-P5 bonds along *b* and, thus, formation of zigzag or *cis-trans* chains. As discussed in [1], deficiency on the P6 site is expected and it is, indeed, experimentally observed.

The short P-P distances in $GdCuP_{2.16}$ ($\delta_{P5\text{-}P5}$ =2.34 Å, $\delta_{P5\text{-}P6}$ =2.23 Å) are similar to those found in the binary rare-earth phosphides. In CeP_2 [6, 7] and LaP_2 [8] phosphorus atoms are joined

into fragments of the zigzag chains of 4 or 3 and 5 atoms with $\delta_{P\text{-}P}$ =2.404-2.453 Å and $\delta_{P\text{-}P}$ =2.197-2.314 Å, respectively. In NdP_5 and LaP_5 [9] phosphorus forms a 3*D* framework and a layer with $\delta_{P\text{-}P}$ =2.162-2.211 Å and $\delta_{P\text{-}P}$ =2.167-2.216 Å.

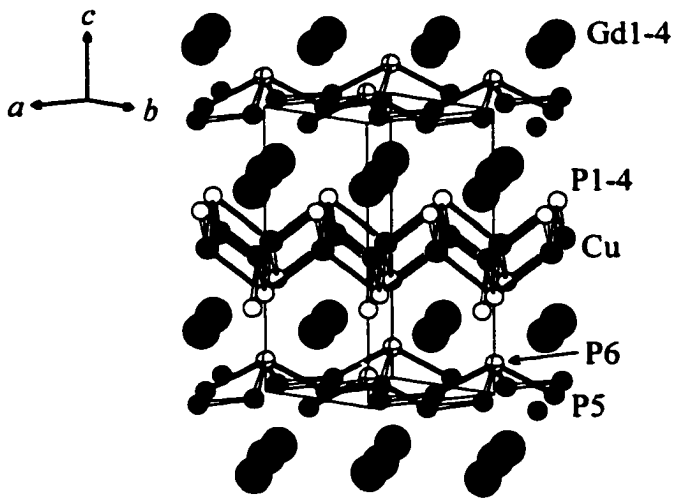

Figure 5. Crystal structure of $GdCuP_{2.16}$.

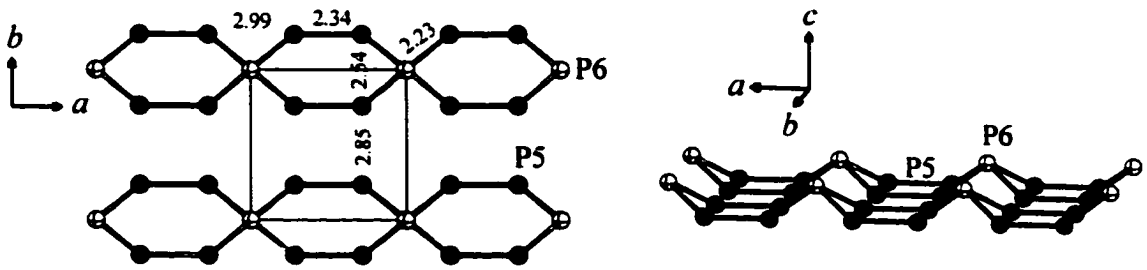

Figure 6. Phosphorus layer in $GdCuP_{2.16}$.

4. Conclusions

The phosphide $GdCuP_{2.16}$ preserves the orthorhombic structure (*Pmm*2 space group) up to 700°C. As judged from the onset of the anisotropic changes in the *a* parameter at 600°C and 700°C, a structural transition is likely to occur at higher temperatures. Lattice and atomic parameters derived from the 25°C powder diffraction data are close to single crystal ones.

Acknowledgement

This research was supported by the Office of the Basic Energy Sciences, Materials Sciences Division, US Department of Energy, DOE. The Ames Laboratory is operated for DOE by Iowa State University under contract No. W-7405-Eng-82.

References

[1] Y. Mozharivskyj, D. Kaczorowski, H. F. Franzen, J. Solid State Chem. 155 (2000) 259.

[2] Y. Mozharivskyj, H. F. Franzen, submitted to J. Phys. Chem.

[3] C. Kittel, in "Introduction to Solid State Physics", 7th ed. John Wiley & Sons, Inc., New York, 1996, p. 122

[4] L. G. Akselrud, Y. M. Grin, V. K. Pecharsky, P. Y. Zavalij, CSD - universal program package for single crystal and powder data treatment, Proc.12th European Crystallographic Meet., Academy of Sciences, Moscow, USSR, August 28-29, 1989, Kristallographiya, Suppl., 155 (1989) 2.

[5] L. S. Andrukhiv, L. A. Lysenko, Y. P. Yarmolyuk, E. I. Gladyshevskii, Dopov. Akad. Nauk Ukr. RSR, Ser. A, (1975) 645.

[6] E. Hassler, T. Johnsson, S. Rundqvist, Acta Chem. Scand. 28, (1974) 123.

[7] Y. Kuz'ma, S. Chykhrij, in "Handb. Phys. Chem. Rare Earths" (K. A. Gschneider, Jr. and L. Eyring, Ed.), Vol. 23, pp. 285-434. Elsevier, Amsterdam, 1996.

[8] H. G. von Schnering, W. Wichelhaus, M. Schulze Nahrup, Z. Anorg. Allg. Chem. 412 (1975) 193.

[9] W. Wichelhaus, H. G. von Schnering, Z. Anorg. Allg. Chem. 419 (1976) 77.

CHAPTER 5. SYMMETRY-BREAKING TRANSITIONS IN $HoCuAs_{2-x}P_x$ and $ErCuAs_{2-x}P_x$ (x = 0-2): CRYSTAL STRUCTURE, APPLICATION OF LANDAU THEORY, MAGNETIC AND ELECTRICAL PROPERTIES

A paper published in Zeitschrift für anorganische und allgemeine Chemie
Z. Anorg. Allg. Chem. **2001**, *201*, 2163

Yurij Mozharivskyj[a], Dariusz Kaczorowski[b] and Hugo F. Franzen[a]
[a]*Department of Chemistry and Ames Laboratory of US DOE, Spedding Hall, Iowa State University, Ames, Iowa 50011, USA*
[b]*W. Trzebiatowski Institute of Low Temperature and Structure Research, Polish Academy of Sciences, P.O. Box 1410, 50-950 Wroclaw, Poland*

Abstract

Crystal structures of compounds undergoing symmetry-breaking transitions have been investigated by the X-ray single crystal and powder methods. While the phases $HoCuAs_2$ through $HoCuAs_{1.33}P_{0.67}$ and $ErCuAs_2$ through ErCuAsP retain the tetragonal $HfCuSi_2$ structure (*P4/nmm* space group), the compounds HoCuAsP through $HoCuAs_{0.33}P_{1.67}$ and $ErCuAs_{0.67}P_{1.33}$ through $ErCuAs_{0.33}P_{1.67}$ undergo orthorhombic distortions to the $GdCuAs_{1.15}P_{0.85}$ structure (*Pmmn* space group). Further distortions follow in the phosphides: $HoCuP_2$ adopts a larger orthorhombic cell (*Cmma*, a = 5.273(3), b = 5.305(3), c = 9.645(5) Å) and $ErCuP_2$ has a monoclinic cell with a doubled parameter, the b parameter in the monoclinic cell ($P2_1/n$, a = 3.737(3), b = 19.239(15), c = 3.728(3) Å, β = 90.09(1)°). Zigzag chains are formed in the phosphorus layer of $ErCuP_2$.

According to Landau theory the transitions from $HoCuAs_{1.33}P_{0.67}$ to HoCuAsP and from ErCuAsP to $ErCuAs_{0.67}P_{1.33}$ can be continuous, and the transitions from $HoCuAs_{0.33}P_{1.67}$ to $HoCuP_2$ and from $ErCuAs_{0.33}P_{1.67}$ to $ErCuP_2$ are necessarily first-order.

The results of magnetic and electrical measurements for $HoCuAs_2$ and $HoCuP_2$ are reported. Due to the magnetic moments localized on Ho atoms both compounds order antiferromagnetically at low temperatures. They exhibit metallic conductivity.

Keywords: copper; holmium; erbium; pnictides; crystal structure; symmetry-breaking transitions; Landau theory.

1. Introduction

Intermetallic compounds with structures of the $BaAl_4$ – type contain 2D square nets of the main group elements [1-11]. The bands formed by the p_x and p_y orbitals of the atoms within these nets are quite dispersed and crossed along symmetry lines in the Brillouin zone (BZ). If the electronic count is favorable, the Fermi level lies at the crossing. The presence of these degenerate half-filled states leads to a large coupling of the vibrational and electronic motions. There is at least one normal mode that will open a gap and lower the energy of the system and, of course, its symmetry as well. These electronic instabilities and the resulting distortions are generalizations of "Peierls" type distortions. In the previous work [1] the $GdCuAs_{2-x}P_x$ series was found to exhibit Peierls instabilities of the As/P or P layers which trigger symmetry-breaking transitions from tetragonal $GdCuAs_2$ through orthorhombic $GdCuAs_{1.15}P_{0.85}$ to orthorhombic $GdCuP_{2.20}$, with the latter having a larger unit cell. In $GdCuAs_{1.15}P_{0.85}$ the distortions are small: the distances in the As/P layer are the same, but the angles deviate slightly from 90°. In $GdCuP_{2.20}$ P dimers are formed along the *a* direction in the P net, these dimers are linked by the additional P atoms on one side of the net. The additional but deficient P site has a stabilizing effect on the dimers by minimizing the distortion along *b* and by preventing, in this way, the formation of the zigzag or other types of chains [1].

Application of the Landau theory to $GdCuAs_{2-x}P_x$ helped us to predict the symmetry of the arsenophosphides and to analyze the nature of the symmetry-breaking transitions. According to Landau theory the transition from $GdCuAs_2$ to $GdCuAs_{1.15}P_{0.85}$ can be continuous, the transition from $GdCuAs_{1.15}P_{0.85}$ to $GdCuP_{2.20}$ is first-order. These distortions in the $GdCuAs_{2-x}P_x$ series are associated with splitting of some peaks in the X–ray powder patterns. We noticed a similar splitting for $HoCuP_2$ and $ErCuP_2$ [1], which could indicate symmetry-breaking transitions in these systems. Here we report structures of the $HoCuAs_{2-x}P_x$ and $ErCuAs_{2-x}P_x$ phases, magnetic and electric properties of $HoCuAs_2$ and $HoCuP_2$ and analyze the observed distortions in terms of the Landau theory. Investigation of the physical properties of the $ErCuAs_{2-x}P_x$ phases and analysis of the electronic structure of the compounds of both series are in progress and they will be reported later.

2. Experimental Part

2.1. Synthesis

The starting materials were powdered holmium and erbium (99.9%, Alfa Aesar), copper (99.99%, Metals Development, Ames laboratory), amorphous red phosphorus (99%, Alfa Aesar) and arsenic (99.99%, Alfa Aesar). Weighing and handling of the samples were performed in an Ar-filled glove box. The powders with a total mass of 0.5 g were intimately mixed, pressed to pellets under a

pressure of 2000 kg using a 10-mm dial tool, and sealed in evacuated silica tubes. For the X-ray powder analysis the samples with compositions $HoCuAs_{2-x}P_x$ (x = 0, 0.33, 0.67, 1.00, 1.33, 1.67, 2.00) and $ErCuAs_{2-x}P_x$ (x = 0, 1.00, 1.33, 1.67, 2.00) were heated at the rate of 20°C/h to 600°C, kept at this temperature for 48 hours and furnace cooled. The samples were ground, pressed, sealed, heated at 40°C/h to 800°C, kept at 800°C for 7 days and cooled.

Single crystals of $HoCuAs_2$, $HoCuAs_{0.99}P_{1.01}$, $HoCuP_2$, $ErCuAs_{1.07}P_{0.93}$ and $ErCuP_2$ were obtained by the iodine gas transport technique in a zone furnace, using silica tubes of ~200mm in length and 10mm in inner diameter. The samples were heated at 20°C/h to 800°C, kept for 10 or 14 days and then furnace cooled. Table 1 summarizes the experimental details of the successful crystal growth: T_1 is the temperature of the end where the samples were placed; the sign → shows the direction of the transport with a resulting crystal growth; the concentration of iodine is given as a mass per silica tube. In case of $HoCuP_2$ crystals were formed inside the bulk sample in the hot end, and iodine can be considered as a mineralizing agent. All crystals (see crystals from the samples HoCuAsP and ErCuAsP in Fig. 1) were shiny well-defined plates and were kinetically stable in the air.

Table 1. Details of the successful crystal growth

Initial Composition	m(I_2), mg	T_1, °C	T_2, °C	Time, days	Position of crystals inside the silica tube
$HoCuAs_2$	80	900→	800	14	cold end
HoCuPAs	40	800→	900	10	middle zone
$HoCuP_2$	80	900	800	10	in the bulk of the sample in the hot end
ErCuAsP	40	800→	900	10	middle zone
$ErCuP_2$	105	850→	750	14	middle zone

HoCuAsP ErCuAsP

Figure 1. Crystals obtained by the gas transport technique from the samples HoCuAsP and ErCuAsP

2.2. X-ray Analysis

The powder patterns of the samples were recorded using Guinier cameras (Enraf Nonius, Cu$K_{\alpha 1}$, Si internal standard), and the exposed and developed films were laser scanned to obtain peak positions. The lattice parameters (Table 2) were derived by the least-squares method using the CSD program package [12]. As was found for the gadolinium series, peak splitting was observed for the holmium and erbium copper arsenophosphides and phosphides, but different peaks were split in the two cases. The phosphides have the most intense and some smaller peaks well split, and this splitting is observed even on the diffractogram (Fig. 2), on the other hand, the mixed compounds have other peaks split and that splitting was seen only on Guinier patterns. The patterns of $HoCuAs_2$, $HoCuAs_{1.67}P_{0.33}$, $HoCuAs_{1.33}P_{0.67}$, $ErCuAs_2$ and ErCuAsP were indexed in the *P4/nmm* space group, the patterns of HoCuAsP, $HoCuAs_{1.33}P_{0.67}$, $HoCuAs_{1.67}P_{0.33}$, $ErCuAs_{1.33}P_{0.67}$ and $ErCuAs_{1.67}P_{0.33}$, showing line splitting similar to that observed for the gadolinium copper arsenophosphides [1], were indexed in the *Pmmn* space group.

Single crystal methods were used to confirm the indexing results, to refine the atomic parameters of the indexed structures and to determine the phosphide structures. Crystals in the form of plates from the $HoCuAs_2$, HoCuAsP, $HoCuP_2$, ErCuAsP and $ErCuP_2$ samples, obtained by the

Table 2. Powder Lattice Parameters for $HoCuAs_{2-x}P_x$ and $ErCuAs_{2-x}P_x$ ($x = 0 - 2$)

Composition.	Sp. Group	*a*, Å	*b*, Å	*c*, Å	*b/a*	*V*, Å^3
$HoCuAs_2$	*P4/nmm*	3.8726(3)	3.8726(3)	9.821(1)	1	147.3
$HoCuAs_{1.67}P_{0.33}$	*P4/nmm*	3.8495(3)	3.8495(3)	9.7932(9)	1	145.1
$HoCuAs_{1.33}P_{0.67}$	*P4/nmm*	3.8204(6)	3.8204(6)	9.765(2)	1	142.5
HoCuAsP	*Pmmn*	3.788(3)	3.803(2)	9.741(4)	1.0040	140.3
$HoCuAs_{0.67}P_{1.33}$	*Pmmn*	3.7661(5)	3.7797(6)	9.724(1)	1.0036	138.4
$HoCuAs_{0.33}P_{1.67}$	*Pmmn*	3.7400(3)	3.7613(4)	9.6991(7)	1.0057	136.4
$HoCuP_2$	*Cmma* [a]	5.2612(8)	5.3088(7)	9.655(1)	1.0090	134.8[b]
$ErCuAs_2$	*P4/nmm*	3.8623(2)	3.8623(2)	9.7941(6)	1	146.1
ErCuAsP	*P4/nmm*	3.7918(5)	3.7918(5)	9.719(2)	1	139.7
$ErCuAs_{0.67}P_{1.33}$	*Pmmn*	3.755(2)	3.768(2)	9.697(4)	1.0035	137.2
$ErCuAs_{0.33}P_{1.67}$	*Pmmn*	3.7308(7)	3.7480(7)	9.683(1)	1.0046	135.4
$ErCuP_2$	$P2_1/n$	3.725(4)	19.276(6) $\beta = 90.46(4)°$	3.724(1)	1.0003[c]	133.7[b]

[a] Not a superstructure of $HoCuAs_{0.33}P_{1.67}$.
[b] $\frac{1}{2}V_{\text{unit cell}}$.
[c] *a/c* ratio.

above-described technique, were checked by the Laue method. Crystals of $HoCuAs_2$ were not twinned, most of the tested crystals from the HoCuAsP, $HoCuP_2$ and ErCuAsP samples were twins, but some single (non-twin) crystals could be found, and those were used for data collection. The diffraction data for holmium arsenide and erbium arsenophosphide ($ErCuAs_{1.07}P_{0.93}$ composition from the structure refinement) indicated the space group *P4/nmm*. The rotation method and data from the two-dimensional CCD detector showed no superstructure for holmium arsenophosphide

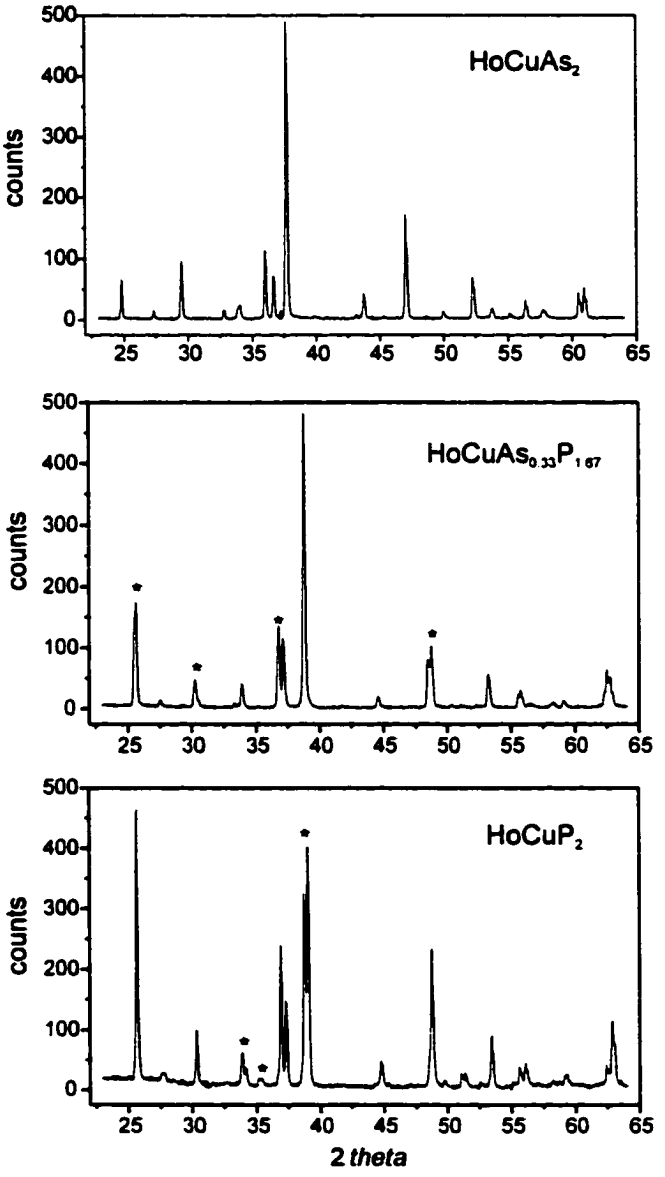

Figure 2. Powder patterns of $HoCuAs_2$ (*P4/nmm* space group), $HoCuAs_{0.33}P_{1.67}$ (*Pmmn* space group) and $HoCuP_2$ (*Cmma* space group) (all are the samples initial compositions). Asterisks indicate splitting of the low angle peaks.

($HoCuAs_{0.99}P_{1.01}$ composition from the structure refinement); only the peaks relevant to the *Pmmn* space group and presented lattice parameters were observed. The data for $HoCuP_2$ gave a larger orthorhombic cell (similar to that of $GdCuP_{2.20}$) with the *Cmma* space group. The structures were refined using the SHELXTL program [13] (Tables 3-7).

Table 3. Crystal Data and Structure Refinements of $HoCuAs_2$, $HoCuAs_{0.99}P_{1.01}$ and $HoCuP_2$ (T=293(2) K, Mo$K\alpha$ - Radiation, Graphite Monochromator, the Refinement Method was Full-Matrix Least-Squares on F^2)

Empirical formula	$HoCuAs_2$	$HoCuAs_{0.99}P_{1.01}$	$HoCuP_2$
Space group	*P4/nmm* (No.129)	*Pmmn* (No.59)	*Cmma* (No.67)
Unit cell dimensions, Å	$a = 3.874(1)$	$a = 3.7919(8)$	$a = 5.273(3)$
	$c = 9.827(2)$	$b = 3.7941(8)$	$b = 5.305(3)$
		$c = 9.7321(3)$	$c = 9.645(5)$
Z	2	2	4
Density (calculated)	8.519 g/cm^3	7.916 g/cm^3	7.149 g/cm^3
Diffractometer	Siemens P4	Siemens SMART	Siemens SMART
2θ range	4.14 to 69.86°	4.18 to 53.98°	4.22 to 58.46°
Index ranges	$-6 \le h \le 6$,	$0 \le h \le 4$,	$-7 \le h \le 7$,
	$-6 \le k \le 6$, $-15 \le l \le 15$	$-4 \le k \le 4$,$-12 \le l \le 12$	$-6 \le k \le 7$,$-13 \le l \le 12$
Reflections collected	810 [$R\sigma = 0.0369$]	690 [$R\sigma = 0.0326$]	1232 [$R\sigma = 0.0882$]
Abs. Correction / Program	empirical from ψ-scan	empirical / SADABS	empirical / SADABS
Independent reflections	235 [$Rint = 0.0541$]	204 [$Rint = 0.0503$]	207 [$Rint = 0.1741$]
Reflections with $I>2\sigma(I)$	229	175	195
Completeness to max 2θ	100.0 %	89.8 %	95.4 %
Data / restraints / par.	235 / 0 / 12	204 / 0 / 20	207 / 1 / 16
Goodness-of-fit on F^2	1.334	1.097	1.096
Final R indices [$I>2\sigma(I)$]	$R_1 = 0.0379$,	$R_1 = 0.0192$,	$R_1 = 0.0492$,
	$wR_2 = 0.0934$	$wR_2 = 0.0295$	$wR_2 = 0.1193$
R indices (all data)	$R_1 = 0.0388$,	$R_1 = 0.0273$,	$R_1 = 0.0535$,
	$wR_2 = 0.0939$	$wR_2 = 0.0314$	$wR_2 = 0.1213$
Extinction coefficient	0.041(5)	0.0050(4)	0.0011(10)
Largest diff. peak / hole	3.60 / –4.16 e./Å^3	1.504 / –2.292 e./Å^3	4.070 / –2.637 e./Å^3

$Rint = \Sigma|Fo^2-Fo^2mean|/\Sigma Fo^2$.
$R\sigma = \Sigma\sigma Fo^2/\Sigma Fo^2$.
$R_1 = \Sigma||Fo|-|Fc||/\Sigma|Fo|$.
$R_w = (\Sigma w\times(Fo^2-Fc^2)^2 / \Sigma w\times(Fo^2)^2)^{1/2}$, $w = 1/(\sigma^2(Fo^2)+(a\times P)^2+b\times P)$.
$GoF = (\Sigma w\times(Fo^2-Fc^2)^2 / (n-p))^{1/2}$ with $w = 1/(\sigma^2(Fo^2)+(a\times P)^2+b\times P)$, n is the number of observed reflections, p is number of parameters refined.

As with $GdCuP_{2.20}$ [1] all examined single crystals of $ErCuP_2$ looked ideal under the microscope, but they were found to be twins by X-rays diffraction. Analysis of the Laue pictures indicated that the plane of twinning was 010 (*b* is the largest axis, monoclinic setting). Rotation around *b* showed superstructure reflections, doubling the *b* parameter to 19.32 Å, rotations around the *a* axis (3.70 Å) and the diagonal (5.24 Å) in the *ac* plane did not result in parameters larger than those expected from the structural analogy with $HoCuP_2$ and $GdCuP_{2.20}$. Further investigation was done on

Table 4. Crystal Data and Structure Refinements of $ErCuAs_{1.07}P_{0.93}$ and $ErCuP_2$ (T=293(2) K, Mo$K\alpha$ - Radiation, Graphite Monochromator, the Refinement Method was Full-Matrix Least-Squares on F^2)

Empirical formula	$ErCuAs_{1.07}P_{0.93}$	$ErCuP_2$
Space group	*P4/nmm* (No.129)	$P2_1/n$ (No.14)
Unit cell dimensions, Å	a = 3.774(1)	a = 3.737(3)
	c = 9.680(3)	b = 19.239(15), β = 90.09(1)°
		c = 3.728(3)
Z	2	4
Density (calculated)	8.181 g/cm^3	7.275 g/cm^3
Diffractometer	Rigaku AFC6R	Siemens SMART
2θ range	4.20 to 53.94°	4.24 to 55.70°
Index ranges	$0 \le h \le 4$,	$-4 \le h \le 4$,
	$-4 \le k \le 4$, $-12 \le l \le 12$	$-24 \le k \le 24$, $-4 \le l \le 2$
Reflections collected	672 [$R\sigma$ = 0.0548]	1455 [$R\sigma$ = 0.1141]
Abs. Correction / Program	empirical from ψ-scan	empirical / XShape
Independent reflections	120 [*Rint* = 0.0989]	207 [*Rint* = 0.1741]
Reflections with $I>2\sigma(I)$	117	450
Completeness to max 2θ	100.0 %	89.6 %
Data / restraints / par.	120 / 0 / 14	563 / 1 / 40
Goodness-of-fit on F^2	1.252	1.011
Final *R* indices [$I>2\sigma(I)$]	R_1 = 0.0463,	R_1 = 0.0680,
	wR_2 = 0.1200	wR_2 = 0.1670
R indices (all data)	R_1 = 0.0475,	R_1 = 0.0778,
	wR_2 = 0.1220	wR_2 = 0.1749
Extinction coefficient	0.013(4)	0.0000(10)
Largest diff. peak / hole	5.270 / –3.088 e./Å^3	4.333 / –3.635 e./Å^3

$Rint = \Sigma|Fo^2-Fo^2mean|/\Sigma Fo^2$.
$R\sigma = \Sigma\sigma Fo^2/\Sigma Fo^2$.
$R_1 = \Sigma||Fo|-|Fc||/\Sigma|Fo|$.
$R_w = (\Sigma w\times(Fo^2-Fc^2)^2 / \Sigma w\times(Fo^2)^2)^{1/2}$, $w = 1/(\sigma^2(Fo^2)+(a\times P)^2+b\times P)$.
$GoF = (\Sigma w\times(Fo^2-Fc^2)^2 / (n-p))^{1/2}$ with $w = 1/(\sigma^2(Fo^2)+(a\times P)^2+b\times P)$, *n* is the number of observed reflections, *p* is number of parameters refined.

a Siemens SMART diffractometer with a CCD detector. Indexing of the reflections resulted in a monoclinic cell with a = 3.737(3), b = 19.239, c = 3.728(3) Å and β = 90.09(1)°. Deviation of the β angle from 90° (Table 1) was clearly observed on the powder pattern: the Guinier film showed a splitting of what originally was the most intense peak. The refinement (Tables 4, 6, 8) was successful with the twinning rule

$$\begin{pmatrix} 0 & 0 & 1 \\ 0 & -1 & 0 \\ 1 & 0 & 0 \end{pmatrix} \begin{pmatrix} \boldsymbol{a} \\ \boldsymbol{b} \\ \boldsymbol{c} \end{pmatrix} = \begin{pmatrix} \boldsymbol{a'} \\ \boldsymbol{b'} \\ \boldsymbol{c'} \end{pmatrix}$$

The twinning in the *ac* plane with the *a* and *c* axes superimposed plus the larger shifts of the P atoms to form zigzag chains obscured the electron density map in the P2 net and did not allow satisfactory refinement of the *x* and *z* parameters of P2. Nevertheless the distortion of the P2 net and the formation of the zigzag chains were obvious in $ErCuP_2$. In this part and below we describe $ErCuP_2$ in the $P2_1/n$ space group in order to make comparison with the other structures and to follow the symmetry-breaking distortions in terms of the Landau theory. The standard setting for $ErCuP_2$ can be achieved by the axis transformation $\boldsymbol{a}, \boldsymbol{b}, \boldsymbol{c} \rightarrow -\boldsymbol{c}, \boldsymbol{b}, \boldsymbol{a}+\boldsymbol{c}$ and the origin shift to 0, ½, ½: $P2_1/c$ space group, a = 3.737(3), b = 19.239(15), c = 5.274(5) Å and β = 134.89(1)°, Er at 4*e* with 0.0211, 0.2486, 0.2699, Cu at 4*e* with 0.0211, 0.2486, 0.2699, P1 at 4*e* 0.5213, 0.1698, 0.2691 and P2 at 4*e* with 0.5213, 0.1698, 0.2691.

Table 5. Atomic and Equivalent Isotropic Displacement Parameters (U_{eq}, Å^2) for $HoCuAs_2$ and $ErCuAs_{1.07}P_{0.93}$ (*P4/nmm* Space Group, $HfCuSi_2$ Type) and $HoCuAs_{0.99}P_{1.01}$ (*Pmmn* Space Group, $GdCuAs_{1.15}P_{0.85}$ Type)

		$HoCuAs_2$					$HoCuAs_{0.99}P_{1.01}$			
Atom		*x*	*y*	*z*	U_{eq}		*x*	*y*	*z*	U_{eq}
Ho	2*c*	¼	¼	0.23719(5)	0.0058(3)	2*a*	¼	¼	0.23947(4)	0.0087(1)
Cu	2*b*	¾	¼	1/2	0.0093(4)	2*b*	¼	¾	0.50016(11)	0.0111(3)
*X*1[a]	2*c*	¼	¼	0.66203(13)	0.0063(3)	2*a*	¼	¼	0.65950(17)	0.0090(6)
*X*2[b]	2*a*	¾	¼	0	0.0097(3)	2*b*	¼	¾	0.00022(11)	0.0133(4)
		$ErCuAs_{1.07}P_{0.93}$								
Er	2*c*	¼	¼	0.2391(1)	0.0042(5)					
Cu	2*b*	¾	¼	1/2	0.0064(7)					
*X*1[a]	2*c*	¼	¼	0.6605(5)	0.0030(13)					
*X*2[b]	2*a*	¾	¼	0	0.0098(9)					

[a] *X*1 = 26.5(8)%As + 73.5(8)%P for $HoCuAs_{0.99}P_{1.11}$ and 29(1)%As + 71(1)%P for $ErCuAs_{1.07}P_{0.93}$.
[b] *X*2 = 72.1(7)%As + 27.9(7)%P for $HoCuAs_{0.99}P_{1.11}$ and 78.1(9)%As + 21.9(9)%P for $ErCuAs_{1.07}P_{0.93}$.

Fig. 3 shows the *b/a* ratio and unit cell volume versus the P amount for $HoCuAs_{2-x}P_x$ and $ErCuAs_{2-x}P_x$ determined from the X-ray powder diffraction data. The nature of the symmetry-breaking transitions, which are discussed below, is indicated. Change in the unit cell volume with increasing phosphorus concentration is nearly linear for the both series. The lattice parameters of $HoCuAs_2$ and $ErCuAs_2$ are in agreement with those reported in [8].

Table 6. Atomic and Equivalent Isotropic Displacement Parameters (U_{eq}, $Å^2$) for $HoCuP_2$ (*Cmma* Space Group) and $ErCuP_2$ ($P2_1/n$ Space Group)

	$HoCuP_2$					$ErCuP_2$				
Atom		*x*	*y*	*z*	U_{eq}		*x*	*y*	*z*	U_{eq}
RE	4*g*	0	¼	0.2350(1)	0.0152(6)	4*e*	0.2305(2)	0.11717(5)	0.7509(2)	0.0125(3)
Cu	4*b*	¼	0	½	0.0167(7)	4*e*	0.2301(5)	0.2514(8)	0.2512(6)	0.0142(7)
P1	4*g*	0	¼	0.6597(6)	0.0147(12)	4*e*	0.2309(11)	0.3302(3)	0.7522(13)	0.0121(11)
P2	4*a*	¼	0	0	0.0163(19)	4*e*	0.2890(20)	0.9989(12)	0.2450(30)	0.0251(17)

Table 7. Interatomic Distances (Å) in $HoCuAs_2$, $HoCuAs_{0.99}P_{1.01}$ and $ErCuAs_{1.07}P_{0.93}$

Atoms	$HoCuAs_2$	$HoCuAs_{0.99}P_{1.01}$	$HoCuP_2$	$ErCuAs_{1.07}P_{0.93}$
RE – 4*X*1	2.9129(8)	2.8566(7)	2P1 at 2.826(2) 2P1 at 2.840(2)	2.840(2)
4*X*2	3.0307(6)	3.0034(10)	2.938(1)	2.986(1)
4Cu	3.2283(7)	2Cu at 3.1647(10) 2Cu at 3.1679(10)	3.167(1)	3.153(1)
Cu – 4*X*1	2.5074(9)	2*X*1 at 2.4502(14) 2*X*1 at 2.4514(13)	2.423(4)	2.445(3)
4Cu	2.7393(7)	2.6821(4)	2Cu at 2.637(1) 2Cu at 2.652(1)	2.6688(4)
4*X*1 – 4Cu	2.5074(9)	2Cu at 2.4502(14) 2Cu at 2.4514(13)	2.423(4)	2.445(3)
4*RE*	2.9129(8)	2.8566(7)	2Ho at 2.826(2) 2Ho at 2.840(2)	2.840(2)
*X*2 – 4*X*2	2.7393(7)	2.6821(4)	2P2 at 2.637(1) 2P2 at 2.652(1)	2.6688(4)
4*RE*	3.0307(6)	3.0060(10)	2.938(1)	2.986(1)

X is As for $HoCuAs_2$, As/P for $HoCuAs_{0.99}P_{1.01}$ and $ErCuAs_{1.07}P_{0.93}$ and P for $HoCuP_2$.

Table 8. Selected Interatomic Distances (Å) in $ErCuP_2$

Atoms	Distance	Atoms	Distance
Er – P1	2.817(5)	Cu – P1	2.400(11)
P1	2.823(5)	P1	2.406(11)
P1	2.825(5)	P1	2.435(10)
P1	2.827(5)	P1	2.439(11)
P2	2.861(19)	2Cu	2.634(2)
P2	2.94(2)	2Cu	2.638(2)
P2	2.956(19)		
P2	2.96(2)		
Cu	3.140(12)	P2 – P2	2.41(2)
Cu	3.142(12)	P2	2.46(2)
Cu	3.184(12)	P2	2.82(2)
Cu	3.185(12)	P2	2.88(2)

2.4. Electric and magnetic measurements

Single crystals of $HoCuAs_2$ and $HoCuP_2$ were used for electric and magnetic studies. Resistance was measured with a computer-automated setup, using a standard DC two-probe method.

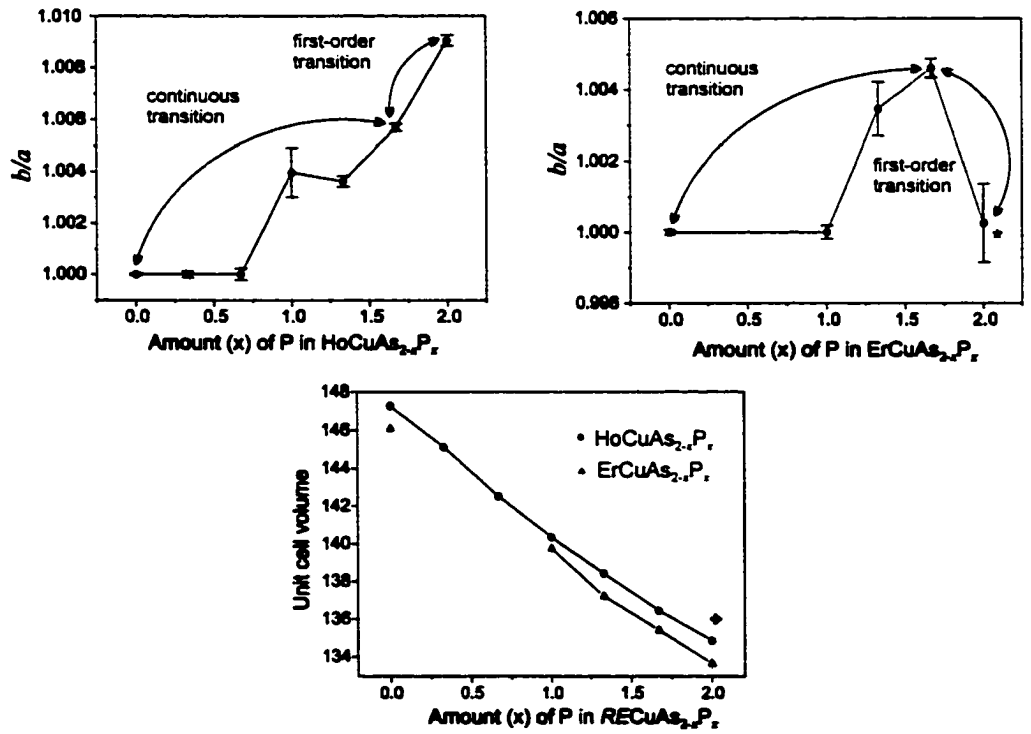

Figure 3. *b/a* ratio and unit cell volume versus phosphorus amounts for $HoCuAs_{2-x}P_x$ and $ErCuAs_{2-x}P_x$ from the X-ray powder data. * *a/c* ratio for $ErCuP_2$. ◆ ½ $V_{unit\ cell}$ for $HoCuP_2$ and $ErCuP_2$.

Electrode connections were made with the use of 50 μm silver wires and indium solder. Samples were cooled in a He flow cryostat. The temperature was measured with a LakeShore DT 470 silicon diode temperature sensor located close to the crystal. Resistance was measured between 285K and 4K in increments of 2K. No indication of thermal hysteresis was observed, showing good temperature equilibrium throughout the measurement cycle.

Magnetic measurements were performed in the temperature range 1.7-300 K and in applied magnetic fields up to 50 kOe employing a Quantum Design MPMS-5 SQUID magnetometer.

3. Results and Discussion

3.1. Structure Descriptions

Tetragonal $HoCuAs_2$ and $ErCuAs_{1.07}P_{0.93}$. No distortion from the tetragonal symmetry was observed for refined $HoCuAs_2$ and $ErCuAs_{1.07}P_{0.93}$. Both compounds (Fig. 4, 5) adopt the $HfCuSi_2$ structure (*P4/nmm* space group), and the powder lattice parameters of $HoCuAs_2$ agree well with those reported: a=3.8724(9) and c=9.822(3) Å [8]. In $ErCuAs_{1.07}P_{0.93}$ positions 2*a* and 2*c* are statistically occupied by As and P atoms, with the P atoms being mostly in the Cu*X*1 block and the As ones in the *X*2 layer. A similar statistical As/P distribution can be assumed for the rest of the tetragonal, as well as orthorhombically distorted, erbium copper arsenophosphides.

Orthorhombic $HoCuAs_{0.99}P_{1.01}$. $HoCuAs_{0.99}P_{1.01}$ (*Pmmn* space group) adopts the orthorhombically distorted version of the $HfCuSi_2$ structure which was originally found in $GdCuAs_{1.15}P_{0.85}$ [1]. Here, the As and P atoms are mixed in the manner observed in $ErCuAs_{1.07}P_{0.93}$ and $GdCuAs_{1.15}P_{0.85}$. The distortion from the tetragonal cell is very small and it results in slight deviation of the angles in the (As/P)2 layer from 90° (Fig. 6).

Orthorhombic $HoCuP_2$. Holmium copper phosphide (*Cmma* space group) undergoes an orthorhombic distortion resulting in a larger unit cell, and this distortion is different from that in $HoCuAs_{0.99}P_{1.01}$. The tetragonal structure and the $HoCu_{1+x}P_{2-x}$ composition for the phosphide from [9] were not confirmed. The unit cell is similar to that of $GdCuP_{2.20}$ [1] but the changes in the P2 layer are less drastic. If phosphorus dimers are formed along the *a* direction in $GdCuP_{2.20}$, only a small difference between the P-P distances along *a* and *b* is observed in $HoCuP_2$ (Fig. 6). Furthermore, no additional phosphorus sites around the P2 net (as in $GdCuP_{2.20}$) were found in $HoCuP_2$.

Monoclinic $ErCuP_2$. Erbium copper phosphide ($P2_1/n$ space group) has its largest lattice parameter doubled relative to the substructure (Fig. 5). The composition and symmetry differ from those assigned in [9]: $ErCu_{1+x}P_{2-x}$ and the *P4/nmm* space group. While the monoclinic distortion of this structure was clearly demonstrated by peak splitting on a Guinier powder pattern, the doubling of

the *b* parameter could be confirmed for sure only by the single crystal methods. In $ErCuP_2$ the displacements of the P2 atoms in the P layer are the largest among the structures under discussion here. This monoclinic distorted version of the tetragonal $HfCuSi_2$ structure with the double *c* parameter (the *b* parameter in the monoclinic structure) has not been previously observed.

Distortion of the X2 layers. The symmetry-breaking transitions in the $GdCuAs_{2-x}P_x$ series

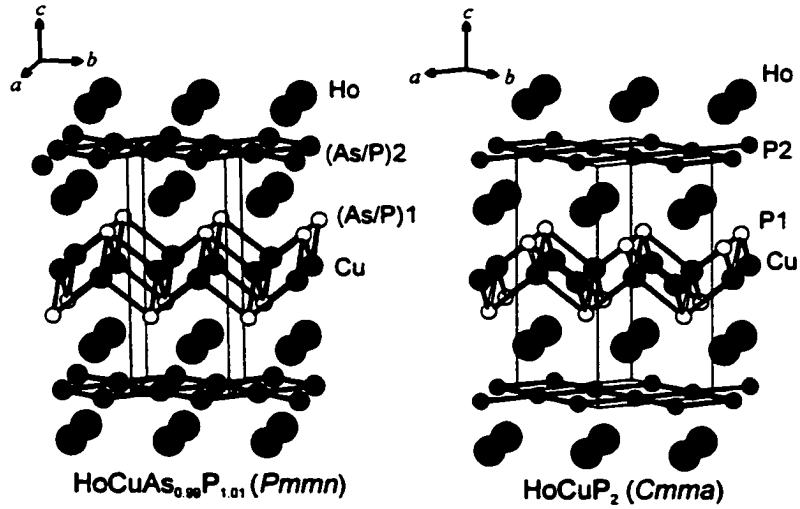

Figure 4. Structures of $HoCuAs_{0.99}P_{1.01}$ and $HoCuP_2$.

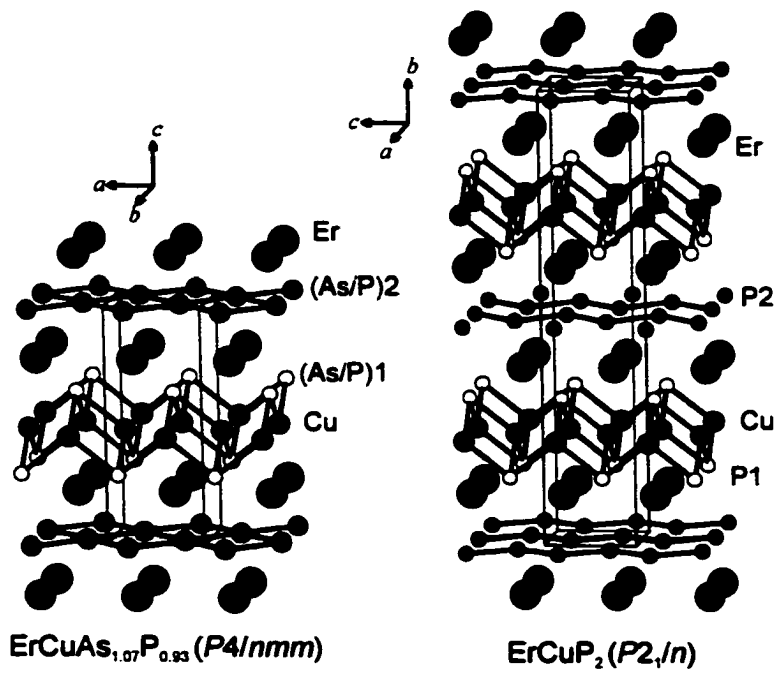

Figure 5. Structures of $ErCuAs_{1.07}P_{0.93}$ and $ErCuP_2$.

were traced to the Peierls instability of the As/P or P nets [1]. Since the As/P and P nets in $HoCuAs_{2-x}P_x$ and $ErCuAs_{2-x}P_x$ are similar to those in $GdCuAs_{2-x}P_x$, they are also subject to the same instability, which may lead to the same or different types of distortion. The electronic structures of the $HoCuAs_{2-x}P_x$ and $ErCuAs_{2-x}P_x$ phases will be discussed in a future paper. The distortions of the As/P layers (Fig. 6) in orthorhombic HoCuAsP through $HoCuAs_{0.33}P_{1.67}$ and $ErCuAs_{0.67}P_{1.33}$ through $ErCuAs_{0.33}P_{1.67}$ follow the same pattern as in $GdCuAs_{1.15}P_{0.85}$ [1]. In $HoCuP_2$, when compared to $HoCuAs_{0.99}P_{1.01}$, the angles in the P2 layer are back to 90° but the P2-P2 distances are now slightly different along *a* and *b*: 2.637(1) and 2.652(1) Å.

Larger changes are observed in the P2 layer of $ErCuP_2$: there are two short P2-P2 distances of 2.41(2), 2.46(2) Å and two long ones of 2.82(2), 2.88(2) Å (Fig. 7), resulting in the formation of the zigzag chains. The short distances are comparable to those in CeP_2 [14] but somewhat smaller than those in LaP_2 [15], where the phosphorus atoms are joined into fragments of zigzag chains of 4 or 3 and 5 atoms with $\delta_{P\text{-}P}$ = 2.404-2.453 Å and $\delta_{P\text{-}P}$ = 2.197-2.314 Å, respectively. A similar type of distortion, leading to zigzag chains and semiconducting properties, was found in $SrZnSb_2$ [4].

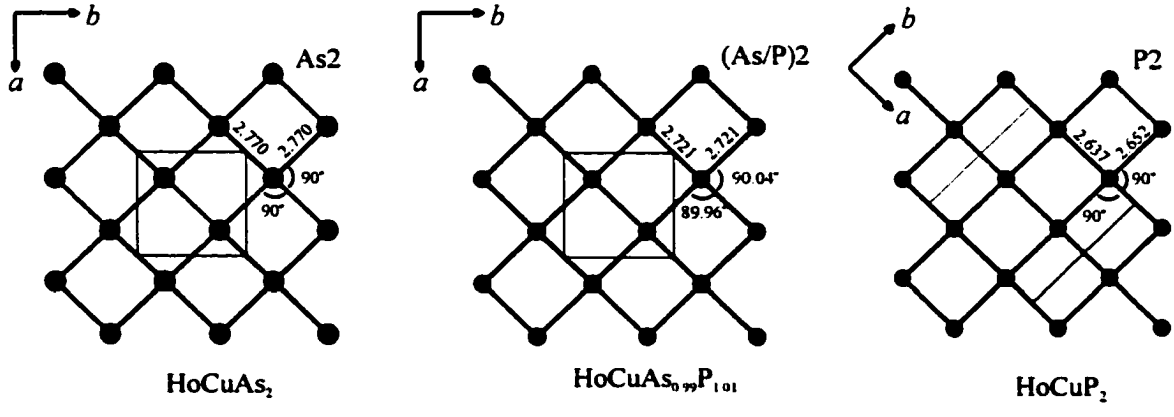

Figure 6. As, As/P and P layers in $HoCuAs_2$, $HoCuAs_{0.99}P_{1.01}$ and $HoCuP_2$.

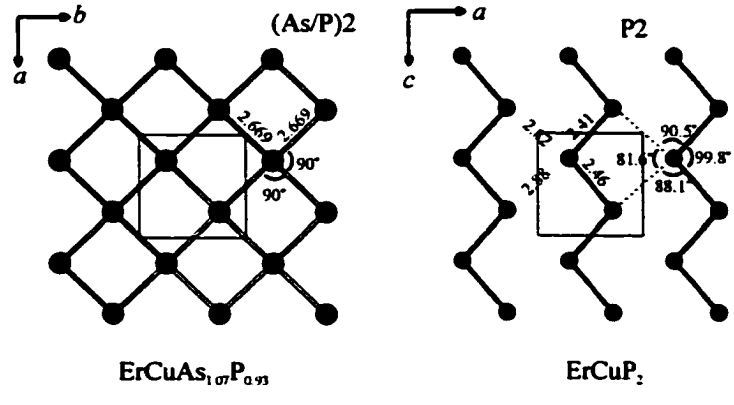

Figure 7. As/P and P layers in $ErCuAs_{1.07}P_{0.93}$ and $ErCuP_2$.

3.2 Symmetry-Breaking Transitions and Landau Theory

The nature of phase transformations in solids can be analyzed using Landau theory [16-18]. This theory gives symmetry constraints for symmetry-breaking transitions, i.e. it answers the questions whether a transition between the high- and low-symmetry structures can occur as a continuous (second-order) one. The theory can also provide a structural model for one of the phases during the continuous symmetry-breaking process, as it did for the gadolinium copper arsenophosphide [1].

Here we apply Landau theory to the symmetry-breaking transitions in $HoCuAs_{2-x}P_x$ and $ErCuAs_{2-x}P_x$ ($x = 0 - 2$).

3.2.1. Transitions from $HoCuAs_{0.67}P_{1.33}$ to HoCuAsP and from ErCuAsP to $ErCuAs_{1.33}P_{0.67}$

The formulas in the title represent the last and the first experimentally determined compositions of the tetragonal and orthorhombic phases in the series $HoCuAs_{2-x}P_x$ and $ErCuAs_{2-x}P_x$ (also see Fig. 3), using the X-ray powder data. The transitions from the tetragonal cells of $HoCuAs_{0.67}P_{1.33}$ and ErCuAsP (*P4/nmm* space group, $HfCuSi_2$ structure type) to the orthorhombic cells of HoCuAsP and $ErCuAs_{1.33}P_{0.67}$ (*Pmmn* space group, $GdCuAs_{1.15}P_{0.85}$ structure type) maintaining the same principal axis direction are similar to the transition from $GdCuAs_2$ to $GdCuAs_{1.15}P_{0.85}$ [1] and, therefore, these transitions can occur continuously.

Here, we will give a brief proof of this conclusion in terms of the Landau theory. Since no superstructures (no loss in the translation symmetry) are created by the distortions from the tetragonal cells to orthorhombic ones, the wave vector of the distortion is $\boldsymbol{k} = 0$ and the irreducible representations of the group of this wavevector $\boldsymbol{k}$ are isomorphous with those of the point group D_{4h}. Among the eight one-dimensional representation there are two representations, B_{1g} and B_{2g}, that yield an orthorhombic cell and preserve the horizontal plane and inversion center. The space group *Pmmn*, corresponding to B_{1g} (Table 9), is the one experimentally found in HoCuAsP and $ErCuAs_{1.33}P_{0.67}$.

The next consideration of the Landau theory is to determine whether any third-order symmetry combination of basis functions is invariant under all operations of the group. If such a

Table 9. One-Dimensional Irreducible Representation B_{1g} of *P4/nmm* at $\boldsymbol{k} = 0$

g	ϵ	C_{4z}	C_{4z}^3	C_{2z}	C_{2x}	C_{2y}	$C_{2(x+y)}$	$C_{2(x-y)}$
$\chi(g)$	1	-1	-1	1	1	1	-1	-1
g	i	$\bar{C}_{4z}$	$\bar{C}_{4z}^3$	σ_z	σ_x	σ_y	σ_{x+y}	σ_{x-y}
$\chi(g)$	1	-1	-1	1	1	1	-1	-1

third-order invariant exists, then a third-order term appears in the Gibbs free energy expansion in the order parameter η, and the transition must be discontinuous [17, 18]. For one-dimensional irreducible representation the particle density, ρ, can be expressed in terms of that of symmetrical form, ρ^o, and one basis function, ϕ:

$$\rho = \rho^o + \eta\phi$$

Since the basis function is symmetric to one half and antisymmetric to the other half of symmetry elements in B_{1g}, no third-order invariant combination of the order parameter can be formed.

Finally, in order for a second-order transition to be allowed the Lifshitz criterion has to be met. According this criterion, the minimum in the Gibbs free energy must be fixed by the symmetry at the reciprocal space point $\boldsymbol{k}$ corresponding to the distortion, i.e., the Taylor expansion of the Gibbs free energy about $\boldsymbol{k}$

$$G(\boldsymbol{k}+\delta\boldsymbol{k}) = G(\boldsymbol{k}) + \alpha\cdot\delta\boldsymbol{k} + \ldots$$

should not contain the $\alpha\cdot\delta\boldsymbol{k}$ term. In the case under consideration inversion is in the point group of the wave vector and therefore α vanishes by symmetry. Thus the Lifshitz condition is satisfied and it follows that $P4/nmm \rightarrow Pmmn$ with $\boldsymbol{a}_{ort} = \boldsymbol{a}_{tet}$, $\boldsymbol{b}_{ort} = \boldsymbol{b}_{tet}$ and $\boldsymbol{c}_{ort} = \boldsymbol{c}_{tet}$ meets all the criteria for a second-order phase transition.

3.2.2. Transition from $HoCuAs_{1.67}P_{0.33}$ to $HoCuP_2$

As in case of $GdCuAs_{1.15}P_{0.85}$ and $GdCuP_{2.20}$ the transition from $HoCuAs_{1.67}P_{0.33}$ (*Pmmn* space group) to $HoCuP_2$ (*Cmma* space group) is between two different subgroups of the parent *P4/nmm* symmetry of the $HoCuAs_2$ structure. The *a* and *b* directions in the arsenophosphide and phosphide correspond to *a* and *b* of *P4/nmm* for $HoCuAs_{1.67}P_{0.33}$ and to the face diagonals of *P4/nmm* for $HoCuP_2$, respectively. Thus, the phases are not in a group-subgroup relationship; therefore, this is necessarily a first-order transition.

3.2.3. Transition from $ErCuAs_{1.67}P_{0.33}$ to $ErCuP_2$

The distortion from the orthorhombic cell of $ErCuAs_{1.67}P_{0.33}$ (*Pmmn* space group) to the monoclinic cell of $ErCuP_2$ ($P2_1/n$ space group) involves doubling of the *c* parameter, which is the *b* parameter in the distorted monoclinic cell. The wave vector $\boldsymbol{k}$ (or set of wave vectors in a star) of the distortion is the one for which any lost translation $\boldsymbol{T}_i$ yields nonintegral values for $\boldsymbol{k}\cdot\boldsymbol{T}_i/2\pi$. Since the lost translations are $\boldsymbol{c}$, $3\boldsymbol{c}$, $5\boldsymbol{c}$, ... but not $2\boldsymbol{c}$, $4\boldsymbol{c}$, ..., the wave vector of the distortion is $\boldsymbol{k} = \boldsymbol{c}^*/2$. This

vector has the full symmetry of the point group D_{2h} of the space group ***Pmmn***, and thus it is the only vector in the star.

The irreducible representations of the group ***g(k)*** of the wave vector can be found from the *loaded small representations* $\hat{\Gamma}(\beta)$ [19] by multiplying them by $e^{-ik\cdot t}$:

$$\Gamma(\beta/t) = e^{-ik\cdot t}\,\hat{\Gamma}(\beta)$$

Due to the fact that the wave vector $\boldsymbol{k} = \boldsymbol{c}^*/2$ is perpendicular to all translations t of the symmetry elements β/t (screw axes and glide plane) of ***Pmmn***, the irreducible representations of the point group D_{2h} form the loaded small representations $\hat{\Gamma}(\beta)$ and consequently the irreducible representations $\Gamma(\beta/t)$ of the group ***g(k)*** of the wave vector $\boldsymbol{k} = \boldsymbol{c}^*/2$.

There are eight one-dimensional irreducible representations in D_{2h} and ***g(k)***. All of them (except for the totally symmetrical one) have four symmetry elements with character $\Gamma(\beta/t) = -1$, which would be lost for cases for which $\boldsymbol{T}_i$ does not include $(2n+1)c_{ort}$, but maintained otherwise since

$$\Gamma(\epsilon/(2n+1)c_{ort})\,\Gamma(\beta/t) = \Gamma(\beta/t + (2n+1)c_{ort}) = 1.$$

Thus, all of these irreducible representations lead to orthorhombic symmetry. On the other hand, at the zone center the B_{1g} representation (Table 10) leads to *P2/n* with no superstructure, and for the *P2/n* case at $\boldsymbol{k} = \boldsymbol{b}^*/2$ ($\boldsymbol{k} = \boldsymbol{c}^*/2$ in the previous orthorhombic cell) a monoclinic cell with the $P2_1/n$ space group and with doubling of the unique axis would occur. Thus the observed transition from $ErCuAs_{1.67}P_{0.33}$ (*Pmmn* space group) to $ErCuP_2$ ($P2_1/n$ space group) is not possible continuously in a single step. It is however possible as *Pmmn* → *P2/n* at the Γ point, followed by doubling of the unique axis ($\boldsymbol{k} = \boldsymbol{b}^*/2$) to give $P2_1/n$.

3.2.4. Twinning of $ErCuP_2$ crystals

As mentioned above, all tested crystals of $ErCuP_2$ were twins, although this was not apparent under the optical microscope. The twinning plane was 010 with the *a* and *c* axes being superimposed. This twinning is very similar to that in $GdCuP_{2.20}$ [1]. Since the largest shifts are in the P layer of $ErCuP_2$, divergence of the distortion directions results in twin formation. The (As/P) layer of $ErCuAs_{1.67}P_{0.33}$ (*Pmmn* space group), which is similar to the (As/P) layer of $HoCuAs_{0.99}P_{1.01}$ (Fig. 5), can be distorted in two different ways to give zigzag chains along *a* or *b* (*a* and *c* in the monoclinic

Table 10. One-Dimensional Irreducible Representation B_{1g} of D_{2h}

g	ϵ	C_{2z}	C_{2x}	C_{2y}	i	σ_z	σ_x	σ_y
$\chi(g)$	1	1	-1	-1	1	1	-1	-1

cell). At the initial stage of the crystal growth, when the lattice is not well defined these two ways will not differ in energy with respect to the already formed lattice and are equally probable at the temperature of the experiment. So, in the formed twin crystal of $ErCuP_2$ one twin component will have phosphorus zigzag chains along *a* and the other will have them along *c*.

3.3. Electrical Conductivity and Magnetic Susceptibility

Two-probe resistance measurements reveal that $HoCuAs_2$, $HoCuAs_{1.33}P_{0.67}$ and $HoCuP_2$ show metallic behavior throughout the temperature range 4 - 285 K (Fig. 8). The resistivities were not determined since the resistance of the contacts in the two probe technique could not been measured exactly. The resistance decreases monotonically for both compounds to 4K. Small resistance anomalies (more prominent in $HoCuAs_2$) are observed in the temperature range of the antiferromagnetic ordering; the temperatures of the resistance increase, detected in the cooling and heating cycles, agree well with the magnetic data. No hysteresis was observed. The anomalies are typically attributed to increased spin-flip scattering in the critical temperature range.

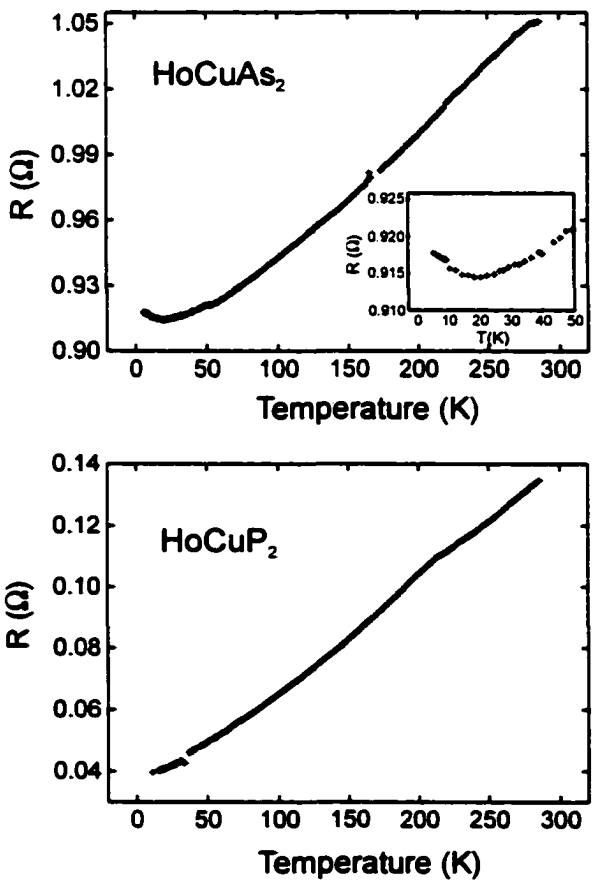

Figure 8. Resistance versus temperature for single crystals of $HoCuAs_2$ and $HoCuP_2$.

The temperature dependencies of the inverse molar magnetic susceptibility of $HoCuP_2$ and $HoCuAs_2$ are presented in Figs. 9a and 9b, respectively. For both compounds the susceptibility above 50 K follows well the Curie-Weiss (CW) law. The CW parameters found by a least-square fitting procedure are as follows: θ_p = 2(1) K and μ_{eff} = 10.62(4) μ_B for the phosphide and θ_p = 3(1) K and μ_{eff} = 10.51(3) μ_B for the arsenide. It is worth noting that the experimental values of the effective magnetic moment are very close to the value expected for a free Ho^{3+} ion with the $4f^{10}$ electronic configuration ($g\sqrt{J(J+1)} = 10.60$). Slight deviations of χ^{-1}(T) from a straight-line behavior, observed for both ternaries below 50 K, result most presumably from crystal field interactions.

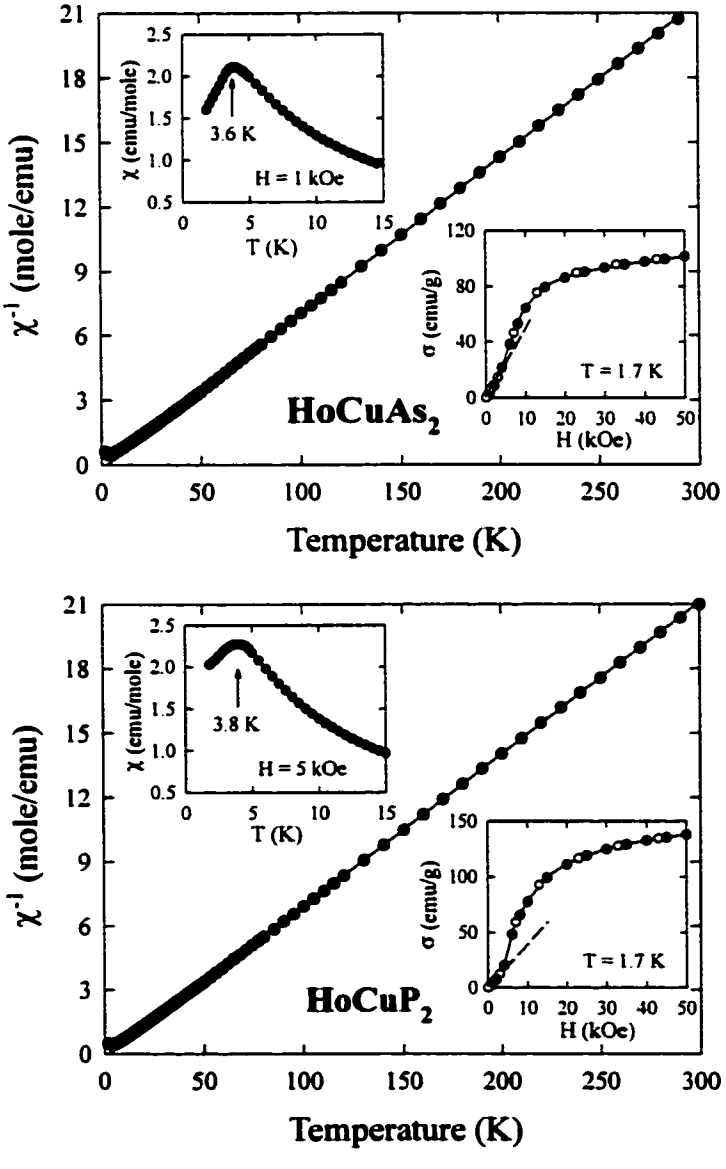

Figure 9. Magnetic susceptibility measured on single crystals of $HoCuAs_2$ and $HoCuP_2$.

As is apparent from the upper insets to Figs. 9a and 9b, showing the behavior of χ(T) at low temperatures, $HoCuP_2$ and $HoCuAs_2$ order antiferromagnetically below 3.8(4) and 3.6(9) K, respectively. An antiferromagnetic nature of the ground state in the two compounds studied is corroborated by characteristic field variations of the magnetization (see the lower insets to Figs. 9a and 9b), which exhibit metamagnetic-like transitions in a field of about 5 kOe. At 1.7 K both σ(H) dependencies show a tendency to saturation in high fields, slightly more prominent in $HoCuAs_2$. The holmium magnetic moment measured at this temperature in 50 kOe amounts to 7.2(1) and 6.9(1) μ_B for the phosphide and the arsenide, respectively. These two values are considerably reduced relative to the value expected for a Ho^{3+} ion ($gJ = 10$) mainly due to a splitting of the $^5I_8$ ground multiplet in a tetragonal crystal field potential.

4. Conclusions

The phases $HoCuAs_{2-x}P_x$ and $ErCuAs_{2-x}P_x$ (x = 0-2) undergo symmetry-breaking transitions with an increase in the phosphorus concentration. $HoCuAs_2$ through $HoCuAs_{1.33}P_{0.67}$ and $ErCuAs_2$ through ErCuAsP retain the tetragonal $HfCuSi_2$ structure (*P4/nmm* space group); HoCuAsP through $HoCuAs_{0.33}P_{1.67}$ and $ErCuAs_{0.67}P_{1.33}$ through $ErCuAs_{0.33}P_{1.67}$ show orthorhombic distortions to the $GdCuAs_{1.15}P_{0.85}$ structure (*Pmmn* space group). The two phosphides have different structures: $HoCuP_2$ adopts a larger orthorhombic cell (*Cmma* space group) and $ErCuP_2$ crystallizes in a monoclinic cell ($P2_1/n$ space group) with a doubled b parameter. The largest structural changes are observed in the P layers of $ErCuP_2$: zigzag chains are formed.

The Landau theory was used for the analysis of the symmetry-breaking transitions. It showed that the transitions from $HoCuAs_{1.33}P_{0.67}$ to HoCuAsP and from ErCuAsP to $ErCuAs_{0.67}P_{1.33}$ can be continuous, the transitions from $HoCuAs_{0.33}P_{1.67}$ to $HoCuP_2$ and from $ErCuAs_{0.67}P_{1.33}$ to $ErCuP_2$ are first-order. If the distortion from $ErCuAs_{0.67}P_{1.33}$ to $ErCuP_2$ occurred through an intermediate step ($P2/n$ space group, no doubling of the b parameter), it could be continuous.

The phases $HoCuAs_2$ and $HoCuP_2$ are metallic conductors and show antiferromagnetic ordering at low temperatures.

Acknowledgements

This research was supported by the Office of the Basic Energy Sciences, Materials Sciences Division, US Department of Energy, DOE. The Ames Laboratory is operated for DOE by Iowa State University under contract No. W-7405-Eng-82.

Special thanks to Dr. Sasha Pecharsky for collecting powder diffraction data.

References

[1] Y. Mozharivskyj, D. Kaczorowski, H. F. Franzen, *J. Solid State Chem.* **2000**, *155*, 259.

[2] G. Gordier, B. Eisenmann, H.Z. Schäfer, *Z. Anorg. Allg. Chem.* **1976**, *426*, 205.

[3] G. Gordier, H.Z. Schäfer, *Z. Naturforsch.* **1977**, *32b*, 383.

[4] E. Brechtel, G. Gordier, H.Z. Schäfer, *Z. Naturforsch.* **1979**, *34b*, 251.

[5] E. Brechtel, G. Gordier, H.Z. Schäfer, *Z. Naturforsch.* **1980**, *35b*, 1.

[6] G. Gordier, H.Z. Schäfer, P. Woll, *Z. Naturforsch.* **1985**, *40b*, 383.

[7] O. Sologub, K. Hiebl, P. Rogl, H. Noël, O. Bodak, *J. Alloys Compd.* **1994**, *210*, 153.

[8] M. Brylak, M.H. Möller, W. Jeitschko, *J. Solid State Chem.* **1995**, *115*, 305.

[9] S.I. Chykhrij, Yu.B. Kuz'ma , S.V. Oryshchyn, *Dopov. Akad. Nauk Ukr. RSR, Ser. B*, **1989**, *3*, 63.

[10] S.I. Chykhrij, G.V. Loukashouk, S.V. Oryshchyn, Yu.B. Kuz'ma, *J. Alloys Compd.* **1997**, *248*, 224.

[11] S.I. Chykhrij, Yu.B. Kuz'ma, S.V. Oryshchyn, B.V. Khabursky, V.S. Fundamenskii, *Dopov. Akad. Nauk Ukr. RSR, Ser. B*, **1990**, *9*, 49.

[12] L.G. Akselrud, Yu.M. Grin, P.Yu. Zavalij, CSD - universal program package for single crystal and powder data treatment, *Proc.12th European Crystallographic Meet., Moscow, August 20-28, 1989,* Academy of Sciences, Moscow, USSR, *Kristallographiya, Suppl.*, **1989**, *155*, 2.

[13] *SHELXTL*, Bruker Analytical X-Ray Systems, Madison, USA 1997.

[14] H.G. von Schnering, W. Wichelhaus, N.M.Schulze, *Z. Anorg. Allg.Chem.* **1975**, *412*, 193.

[15] W. Wichelhaus, H.G. von Schnering, *Z. Anorg. Allg.Chem.* **1976**, *419*, 77.

[16] L.D. Landau, E.M. Lifshitz, *Statistical Physics*, Vol. 5, Permagon Press, London, 1958.

[17] H.F. Franzen, *Chem. Mater.* **1990**, *2*, 486.

[18] H.F. Franzen, *Basic Principles of Symmetry and Stability of Crystalline Solids*, World Scientific, Singapore, 1994.

[19] O.V. Kovalev, *Irreducible Representations of the Space Groups*, Gordon and Breach, New York, 1961.

CHAPTER 6. SYMMETRY-BREAKING TRANSITIONS IN $SmCu_{1+\delta}As_{2-x}P_x$ (δ= 0-0.2, x = 0-2). EFFECT OF P AND ADDITIONAL Cu ATOMS ON CRYSTAL STRUCTURES. MAGNETIC PROPERTIES

A paper accepted for publication in Zeitschrift für anorganische und allgemeine Chemie

Yurij Mozharivskyj[a,b], Alexandra O. Pecharsky[b], Sergej Bud'ko[b], and Hugo F. Franzen[a,b]

[a]*Department of Chemistry and* [b]*Ames Laboratory of US DOE,*

Iowa State University, Ames, Iowa 50011, USA

Abstract

Crystal structures of the compounds $SmCu_{1+\delta}As_{2-x}P_x$ (δ = 0-0.2, x = 0-2) undergoing symmetry-breaking transitions and $SmCuP_{2.3}$ have been investigated by the X-ray single crystal and powder methods. While the phases $SmCuAs_2$ through $SmCuAs_{1.22}P_{0.78}$ retain the tetragonal $HfCuSi_2$ structure (*P4/nmm* space group), the compounds $SmCuAs_{1.11}P_{0.89}$ through $SmCuAs_{0.56}P_{1.44}$ adopt the $GdCuAs_{1.15}P_{0.85}$-type structure (*Pmmn* space group), an orthorhombic variant of the $HfCuSi_2$-type. Further distortion follows in $SmCuAs_{0.33}P_{1.67}$ through $SmCuP_{2.3}$, the powder patterns of which were tentatively indexed in the *P2/n* space group (*P2/c* in a standard setting). According to Landau theory the transitions from tetragonal $SmCuAs_{1.22}P_{0.78}$ to orthorhombic $SmCuAs_{1.11}P_{0.89}$ and from orthorhombic $SmCuAs_{0.56}P_{1.44}$ to monoclinic $SmCuAs_{0.33}P_{1.67}$ can be continuous. Introducing extra copper into some of the orthorhombic arsenophosphides restabilizes tetragonal phases ($0 < \delta \leq 0.2$) with the *P4/nmm* symmetry, and the reverse transition *Pmmn* → *P4/nmm* can be continuous. Inserting copper atoms into monoclinic $SmCuP_2$ yields the $SmCu_{1+\delta}P_2$ phosphides with *Cmmm* symmetry, and this transition is first-order.

Single crystals of $SmCu_{1.05}As_{1.67}P_{0.33}$, $SmCu_{1.07}As_{0.85}P_{1.15}$ and $SmCu_{1.15}P_2$ have been prepared using iodine as a mineralizing agent. Their structures have partially occupied Cu sites around the square As/P or P layers and they are a stuffed variant of the $HfCuSi_2$ structure for $SmCu_{1.05}As_{1.67}P_{0.33}$ (*P4/nmm*, a = 3.9163(6), c = 9.932(2) Å), a stuffed $GdCuAs_{1.15}P_{0.85}$ structure for $SmCu_{1.07}As_{0.85}P_{1.15}$ (*Pmmn*, a = 3.859(1), b = 3.862(1), c = 9.852(3) Å) and a $CeCu_{1.12}P_{1.97}$-type structure for $SmCu_{1.15}P_2$ (*Cmmm*, a = 5.453(3), b = 19.511(10), c = 5.439(3) Å). The P net in $SmCu_{1.15}P_2$ is broken into rectangular units. The results of magnetic measurements for SmCuAsP are reported.

Keywords: samarium copper pnictides; crystal structure; symmetry-breaking transitions; Landau theory; magnetic properties.

1. Introduction

Among the vast variety of intermetallic compounds, the phases containing 2D square nets of a main group element, e.g., GdPS [1], $SrZnSb_2$ [2], $RECuAs_{2-x}P_x$ [3, 4] (*RE* is a rare-earth element), are of the particular interest since they are susceptible to structural distortions. The electronic instability of these nets is a generalization of the well known "Peierls" instability [5, 6]. Peierls-type instabilities can result in symmetry-breaking transitions and are often accompanied by metal-to-semiconductor transitions (e.g., CeAsS [7]). For experimentalists the synthesis and characterization of this type of compound still remains a large field to explore and an opportunity to find new compounds with interesting properties, while for theoreticians the electronic analysis of the instabilities can give more insight into relationship between electronic and crystal structures.

The phases recently investigated in the $GdCuAs_{2-x}P_x$ [3], $HoCuAs_{2-x}P_x$ and $ErCuAs_{2-x}P_x$ [4] series undergo transitions from the tetragonal structures of the $HfCuSi_2$ type (*P4/nmm* space group) to the orthorhombicly distorted structures of the $GdCuAs_{1.15}P_{0.85}$ type (*Pmmn* space group), and then to further distorted structures of the phosphides $GdCuP_{2.20}$, $HoCuP_2$ and $ErCuP_2$. Formation of dimers in the P layer of $GdCuP_{2.20}$ and P zigzag chains in $ErCuP_2$ were found to result from Peierls-type instabilities of the square P nets. On the other hand, the symmetry-breaking *P4/nmm* → *Pmmn* transitions in the arsenophosphides $RECuAs_{2-x}P_x$ cannot have their origin in the electronic instabilities of the As/P layers since there is no opening of a band gap upon the distortion [8]. Group theoretical analysis of the transformations in the $RECuAs_{2-x}P_x$ series has shown that the *P4/nmm* → *Pmmn* distortions correspond to a single irreducible representation B_{1g} and can be continuous.

Combining results of Landau theory with those of electronic analysis and geometric considerations has revealed that the orthorhombic structures of the arsenophosphides are structural adaptations to the smaller P atoms. Stability of the tetragonal phases ($HfCuSi_2$ type) with respect to orthorhombic distortions can be evaluated through a new parameter called the relative interatomic distance, which represents separation between the atoms in the square or distorted As/P nets [8]. Analysis of the relative interatomic distances in $RECuAs_2$ showed that the structures with La, Ce and Pr can remain tetragonal only if some extra atoms are taken into the structure around the As layer. This conclusion was confirmed by the results of single crystal refinements on the arsenides $LaCu_{1.23(1)}As_2$, $CeCu_{1.10(1)}As_2$ and $PrCu_{1.09(1)}As_2$ [9]. Furthermore, the relative interatomic distances in the tetragonal samarium copper arsenophosphides were found to be too large for these phases to

remain tetragonal. A thorough analysis of the $SmCuAs_{2-x}P_x$ series was needed to see if there are extra Cu atoms in these phases. Furthermore, samarium copper phosphides were reported to have two compositions with different structures: $SmCu_{1+x}P_{2-x}$ with the $HfCuSi_2$ structure [10] and $SmCuP_2$ with the $SrZnBi_2$ structure [11]. Since there is a square net of P atoms in both structures, we could expect symmetry-breaking transitions resulting from the Peierls-type instabilities.

2. Experimental

2.1. Synthesis

The samples were synthesized in two different ways: 1) by annealing powders at 600-900°C and 2) by mineralizing these samples at 800°C using iodine. The annealed powders did not yield single crystals suitable for X-ray diffraction and their compositions are reported here as the initial compositions used in the synthesis. The justification for this is that these samples resulted in single phases to powder X-ray diffraction. It is well known that powder X-ray diffraction is not sensitive to impurities at the 1-5% level, however. The composition reported for the mineralized samples, which yielded single crystals used in X-ray diffraction, are based on the refined single crystal structures.

The starting materials were powdered samarium (99.9 wt.%, Alfa Aesar), copper (99.99 wt.%, Metals Development, Ames laboratory), amorphous red phosphorus (99 wt.%, Alfa Aesar) and arsenic (99.99 wt.%, Alfa Aesar). Weighing and handling of samples with the compositions $SmCu_{1+\delta}As_{2-x}P_x$ (δ = 0-0.3, x = 0-2, Table 1, 2) and $SmCuP_{2.3}$ were performed in an Ar-filled glove box. The powders with a total mass of 0.5 g were thoroughly mixed, pressed to pellets under 3000 kg using a 10-mm dial tool, and sealed in evacuated silica tubes. Samples for X-ray powder analysis were heated at the rate of 20°C/h to 600°C, kept at this temperature for 48 hours and furnace cooled. To assure homogeneity the sintered samples were ground, pressed, sealed in silica tubes, heated at 100°C/h to 800°C, kept at 800°C for 5 days and cooled, the last step was repeated again while the annealing time was increased to 7 days. Although some samples were later annealed at 900°C for 7days, their Guinier patterns showed that sample homogeneity was reached after the third sintering at 800°C and that the subsequent annealing at 900°C did not improve the homogeneity. The sample with the overall composition $SmCuP_{2.3}$ annealed at 800°C contained some elemental phosphorus, thus the $SmCuP_{2.3}$ phosphide partially decomposes in the sealed tube at 800°C, and the initial composition does not represent the actual composition.

Since sintering of all powder samples at 800°C or 900°C did not yield crystals suitable for X-ray studies, a mineralization technique was used for crystal growth instead. The samples with the initial compositions $SmCuAs_{1.67}P_{0.33}$, $SmCuAs_{0.67}P_{1.33}$, $SmCuP_2$, $SmCuP_{2.3}$ and $SmCu_{1.16}P_2$ were

annealed at 800°C (750°C for $SmCuP_{2.3}$) in silica tubes with iodine as a mineralizing agent. The samples were heated at 20°C/h to the given temperatures, kept for 14 days and then furnace cooled. Air-stable crystals were obtained as rectangular plates with silver luster from the $SmCuAs_{1.67}P_{0.33}$ and $SmCuAs_{0.67}P_{1.33}$ (Fig. 1) samples and with black metallic luster from the $SmCu_{1.16}P_2$, $SmCuP_2$ (Fig. 1) and $SmCuP_{2.3}$ samples. Crystals from $SmCu_{1.16}P_2$, $SmCuP_2$ and $SmCuP_{2.3}$ were twinned (see crystals from $SmCuP_2$ in Fig. 1), but they could be "sliced" into single crystals.

2.2. X-ray Powder Analysis

The powder patterns of the $SmCu_{1+\delta}As_{2-x}P_x$ samples were recorded using Guinier cameras (Enraf Nonius, $CuK_{\alpha 1}$, Si internal standard), and the exposed and developed films were laser scanned to obtain peak positions. The lattice parameters (Table 1, 2) were derived by the least-squares method using the CSD program package [12].

Analysis of the $SmCuAs_{2-x}P_x$ samples (δ=0). The $SmCuAs_{2-x}P_x$ formula denotes the composition used for the sample preparation (no excess copper) and, probably, does not represent the real compositions of the dominant phases in the annealed samples. We believe that all phases of interest in the $SmCuAs_{2-x}P_x$ powder samples have additional copper atoms in their structures. This conclusion pertains to the arsenide and the tetragonal and orthorhombic arsenophosphides, and it follows from the results of the single crystal refinements (on $SmCu_{1.05}As_{1.66}P_{0.33}$ and $SmCu_{1.07}As_{0.85}P_{1.15}$) and from the comparison of the existence regions of the samarium and gadolinium arsenophosphides coupled with the analysis of the relative interatomic distances for the Cu1 and (As/P)2 layers, as discussed below. Since the phases from the $SmCuAs_{2-x}P_x$ powders have only a small excess of Cu, the amount of a secondary phase formed is small and below the detection limit of the X-ray powder methods. The monoclinic phosphides $SmCuP_2$ and $SmCuP_{2.3}$ do not seem

$SmCuAs_{0.67}P_{1.33}$ $SmCuP_2$

Fig. 1 Twin crystals obtained from the $SmCuAs_{0.67}P_{1.33}$ and $SmCuP_2$ samples through the reaction with iodine as a mineralizing agent.

to have additional copper atoms in their structures, i.e., $\delta = 0$, because introducing extra copper into $SmCuP_2$ leads to an orthorhombic phase.

Table 1. Powder Lattice Parameters for $SmCuAs_{2-x}P_x$

Composition.	Sp. Group	*a*, Å	*b*, Å	*c*, Å	*b/a*	*V*, Å^3
$SmCuAs_2$	*P4/nmm*	3.9369(3)	3.9369(3)	9.980(1)	1	154.68(2)
$SmCuAs_{1.67}P_{0.33}$	*P4/nmm*	3.9298(5)	3.9298(5)	9.924(1)	1	153.26(3)
$SmCuAs_{1.33}P_{0.67}$	*P4/nmm*	3.9032(3)	3.9032(3)	9.903(1)	1	150.87(2)
$SmCuAs_{1.22}P_{0.78}$	*P4/nmm*	3.8863(8)	3.8863(8)	9.919(2)	1	149.81(5)
$SmCuAs_{1.11}P_{0.89}$	*Pmmn*	3.8659(8)	3.8816(8)	9.913(2)	1.0041(3)	148.75(5)
SmCuAsP	*Pmmn*	3.8513(3)	3.8715(4)	9.9176(7)	1.0052(1)	147.87(2)
$SmCuAs_{0.89}P_{1.11}$	*Pmmn*	3.8520(9)	3.8691(9)	9.898(2)	1.0044(3)	147.52(6)
$SmCuAs_{0.78}P_{1.22}$	*Pmmn*	3.8438(9)	3.8618(9)	9.891(1)	1.0047(3)	146.82(5)
$SmCuAs_{0.67}P_{1.33}$	*Pmmn*	3.8366(7)	3.8566(7)	9.881(1)	1.0052(3)	146.20(4)
$SmCuAs_{0.56}P_{1.44}$	*Pmmn*	3.830(1)	3.850(1)	9.880(3)	1.0052(4)	145.69(7)
$SmCuAs_{0.33}P_{1.67}$	*P2/n*	3.836(1)	3.8429(7)	9.827(1) γ=90.13(1)°	1.0018(3)	144.86(5)
$SmCuP_2$	*P2/n*	3.8266(4)	3.8311(6)	9.775(1) γ=90.155(5)°	1.0012(2)	143.30(3)
$SmCuP_{2.3}$	*P2/n*	3.8122(4)	3.8188(9)	9.806(1) γ=90.594(7)°	1.0017(3)	142.75(4)

Table 2. Powder Lattice Parameters for $SmCu_{1-\delta}As_{2-x}P_x$ Phases (δ = 0-0.2, x = 0-2)

Composition.	Sp. Group	*a*, Å	*b*, Å	*c*, Å	*b/a**	*V*, Å^3
$SmCuAs_2$	*P4/nmm*	3.9369(3)	3.9369(3)	9.980(1)	1	154.68(2)
$SmCu_{1.1}As_2$	*P4/nmm*	3.9458(7)	3.9458(7)	9.964(2)	1	155.13(5)
SmCuAsP	*Pmmn*	3.8513(3)	3.8715(4)	9.9176(7)	1.0052(1)	147.87(2)
$SmCu_{1.1}AsP$	*Pmmn*	3.8669(7)	3.8784(8)	9.897(2)	1.0030(3)	148.43(5)
$SmCu_{1.2}AsP$	*Pmmn*	3.868(1)	3.8823(7)	9.907(2)	1.0037(3)	148.77(6)
$SmCuAs_{0.67}P_{1.33}$	*Pmmn*	3.8366(7)	3.8566(7)	9.881(1)	1.0052(3)	146.20(4)
$SmCu_{1.1}As_{0.67}P_{1.33}$	*P4/nmm*	3.8602(4)	3.8602(4)	9.853(1)	1	146.82(3)
$SmCu_{1.2}As_{0.67}P_{1.33}$	*P4/nmm*	3.8621(5)	3.8621(5)	9.860(1)	1	147.07(3)
$SmCuP_2$	*P2/n*	3.8266(4)	3.8311(6)	9.775(1) γ=90.155(5)°	1.0012(2)	143.30(3)
$SmCu_{1.2}P_2$	*Cmmm*	5.4331(8)	19.468(2)	5.4329(8)	1.00004(21)	574.6(1)

* *a/c* for $SmCu_{1.2}P_2$

The lattice parameters of $SmCuAs_2$ are in agreement with those reported in [13]. As is the case with the gadolinium, holmium and erbium $RECuAs_{2-x}P_x$ series [3, 4], peak splitting was observed for the samarium copper arsenophosphides and phosphides, but different peaks were split for the two structures. The diffractograms of $SmCuAs_{0.33}P_{1.67}$, $SmCuP_2$ and $SmCuP_{2.3}$ exhibit substantial peak splitting, as shown for $SmCuP_{2.3}$ in Figure 2. On the contrary, the orthorhombic arsenophospides $SmCuAs_{1.11}P_{0.89}$ through $SmCuAs_{0.56}P_{1.44}$ (*Pmmn* space group) have other peaks split and this splitting is observable only on the Guinier patterns. $SmCuAs_2$ through $SmCuAs_{1.22}P_{0.78}$ preserve tetragonal structures and their Guinier patterns were indexed in the *P4/nmm* space group.

The tetragonal and orthorhombic $SmCuAs_{2-x}P_x$ phases were anticipated from the existence of similar phases in the previously studied systems with Gd, Ho and Er, and the indexing results confirmed their existence. On the other hand, it was experimentally shown [3, 4] that, although the crystal structures of the phosphides are derived from the tetragonal $HfCuSi_2$ type, the structures vary with the rare-earth element and, in general, they cannot be predicted. Small changes in the P layers

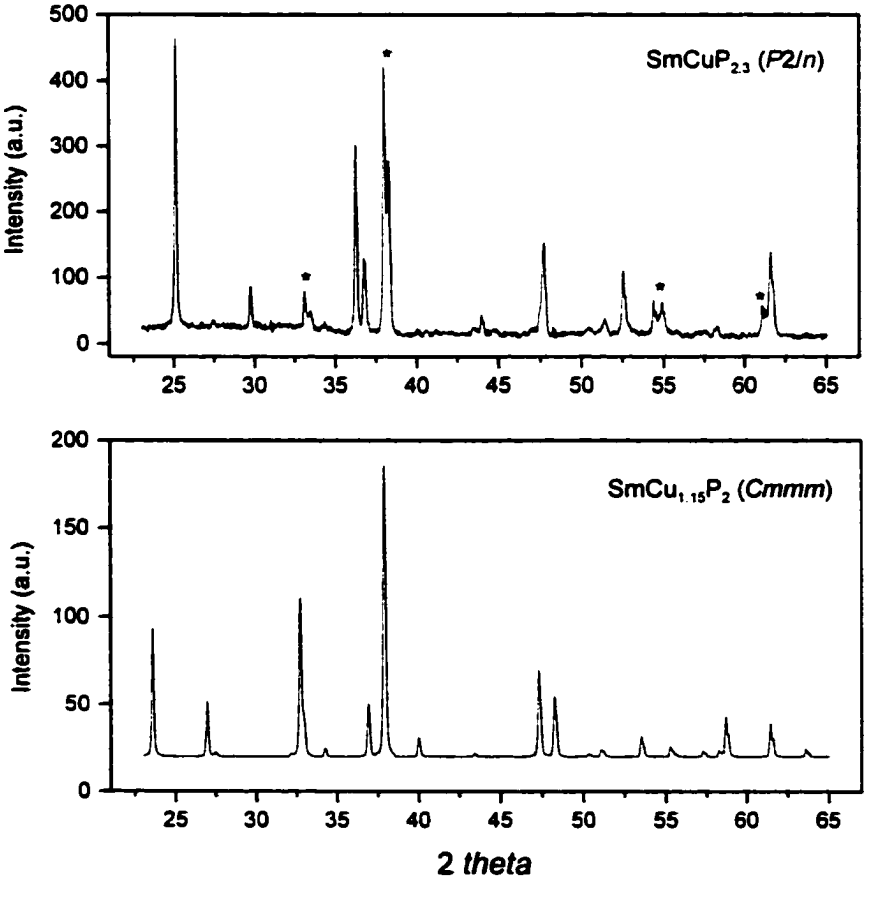

Figure 2. Powder patterns of $SmCuP_{2.3}$ (experimental) and $SmCu_{1.15}P_2$ (calculated). Asterisks indicate splitting of some peaks for $SmCuP_{2.3}$.

give rise to different unit cells and different symmetries: *Pmm2*, a = 5.3747(9), b = 5.3830(9), c = 9.7376(16) Å for $GdCuP_{2.20}$; *Cmma*, a = 5.273(3), b = 5.305(3), c = 9.645(5) Å for $HoCuP_2$ and $P2_1/n$, a = 3.737(3), b = 19.239(15), c = 3.728(3) Å, β = 90.09(1)° for $ErCuP_2$. The reflections corresponding to these supercells are usually very weak, they can be missed or wrongly interpreted in the process of powder pattern indexing, therefore single crystal analysis is the best way to determine the structures. Since crystals suitable for the X-ray studies could not be obtained from the sintered powders of $SmCuAs_{0.33}P_{1.67}$, $SmCuP_2$ and $SmCuP_{2.3}$, we tentatively indexed their powder patterns in the $P2/n$ space group, based upon the assumption that the orthorhombic-to-monoclinic distortion is a continuation of the tetragonal-to-orthorhombic process, as discussed below. The monoclinic unit cells presented in Table 1 are in a non-standard setting. The standard setting for $SmCuAs_{0.33}P_{1.67}$, $SmCuP_2$ and $SmCuP_{2.3}$ can be achieved through the axis transformation ***a, b, c*** → ***- a, c, a+b***: e.g., for $SmCuP_{2.3}$ the standard setting is the $P2/c$ space group, a = 3.8122(4), b = 9.806(1), c = 5.368(1) Å and β = 134.653(7)°.

As was mentioned above, $SmCuP_{2.3}$ lost some P during the annealing. Therefore, we could not assign an exact composition to the phosphide, and without knowing the crystal structure we cannot explain why the unit cell volume of the monoclinic phase from the $SmCuP_{2.3}$ sample is smaller than the unit cell volume of the phase from the $SmCuP_2$ sample, and why the distortion (as judged by the γ angle) is larger in $SmCuP_{2.3}$ (Table 1). But since the phosphides with the nominal compositions $SmCuP_2$ and $SmCuP_{2.3}$ had different unit cell volumes, it is suggested that there is a homogeneity region in phosphorus for the phases. There was no indication of excess copper in these monoclinic phosphides.

Sintering of the $SmCuP_2$ and $SmCuP_{2.3}$ samples at 800°C did not yield crystals suitable for diffraction studies, however annealing these samples with iodine as a mineralizing agent produced crystals richer in Cu: namely, $SmCu_{1.147(3)}P_2$ and $SmCu_{1.117(4)}P_2$ (the compositions are taken from the single crystal refinements). The symmetry of these copper rich phosphides (*Cmmm* space group) is different from that of the structures of $SmCuAs_{0.33}P_{1.67}$, $SmCuP_2$ and $SmCuP_{2.3}$ prepared as powders (see the experimental diffractogram of $SmCuP_2$ and calculated diffractogram of $SmCu_{1.15}P_2$ in Figure 2).

Analysis of the $SmCu_{1+\delta}As_{2-x}P_x$ samples (δ = 0–0.2). The orthorhombic phosphides $SmCu_{1+\delta}P_2$ (*Cmmm* space group) with excess copper, obtained initially as single crystals during the mineralization reaction, could also be prepared as powders. Only the $SmCu_{1.2}P_2$ sample was a homogeneous orthorhombic phase, whereas the $SmCu_{1.1}P_2$ and $SmCu_{1.16}P_2$ samples contained both the monoclinic (*P2/n* space group) and orthorhombic phases, and $SmCu_{1.3}P_2$ contained the

orthorhombic phase and another unidentified phase. Under the assumption that the phases present were equilibrated by the heat treatment, the coexistence of the monoclinic and orthorhombic phases in the same samples indicates that the transition between the two structures is first-order, and that the homogeneity range for the orthorhombic phase does not extend all the way from $SmCuP_2$ to $SmCu_{1.2}P_2$. The similarity in the *a* and *c* lattice parameters that makes the peak splitting undetectable on a powder pattern, and the *Cmmm* symmetry (Table 2) suggest a smaller tetragonal cell for the $SmCu_{1.2}P_2$ phase (*I4/mmm*, $a = b = 3.8417$, $c = 19.468$ Å), but presence of superstructure reflections during the single crystal studies clearly indicates the larger orthorhombic cell.

The other $SmCuAs_{2-x}P_x$ phases ($x < 2$) can take extra copper into their structures and their compositions can be presented as $SmCu_{1+\delta}As_{2-x}P_x$. The homogeneity range depends on a compound, e.g., for $SmCu_{1+\delta}AsP$ and $SmCu_{1+\delta}As_{0.67}P_{1.33}$ it extends to $\delta = 0.2$, while for $SmCu_{1+\delta}As_2$ it does not reach $\delta = 0.2$ (Table 2), but in none of the phases investigated it reached $\delta = 0.3$. Since our primary focus was on symmetry-breaking transitions introduced through the As/P substitution but not through the additional Cu atoms, only some of the $SmCu_{1+\delta}As_{2-x}P_x$ phases were investigated for their homogeneity regions in copper.

Introducing extra Cu atoms into tetragonal $SmCuAs_2$ and orthorhombic SmCuAsP changes the lattice parameters but their symmetries remain the same. On the other hand, as discussed below, inserting additional copper into orthorhombic $SmCuAs_{0.67}P_{1.33}$ and monoclinic $SmCuP_2$ leads to tetragonal and orthorhombic structures, respectively (Table 2).

2.3. X-ray Single Crystal Analysis

The quality of all crystals was checked prior to data collection using the Laue method. Crystals from the $SmCuAs_{0.67}P_{1.33}$ sample looked ideal under the optical and electron microscopes (see Fig. 1), but they were twins under X–rays. Analysis of the Laue pictures indicated that the plane of twinning was 001. This twinning was similar to that observed for $GdCuP_{2.20}$ and $ErCuP_2$ [3, 4], so a similar twinning rule with *a* and *b* being superimposed was used during the refinement process. Rotation along *a* showed no superstructure reflections, and further investigations were conducted on a single crystal diffractometer. The structure was solved and refined in the *Pmmn* space group (Table 3-5). Large residual electron density was observed around the (As/P)2 layer. Assigning Cu atoms to this additional but only partially occupied position resulted in a smoother difference Fourier map and lower *R*-factor (0.0390 instead of 0.0461). The Hamilton test [14] indicated that probability of the additional electron density on the site, assumed here to be associated with Cu, is higher than 0.995. The extra amount of copper was later confirmed by an EDS analysis. The refinement yielded As/P

statistical mixtures on the two sites and led to the $SmCu_{1.074(4)}As_{0.854(6)}P_{1.146(6)}$ composition, with the As/P ratio being slightly different from that used for the single crystal growth.

Rotation around the *a* axis and the *ab* diagonal showed no superstructure reflections for a crystal from the $SmCuAs_{1.67}P_{0.33}$ sample. Structure solution and refinement were performed in the *P4/nmm* space group (Table 3), which supported the results of the powder indexing. As in the case with $SmCu_{1.07}As_{0.85}P_{1.15}$, significant residual electron density was observed around the (As/P)2 layer on the difference Fourier map. From the analysis of the interatomic distances and from the analogy to the orthorhombic arsenophosphide, Cu atoms were put in this position. With the second Cu site the refinement yielded a smother difference Fourier map and lower *R*-factor (0.0176 instead of 0.0194). Again, the Hamilton test [14] indicated that probability of the additional electron density being present in the structure is very high (larger than 0.995). The As and P atoms are statistically mixed on the two positions and their refined ratio ($SmCu_{1.046(6)}As_{1.667(6)}P_{0.333(6)}$) is close to the initial one used for the synthesis ($SmCuAs_{1.67}P_{0.33}$). Atomic parameters are presented in Table 4 and interatomic distances are given in Table 5.

The same methods were also used to study crystals from the samples $SmCu_{1.16}P_2$, $SmCuP_2$ and $SmCuP_{2.3}$. The rotation method, employed for a crystal from each sample, indicated doubling of the *a* and *c* parameter, but no superstructure reflections were observed along the *ab* diagonal (the basic cell and parameters are similar to those of tetragonal $SmCu_{1.05}As_{1.67}P_{0.33}$). Further investigations of the crystals from $SmCuP_2$ and $SmCuP_{2.3}$ were done on a Siemens SMART diffractometer with a CCD detector and of the crystal from $SmCu_{1.16}P_2$ on a four-circle Rigaku AFC6R diffractometer. Indexing of the reflections resulted in orthorhombic unit cells, e.g., a=5.453(3), b=19.51(1) and c=5.439(3) Å for the crystal from the $SmCuP_2$ sample. The relationship between the basic and 4-times enlarged orthorhombic cells for the phosphides can be written as $\boldsymbol{b}_{ort} = 2\boldsymbol{c}_{basic}$, $\boldsymbol{a}_{ort} = (\boldsymbol{a}_{basic}+\boldsymbol{b}_{basic})$, $\boldsymbol{c}_{ort}= (\boldsymbol{a}_{basic} - \boldsymbol{b}_{basic})$. The structures of the crystals from $SmCuP_2$ and $SmCuP_{2.3}$ were solved in *Cmmm* (see Table 3 for the data on the crystal from $SmCuP_2$). During the refinements (SHELXTL program, [15]) significant residual electron densities was observed on two sides of the P nets. On the basis of the interatomic distances Cu atoms were assigned to the site (Cu2 in Table 5, 6; the Hamilton test gave a significance level of more than 0.995 to the additional electron density) and this resulted in the $SmCu_{1.147(3)}P_2$ and $SmCu_{1.117(4)}P_2$ compositions, which were later confirmed by an EDS analysis. Tables 3, 4 and 6 show the data only for the $SmCu_{1.147(3)}P_2$ crystal from the $SmCuP_2$ sample, the results for $SmCu_{1.117(4)}P_2$ from the $SmCuP_{2.3}$ sample are very similar and are not presented here. Similar lattice parameters and the same symmetry for the crystal from the $SmCu_{1.16}P_2$ sample indicated the same structure, therefore further investigations were not performed on that crystal.

Table 3. Crystal Data and Structure Refinements of $SmCu_{1.05}As_{1.67}P_{0.33}$, $SmCu_{1.07}As_{0.85}P_{1.15}$ and $SmCu_{1.15}P_2$

Empirical formula	$SmCu_{1.05}As_{1.67}P_{0.33}$	$SmCu_{1.07}As_{0.85}P_{1.15}$	$SmCu_{1.15}P_2$
Space group	*P4/nmm* (No.129)	*Pmmn* (No.59)	*Cmmm* (No.65)
Unit cell dimensions, Å	a = 3.9163(6) c = 9.932(2)	a = 3.859(1) b = 3.862(1) c = 9.852(3)	a = 5.453(3) b = 19.511(10) c = 5.439(3)
Z	2	2	8
Density (calculated)	7.679 g/cm^3	7.185 g/cm^3	6.546 g/cm^3
Diffractometer	Rigaku AFC4R	Rigaku AFC4R	Siemens SMART
2θ range	4.10 to 53.52°	4.14 to 54.04°	4.18 to 55.78°
Index ranges	$0 \le h \le 5$, $-5 \le k \le 5$, $-12 \le l \le 12$	$-5 \le h \le 5$, $-5 \le k \le 5$, $-5 \le l \le 12$	$-7 \le h \le 7$, $-25 \le k \le 24$,$-6 \le l \le 7$
Reflections collected	716 [$R\sigma$ = 0.0351]	957 [$R\sigma$ = 0.0204]	2334 [$R\sigma$ = 0.0326]
Abs. Correction / Program	empirical from ψ-scan	empirical from ψ-scan	empirical / SADABS
Independent reflections	127 [*Rint* = 0.0577]	957*	410 [*Rint* = 0.1581]
Reflections with $I>2\sigma(I)$	122	791	311
Completeness to max 2θ	100.0 %	96.7 %	94.7 %
Data / restraints / par.	127 / 0 / 17	957 / 0 / 23	410 / 0 / 34
Goodness-of-fit on F^2	1.214	1.150	1.047
Final R indices [$I>2\sigma(I)$]	R_1 = 0.0176, wR_2 = 0.0404	R_1 = 0.0390, wR_2 = 0.1206	R_1 = 0.0433, wR_2 = 0.1052
R indices (all data)	R_1 = 0.0196, wR_2 = 0.0410	R_1 = 0.0507, wR_2 = 0.1341	R_1 = 0.0541, wR_2 = 0.1109
Extinction coefficient	0.028(2)	0.030(2)	0.0014(3)
Largest diff. peak / hole	1.507 / –1.008 e./Å^3	3.427 / –3.928 e./Å^3	2.469 / –2.139 e./Å^3

Note. T=293(2) K, Mo$K\alpha$ radiation, graphite monochromator, the refinement method was full-matrix least-squares on F^2.

* Symmetry equivalent and Friedel opposite reflections were not merge for the refinement. Twin ratio is 0.45

$Rint = \Sigma|Fo^2-Fo^2mean|/\Sigma Fo^2$.

$R\sigma = \Sigma\sigma Fo^2/\Sigma Fo^2$.

$R_1 = \Sigma||Fo|-|Fc||/\Sigma|Fo|$.

$wR_2 = (\Sigma w\times(Fo^2-Fc^2)^2 / \Sigma w\times(Fo^2)^2)^{1/2}$, $w = 1/(\sigma^2(Fo^2)+(a\times P)^2+b\times P)$.

$GoF = (\Sigma w\times(Fo^2-Fc^2)^2 / (n-p))^{1/2}$ with $w = 1/(\sigma^2(Fo^2)+(a\times P)^2+b\times P)$, n is the number of observed reflections, p is number of parameters refined.

2.4. EDS Analysis

EDS quantitative elemental analyses of crystals from the $SmCuP_2$ and $SmCuAs_{0.67}P_{1.33}$ samples were performed on a Hitachi S-2460N variable pressure scanning electron microscope, equipped with a Oxford Instruments Link Isis Model 200 X-ray analyzer. The single crystals of CuP_2,

prepared by the gas transport technique, were used as standards to determine the Cu/P ratio in the samarium copper phosphide crystals. The lattice parameters of the CuP_2 crystals were checked on a single crystal diffractometer. A data set for one crystal was collected and the structure was refined to check the composition.

No oxygen was observed in the crystals of CuP_2, the samarium copper phosphide and arsenophosphide. The analyses of three crystals from each sample (crystals from each sample are shown in Fig. 1) gave average compositions of $SmCu_{1.13}P_{1.99}$ and $SmCu_{1.06}As_{0.73}P_{1.22}$. The Cu/P ratio for the phosphide clearly indicated extra copper and agreed well with the results of the single crystal refinement ($SmCu_{1.15}P_2$). The Sm/Cu ratio of 1/1.06 in the arsenophosphide also showed additional cooper and it was close to that of 1/1.07 from the single crystal refinement ($SmCu_{1.07}As_{0.85}P_{1.15}$).

Table 4. Atomic and Equivalent Isotropic Displacement Parameters (U_{eq}, $Å^2$) for $SmCu_{1.05}As_{1.67}P_{0.33}$ (*P4/nmm*), $SmCu_{1.07}As_{0.85}P_{1.15}$ (*Pmmn*) and $SmCu_{1.15}P_2$ (*Cmmm*)

Atoms	Wyckoff position	Occupancy	*x*	*y*	*z*	U_{eq}
			$SmCu_{1.05}As_{1.67}P_{0.33}$			
Sm	2*c*	1	¼	¼	0.24129(5)	0.0067(2)
Cu1	2*b*	1	¾	¼	½	0.0106(3)
Cu2	2*c*	0.046(6)	¼	¼	0.8721(31)	0.029(9)
(As/P)1	2*c*	0.702As +0.298(5)P	¼	¼	0.6545(1)	0.0080(4)
(As/P2	2*a*	0.965As +0.035(3)P	¾	¼	0	0.0145(3)
			$SmCu_{1.07}As_{0.85}P_{1.15}$			
Sm	2*a*	1	¼	¼	0.24159(5)	0.0101(2)
Cu1	2*b*	1	¼	¾	0.49952(13)	0.0115(3)
Cu2	2*a*	0.074(4)	¼	¼	0.8964(20)	0.023(6)
(As/P)1	2*a*	0.181As +0.819(4)P	¼	¼	0.65256(19)	0.0103(6)
(As/P)2	2*b*	0.672As +0.328(4)P	¼	¾	0.00020(16)	0.0234(5)
			$SmCu_{1.15}P_2$			
Sm1	4*i*	1	0	0.38371(5)	0	0.0123(4)
Sm2	4*j*	1	0	0.12173(5)	½	0.0102(4)
Cu1	8*m*	1	¼	¼	0.2484(2)	0.0118(5)
Cu2	4*i*	0.294(6)	0	0.0490(4)	0	0.026(2)
P1	4*j*	1	0	0.3259(2)	½	0.0090(9)
P2	4*i*	1	0	0.1735(2)	0	0.0091(9)
P3	8*o*	1	0.2631(7)	0	0.2917(7)	0.032(1)

Table 5. Interatomic Distances (Å) in $SmCu_{1.05}As_{1.67}P_{0.33}$ (*P4/nmm*) and $SmCu_{1.07}As_{0.85}P_{1.15}$ (*Pmmn*)

Atoms	$SmCu_{1.05}As_{1.67}P_{0.33}$	$SmCu_{1.07}As_{0.85}P_{1.15}$	Atoms	$SmCu_{1.05}As_{1.67}P_{0.33}$	$SmCu_{1.07}As_{0.85}P_{1.15}$
Sm-4*X*1	2.9563(6)	2.9221(8)	*X*1-Cu2	2.16(3)	2.40(2)
4Cu2	2.989(12)	3.050(9)	4Cu1	2.4878(9)	2Cu1 at 2.443(1)
4*X*2	3.0948(6)	2*X*2 at 3.063(1)			2Cu1 at 2.450(1)
		2*X*2 at 3.066(1)	4Sm	2.9563(6)	2.9221(8)
4Cu1	3.2306(6)	2Cu1 at 3.192(1)			
		2Cu1 at 3.198(1)			
			*X*2-4Cu2	2.334(17)	2Cu2 at 2.181(9)
Cu1-4*X*1	2.4878(9)	2*X*1 at 2.443(1)			2Cu2 at 2.185(9)
		2*X*1 at 2.450(1)	4*X*2	2.7692(4)	2.7297(4)
4Cu	2.7692(4)	2.7297(4)	4Sm	2.9563(6)	2Sm at 3.063(1)
					2Sm at 3.066(1)
Cu2-1*X*1	2.16(3)	2.40(2)			
4*X*2	2.334(17)	2*X*2 at 2.182(9)			
		2*X*2 at 2.185(9)			
4Sm	2.989(12)	3.050(9)			

*X*1 is (As/P)1 and *X*2 is (As/P)2.

Table 6. Selected Interatomic Distances (Å) in $SmCu_{1.15}P_2$ (*Cmmm*)

Atoms	Distances	Atoms	Distances
Sm1 – 2P1	2.944(2)	Cu2 – Cu2	1.913(14)
2P2	2.946(2)	4P3	2.343(5)
2Cu2	3.026(3)		
4P3	3.055(2)	P1 – 4Cu1	2.434(3)
4Cu1	3.290(1)		
		P2 – Cu2	2.429(9)
Sm2 – 2P4	2.901(2)	4Cu1	2.431(2)
2P1	2.911(2)		
4P3	2.977(2)	P3 – P3	2.266(8)
2Cu2	3.067(4)	2Cu2	2.343(5)
4Cu1	3.161(1)	P3	2.584(8)
		P3	2.869(8)
Cu1 – 2P2	2.431(3)	P3	3.173(8)
2P1	2.434(3)		
Cu1	2.702(2)		
2Cu1	2.726(1)		
Cu1	2.736(2)		

2.5. Magnetic Measurements

Dc magnetization measurements were performed for the SmCuAsP powder sample in the temperature range 1.8-300 K and in an applied magnetic field of 10 kOe employing a Quantum Design MPMS-5 SQUID magnetometer.

3. Results and Discussion

3.1. Structural Changes in $SmCu_{1+\delta}As_{2-x}P_x$

Structural changes in $SmCu_{1+\delta}As_{2-x}P_x$ can be divided into two groups with respect to the methods that introduce them. The first group involves the *P4/nmm→Pmmn* and *Pmmn→P2/n* transitions that occur upon As/P substitution, the second one consists of the *Pmmn→P4/nmm* and *P2/n→Cmmm* transformations, imposed through introducing extra copper into the structures. These structural changes, established from the analysis of the $SmCu_{1+\delta}As_{2-x}P_x$ powder samples, are summarized in Fig. 3. The transitions in $SmCuAs_{2-x}P_x$ ($\delta = 0$) driven by the As/P substitution are represented in Fig. 4**a** as a change in the *b/a* ratio versus the phosphorus amount. As in the *RE*$CuAs_{2-x}P_x$ series with gadolinium (Fig. 4**c**), holmium and erbium [3, 4] substitution of P for As in $SmCuAs_{2-x}P_x$ leads to the *P4/nmm→Pmmn* transition, which is followed by a second transition. The second transitions differ for each series, and for the samarium case it is *Pmmn→P2/n*.

New to the *RE* = Sm case are the presence of extra copper in the structures of $SmCu_{1+\delta}As_{2-x}P_x$ and the structural transitions due to this extra copper. The phases *RE*$CuAs_{2-x}P_x$ (*RE* = Gd, Ho or Er)

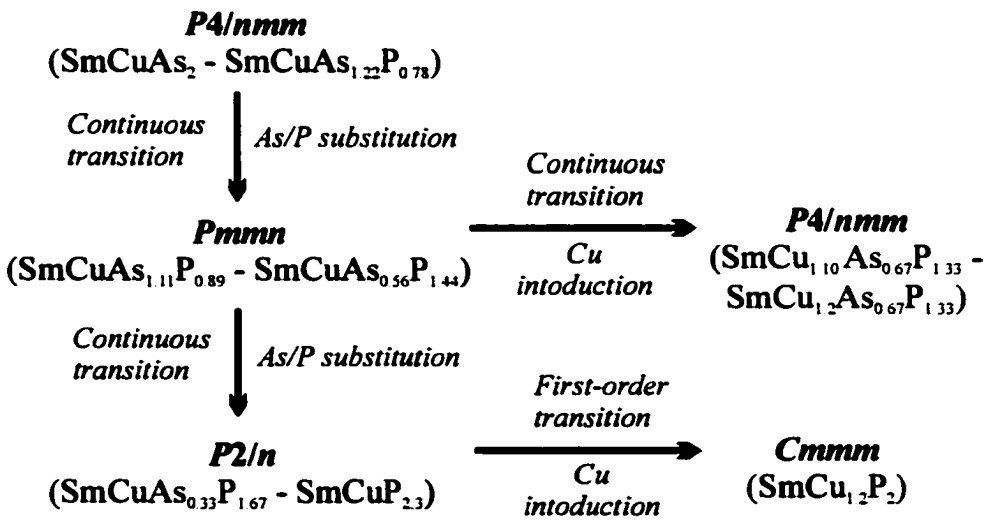

Figure 3. Structural changes in the $SmCu_{1+\delta}As_{2-x}P_x$ series (powder data).

are not found to take in any additional Cu atoms [3, 4], on the contrary, all investigated $SmCu_{1+\delta}As_{2-x}P_x$ phases (except for monoclinic $SmCuP_2$ and $SmCuP_{2.3}$) have some homogeneity ranges. Variations in the copper amount do not change the symmetries of $SmCu_{1+\delta}As_2$, $SmCu_{1+\delta}AsP$ and probably of all the phases $SmCu_{1+\delta}As_{2-x}P_x$ with $0 < x < 1$. On the other hand, the orthorhombic $SmCu_{1+\delta}As_{0.67}P_{1.33}$ and, very likely, the other orthorhombic arsenophosphides $SmCu_{1+\delta}As_{2-x}P_x$ with $1.33 < x < 1.44$ transform to tetragonal phases at some value of δ (Table 2).

3.2. Landau Theory and Symmetry-Breaking Transitions in $SmCu_{1+\delta}As_{2-x}P_x$

The importance of Landau theory [16-18] to structural chemistry is twofold; it answers the question of whether a transition between the high- and low-symmetry structures can occur as second-order (continuous). Secondly, it can provide a structural model for one of the phases during the

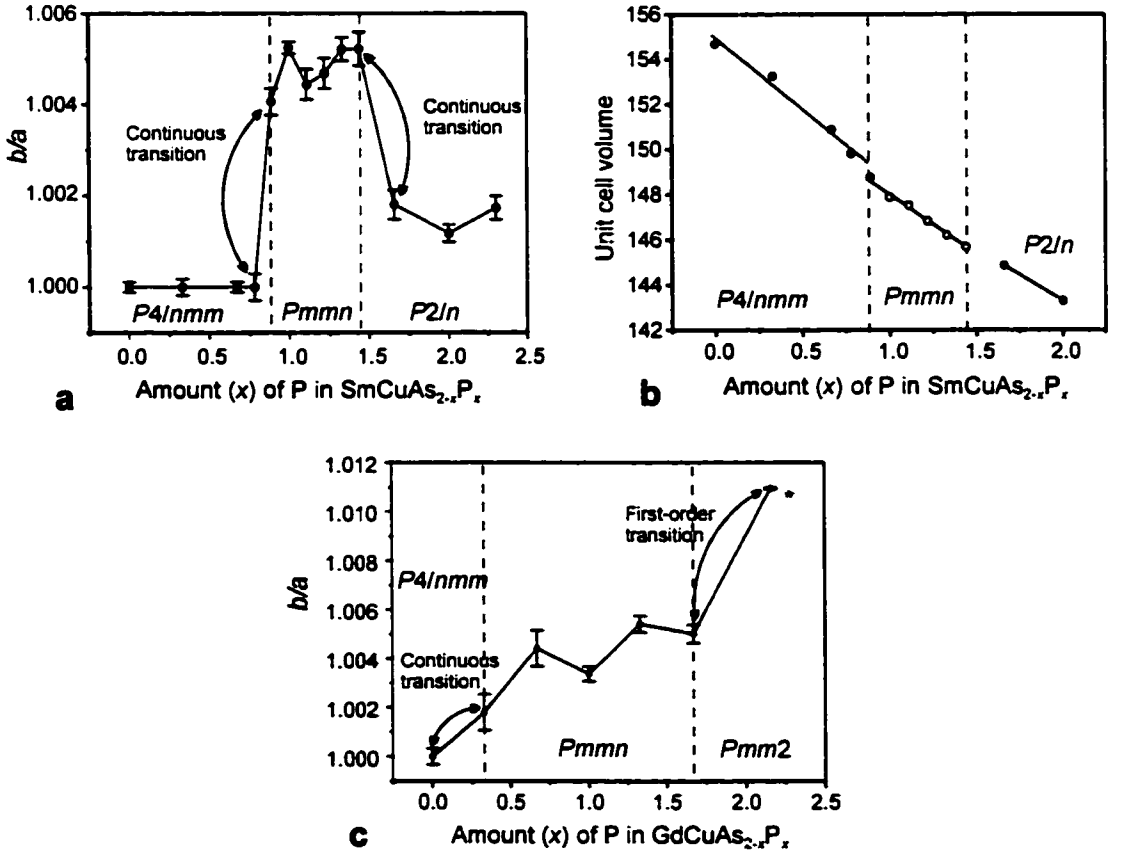

Figure 4. *b/a* ratio (**a**) and unit cell volume (**b**) versus phosphorus amounts for $SmCuAs_{2-x}P_x$ (X-ray powder data, the compositions are nominal). *b/a* ratio in (**c**) indicates the symmetry-breaking transitions in $GdCuAs_{2-x}P_x$. Dashed lines show the experimentally established existence regions for the orthorhombic arsenophosphides. Discontinuity in the unit cell volume curve during the *P4/nmm*→*Pmmn* distortion is artificially produced (not real) to illustrate the step in the slope. * $\frac{1}{2}V_{\text{unit cell}}$ for $GdCuP_{2.16}$.

continuous symmetry-breaking process, as it did for the gadolinium copper arsenophosphide [3]. The determination of an irreducible representation to which a transition belongs can be very helpful in the analysis of electronic structures and driving forces of symmetry-breaking transitions in the solid state. In the case of the orthorhombic distortions in $RECuAs_{2-x}P_x$ [3, 4] the combination of Landau theory, band structure calculations and symmetry analysis of the bonding in the As/P layers showed that the distortions are not governed by a Peierls-type instability but are the results of the structural adaptations to the smaller P atoms [8].

One of the important conclusions of Landau theory for a second-order phase transition is that below the transition temperature the high-symmetry structure is at a maximum in the Gibbs free energy. Therefore the phase is unstable (not metastable) and will transform with time. This time can be very long for order-disorder transitions requiring diffusion, especially at low temperatures. However, for second-order displacive transitions this time is always negligibly small. While studying the $SmCuAs_{2-x}P_x$ samples we obtained the tetragonal phase (*P4/nmm* space group) for the $SmCuAs_{0.67}P_{1.33}$ powder sample, the composition of which falls into the orthorhombic region (Fig. 4). Since the *P4/nmm* → *Pmmn* transition is a displacive second-order (continuous) one, it followed that the $SmCuAs_{0.67}P_{1.33}$ sample was not equilibrated and was inhomogeneous. The inhomogeneity did not arise from differences in the As/P ratio since the lattice parameters of the dominant tetragonal phase (a = 3.8563(3), c = 9.868(1) Å, V = 146.75(2) Å^3) were those characteristic of the As/P ratio of 0.67/1.33 (the lattice parameters of the neighboring orthorhombic phases were taken as the basis for the comparison). The presence of additional copper atoms in the structure was therefore assumed to have stabilized the tetragonal structure in the $SmCuAs_{0.67}P_{1.33}$ sample. Extensive annealing homogenized the $SmCuAs_{0.67}P_{1.33}$ sample and yielded the expected orthorhombic structure. The annealing of the $SmCu_{1.1}As_{0.67}P_{1.33}$ and $SmCu_{1.2}As_{0.67}P_{1.33}$ samples always gave the tetragonal phases, thus proving that the additional copper atoms stabilize the tetragonal structure.

P4/nmm→Pmmn→P2/n transitions from tetragonal $SmCuAs_{1.22}P_{0.78}$ to orthorhombic $SmCuAs_{1.11}P_{0.89}$ and *from orthorhombic $SmCuAs_{0.56}P_{1.44}$ to monoclinic $SmCuAs_{0.33}P_{1.67}$*. The Landau theory can be used as a basis for analyzing the transitions

$$P4/nmm \rightarrow Pmmn \rightarrow P2/n.$$

The tetragonal to orthorhombic distortion has been discussed previously [3, 4] and was shown to correspond to the B_{1g} irreducible representation of *P4/nmm* at $\boldsymbol{k}$ = 0 ($\boldsymbol{k}$ is the wave vector of the distortion). The orthorhombic arsenophosphides (*Pmmn* space group) studied here appear to break the tetragonal symmetry continuously and thus undergo a transition analogous to those in $GdCuAs_{2-x}P_x$,

$HoCuAs_{2-x}P_x$ and $ErCuAs_{2-x}P_x$. The reverse structural transition *Pmmn* → *P4/nmm*, driven by introduction of extra copper into the $SmCuAs_{0.67}P_{1.33}$ structure, is then also continuous.

As discussed in a separate paper [8], the *P4/nmm* → *Pmmn* distortion, originating from the B_{1g} vibrational (phonon) mode of the Cu1 atoms, provides better bonding for smaller P atoms through tighter packing. A volume decrease upon the *P4/nmm* → *Pmmn* transition can be inferred from the data in Fig. 4**b**. There is a step down in the slopes of the unit cell volumes versus the phosphorus amount for the two structures, which clearly indicates tighter packing for the orthorhombic structure. However, it must be remembered that at the transition point the change in the unit cell volume is continuous.

The orthorhombic to monoclinic transition (*Pmmn* → *P2/n*) occurs with no loss of the translational symmetry ($\boldsymbol{a}_{mon} = \boldsymbol{a}_{ort}$, $\boldsymbol{b}_{mon} = \boldsymbol{b}_{ort}$, $\boldsymbol{c}_{mon} = \boldsymbol{c}_{ort}$ and $\boldsymbol{k} = 0$). In the course of the X-ray powder analysis, none of the samples exhibited a two-phase orthorhombic-monoclinic transition region. Therefore we conclude that the transition occurs continuously and appears in all respects to be a continuation of the tetragonal to orthorhombic transition, i.e., corresponds to the B_{1g} irreducible representations of the point group D_{2h} (Table 7). Accordingly, we suggest the *P2/n* symmetry for the monoclinic phase, a suggestion that will require confirmation by single crystal analysis.

P2/n → Cmmm transition from $SmCuP_2$ to $SmCu_{1.15}P_2$. The transition from the monoclinic $SmCuP_2$ structure (*P2/n* space group) to the orthorhombic $SmCu_{1.15}P_2$ structure (*Cmmm* space group) occurs upon introducing additional copper atoms into the structure of $SmCuP_2$. Since the two structures were observed to coexist in the two samples, it is concluded that this *P2/n* → *Cmmm* transition is first-order.

Table 7. One-Dimensional Irreducible Representation B_{1g} of *Pmmn* at $\boldsymbol{k} = 0$

g	ϵ	C_{2z}	C_{2x}	C_{2y}	i	σ_z	σ_x	σ_y
$\chi(g)$	1	1	-1	-1	1	1	-1	-1

3.3. Structure Description

Tetragonal $SmCu_{1.05}As_{1.67}P_{0.33}$. $SmCu_{1.05}As_{1.67}P_{0.33}$ adopts a stuffed variant of the $HfCuSi_2$ structure (*P4/nmm* space group) in which the additional Cu2 atoms partially occupy the square pyramidal site. This structure was reported by *Wang, McDonald* and *Mar* for $CeCu_{1.10(1)}As_2$ and $PrCu_{1.09(1)}As_2$ [9]. Alternatively, the structure of $SmCu_{1.05}As_{1.67}P_{0.33}$ can be seen as the $CaBe_2Ge_2$ structure (*P4/nmm* space group) [19] with a highly deficient Cu2 site. If the second view is adopted,

then the (As/P)2 atoms are considered to be tetrahedrally coordinated by the Cu2 atoms and primarily bound to Cu2. However since the structural distortions originate from the instabilities associated with the square nets, the first description is better suited to this discussion.

In $SmCu_{1.05}As_{1.67}P_{0.33}$ positions 2*a* and 2*c* are statistically occupied by As and P atoms, with the P atoms being mostly in the Cu(As/P)1 block. As was shown for $GdCuAs_{1.15}P_{0.85}$ [3], the geometrical and electronic factors favor separation of the As and P atoms on positions 2*a* and 2*c* while mixing is favored by the configurational entropy. Therefore for this compound, as well as for the rest of the tetragonal and orthorhombicly distorted samarium copper arsenophosphides, entropy wins out and statistical As/P distributions occur.

Presence of the additional Cu atoms around the (As/P)2 net was predicted from the analysis of the *relative interatomic distances* for the $SmCuAs_{1.67}P_{0.33}$ powder [8]. The *relative interatomic distance* is the ratio between the As/P–As/P or Cu–Cu interatomic distances in the *ab* plane and the element diameters (for the As/P layers it is a sum of the As and P radii weighted by the composition). In tetragonal $SmCuAs_2$, or other rare-earth copper arsenides, the Cu net is structurally the same as the As2 layer (see Cu1 and (As/P)2 in orthorhombic $SmCu_{1.07}As_{0.85}P_{1.15}$ in Fig. 5). The element radii of the As and Cu atoms are close to each other: 1.245 Å and 1.278 Å, respectively. So, the relative interatomic distances in the horizontal As and Cu layers are similar in the tetragonal *RE*$CuAs_2$ phases. When smaller P atoms (r_P = 1.105 Å for the white modification) are introduced in the As square net, the relative interatomic distance for P becomes much larger than those for As and Cu, and accordingly the site is less favorable for the P atom occupation.

There are two known ways to increase packing and more effectively bind the P atoms in the structure. One is the *P*4/*nmm* → *Pmmn* distortion resulting from the B_{1g} vibrational (phonon) mode of the (As/P)2 and Cu1 atoms, the other is to take some additional atoms into the structure in the vicinity of the P atoms [8]. The $SmCu_{1.05}As_{1.67}P_{0.33}$ phase follows the second path and preserves the tetragonal symmetry. The same stabilization mechanism can be assumed for the rest of the tetragonal arsenophosphides, including $SmCu_{1.1}As_{0.67}P_{1.33}$ and $SmCu_{1.2}As_{0.67}P_{1.33}$ obtained upon introducing additional copper atoms into orthorhombic $SmCuAs_{0.67}P_{1.33}$.

The presence of the Cu2 site in the tetragonal arsenophosphides with the nominal compositions $SmCuAs_{2-x}P_x$ can be also predicted if one compares existence regions of the tetragonal and orthorhombic phases in the $SmCuAs_{2-x}P_x$ and $GdCuAs_{2-x}P_x$ series (Fig. 4**a** and **c**). In $GdCuAs_{2-x}P_x$ the only known tetragonal phase is $GdCuAs_2$, all the arsenophosphides are orthorhombic. Since Sm atoms are larger than the Gd atoms, the relative interatomic distances in the As/P nets of the Sm arsenophosphides are larger than those in the orthorhombic Gd arsenophosphides and therefore one

could expect the Sm arsenophosphides to be orthorhombic as well. Instead $SmCuAs_{1.67}P_{0.33}$ through $SmCuAs_{1.22}P_{0.78}$ are tetragonal, and the reason for that is presence of additional copper atoms around the As/P nets. Although the compositions $SmCuAs_{1.67}P_{0.33}$ through $SmCuAs_{1.22}P_{0.78}$ are used in the text, it is understood that the structures of the tetragonal arsenophosphides have extra copper.

Orthorhombic $SmCu_{1.07}As_{0.85}P_{1.15}$. $SmCu_{1.07}As_{0.85}P_{1.15}$ (*Pmmn* space group, Fig. 5) adopts a stuffed version of the $GdCuAs_{1.15}P_{0.85}$ structure (*Pmmn*), which is the orthorhombicly distorted $HfCuSi_2$ structure. This relationship between the three structures can be written as

$HfCuSi_2$ (*P4/nmm*) → $GdCuAs_{1.15}P_{0.85}$ (*Pmmn*) → $SmCu_{1.07}As_{0.85}P_{1.15}$ (*Pmmn*).

The first arrow indicates a structural deformation and, as discussed above, can be continuous. The second transition occurs with filling the Sm/P tetragonal antiprismatic voids by the Cu2 atoms. Here, the As and P atoms are mixed in the manner observed in tetragonal $SmCu_{1.05}As_{1.67}P_{0.33}$, and the same energetic and entropy factors govern the As/P distribution. The distortion from the tetragonal cell of $SmCu_{1.05}As_{1.67}P_{0.33}$ is very small and it results in slight deviation of the angles in the (As/P)2 layer from 90° (see Fig. 7). Due to the smaller lattice parameters (the result of the larger P concentration)

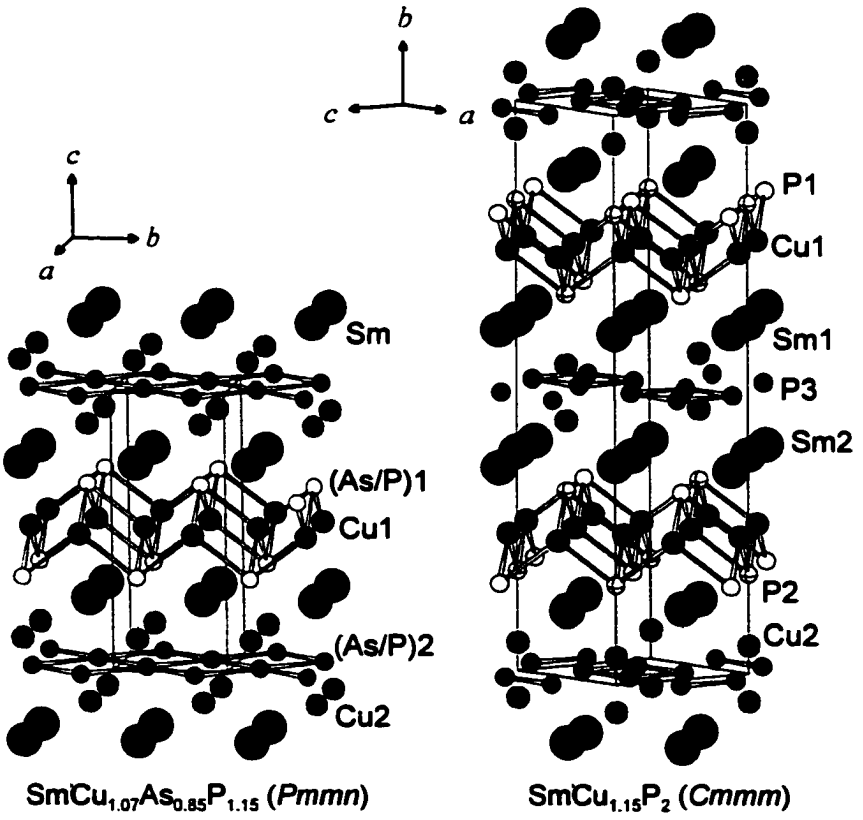

Figure 5. Structure of $SmCu_{1.07}As_{0.85}P_{1.15}$ and $SmCu_{1.15}P_2$.

the (As/P)2-Cu2 distances are smaller than the corresponding ones in the tetragonal arsenophosphide.

Above we pointed out that the additional Cu2 atoms in $SmCu_{1.05}As_{1.67}P_{0.33}$ (*P4/nmm* space group) provide a tighter environment for the (As/P)2 atoms and thus stabilize the tetragonal structure. But the small number of Cu2 atoms is not sufficient to preserve the tetragonal structure for the arsenophosphides with larger phosphorus amount, and these phosphorus-rich arsenophosphides, including $SmCu_{1.07}As_{0.85}P_{1.15}$, adopt the orthorhombic structure. Yet introducing more copper (up to δ = 0.2) into some arsenophosphides does lead to the tetragonal structure, e.g., $SmCu_{1.1}As_{0.67}P_{1.33}$ and $SmCu_{1.2}As_{0.67}P_{1.33}$. The question that arises is why the phases do not incorporate even more Cu2 atoms ($\delta > 0.2$) and keep the tetragonal structure. As will be discussed in the next paper, their presence destabilizes the bonding in the (As/P)2 net, so the structures of $SmCu_{1+\delta}As_{2-x}P_x$ represent a fine balance of the electronic, geometric factors and Coulomb forces.

Orthorhombic $SmCu_{1.15}P_2$. Samarium copper phosphide (*Cmmm* space group) displays an orthorhombic distortion resulting in a larger unit cell (Fig. 5), and this distortion is different from those previously observed in the *RE*$CuAs_{2-x}P_x$ compounds. The structure is related to tetragonal $HfCuSi_2$. The largest changes, relative to the tetragonal structure, occur in the P3 layers where discrete rectangular units are formed, with additional Cu2 atoms above and below the P3 layer. Distortions in the P3 layer lead to the larger unit cell parameters in the *ab* plane (the *ac* plane for the *Cmmm* symmetry), as compared to those of the tetragonal phases, and to the loss of C_{4z}. Shift by $\tau = \frac{1}{2}(\boldsymbol{a} + \boldsymbol{b})$ of every second $HfCuSi_2$-type unit cell results in the doubling of the *c* parameter in the $SmCu_{1.15}P_2$ structure (the *b* parameter in the *Cmmm* space group). This different stacking along *c* supports the first-order nature of the *P2/n* → *Cmmm* transition from $SmCuP_2$ to $SmCu_{1.15}P_2$ since the shift η, if it occurred continuously from $\tau = 0$ (*P2/n*, $SmCuP_2$) to $\tau = \frac{1}{2}(\boldsymbol{a} + \boldsymbol{b})$ (*Cmmm*, $SmCu_{1.15}P_2$), would produce a symmetry different from *Cmmm* for $0 < \tau < \frac{1}{2}(\boldsymbol{a} + \boldsymbol{b})$.

In $SmCu_{1.15}P_2$ all interatomic distances, except for those involving Cu2, are similar to the corresponding distances observed in the other *RE*$CuAs_{2-x}P_x$ series [3, 4] and they are close to the sums of the element radii ($r_{Cu}+r_{Sm}$=1.28+1.81=3.09 Å and $r_{Cu}+r_P$=1.28+1.11= 2.39 Å). Cu2-Cu2 bonding of 1.91 Å is unlikely to occur through the P3 layer, a pair of such facing Cu2 atoms will experience repulsion. The Cu2 atoms need not to face each other given the ~1/3 distribution on this copper site.

The atomic arrangement in $SmCu_{1.15}P_2$ is similar to that in $CeCu_{1.12}P_{1.97}$ (*Cmmm* space group, *a* = 19.649(5), *b* = 5.550(1), *c* = 5.522(1) Å) reported by *Möller* and *Jeitschko* [20]. Partial occupancies were assigned to all three phosphorus sites (0.98(2) for P1, 0.99(2) for P2 and 0.98(3) for P3). *Möller* and *Jeitschko* observed the same orthorhombic structure for $LaCu_{1+\delta}P_{-2}$ and $LaAg_{1+\delta}P_{-2}$,

and they also reported high temperature tetragonal modifications of $CeCu_{1+\delta}P_{\sim 2}$ and $LaAg_{1+\delta}P_{\sim 2}$ but neither transition temperatures nor structural parameters for these tetragonal phases were given.

When prepared as powders, the phosphides without excess copper ($\delta = 0$) have the monoclinic structure (*P2/n* space group), while the phosphides with extra copper ($\delta > 0$ in $SmCu_{1+\delta}P_2$) adopt the orthorhombic structure (*Cmmm* space group). Mineralization reactions on these phosphides, with or without excess copper, always yielded the orthorhombic phases. In [10] the phosphide prepared at 800°C as a powder with the initial composition $SmCuP_2$ was assigned the $HfCuSi_2$-type, in which Cu and P are statistically mixed on the 2*c* site ($SmCu_{1+x}P_{2-x}$ composition, *P4/nmm*, $a = 3.814$ and $c = 9.759$ Å), although peak splitting similar to that in $SmCuP_{2.3}$ (Fig. 2) of our experiments was observed. We believe that the structure of $SmCu_{1+x}P_{2-x}$ is the same as the structure of the monoclinic arsenophosphides $SmCuP_2$ and $SmCuP_{2.3}$ reported here. Later *Chykhrii* conducted preliminary single crystal studies (Laue, rotation, de Jong - Bouman methods) on a crystal of the samarium copper phosphide prepared through iodine gas transport at 1100-1200°C and found doubling only of the *c* parameter [11]. The tetragonal $SrZnBi_2$ structure with no statistical mixture was now assumed ($SmCuP_2$ composition, *I4/mmm* space group, $a = 3.839$ and $c = 19.431$ Å) and the atomic parameters for $SmCuP_2$ were refined using the powder data form the crushed single crystals at the room temperature. Although it is possible that the orthorhombic form of the samarium copper phosphides (*Cmmm* space group) transforms into the tetragonal modification (*I4/mmm* space group) upon heating to temperatures higher than 800°C, it is more likely that the real symmetry of the phosphide crystal was *Cmmm* (superstructure reflections are very weak and could be missed; the similarity in the *a* and *c* parameters does not give noticeable peak splitting on a diffractogram).

Distortion of the P layers in orthorhombic $SmCu_{1.15}P_2$. The Peierls-type instability of the square net of the VA elements was considered by *Hulliger*, *Schmeltzer* and *Schwarzenbach* [1]. They proposed three types of the distortion: (a) formation of discrete squares as met in the skutterudite-type structure of CoP_3 [21], (b) zigzag chains as found in CeAsS [7] , $ErCuP_2$ [4] and (c) *cis-trans* chains as realized in GdPS [1] (Fig. 6). The structure of $SmCu_{1.15}P_2$ is an example of the (a)-type distortion. The instability of its P3 layer and the electronic structure will be discussed in a future paper.

The (As/P) and P layers of $SmCu_{1.05}As_{1.67}P_{0.33}$, $SmCu_{1.07}As_{0.85}P_{1.15}$ and $SmCu_{1.15}P_2$ are shown in Fig. 7. In $SmCu_{1.05}As_{1.67}P_{0.33}$ the (As/P) net is square and all distances are the same, the additional Cu2 atoms are at the apices of the square pyramid staggered with respect to each other (giving rise to the *n*-glide plane). The same arrangement is found in $SmCu_{1.07}As_{0.85}P_{1.15}$, but now the As/P net is slightly distorted (the angles are not right). In $SmCu_{1.15}P_2$ the P3 rectangles are formed, the distances are much shorter between the atoms in these units ($d = 2.266$ and 2.584 Å) than between the atoms of

the different units (d = 2.869 and 3.173 Å). The additional Cu2 atoms on each side of the P3 layer eclipse each other along the b direction and are located between the P3 units. The shortest P3-P3 distance of 2.266 Å in $SmCu_{1.15}P_2$ is close to the single bond distances of 2.22-2.25 Å in the layers of the black phosphorus [22] and the P-P distance of 2.268 Å in the phosphorus dimers of $GdCuP_{2.20}$ [3]. The second shortest P3-P3 bond of 2.584 Å cannot be seen as a single bond and is even larger than those in $ErCuP_2$ [4] and CeP_2 [23] where the phosphorus atoms are joined into zigzag chains or fragments of chains with relatively large distances of 2.41-2.46 Å and 2.404-2.453 Å, respectively. Interestingly, the separation distance of 2.869 Å in $SmCu_{1.15}P_2$ is close to the distances of 2.82 and 2.88 Å between the zigzag chains in $ErCuP_2$.

3.5. Magnetic Susceptibility

Low temperature dc susceptibility (inset to Fig. 8) for the SmCuAsP powder implies a long-range magnetic ordering at T=19 K. Susceptibility increases with decrease of temperature below ~10K, that may be indicative either of another (spin reorientation) transition below our temperature

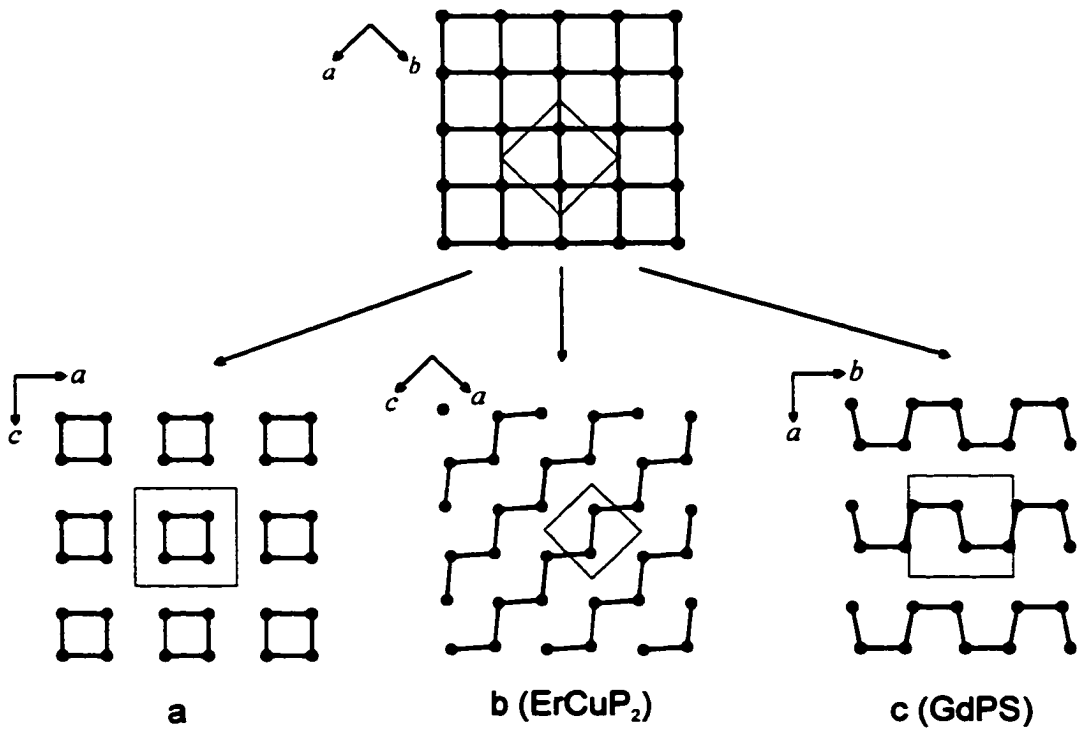

Figure 6. Three possibilities for the formation of the P^{1-} polyanions by distorting a plane square net in the $HfCuSi_2$-type structure. Above: undistorted square net as in $SmCu_{1.05}Cu_{1.67}P_{0.33}$; (**a**) discrete squares (rectangles are found in $SmCu_{1.15}P_2$); (**b**) zigzag chains in the P layer of $ErCuP_2$; (**c**) *cis-trans* chains in the P layer of GdPS.

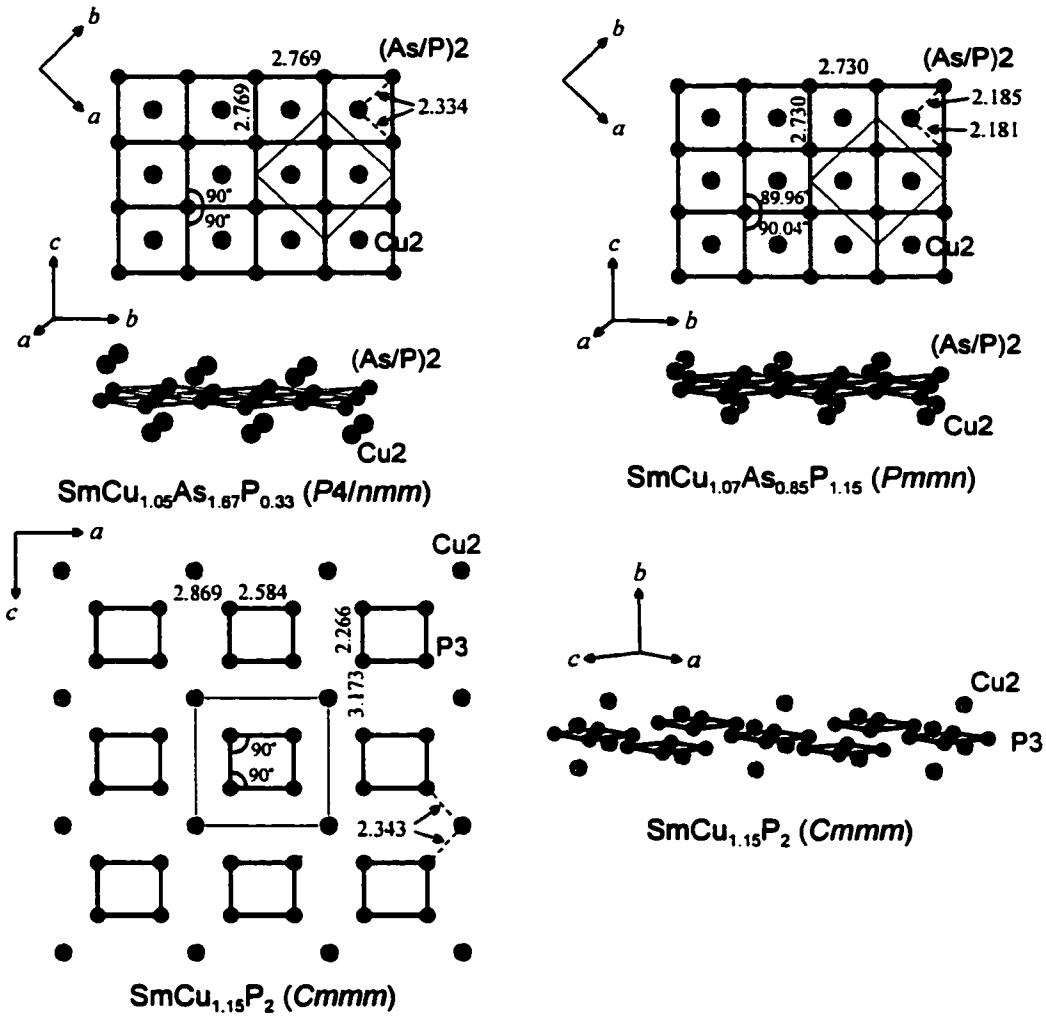

Figure 7. As/P and P layers in $SmCu_{1.05}As_{1.67}P_{0.33}$, $SmCu_{1.07}As_{0.85}P_{1.15}$ and $SmCu_{1.15}P_2$.

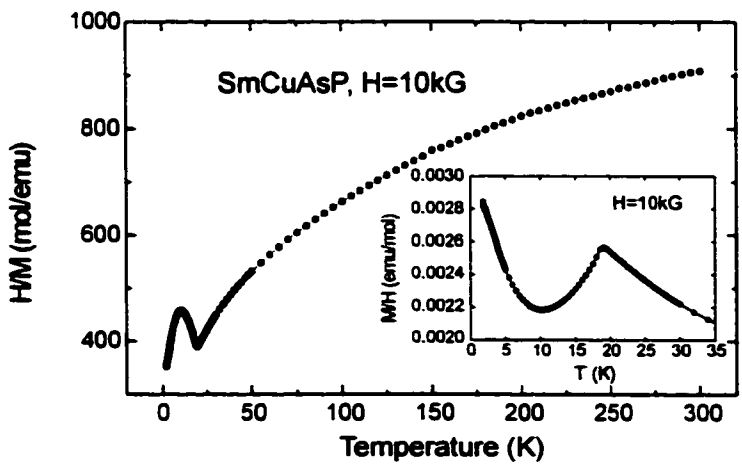

Figure 8. Magnetic susceptibility for the SmCuAsP powder.

range or of a signal coming from possible very small amount of paramagnetic impurities.

At higher temperatures, in the paramagnetic region, the inverse susceptibility of SmCuAsP is non-linear and tends to become temperature independent at high temperatures (Fig. 8). This behavior is often observed in the Sm containing compounds, since the first excited state of the Hund's rule multiplet ($J = 7/2$) is very close to the excited state ($J = 5/2$).

4. Conclusions

Single crystal refinement and EDS analysis show excess copper in single crystals of tetragonal $SmCu_{1.05}As_{1.67}P_{0.33}$ and orthorhombic $SmCu_{1.07}As_{0.85}P_{1.15}$. The X-ray powder techniques are insensitive to small (1-5%) excess of Cu and it suggested that small amounts of extra copper occur in all tetragonal and orthorhombic arsenophosphides. The distribution of this copper appears to depend upon heat treatment. Because the transformation of the tetragonal phase to the orthorhombic phase in the $SmCuAs_{0.67}P_{1.33}$ sample upon the heat treatment could not result from a structural barrier, it is suggested that the heat treatment redistributed the Cu atoms through diffusion and established the equilibrium. Since the single crystal result for the tetragonal phase yielded excess copper, and since the introduction of Cu into the orthorhombic arsenophosphide yielded the tetragonal phase, it is concluded that Cu stabilizes the tetragonal phase. Because the compositions of the powder phases are nominal, it is possible that there is excess copper in the tetragonal arsenophosphides over much of their existence region, i.e., that a hidden variable in Fig. 4a is variable Cu content. The stabilization of the tetragonal form by excess Cu was explained by relative interatomic distance arguments [8].

Acknowledgement

This research was supported by the Office of the Basic Energy Sciences, Materials Sciences Division, US Department of Energy, DOE. The Ames Laboratory is operated for DOE by Iowa State University under contract No. W-7405-Eng-82.

References

[1] F. Hulliger, R. Schmelczer, D. Schwarzenbach, *J. Solid State Chem.* **1977**, *21*, 371.

[2] E. Brechtel, G. Cordier, H. Schäfer, *Z. Naturforsch., B: Anorg. Chem., Org. Chem.* **1979**, *34B*, 251.

[3] Y. Mozharivskyj, D. Kaczorowski, H. F. Franzen, *J. Solid State Chem.* **2000**, *155*, 259.

[4] Y. Mozharivskyj, D. Kaczorowski, H. F. Franzen, *Z. Anorg. Allg. Chem.* **2001**, *627*, 2163.

[5] R. E. Peierls, *Quantum Theory of Solids*, Oxford University Press, London 1955.

[6] T. A. Albright, J. K. Burdett, M.-H. Whangbo, *Orbital Interactions in Chemistry*, Wiley, New York 1985.

[7] G. Sfez, C. Adolphe, *Bull. Soc. Fr. Mineral. Cristallogr.* **1972**, *95*, 553.

[8] Y. Mozharivskyj, H. F. Franzen, *submitted to J. Phys. Chem.*

[9] M. Wang, R. McDonald, A. Mar, *J. Solid State Chem.* **1999**, *147*, 140.

[10] S. I. Chykhrij, Y. B. Kuz'ma, S. V. Oryshchyn, *Dopov. Akad. Nauk Ukr. RSR, Ser. B* **1989**, *3*, 63.

[11] S. I. Chikhrii, *Zh. Neorg. Khim.* **1990**, *35*, 1656.

[12] L. G. Akselrud, Y. M. Grin, V. K. Pecharsky, P. Y. Zavalij, CSD - Universal Program Package for Single Crystal and Powder Data Treatment, *Proc.12th European Crystallographic Meet., August 28-29,* 1989, Academy of Sciences, Moscow, USSR, *Kristallographiya, Suppl.*, **1989**, *155*, 2.

[13] M. Brylak, M. H. Möller, W. Jeitschko, *J. Solid State Chem.* **1995**, *115*, 305.

[14] W. C. Hamilton, *Acta Cryst.* **1965**, *18*, 502.

[15] *SHELXTL*, Bruker Analytical X-Ray Systems, Madison, USA 1997.

[16] L. D. Landau, E. M. Lifshits, *Statistical Physics*, Vol. 5, Pergamon Press, London 1958.

[17] H. F. Franzen, *Chem. Mater.* **1990**, *2*, 486.

[18] H. F. Franzen, *Physical Chemistry of Solids*, World Scientific, Singapore 1994.

[19] B. Eisenmann, N. May, W. Müller, H. Schäfer, *Z. Naturforsch. B* **1972**, *27*, 1155.

[20] M. H. Möller, W. Jeitschko, Ternary Rare Earth Copper and Silver Pnictides with $TnCr_2Si_2$ - Related Structures, *VIII Int. Conf. On Solid State Compounds of Transition Elements*, 1985, Vienna, Austria, *Extended Abstracts*, **1985**, P4 A14.

[21] S. Rundqvist, N. O. Ersson, *Ark. Kemi* **1968**, *30*, 103.

[22] A. Brown, S. Rundqvist, *Acta Cryst.* **1965**, *19*, 684.

[23] E. Hassler, T. Johnsson, S. Rundqvist, *Acta Chem. Scand.* **1974**, *28*, 123.

CHAPTER 7. ELECTRONICALLY DRIVEN DISTORTIONS OF PHOSPHORUS NETS IN $ErCuP_2$ AND $SmCu_{1.15}P_2$. ROLE OF RARE-EARTH AND ADDITIONAL COPPER ATOMS

A paper to be submitted

Yurij Mozharivskyj and Hugo F. Franzen

Department of Chemistry and Ames Laboratory of US DOE, Spedding Hall, Iowa State University, Ames, Iowa 50011, USA

Abstract

The distortions of the square P nets in monoclinic $ErCuP_2$ and orthorhombic $SmCu_{1.15}P_2$, whose structures can be derived from that of $HfCuSi_2$, are consequences of the Peierls instability of the nets. Formation of phosphorus zigzag chains in $ErCuP_2$ and rectangular units in $SmCu_{1.15}P_2$ are two different ways to minimize the energy through opening band gaps. Since Er *d* orbitals form bands in the energy gaps of the P zigzag chains and there is non-zero density of states at the Fermi level for $ErCuP_2$, the phosphide is a metal, as confirmed by the conductivity measurement. Presence of the additional copper atoms that fill voids around the P layer in $SmCu_{1.15}P_2$ is anticipated from the structural analysis and is due to the matrix effect of the large Sm atoms. These additional copper atoms prevent formation of short P-P distances along one direction in the P net and therefore also a gap opening along the corresponding direction in reciprocal space. From the electronic considerations the presence of the additional Cu atoms is unfavorable and a site deficiency is expected.

Keywords: erbium copper diphosphide; samarium copper diphosphide; electronic structure; Peierls instability of the phosphorus square net.

Introduction

While one-dimensional (1D) solids with partially filled bands have an innate tendency (known as a Peierls instability or as a charge density wave) to lower their electronic energy through a gap opening at the Fermi level [1-3], phases with 2D nets undergo similar energy-lowering distortions only in some cases. There are many prerequisites for a compound with a square net to exhibit this instability and a subsequent gap opening, but the two most important are the presence of degenerate states, such as crossing bands, at the Fermi level and separation of these bands from other bands.

Obviously these two conditions require a specific electron count and put restrictions on the elemental compositions of the compounds and their structural motifs. There exist a number of compounds that meet all these criteria and show interesting structural and electronic transitions, e.g., GdPS [4], CeAsS [5,6], $EuSb_2$ [7], $SrZnSb_2$ [8], $CaSb_2$ [9] and $CaAl_4$ [10]. In all cases square nets are formed from the main group elements, and these nets provide a band separation and therefore an energetic gain upon distortion. A small change in the electron count or the energy of the orbitals may fully suppress a distortion, e. g., the high-symmetry structure of $YbSb_2$ [11,12] is attributed to the presence of some Yb atoms (~2%) in the trivalent state [13,14] and substitution of Sb by less electronegative Bi gives tetragonal $SrZnBi_2$ [15] with square Bi layers.

In recent studies [16-18] we have observed the rare-earth copper phosphides to undergo distortions, with the largest changes occuring in the P nets. In $GdCuP_{2.20}$ [16] P dimers are formed in the phosphorus layer, in $ErCuP_2$ [17] zigzag chains of phosphorus similar to those in $SrZnSb_2$ [8] appear and in $SmCu_{1.15}P_2$ [18] the phosphorus net is broken into 4-member units. The electronic structure of $GdCuP_{2.20}$ was analyzed and the distortion was traced back to the crossing of bands consisting mainly of phosphorus p_x and p_y orbitals. Formation of the P-P single bonds (P dimers) along one direction in $GdCuP_{2.20}$ leads to a band gap opening along the corresponding direction in reciprocal space and consequently to energy lowering. Presence of an additional but deficient phosphorus site on one side of the P net prohibits formation of single bonds along the second direction and thus prevents formation of zigzag or *cis-trans* chains [16].

The structure of $SmCu_{1.15}P_2$ [18] contains rectangular units in the P net. This type of distortion was originally proposed by Hulliger, Schmelczer and Schwarzenbach [4] as one of the three ways for deforming a square layer of a main group element that exhibits the Peierls instability. A cerium copper phosphide with a structure similar to that of $SmCu_{1.15}P_2$ was reported by Möller and Jeitschko [19], but the electronic structure was not analyzed and no explanation for the formation of the four-atom units was given. In this paper we discuss the electronic factors that lead to the deformation of the P nets in $SmCu_{1.15}P_2$ and $ErCuP_2$ and compare the conclusions with the measured conductivity for $ErCuP_2$.

Crystal Structures of $ErCuP_2$ and $SmCu_{1.15}P_2$

Structures of $ErCuP_2$ and $SmCu_{1.15}P_2$ (Figure 1) are distorted variants of $SrZnSb_2$ and $SrZnBi_2$ which, in turn, can be derived from $HfCuSi_2$ [20]. Before we proceed to a detailed analysis of the structures, we would like to point out that besides the P layers and the additional Cu atoms the two

structures differ in the stacking of $HfCuSi_2$ fragments. In $ErCuP_2$ the two $HfCuSi_2$-type units are directly stacked over each other, while in $SmCu_{1.15}P_2$ one $HfCuSi_2$-type unit is shifted by ½ *a*.

Our choice of description of $ErCuP_2$ and $SmCu_{1.15}P_2$ evokes breaking the structures into layers and analyzing their electronic structure. Under this approach the two structures are made from the phosphorus, rare-earth and copper-phosphorus layers. The copper-phosphorus block consists of Cu atoms tetrahedrally coordinated by P atoms. This block is followed by a rare-earth layer and then by a phosphorus net with twice the atomic density. $SmCu_{1.15}P_2$ contains additional Cu nets above and below the P net. Since these nets are four times less dense than the P nets and their occupancy is less than 30%, it is reasonable to view them as additional Cu sites without short Cu-Cu bonds of 1.91 Å across the net.

The rare-earth and copper-phosphorus layers are slightly distorted. The phosphorus nets in both compounds undergo much more severe distortions: with zigzag chains formed in $ErCuP_2$ and rectangular units formed in $SmCu_{1.15}P_2$ (Fig. 2). The intrachain P-P distances of 2.41 and 2.46 Å in $ErCuP_2$ and the shorter intraunit distance of 2.266 Å in $SmCu_{1.15}P_2$ are comparable to single bond distances in CeP_2 [21] and LaP_2 [22], where the phosphorus atoms are joined into fragments of zigzag chains of 4 or 3 and 5 atoms with $\delta_{P\text{-}P}$ = 2.404-2.453 Å and $\delta_{P\text{-}P}$ = 2.197-2.314 Å, respectively. The longer intraunit bond of 2.584 Å in $SmCu_{1.15}P_2$ cannot be viewed as single and is obviously of an intermediate order. As discussed below, this longer bond results when additional Cu2 atoms are present. Interestingly, the separation between the zigzag chains and rectangular units is similar. This structural analysis clearly suggests that the formation of phosphorus single bonds from electrons delocalized in the square nets leads to the deformation of these nets in $ErCuP_2$ and $SmCu_{1.15}P_2$. To understand energy gains upon these symmetry lowerings we will analyze the electronic structures of the two phases.

Distortion paths of a square net of a main group element were considered by Hulliger, Schmelczer and Schwarzenbach [4]. They proposed three possible distortion types (Fig. 3). The zigzag chains of $ErCuP_2$ and the four-atom units of $SmCu_{1.15}P_2$ are two of these three types. The third possibility, formation of the *cis-trans* chains, is experimentally found in GdPS [4].

Electronic Structure of $ErCuP_2$

Electronic Structure of Phosphorus Square Net

As mentioned above, the formation of the zigzag chains in $ErCuP_2$ is the result of a Peierls instability of the square P net. We start our analysis with an electron count. The P1 atoms have no close anion neighbors (see Fig. 1) and are assumed to be P^{3-}. The Cu atoms are primarily bound to P1,

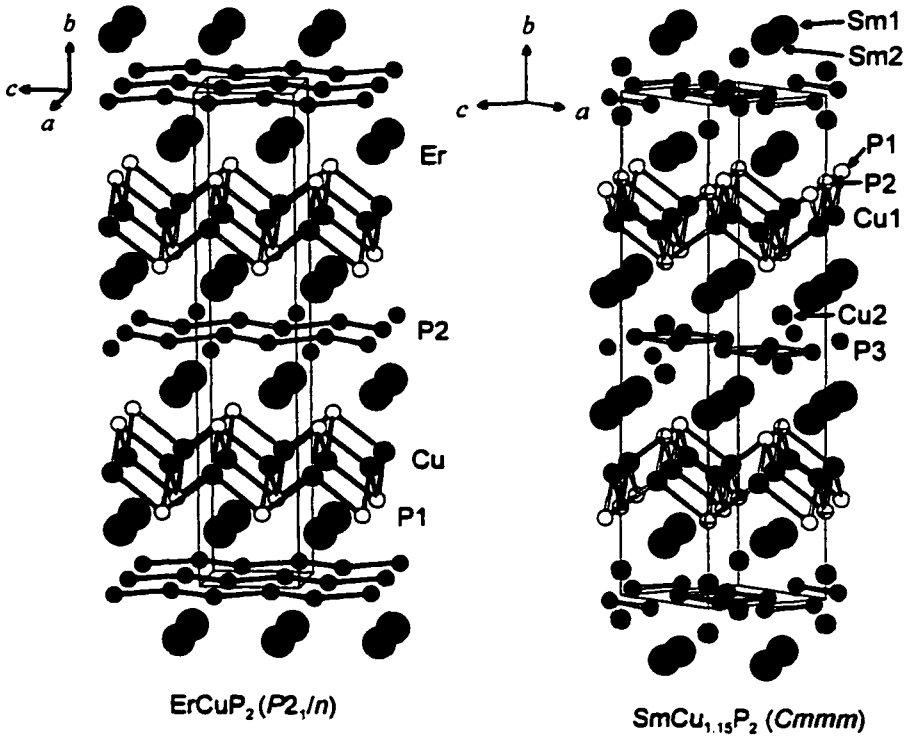

Figure 1. Structure of $ErCuP_2$ and $SmCu_{1.15}P_2$. Occupancy of Cu2 is ~29%.

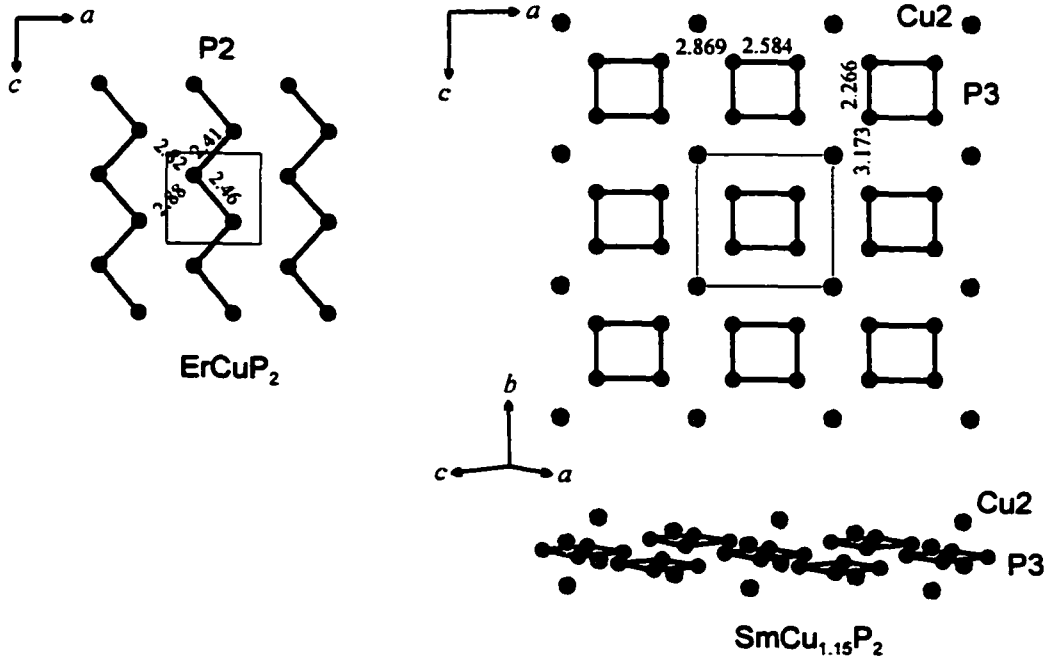

Figure 2. Zigzag chains and rectangular units in the phosphorus nets of $ErCuP_2$ and $SmCu_{1.15}P_2$.

they are donors of one electron (d^{10} configuration) and can be counted as Cu^{+}. The d^{10} configuration is supported by a band structure calculation that shows the *d* states to be below the Fermi level. The Er atoms have P atoms as the closest neighbors, there are no short Er-Er distances, and therefore they can be viewed as Er^{3+}. Although no magnetic measurements have been performed for the erbium copper phosphide, the magnetic data for similar phases with gadolinium and holmium yield magnetic moments expected for free Gd^{3+} and Ho^{3+} and allow us to consider the Gd, Ho and Er atoms to have 3+ charge. Also, the magnetic data show that the *f* orbitals are localized and their role in the bonding is small. Based on the above oxidation state assignments the electronic structure can be described as $(Er^{3+})(Cu^{+})(P(1)^{3-})(P(2)^{-})$.

The P1 bands are not very disperse since the P1-P1 separation is large. On the other hand, the P2-P2 distances are small (Fig. 2), the P2 bands are dispersed and the Fermi level resides at these bands. To trace the origin of the formation of the P zigzag chains we can limit the analysis of the band structure to the P net. We start with a hypothetical tetragonal structure of $ErCuP_2$ (*P4/nmm* space group as for tetragonal $ErCuAs_2$) and consider a square net of phosphorus. There are two P atoms per net in each unit cell (solid lines in Fig. 4**a**). If the origin is shifted, a centered 2D unit cell becomes obvious (shaded area in Fig. 4**a**). The band structure of the centered lattice can be generated from that of the primitive lattice (shaded area in Fig. 4**b**) by a folding procedure. The corresponding Brillouin zones (BZs) are shown in Fig. 5**a** and **c**, and the band structure of the square lattice with the primitive unit cell shown in Fig. 5**a** is plotted along Γ-X'-M'-Γ. The first BZ of the primitive lattice (the shaded area in Fig. 5**a**) corresponds to the second BZ of the centered lattice. The first BZ of the centered lattice (the shaded area in Fig. 5**c**) can be generated by folding back the areas of the BZ of the centered lattice that are not in the first BZ of the centered lattice. The procedure is schematically shown in Fig. 5**b** as the folding of the X' Y' M' area onto the X' Y' Γ area. Mapping X'-M' on Γ-X' and folding Γ-M' back generate the band structure along M-Γ and Γ-X for the conventional cell. The band structure along X-M is obtained by connecting corresponding levels at X and M. The bands stick together along X-M due to the nonsymmorphic symmetry element (an *n* glide plane).

We would like to address the *s*-*p* mixing of the bands. The character of the bands at the symmetry points Γ, X' and M' is indicated in Fig. 5**a**. Because of the same symmetry (the same irreducible representations) the p_x, p_y and *s* crystal orbitals mix along Γ-X'-M'-Γ and thus the *p* bands have contributions from the *s* orbitals and vice versa. The dashed lines indicate the shape the bands would have without mixing.

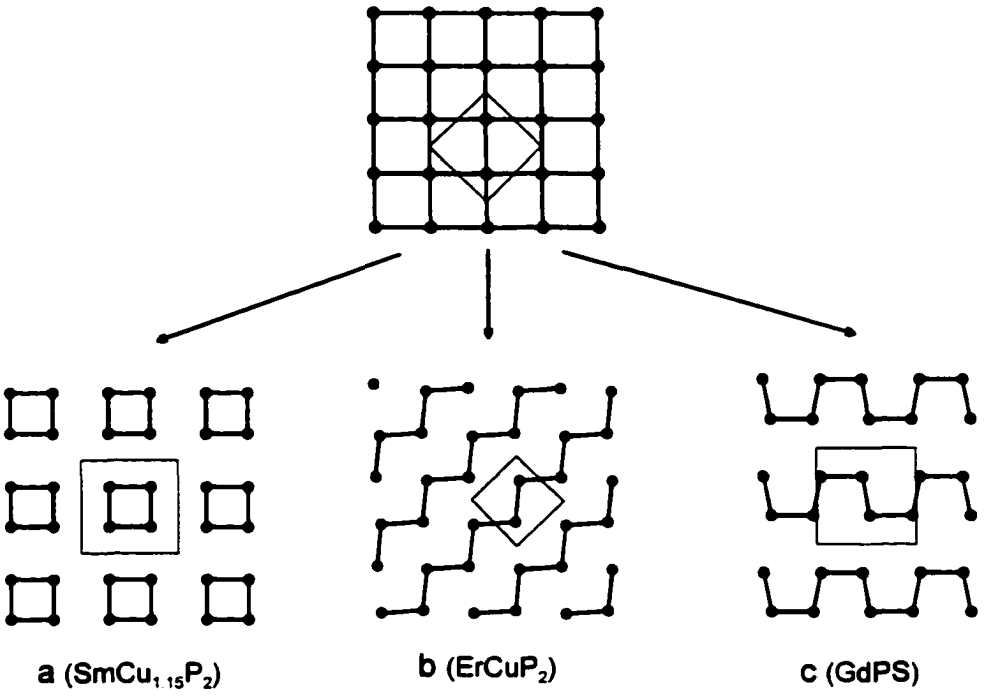

Figure 3. Three ways to distort the square phosphorus net (above): (a) discrete squares (rectangles are found in $SmCu_{1.15}P_2$); (b) zigzag chains as in $ErCuP_2$; (c) *cis-trans* chains as in GdPS.

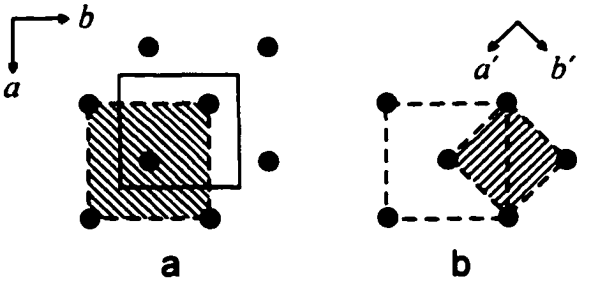

Figure 4. (**a**) Different choices of the conventional cell for tetragonal $ErCuP_2$. (**b**) Primitive cell (shaded area).

From Phosphorus Square Net to Monoclinic $ErCuP_2$. Resistance of $ErCuP_2$

We will focus neither on the details of the whole band structures of $ErCuP_2$ and $SmCu_{1.15}P_2$ nor on how to generate them. However we will have a close look at the band structure of the P nets in order to trace the origin of the distortions and to understand the role of the Er-P interactions and the additional Cu atoms. Step-by-step constructions of the band structures of the structurally related phases GdPS (ZrSiS type), $CaBe_2Ge_2$ and $BaMn_2P_2$ ($ThCr_2Si_2$ type) are presented elsewhere [3,14,23,24].

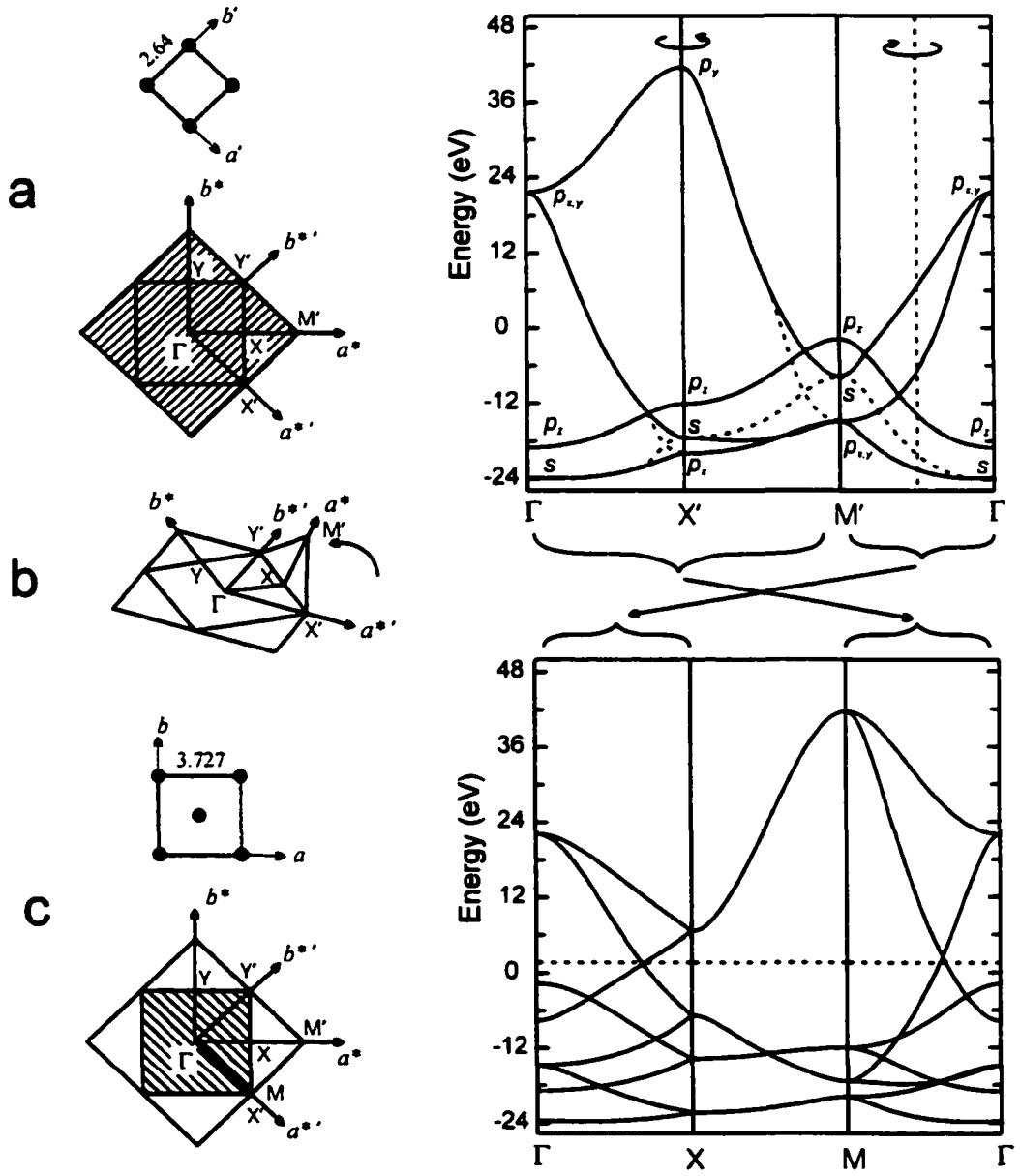

Figure 5. (**a**) Primitive phosphorus cell, the corresponding first BZ (shaded area) and band structure. (**b**) Folding back procedure. (**c**) Conventional phosphorus cell, the corresponding first BZ (shaded area) and band structure. Dashed lines in (**a**) show the shape of the bands without mixing

If we calculate the band structure of tetragonal $ErCuP_2$ (not presented here), we will see bands around the Fermi level to have a behavior similar to that of the P layer in Fig. 5c, and the Fermi level will reside at the crossing. The presence of a crossing at the Fermi level is an indication of a Peierls instability of the square P net. The distortion process from the tetragonal to monoclinic phosphorus

layers in $ErCuP_2$ and a gap opening can be broken into several steps (Fig. 6). We start with the square net. Due to the four-fold symmetry of the net the p_x and p_y bands are degenerate at Γ (Fig. 6**a**). Reduction of the symmetry from tetragonal to orthorhombic ($P4/nmm \rightarrow Pmmn$, $a < b$) lifts the $p_{x,y}$ degeneracy, but the mirror planes and the crossings remain (Fig. 6**b**). When only the vertical mirror plane containing the b axis is removed, zigzag chains with equal intrachain distances are formed, the band crossings disappear and gaps open up along Γ-Y and M-Γ (Fig. 6**c**). As a consequence the electronic energy is lowered. The driving force for the distortion can be revealed by examining the symmetry of the orbitals. The vertical symmetry plane divided the $p_{x,y}$ crystal orbitals into those symmetric and those antisymmetric with respect to the symmetry, these orbitals belonged to two different irreducible representations and crossed along Γ-Y and M-Γ. When the symmetry is broken, the vertical mirror plane is lost, these crystal orbitals belong to one irreducible representation and mix.

Further reduction of the symmetry (loss of the horizontal mirror planes) generates the P net of monoclinic $ErCuP_2$. In this structure the atoms in the chains move up and down relative to the plane, creating long and short distances within the chains (see Fig. 2). This distortion process, which is similar to that for the polyacetylene, removes the crossing and opens a band gap along Γ-X (Fig. 6**d**). The overall distortion lowers the electronic energy of the phosphorus net by pushing the bonding states down and antibonding ones up and gives an energy gain of 1.53eV per two phosphorus layers in a unit cell.

We expect to see a similar behavior of the phosphorus bands in the band structure of $ErCuP_2$ (Fig. 7). Indeed, the bands below the Fermi level have features characteristic of the zigzag P chains and they lie in the same energy range. However, there are many bands above the Fermi level in the energy region which was empty for the P net. Some of these bands cross the Fermi level. Considering orbital energies of the elements (see Table 3), one can conclude that Er d orbitals form the bands just above the Fermi level. There is contribution from other orbitals, but the largest contribution comes from the Er d orbitals. To understand the role of Er atoms we will consider bands 1-8 along Γ-Z just below and above the Fermi level. First we examine p_x crystal orbitals (CO) of the P zigzag chain at the Z symmetry point (COs I and II in Fig. 6**d**). There are two phosphorus atoms per unit cell in one net, therefore there are two p_x COs (Fig. 8) that give two bands. There are short and long intrachain distances and since the shorter bonds are stronger than the longer ones, energies of these p_x COs are different:-7.8 eV for CO I and -7.0 eV for CO II. There are two P nets in the unit cell of $ErCuP_2$, therefore the COs I and II are doubly degenerate. The next two COs III and IV are made from the hybrid sp_z orbitals, they are high in energy and are not of interest.

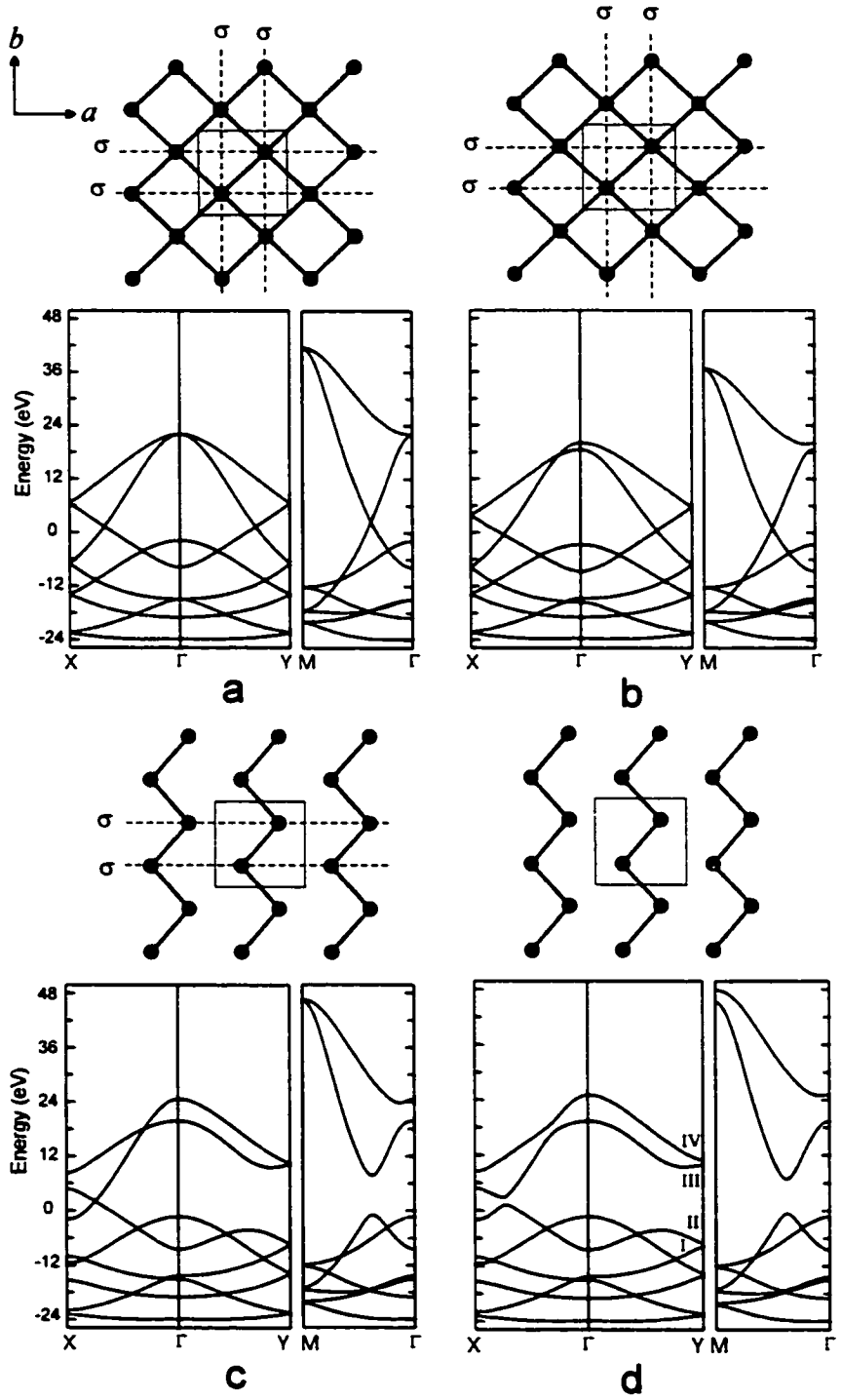

Figure 6. Evolution of the band structure of the planar phosphorus net when the $ErCuP_2$ distortion is carried out in four steps. The essential symmetry elements (mirror planes) are indicated by dashed lines. (**a**) Band structure of an ideal square lattice with full tetragonal symmetry (*P4/nmm*). (**b**) After the tetragonal symmetry is reduced to orthorhombic (*P4/nmm*→*Pmmn*, $a < b$). The mirror planes and the band crossings are still present. (**c**) The vertical mirror planes are removed. Zigzag chains with equal intrachain distances are formed and gaps occur along Γ-*Y* and Γ-*M*. (**d**) After the horizontal mirror planes are gone and the distortion is complete.

At the Z symmetry point the erbium d_{xy} orbital has the correct symmetry to interact with the phosphorus p_x COs. Although the erbium p_x also orbital has the right topology, its interaction with the phosphorus p_x COs is small due to its high energy. The resulting bonding COs (Fig. 9**a**' and **a**") have the largest contribution from the phosphorus p_x orbitals and they are pushed down in energy (-9.3 and -8.9 eV versus -7.8 and -7.0 eV), the antibonding COs have the largest contribution from the erbium d_{xy} orbitals and they are pushed up (out of the energy region shown). These bonding COs I and II form four bands 1-4 that are doubly degenerate at the Z symmetry point, but are split otherwise. Splitting between the two pairs of bands 1,2 and 3,4 at Z results from the splitting of the original phosphorus p_x COs. The behavior of the bands 1-4 along Z-Γ is similar to that of the bands I and II of the phosphorus zigzag chain (I and II in Fig. 6**d**).

Bands 5-8 come mainly from the Er $d_{x^2-y^2}$ orbitals that do not have the proper symmetry at Z to interact with the phosphorus p_x COs I and II (Fig. 9**b**' and **b**"). Splitting of the bands is similar to that for bands 1-4 and results from the interaction with Cu p_y orbitals. On going from Z to Γ the bands 5-8 are pushed up since at Γ the Er $d_{x^2-y^2}$ orbitals interact in an antibonding manner with P1 p_y orbitals. This interaction picture is simplified (there is always mixing of other orbitals), but it helps to understand the nature of the bands around the Fermi level. Similar energy changes and interactions occur for the phosphorus p_z COs and erbium orbitals at the X symmetry point. The discussed effect of the Er atoms on the P layer can be followed through the DOS of Fig. 10. Significant Er density of states below the Fermi level indicates the analyzed Er-P interactions. Above the Fermi level the Er contribution becomes larger and it comes mainly from the d orbitals. Calculation of the total electronic energy indicates that the monoclinic phosphide is more stable by 0.72eV per unit cell than a hypothetical tetragonal one. So, the energy gain of 1.53eV associated with the formation of the zigzag chains in the phosphorus net is transferred, although not entirely, into the structure of $ErCuP_2$.

From the band structure of the zigzag chains (Fig. 6**d**) the phosphorus layer by itself would be expected to be a 2D semiconductor. On the other hand the band structure and DOS of the whole $ErCuP_2$ structure indicate metallic properties for the phosphide. To verify the prediction of the band structure analysis the electrical resistance was measured in the 1.9-300 K range. The data show $ErCuP_2$ to be a metal. The overall character of the curve and the low temperature behavior of the resistance (the insert in Fig. 11) are similar to those for $GdCuP_2$, $GdCuAs_2$ [16], $HoCuP_2$ and $HoCuAs_2$ [17], which are good metals and undergo antiferromagnetic orderings at low temperatures. The peak on the resistance curve of $ErCuP_2$ is attributed to an increased spin-flip scattering in the critical temperature range.

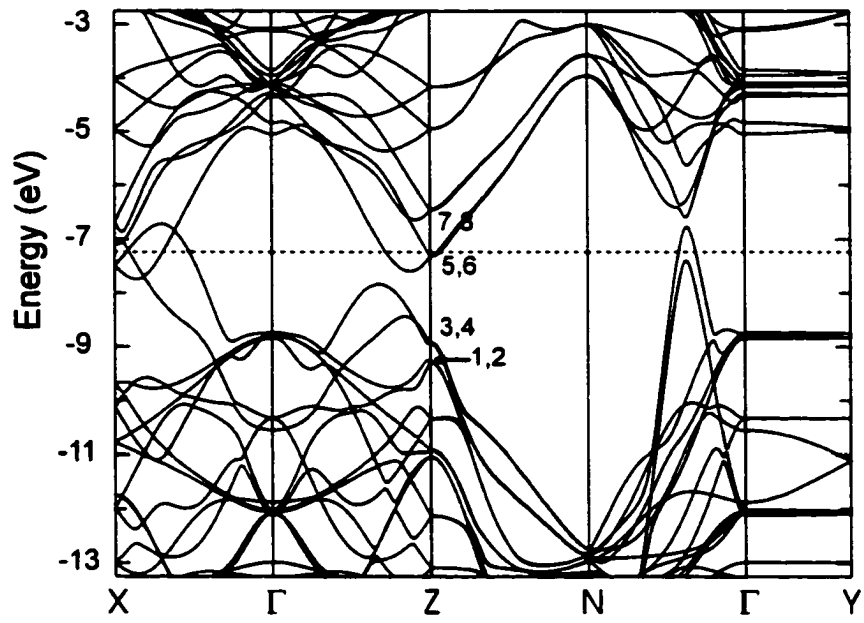

Figure 7. Band structure of $ErCuP_2$. The numbers indicate the bands considered in the text.

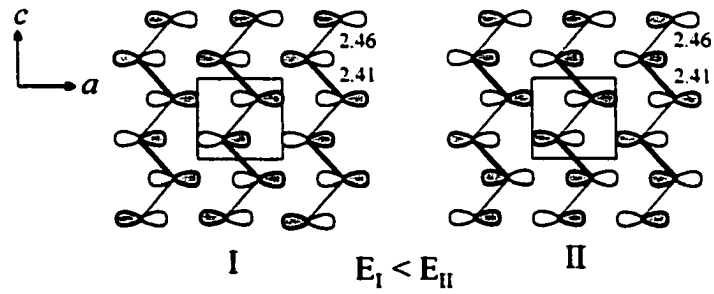

Figure 8. p_x crystal orbitals (COs) of the P zigzag chains at the Z symmetry point. Thick and thin lines represent short and long intrachain bonds.

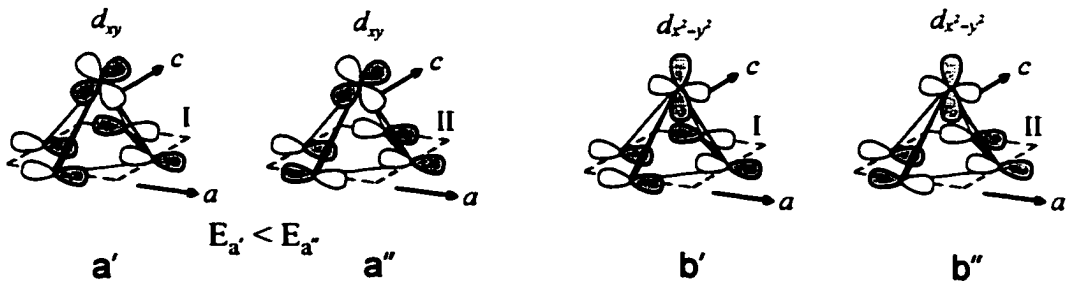

Figure 9. Interaction between the p_x COs of the P zigzag chains and the Er orbitals at the Z point.

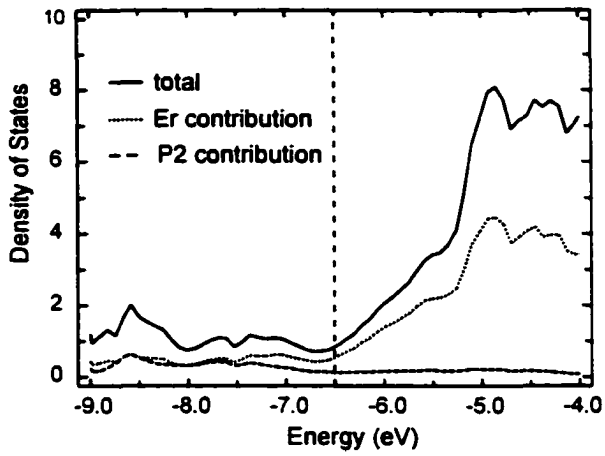

Figure 10. Total and projected DOS for $ErCuP_2$.

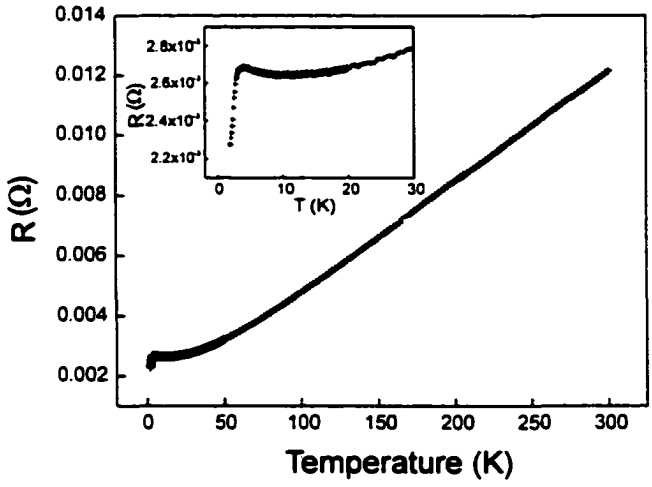

Figure 11. Resistance versus temperature for the $ErCuP_2$ powder.

Electronic Structure of $SmCu_{1.15}P_2$

Electronic Structure and Distortion of Phosphorus Square Net

As in the case with $ErCuP_2$, we start with the analysis of the phosphorus net in $SmCu_{1.15}P_2$ and assume it to be square. Neglecting the additional and deficient Cu2 site, an electron count $((Sm^{3+})(Cu(1)^{+})(P(1\text{-}2)^{3-})(P(3)^{-}))$ yields a negative charge for the P3 atoms in the square net. There are four atoms in the conventional unit cell (Fig. 12**a**). The band structure could be generated from that of the primitive lattice (shaded area in Fig. 12**b**) by a folding procedure but the construction would be less transparent than that for $ErCuP_2$. The reason is that the first BZ of the primitive cell (open and shaded area in Fig. 13) corresponds to the fourth BZ of the conventional cell (open area), and the

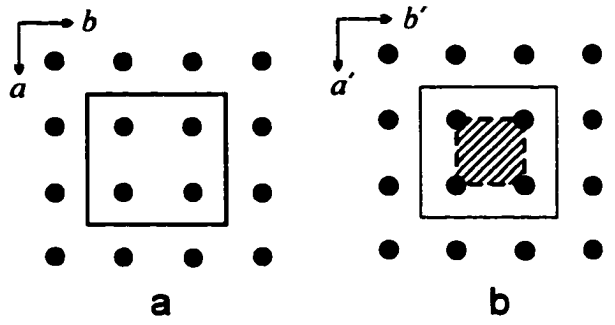

Figure 12. Conventional (**a**) and primitive (**b**) cells for tetragonal $SmCu_{1.15}P_2$. The P atoms are at $x = y = ¼$.

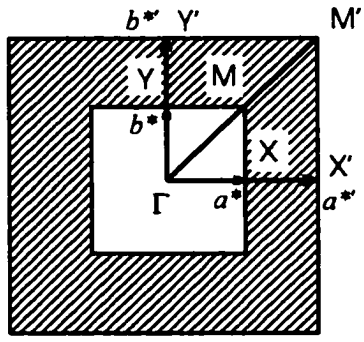

Figure 13. The first BZs of the conventional (open area) and primitive (shaded and open area) cells.

band construction would require a double folding, e.g., the Γ-X line is obtained by mapping of Y'-M' onto Γ- X' and then by folding Y'-M' and Γ- X'.

We can generate a schematic band structure by considering only the p_x and p_y orbitals in the P^- square net. This is a reasonable approach if the s-p mixing is neglected. Since the energy of the P s orbital is low, and the p_z orbitals do not overlap significantly, the s and p_z bands would lie below the Fermi level and would be fully occupied. Under these circumstances the p_x and p_y orbitals will give highly dispersed, half-occupied bands. There are four P3 atoms in the unit cell and therefore four types of crystal orbitals can be formed from the half-filled p_x and p_y atomic orbitals. Figure 14 shows the p_y crystal orbitals at the Γ point for one unit cell. The evolution of the bands along Γ-Y is schematically presented in Fig. 15**a**. The $p_y\sigma\pi^*$ and $p_y\sigma^*\pi$ bands cross and the same will be observed for $p_x\sigma\pi^*$ and $p_x\sigma^*\pi$ bands along Γ-X. The Fermi level resides at the crossing, and therefore the phosphorus square net is ready for distortion.

Reduction of the symmetry from tetragonal to orthorhombic, as in $SmCu_{1.15}P_2$, while keeping the P3 atoms at x = y = ¼, breaks the degeneracy of the p_x and p_y bands, but the crossing remains (Fig. 15**b**). The shifts along the b direction, leading to distances of around 2.27 Å, pulls down the bonding $p_y\sigma\pi$ and $p_y\sigma\pi^*$ states and push up the antibonding $p_y\sigma^*\pi$ and $p_y\sigma^*\pi^*$ ones, leading to an energy gain and a gap opening along Γ-Y (Fig. 15**c**). The shifts along the a direction, producing P-P bonds of around 2.58 Å, lowers the energy of the bonding p_x bands, but the interactions are too weak to open a band gap along Γ-X. If we consider the b axis to be the c axis, we get a schematic band structure of the P3 net in $SmCu_{1.15}P_2$. In constructing the band structure of the distorted P net, we neglected not only the s-p mixing but also the p_x–p_y interactions (p_x–p_z for the *Cmmm* cell), which occurs because of the loss of the mirror planes through the P atoms. Although the two effects

complicate the calculated band structure (Fig. 16), the general features of the simplified variant are easily recognizable. As expected there is a band gap along *Γ-Z* and a crossing along *Γ-X*.

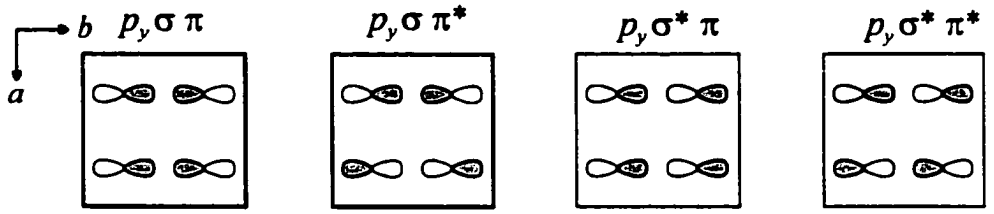

Figure 14. Phosphorus p_y COs for the conventional cell at Γ.

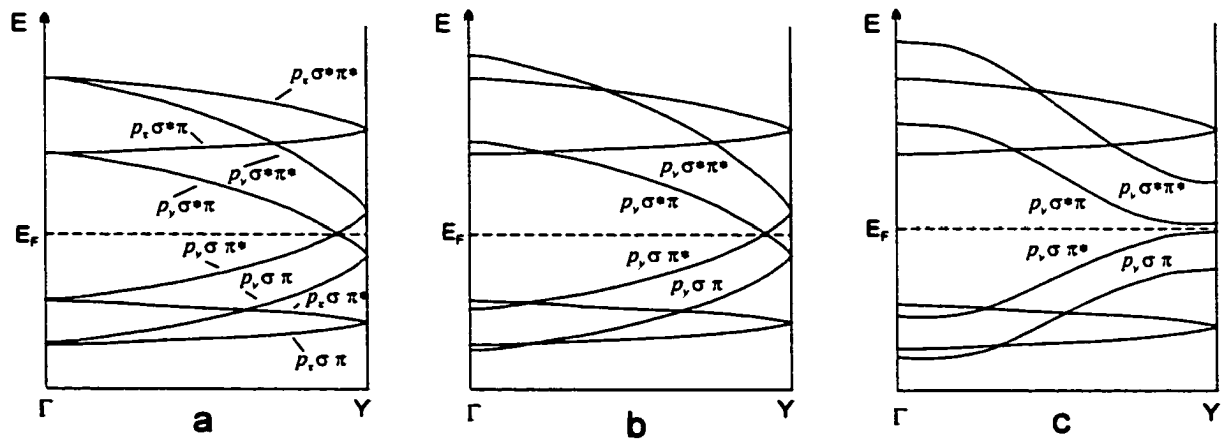

Figure 15. Schematic band structure of the P3$^-$ layer of $SmCu_{1.15}P_2$. Only p_x and p_y bands are shown along Γ-*Y*. (**a**) The P3$^-$ net is square. (**b**) After an orthorhombic distortion ($b < a$). (**c**) Short and long P-P distances are formed along *b*.

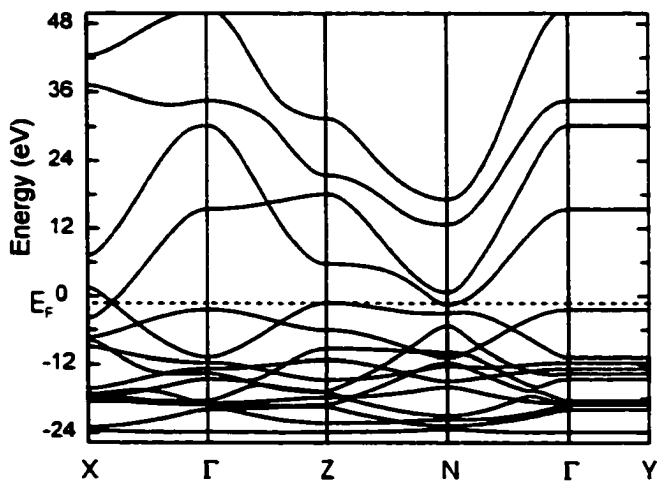

Figure 16. Calculated band structure of the P3$^-$ layer of orthorhombic $SmCu_{1.15}P_2$.

Role of Additional Cu Atoms in the $SmCu_{1.15}P_2$ Structure

One question that remains unanswered is why, despite a substantial energy gain from a gap opening the phosphorus net, is the crossing along Γ-X preserved? If we had a 1D phosphorus chain with atomic separations similar to those along a, the same problem could be presented as a liner chain of the P atoms versus a broken chain consisting of dimers P_2^{4-} (Fig. 17). Obviously, the dimers are formed if there is one more electron per phosphorus atoms, otherwise the linear chain is obtained. As for the phosphorus net we can expect an electron deficiency to result in delocalized bonding along Γ-X. In the case of $SmCu_{1.15}P_2$ the additional Cu2 atoms serve as a sink for electrons from the highly dispersed p_x bands. There are no short Cu-Cu bonds (remember 29% occupancy of the Cu2 site), therefore we can imagine interaction of the localized Cu states with the delocalized p_x and p_z COs (Fig. 18). The copper d and s orbitals are below the Fermi level that resides at the crossing, in the middle of the p_x band. The d states are filled (d^{10} configuration of the Cu atoms), but the s states are half occupied and can accommodate electrons from the higher occupied phosphorus states, mostly from the p_x band. The calculated band structure for the $(CuP_4)^{4-}$ layer supports the argument (Fig. 19). As expected, there are nine additional bands: five narrow bands around −14eV, a single, also localized band just below the Fermi level and three bands above the Fermi level, with the highest one being very dispersed and mainly of copper p_z character. The fact that these bands arise primarily from to the Cu2 atoms can be seen from the decomposition of the DOS (Fig. 20): the energies of the largest Cu contribution match the positions of the localized bands of $(CuP_4)^{4-}$.

The above analysis of the $(CuP_4)^{4-}$ layer indicates the following: (1) the additional copper atoms take electrons away from the region around the crossing and, thus, remove the Peierls instability and the energy gain associated with a gap opening along Γ-X. (2) The gap and energy gain along Γ-Z are mostly unaffected by the Cu2 atoms, (3) the $(CuP_4)^{4-}$ layer and the whole $SmCu_{1.15}P_2$ structure should be good metallic conductor. An interesting question is, what if two band gaps, along Γ-X and Γ-Z, were formed anyway? In this scenario electrons would flow from the top of the two valence phosphorus p_x and p_z bands into the copper s states. The energy gain, derived from the gaps, would almost disappear, so the structure chooses to make only one gap and to keep the energy of this gap by filling the Cu states from the other band. This occurs only when the number of copper states is small, which means that the Cu2 site must be highly deficient (this is the case in $SmCu_{1.15}P_2$). With a fully occupied Cu2 position the $SmCu_2P_2$ structure would be unstable not only due to the great repulsion between the closely spaced Cu2 atoms (δ = 1.91 Å across the P net) but also due to the lost P-P bonding. Stability of the AB_2X_2 compounds (B = a transition metal or a main group element, X = a 14 or 15group element) with the respect to the two structure types $ThCr_2Si_2$ [25] and $CaBe_2Ge_2$ [26] has

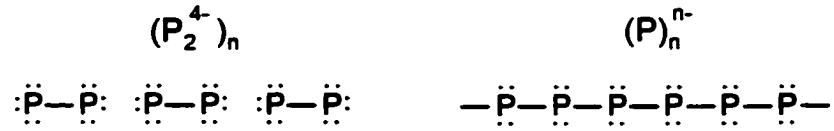

Figure. 17. A broken chain consisting of the P_2^{4-} dimers and a linear chain of the P^- anions.

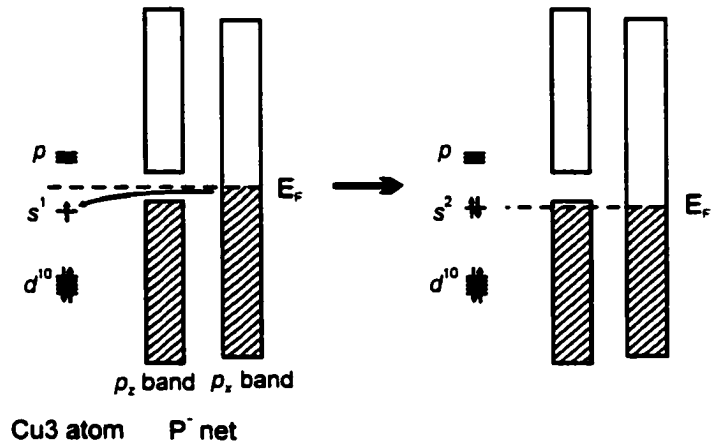

Figure 18. Electron transfer from the P bands to the half occupied Cu *s* states.

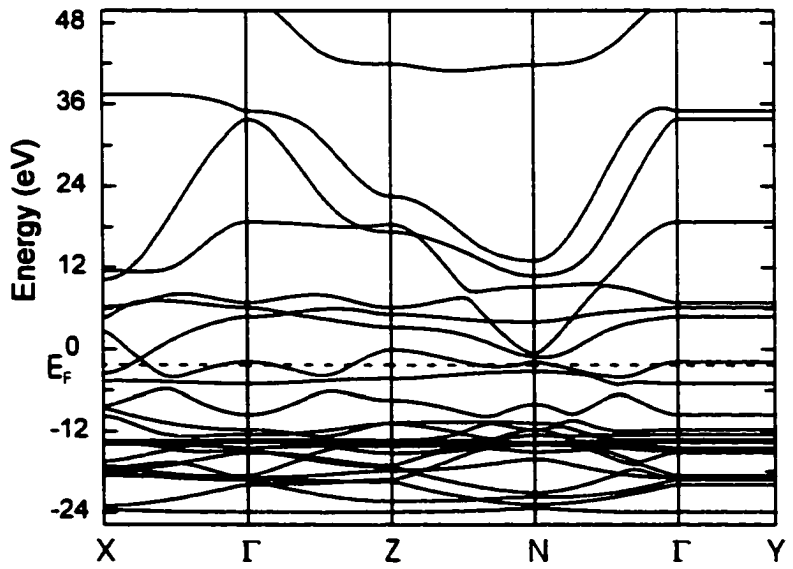

Figure 19. Calculated band structure of the $(Cu(2)P(3)_4)^{4-}$ layer of orthorhombic $SmCu_{1.15}P_2$.

been analyzed previously [3,23,24]. The relevant conclusion is that compounds with *B* and *X* much different in the electronegativity adopt the $ThCr_2Si_2$ structure (Fig. 21). For hypothetical $SmCu_2P_2$ it means that the Cu2 and P3 atoms must be exchanged to yield a stable structure, and for the real

$SmCu_{1.15}P_2$ structure it means that a larger occupancy for Cu2 is unlikely. The latter argument is supported by the experiments soon to be reported [18].

We omit consideration of the complete band structure of $SmCu_{1.15}P_2$ since it does not contribute to further understanding the distortion process. We only mention that there are Sm-P3 interactions that are similar to the Er-P2 ones in $ErCuP_2$. However the Sm *d* orbitals and thus the *d* bands are higher in energy than those of Er.

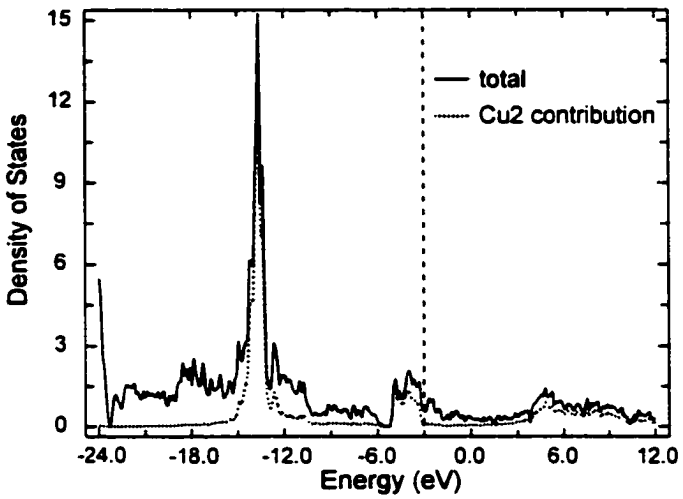

Figure 20. Total and projected DOS for the $(Cu(2)P(3)_4)^{+}$ layer.

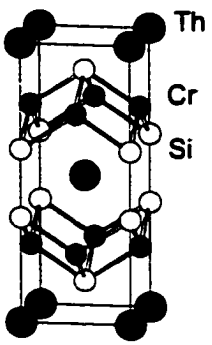

Figure 21. Structure of $ThCr_2Si_2$.

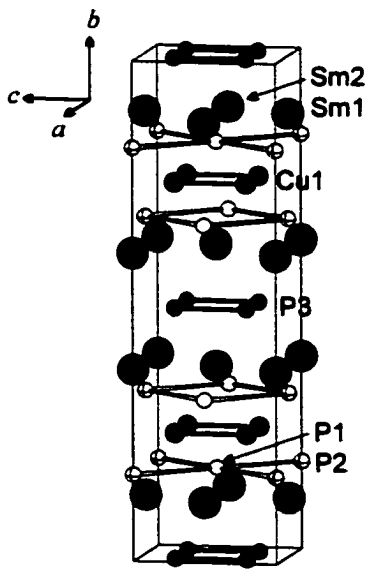

$SmCuP_2$ (tetragonal)

Figure 22. Hypothetical tetragonal $SmCuP_2$.

$SmCu_{1.15}P_2$ Structure versus $ErCuP_2$ Structure

Despite some differences in the symmetries, unit cell dimensions and distortion types of the P nets in $ErCuP_2$ and $SmCu_{1.15}P_2$ the most important difference is the presence of the Cu2 atoms around the P net in $SmCu_{1.15}P_2$ (see Fig. 2). Both the zigzag chain and the four-atom unit are ways to minimize the energy of the phosphorus layers and they are expected from Peierls instabilities. The Cu2 atoms seem to be additional and their existence cannot be predicted from electronic considerations, besides they are not found in $ErCuP_2$ or $HoCuP_2$. To understand this phenomenon we have to go beyond the analysis of the phosphorus net.

We start with a hypothetical tetragonal $SmCuP_2$ structure, whose lattice parameters ($a = b =$ 5.445, c = 19.511 Å) are derived from those of $SmCu_{1.15}P_2$. We use a different structural approach than before (Fig. 22). The CuP block can be broken into a central square Cu net and into two less dense square P1 nets. The Cu net is structurally the same as the P3 net, and the Cu-Cu distances of 2.72 Å are equal to the P3-P3 ones. When the element radii (r_{Cu} = 1.278 Å and r_P = 1.105 Å for the white modification) are compared, it becomes clear that the Cu atoms are close to each other while the P3 atoms are well separated and, besides, the Cu environment is much tighter due to the presence of the P1-2 atoms. This idea is better conveyed through the sphere packing shown in Fig. 23, with the sphere dimensions being equal to the element radii. Both Cu and P3 layers are surrounded by Sm layers on both sides, but there are additional P1, P2 atoms in the tetragonal antiprismatic holes made by the Sm and Cu atoms on each side on the Cu layers. These phosphorus atoms form tetrahedra around Cu. The same tetragonal antiprismatic voids are empty around the P3 layers. Obviously these voids can be occupied by Cu atoms and that is exactly what happens in $SmCu_{1.15}P_2$. However as we discussed it in the previous section, a full Cu2 occupancy is unlikely. The voids can also be occupied by additional P atoms, e. g., $GdCuP_{2.20}$, but as was shown in [16], a P deficiency of around 20% is to be expected and is experimentally observed. In each case the additional atoms provide extra bonding, mainly, with the surrounding atoms, but their effect on the P nets is destabilizing.

So far we have focused only on the atomic dimensions of Cu and P and neglected the size of the rare-earth element. The matrix effect of the rare earths in these types of compounds is important and both the geometric and electronic aspects of this effect must be considered. The size of the voids and thus possibility of their occupancy is directly related to rare-earth radii. In $SmCu_{1.15}P_2$ and $GdCuP_{2.20}$ the rare-earth metals and thus the voids are large enough to accommodate smaller Cu or P atoms, in $HoCuP_2$ and $ErCuP_2$ the voids are already too small and they remain empty. Now, we can also explain why $GdCuP_{2.20}$ has extra P atoms and $SmCu_{1.15}P_2$ extra Cu atoms. Due to the lanthanide contraction the Gd atoms are smaller than Sm, and the smaller voids can accommodate only smaller P

atoms. A somewhat similar trend is observed for $RECu_{1+x}As_2$: the arsenides of the larger rare-earth elements contain extra Cu ($LaCu_{1.23(1)}As_2$, $CeCu_{1.10(1)}As_2$ and $PrCu_{1.09(1)}As_2$ [27]), while the phases with the smaller elements are reported to have the $RECuAs_2$ composition [28].

The electronic consequences of the matrix effect of rare earth elements are subtler. In phases with smaller rare earths the P atoms in the nets are closer, the overlap between the P orbitals is larger and therefore the bands are more disperse. Extra Cu or P atoms present in the voids would still drain electrons from the bonding $p_{x,y}$ states but not from the more antibonding s or p_z states. In overall, the bonding in the P net of the phosphides with smaller rare earths would be weakened more than in the phosphides with larger rare earths.

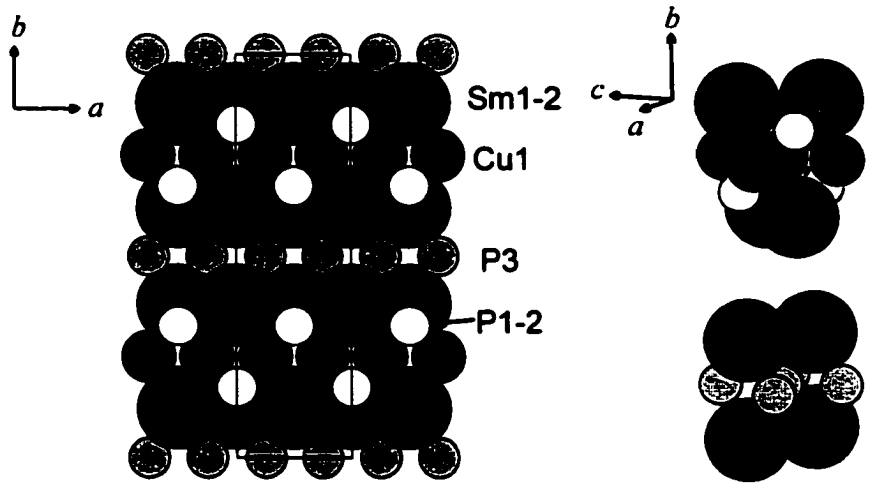

Figure 23. Sphere packing and coordination environment of Cu1 and P3 in tetragonal $SmCuP_2$.

Acknowledgements

This research was supported by the Office of the Basic Energy Sciences, Materials Sciences Division, US Department of Energy, DOE. The Ames Laboratory is operated for DOE by Iowa State University under contract No. W-7405-Eng-82.

Special thanks to Dr. Serdej Bud'ko for performing the resistance measurement.

Appendix

The band structure calculations were performed by the extended Hückel tight binding (EHTB) method [29]. Lattice and atomic parameters from the single crystal refinements of $ErCuP_2$ [17] and $SmCu_{1.15}P_2$ [18] were used in the calculations (Table 1). The additional Cu2 site in $SmCu_{1.15}P_2$ was

considered to be ¼ occupied (the resulting composition was $SmCu_{1.125}P_2$). The orbital energies and coefficients for the Slater-type orbitals were taken from [30]. The parameters for Er, Sm and Cu were refined by the alternating charge iteration technique, while the P parameters were kept constant (Table 2). Since the *f* orbitals are well localized (as seen from the magnetic data [16-18]), their role in the bonding was anticipated to be small, and they were not included into the calculations.

Table 1. Atomic Parameters for $ErCuP_2$ ($P2_1/n$ Space Group, a = 3.737, b = 19.239, c = 3.728 Å and β = 90.09°) and $SmCu_{1.15}P_2$ (*Cmmm* Space Group, a = 5.453, b = 19.511 and c = 5.439 Å)

Atom		*x*	*y*	*z*
		$ErCuP_2$		
Er	4*e*	0.2305	0.11717	0.7509
Cu	4*e*	0.2301	0.2514	0.2512
P1	4*e*	0.2309	0.3302	0.7522
P2	4*e*	0.2890	0.9989	0.2450
		$SmCu_{1.15}P_2$		
Sm1	4*i*	0	0.38371	0
Sm2	4*j*	0	0.12173	½
Cu1	8*m*	¼	¼	0.2484
Cu2*	4*i*	0	0.0490	0
P1	4*j*	0	0.3259	½
P2	4*i*	0	0.1735	0
P3	8*o*	0.2631	0	0.2917

* Occupancy of the Cu2 site is 29%

Table 2. Parameters for the Extended Hückel Tight-Binding Calculations

Atom	Orbital	H_{ii}, eV, $ErCuP_2$	H_{ii}, eV, $SmCu_{1.125}P_2$[a]	ξ_1	c_1[b]	ξ_2	c_2[b]
Er	6s	-8.29		1.54	1.00		
Er	6p	-5.40		1.54	1.00		
Er	5d	-7.72		2.81	0.7063	1.216	0.4834
Sm	6s		-10.38	1.40	1.00		
Sm	6p		-7.24	1.40	1.00		
Sm	5d		-5.58	2.747	0.7184	1.267	0.4447
Cu	4s	-8.91	-8.87	2.20	1.00		
Cu	4p	-4.88	-4.85	2.20	1.00		
Cu	3d	-13.69	-13.62	5.95	0.5933	2.30	0.5744

Table 2. (continued)

Atom	Orbital	H_{ii}, eV, $ErCuP_2$	H_{ii}, eV, $SmCu_{1.125}P_2$[a]	ξ_1	c_1[b]	ξ_2	c_2[b]
P	3p	-18.60	-18.60	1.75	1.00		
P	3p	-14.00	-14.00	1.30	1.00		

[a] The composition $SmCu_{1.125}P_2$ was taken for the calculations.
[b] Coefficients used in the double-zeta Slater-type orbitals.

References

(1) Peierls, R. E. *Quantum Theory of Solids*; Oxford University Press: London, 1955.

(2) Albright, T. A.; Burdett, J. K.; Whangbo, M.-H. *Orbital Interactions in Chemistry*; Wiley: New York, 1985.

(3) Hoffmann, R. *Solids and Surfaces*; VCH: New York, 1988.

(4) Hulliger, F.; Schmelczer, R.; Schwarzenbach, D. *J. Solid State Chem.* **1977**, *21*, 371-374.

(5) Sfez, G.; Adolphe, C. *Bull. Soc. Fr. Mineral. Cristallogr.* **1972**, *95*, 553-557.

(6) Ceolin, R.; Rodier, N.; Khodadad, P. *J. Less-Common Met.* **1977**, *53*, 137-140.

(7) Hulliger, F.; Schmelczer, R. *J. Solid State Chem.* **1978**, *26*, 389-396.

(8) Brechtel, E.; Cordier, G.; Schäfer, H. *Z. Naturforsch., B: Anorg. Chem., Org. Chem.* **1979**, *34B*, 251-255.

(9) Deller, K.; Eisenmann, B. *Z. Anorg. Allg. Chem.* **1976**, *425*, 104-108.

(10) Miller, G. J.; Li, F.; Franzen, H. F. *J. Am. Chem. Soc.* **1993**, *115*, 3739-3745.

(11) Wang, R.; Bodnar, R.; Steinfink, H. *Inorg. Chem.* **1966**, *5*, 1468-1470.

(12) Bodnar, R. E.; Steinfink, H. *Inorg. Chem.* **1967**, *6*, 327-330.

(13) Bodnar, R. E.; Steinfink, H.; Narasimhan, K. S. V. L. *J. Appl. Phys.* **1968**, *39*, 1485-1489.

(14) Tremel, W.; Hoffmann, R. *J. Am. Chem. Soc.* **1987**, *109*, 124-140.

(15) Cordier, G.; Eisenmann, B.; Schäfer, H. *Z. Anorg. Allg. Chem.* **1976**, *426*, 205-214.

(16) Mozharivskyj, Y.; Kaczorowski, D.; Franzen, H. F. *J. Solid State Chem.* **2000**, *155*, 259-272.

(17) Mozharivskyj, Y.; Kaczorowski, D.; Franzen, H. F. *Z. Anorg. Allg. Chem.* **2001**, *627*, 2163-2172.

(18) Mozharivskyj, Y.; Pecharsky, A. O.; Bud'ko, S. L.; Franzen, H. F. *submitted to Z. Anorg. Allg. Chem.*

(19) Möller, M. H.; Jeitschko, W. In *VIII Int. Conf. On Solid State Compounds of Transition Elements*; Extended Abstracts: Vienna, Austria, 1985, p P4 A14.

(20) Andrukhiv, L. S.; Lysenko, L. A.; Yarmolyuk, Y. P.; Gladyshevskii, E. I. *Dopov. Akad. Nauk Ukr. RSR, Ser. A* **1975**, 645-648.

(21) Hassler, E.; Johnsson, T.; Rundqvist, S. *Acta Chem. Scand.* **1974**, *28*, 123-124.

(22) Von Schnering, H. G.; Wichelhaus, W.; Schulze Nahrup, M. *Z. Anorg. Allg. Chem.* **1975**, *412*, 193-201.

(23) Zheng, C.; Hoffmann, R. *J. Am. Chem. Soc.* **1986**, *108*, 3078-3088.

(24) Hoffmann, R.; Zheng, C. *J. Phys. Chem.* **1985**, *89*, 4175-4181.

(25) Ban, Z.; Sikirica, M. *Acta Cryst.* **1965**, *18*, 594-599.

(26) Eisenmann, B.; May, N.; Müller, W.; Schäfer, H. *Z. Naturforsch. B* **1972**, *27*, 1155-1157.

(27) Wang, M.; McDonald, R.; Mar, A. *J. Solid State Chem.* **1999**, *147*, 140-145.

(28) Brylak, M.; Möller, M. H.; Jeitschko, W. *J. Solid State Chem.* **1995**, *115*, 305-308.

(29) Ren, J.; Liang, W.; Whangbo, M.-H., Crystal and Electronic Structure Analyser (CAESAR), North Carolina State University, Raleigh, NC, 1998.

(30) Alvarez, S. "Table of Parameters for Extended Hückel Calculations," Barcelona,1987.

CHAPTER 8. DISTORTIONS FROM THE TETRAGONAL $HfCuSi_2$-TYPE STRUCTURES TO THE ORTHORHOMBIC $GdCuAs_{1.15}P_{0.85}$-TYPE STRUCTURES IN $REMX_2$ (*RE* = RARE EARTH; *M*= Cu, Ag; *X*=P, As, Sb): MISMATCH BETWEEN THE SIZES OF THE *M* AND *X* ATOMS

A paper submitted to Journal of Physical Chemistry

Yurij Mozharivskyj and Hugo F. Franzen

Department of Chemistry and Ames Laboratory of US DOE, Spedding Hall, Iowa State University, Ames, Iowa 50011, USA

Abstract

The $RECuAs_{2-x}P_x$ phases undergo symmetry-breaking transitions from tetragonal $HfCuSi_2$-type structures (*P4/nmm* space group) to orthorhombic $GdCuAs_{1.15}P_{0.85}$-type structures (*Pmmn* space group) upon substitution of arsenic by phosphorus. According to Landau theory the distortions correspond to the B_{1g} irreducible representation and can be continuous. The *P4/nmm* → *Pmmn* transitions are not caused by a Peierls-like instability of the square As/P nets but result from a structural adaptation for the smaller P atoms. The stability of the tetragonal $RECuAs_{2-x}P_x$ and other $REMX_2$ structures with respect to the orthorhombic distortion can be characterized by a relative interatomic distance in the As/P or *X* layer. While the tetragonal phases have small relative As/P-As/P or *X*-*X* interatomic distances, the orthorhombic phases have larger distances.

Keywords: rare earth transition metal pnictides; symmetry-breaking transitions; Landau theory; normal modes; size effects.

Introduction

The Landau theory of symmetry-breaking transitions allows determination of broken symmetries that occur with a change in temperature or composition. However, the complexity of the solid state enters when the required energetic stabilization of the distorted form is considered. Terms from band energy, Madelung energy and size effects can all be considered, and their complex interplay is generally difficult to analyze. The compounds considered here, because of the variation in chemical content (P/As substitutions, compounds containing Cu or Ag as the transition element)

allow, with the aid of band structures and group theory, a partial unraveling of the factors important in the tetragonal to orthorhombic distortions in the $HfCuSi_2$-type structures.

Intermetallic compounds with 2D square nets of the main group elements are interesting because they often exhibit Peierls instabilities and undergo symmetry-breaking transitions (e.g., GdPS[1], CeAsS[2], $SrZnSb_2$[3], $EuSb_2$[4], $CaAl_4$[5], $GdCuP_{2.20}$[6], etc.). The reason for these distortions lies in the half filling of the widely dispersed bands centered on the main group elements. These broad bands, formed mainly by p_x and p_y orbitals, cross along some symmetry lines in the Brillouin zone and the Fermi level lies at the crossing: an ideal situation for a distortion and gap opening[6,7]. One of the prerequisites for a subsequent distortion is a separation of the valence band and the rare-earth *d* orbitals[7]. Even if these conditions are met, it is possible that a distortion does not occur, e.g., $EuSb_2$ ($CaSb_2$ type)[4] and $RECu_{1+\delta}P_{2+x}$[6,8,9] distorts but $YbSb_2$ ($ZrSi_2$ type)[10] and $RECuAs_2$[11] do not.

In the $RECuAs_{2-x}P_x$ series[6,8,9] the symmetry-breaking transitions are complicated and, as we show below, they cannot be characterized as mere consequences of a Peierls instability. The arsenides and some arsenophosphides adopt the tetragonal $HfCuSi_2$-type structure (*P4/nmm* space group), which can be "continuously" distorted into the orthogonal $GdCuAs_{1.15}P_{0.85}$-type structure (*Pmmn* space group) upon partial substitution of arsenic by phosphorus. This transition corresponds to a single irreducible representation and, according to Landau theory, can be continuous[6,8]. In the orthorhombic structures the originally square As/P nets are slightly distorted: all distances within the As/P layers are the same, but the angles deviate from 90° (but by less than 1°). The band crossing still remains and electronic considerations in terms of the Peierls instability cannot explain the observed distortion. When nearly all of the arsenic in $RECuAs_{2-x}P_x$ is replaced by phosphorus, the orthorhombic structures distort further. In the phosphides $GdCuP_{2.20}$[6], $ErCuP_2$[8] and $SmCu_{1.15}P_2$[9] the band crossing is avoided and their structures can be viewed as results of Peierls instabilities of the square nets of the phosphorus atoms.

The $RECuAs_2$ (*P4/nmm* space group)[11] and $REAgAs_2$ (*Pmmn* space group)[12] series have the As atoms in the square or nearly square nets, but in the case of the silver containing compounds the structures are distorted. Although it appears to be different from the As/P substitution in $RECuAs_{2-x}P_x$, the replacement of the smaller Cu atoms by the larger Ag atoms has the same effect on the structure. If one omits slight changes in the electronic structures and considers the structural aspect of the Cu/Ag replacement, it becomes obvious that the Ag atoms exert a matrix effect on the As atoms in the square net that is similar to that of the Cu atoms on the P atoms in the As/P layer.

In this paper we combine the conclusions of Landau theory[6,8] with the electronic structures of the tetragonal and orthorhombic $RECuAs_{2-x}P_x$ phases to show that the continuous symmetry-breaking

P4/nmm → *Pmmn* transitions are not caused by Peierls instabilities of the square As/P nets. Then we show that the distortions provide better packing and thus greater stabilization energy through a larger Madelung contribution. And finally we generalize the results obtained for other known rare-earth copper and silver pnictides of the $REMX_2$ composition.

Band structure calculations were performed using the extended Hückel tight-binding (EHTB) method[13]. Lattice and atomic position parameters (Table 3) from the single crystal refinements of $GdCuAs_2$[6] were used in the calculations. The powder lattice parameters of GdCuAsP (a_{orth} = 3.8314(8), b_{orth} = 3.8443(8), c_{orth} = 9.8613(9) Å and V_{orth} = 142.25(4) Å^3) and atomic parameters of $GdCuAs_{1.15}P_{0.85}$[6] (Table 3) were taken for the calculation of the band structure and the total electronic energy of GdCuAsP. Since the As/P ratio is around 3/1 in the (As/P)2 net and is the inverse in the Cu(As/P)1 layer, a cell with a doubled *a* parameter was constructed to account for the As/P mixtures. A hypothetical tetragonal cell for GdCuAsP with $a_{tet} = b_{tet} = b_{orth}$ = 3.8443, c_{tet} =9.8613 Å and V_{tet} = 145.74 Å^3 was derived from the analysis of the lattice parameters of the tetragonal and orthorhombic phases in the $RECuAs_{2-x}P_x$ series[6,8,9]. The atomic parameters for the tetragonal structure were assumed to be the same as for the orthorhombic one, but with z = ½ for Cu and z = 0 for (As/P)2.

The orbital energies and coefficients for the Slater-type orbitals were taken from[14]. The parameters for Gd and Cu were refined by the alternating charge iteration technique, while the As and P parameters were kept constant (Table 1).

Table 1. Parameters for the Extended Hückel Tight-Binding Calculations

Atom	Orbital	H_{ii}, eV, $GdCuAs_2$	H_{ii}, eV, GdCuAsP	ξ_1	c_1[a]	ξ_2	c_2[a]
Gd	6s	-7.61	-7.59	1.369	1.00		
Gd	6p	-5.03	-5.01	1.369	1.00		
Gd	5d	-8.05	-8.02	2.747	0.7184	1.267	0.4447
Cu	4s	-9.46	-9.11	2.20	1.00		
Cu	4p	-5.30	-5.03	2.20	1.00		
Cu	3d	-14.55	-14.00	5.95	0.5933	2.30	0.5744
As	4s	-16.22	-16.22	2.23	1.00		
As	4p	-12.16	-12.16	1.89	1.00		
P	3p		-18.60	1.75	1.00		
P	3p		-14.00	1.30	1.00		

[a] Coefficients used in the double-zeta Slater-type orbitals.

Structural Changes in *RE*CuAs$_{2-x}$P$_x$

Since the transitions between the arsenide and arsenophosphide structures are the same for the Sm, Gd, Ho and Er series, only the GdCuAs$_{2-x}$P$_x$ phases will be considered here. GdCuAs$_2$ has a tetragonal HfCuSi$_2$-type structure. Upon an As/P substitution this tetragonal structure distorts to an orthorhombic GdCuAs$_{1.15}$P$_{0.85}$-type structure[6] (Fig. 1). Changes in symmetry and lattice parameters for GdCuAs$_{2-x}$P$_x$ are summarized in Table 2 and Fig. 2. Table 3 gives the atomic parameters for GdCuAs$_2$ and GdCuAs$_{1.15}$P$_{0.85}$ obtained from the refinements of single crystal data[6]. The structural changes are best visualized by viewing layers of the As2 and (As/P)2 atoms (Fig. 3).

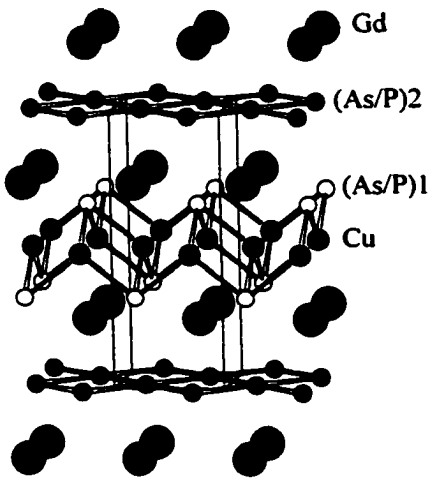

Figure 1. Structure of GdCuAs$_{1.15}$P$_{0.85}$ (*Pmmn* space group).

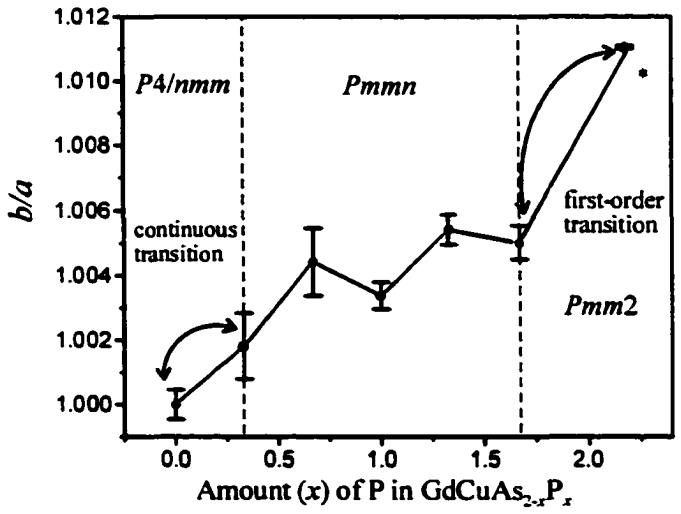

Figure 2. *b/a* ratio versus phosphorus amount in GdCuAs$_{2-x}$P$_x$. Dashed lines show the experimentally established regions for the orthorhombic arsenophosphides. *Composition of the phosphide is GdCuP$_{2.16}$ (Rietveld refinement).

Table 2. Powder Lattice Parameters for the $GdCuAs_{2-x}P_x$ Phases

Composition	Sp. Group	*a*, Å	*b*, Å	*c*, Å	*b/a*	*V*, Å^3
$GdCuAs_2$	*P4/nmm*	3.9112(9)	3.9112(9)	9.930(3)	1	152.90(7)
$GdCuAs_{1.67}P_{0.33}$	*Pmmn*	3.883(2)	3.890(2)	9.908(4)	1.0018(7)	149.7(1)
$GdCuAs_{1.33}P_{0.67}$	*Pmmn*	3.850(2)	3.867(2)	9.888(4)	1.0044(7)	147.2(1)
GdCuAsP	*Pmmn*	3.8314(8)	3.8443(8)	9.8613(9)	1.0034(3)	145.25(4)
$GdCuAs_{0.67}P_{1.33}$	*Pmmn*	3.8072(9)	3.8278(9)	9.843(2)	1.0054(3)	143.44(6)
$GdCuAs_{0.33}P_{1.67}$	*Pmmn*	3.793(1)	3.812(1)	9.822(2)	1.0050(4)	142.01(6)
$GdCuP_{2.16}$[a]	*Pmm2*[b]	5.3284(1)	5.3868(1)	9.7487(3)	1.01096(3)	279.82(1)

[a] Composition from the Rietveld refinement. Composition from the single crystal refinement is $GdCuP_{2.20}$.
[b] not a superstructure of $GdCuAs_{0.33}P_{1.67}$.

Table 3. Atomic Parameter for $GdCuAs_2$ (*P4/nmm* Space Group, $HfCuSi_2$ Type) and $GdCuAs_{1.15}P_{0.85}$ (*Pmmn* Space Group)

	$GdCuAs_2$				$GdCuAs_{1.15}P_{0.85}$			
Atom		*x*	*y*	*z*		*x*	*y*	*z*
Gd	2*c*	¼	¼	0.23844(8)	2*a*	¼	¼	0.24108(4)
Cu	2*b*	¾	¼	1/2	2*b*	¼	¾	0.49989(12)
*X*1[a]	2*c*	¼	¼	0.65810(18)	2*a*	¼	¼	0.65545(16)
X2[b]	2*a*	¾	¼	0	2*b*	¼	¾	0.00005(11)

[a] *X*1 = 32.8(8)%As + 67.2(8)%P for $GdCuAs_{1.15}P_{0.85}$.
[b] *X*2 = 82.1(6)%As + 17.9(6)%P for $GdCuAs_{1.15}P_{0.85}$.

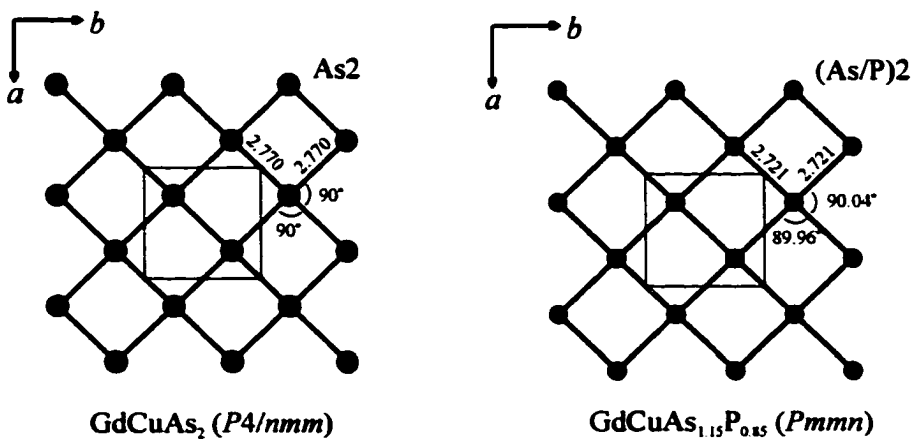

$GdCuAs_2$ (*P4/nmm*) $GdCuAs_{1.15}P_{0.85}$ (*Pmmn*)

Figure 3. As and As/P layers in $GdCuAs_2$ and $GdCuAs_{1.15}P_{0.85}$.

Upon the second-order transition (its nature is discussed below) the *a* and *b* parameters become slightly different, the maximum *b/a* ratio achieved is 1.0054(3). Since the (As/P)2 and Cu atoms move up and down from the horizontal planes, the four-fold axis is lost. The (As/P2) and Cu shifts in $GdCuAs_{1.15}P_{0.85}$ are very small ($z_{As/P}$ = 0.00005(11) and z_{Cu} = 0.49989(12)), with the Cu shifts being larger. Similar small displacements are observed for refined orthogonal $HoCuAs_{0.99}P_{1.01}$[8], $SmCu_{1.16}As_{0.86}P_{1.14}$[9] and $NdAgAs_2$[12], but in the latter phase the As shifts are the largest and the Ag shifts are close to zero: *z* = 0.9955(6) for As2 and *z* = 0.5001(5) for Ag.

The structural distortions in $GdCuAs_{2-x}P_x$, as well as in $SmCuAs_{2-x}P_x$, $HoCuAs_{2-x}P_x$ and $ErCuAs_{2-x}P_x$, result when As atoms are substituted by smaller P atoms. If the P atoms are introduced in the square As layer a mismatch occurs between the optimal distances in the (As/P)2 layer and the *a*, *b* dimensions, determined by the matrix effect of the larger Cu atoms. This mismatch and its consequences are best characterized by the relative interatomic distances in the As/P net and this approach is presented in detail below ("Size Effect in *RE*$CuAs_{2-x}P_x$"). For smaller P atoms the bonding would be optimized with shorter interatomic distances. Shorter interatomic distances for the P atoms in the structure lead to a smaller unit cell volume and an orthorhombic structural rearrangement.

To answer the question of whether the packing is optimized in this way, unit cell volumes of undistorted and distorted structures with the same composition must be compared. This direct comparison is impossible for the *P4/nmm* → *Pmmn* transition, which follows from the fact that a high-symmetry structure cannot be obtained below the transition temperature in the case of a displacive second-order structural transition. However, a tighter packing upon the *P4/nmm* → *Pmmn* transition can be inferred from the changes in the unit cell volume in the *RE*$CuAs_{2-x}P_x$ series (see "Size Effect in *RE*$CuAs_{2-x}P_x$").

Symmetry-Breaking Transitions *P4/nmm* → *Pmmn* in Terms of Landau Theory

The continuous symmetry-breaking transitions *P4/nmm* → *Pmmn* in the $GdCuAs_{2-x}P_x$[6], $HoCuAs_{2-x}P_x$, $ErCuAs_{2-x}P_x$[8] and $SmCuAs_{2-x}P_x$[9] series do not create a superstructure. We will analyze only the $GdCuAs_{2-x}P_x$ case (Fig. 2, Table 2), but the results obtained can be equally applied to other *RE*$CuAs_{2-x}P_x$ series. Since no translation is lost during the distortions, the ***k***-vector to which the distortions correspond is ***k*** = 0 and the irreducible representations are isomorphous with those of the point group D_{4h} for $GdCuAs_2$.

One of the considerations of Landau theory[15-17] is that a continuous symmetry-breaking transition must correspond to a single irreducible representation (IR). There are eight one- and two

two-dimensional IRs at $\boldsymbol{k}$ = 0. The two-dimensional representations would result in distorted structures with 4 symmetry elements, corresponding to monoclinic centrosymmetric or orthorhombic noncentrosymmetric subgroups, which are not the case here and, therefore, they are not of interest. All one-dimensional representations, except the totally symmetric one, result in a loss of all symmetry operations with character -1, and they, accordingly, lead to a halving of the number of the rotational symmetry elements, and thus to space groups with eight essential symmetry elements. Four of the seven subgroups have orthorhombic unit cells, but only two (from the B_{1g} and B_{2g} representations) preserve the horizontal plane and inversion center. The space group *Pmmn*, corresponding to B_{1g} (Table 4), is the one found experimentally in $GdCuAs_{1.15}P_{0.85}$.

For a transition to be continuous an expansion of the Gibbs free energy in the order-disorder parameter, η, should not contain any third-order combination of the basis functions. In the case of the one-dimensional irreducible representation B_{1g} a basis function is symmetric to one half and antisymmetric to the other half of the symmetry elements. Thus, no third-order invariant can be formed and the *P4/nmm* → *Pmmn* transition with $\boldsymbol{a}_{ort} = \boldsymbol{a}_{tet}$, $\boldsymbol{b}_{ort} = \boldsymbol{b}_{tet}$ and $\boldsymbol{c}_{ort} = \boldsymbol{c}_{tet}$ follows the Landau conditions for a second-order phase transition.

The last criterion, which must be met for a second-order phase transition from $GdCuAs_2$ (*P4/nmm*) to $GdCuAs_{1.15}P_{0.85}$ (*Pmmn*), is the Lifshitz criterion. It requires a minimum in the Gibbs free energy to be fixed by the symmetry at the $\boldsymbol{k}$ vector corresponding to the transition. This condition prevents a decrease of the Gibbs free energy with a change of the $\boldsymbol{k}$ vector and, therefore, excludes the possibility of continuous distortion to a modulated structure. In the case under consideration inversion symmetry is in the point group of the wave vector and thus the reciprocal space point meets the Lifshitz criterion.

Table 4. One-Dimensional Irreducible Representation B_{1g} of *P4/nmm* at Γ

g	ϵ	C_{4z}	C_{4z}^3	C_{2z}	C_{2x}	C_{2y}	$C_{2(x+y)}$	$C_{2(x-y)}$
$\chi(g)$	1	-1	-1	1	1	1	-1	-1
g	i	$\bar{C}_{4z}$	$\bar{C}_{4z}^3$	σ_z	σ_x	σ_y	σ_{x+y}	σ_{x-y}
$\chi(g)$	1	-1	-1	1	1	1	-1	-1

Landau Theory and Bonding for *P4/nmm* → *Pmmn* Transitions

Imposing the constraint of correspondence of a second-order transition to a single irreducible representation, Landau theory determines, in this way, the symmetry of the normal mode (lattice vibration) that leads to the distortion. In our case, the symmetry of the normal mode involved in the

P4/nmm → *Pmmn* distortion is B_{1g}. Although Landau theory is of use in describing the nature of transitions, it cannot explain, however, the electronic or geometric factors causing these symmetry-breaking transitions.

Since the band structure of $GdCuAs_2$ (*P4/nmm*) (Fig. 4) has widely dispersed bands that cross each other, and the Fermi level lies at the crossing, at first it appears that a Peierls instability can lead to the observed *P4/nmm* → *Pmmn* distortions. This electronic instability resulting in the symmetry breaking is associated with a strong interaction of electronic states through the B_{1g} normal mode. In

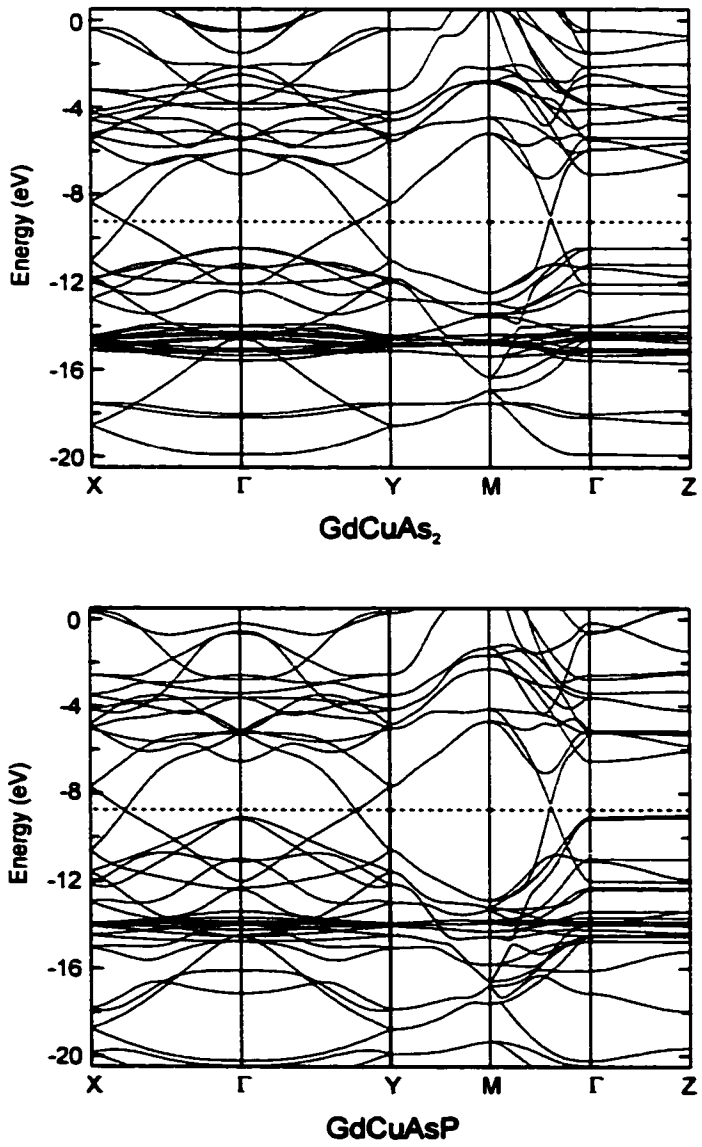

Figure 4. Band structure of $GdCuAs_2$ (*P4/nmm* sp. group) and GdCuAsP (*Pmmn* sp. group). Here, in GdCuAsP the *X*1 site is occupied only by P and the *X*2 site is occupied only by As.

general it is possible that this interaction results in a gap opening at the Fermi level (a first-order Peierls distortion) or in changes in energy of the states below and above the Fermi level without opening a gap (a second-order Peierls distortion). In each case the energy of the system would be lowered and the crystal symmetry reduced. The two distortion types and energetic gains associated with them are considered below.

Electronic States of $GdCuAs_2$ and B_{1g} Normal Mode

Electronic states involved in mixing through the B_{1g} normal mode are those for which the direct product of their irreducible representations contains the irreducible presentation B_{1g}. Group theoretical analysis shows that the B_{1g} normal mode is associated with vibrations of the Cu and As2 atoms and, therefore, that electronic states of the Cu or As2 must be involved in the interaction (here, we have assumed no P in the structure). Also, the mixing states must occur above and below the Fermi level to give an energy gain upon distortion and the energy separation between them should be small, since the strength of orbital mixing is inversely proportional to the energy difference between them. Thus we need to consider only bands in the vicinity of the Fermi level for $GdCuAs_2$ (Fig. 4).

Using an orbital picture, symmetry of the bonding and antibonding As2 molecular orbitals at the Γ point can be easily deduced (e.g., p_x and p_y orbitals in Fig. 5). The orbital interaction leading to formation of these MOs and their relative energies at the Γ point are presented in Fig. 6. Here, we assume a negative charge for the As2 atoms in order to have the correct filling of the states. A delocalized picture, showing the change in energy of the As2 states along the symmetry lines in the first Brillouin zone, is given in Fig. 7. There is a crossing of two bands and the Fermi level falls exactly at the crossing. States at the crossing have the largest contribution from the As2 p_x and p_y orbitals. These bands are also the ones that cross at the Fermi level in the complete band structure of $GdCuAs_2$ and that is why they are considered in detail here. However, the crossing of the bands and associated Peierls instability does not lead to the observed orthorhombic distortion at $\boldsymbol{k} = 0$ since the direct product ($E_g \otimes E_u = A_{1u} + A_{2u} + B_{1u} + B_{2u}$) of the irreducible representations of the As2 antibonding $p^*_{x,y}$ and bonding $p_{x,y}$ orbitals does not contain the B_{1g} representation that corresponds to the observed transition from $GdCuAs_2$ to $GdCuAs_{1.15}P_{0.85}$. Thus the $p_{x,y}$ bands do not mix and the crossing remains (Fig. 4).

On the other hand, the mixing of the As2 p^*_z molecular orbitals (B_{1g} symmetry), that are below the Fermi level, with the Gd s or d_{z^2} molecular orbitals (A_{1g} symmetry), that are above, is allowed through the normal mode B_{1g} at the Γ point. This normal mode is associated with vibration of the As2 atoms as shown in Fig. 8a. Also allowed is a mixing between the Cu p^*_z, s^* MOs (B_{1g}, A_{2u}

symmetries) with the As1 s and p_z MOs (A_{1g}, B_{2u} symmetries), respectively, through the B_{1g} mode, which now is attributed to the Cu vibrations (Fig. 8b). There are some other states coupled through the B_{1g} modes, but all the states can be divided into two groups: those that are coupled through the As2 vibrations and the others that are coupled through the Cu vibrations.

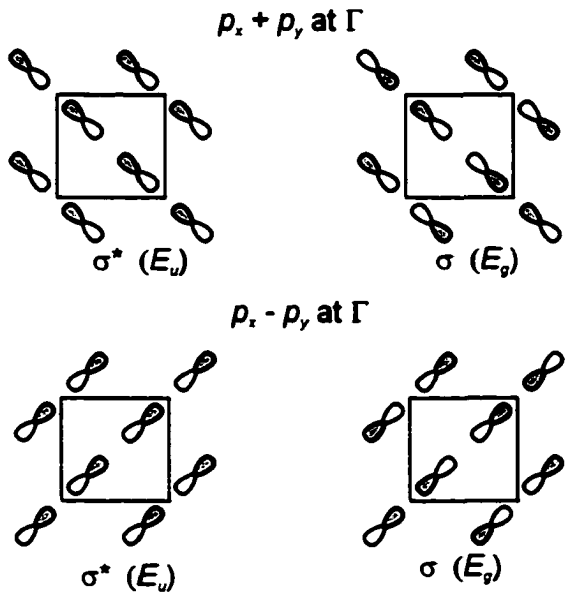

Figure 5. Molecular orbitals (MOs) from the p_x and p_y orbitals of the As2 atoms and their symmetries at Γ.

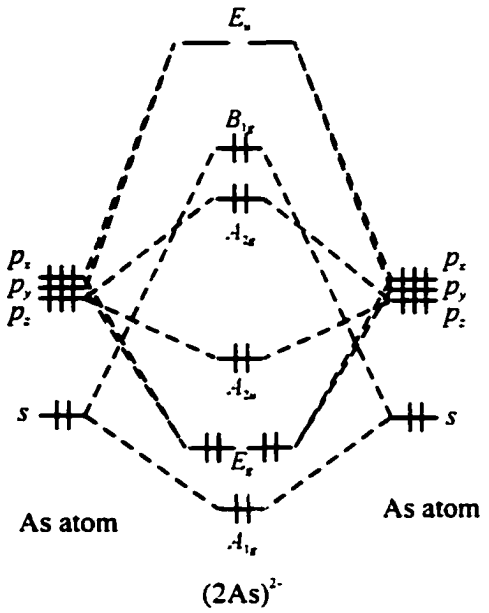

Figure 6. Symmetries of MOs formed from the As2 orbitals and their relative energies at Γ. As atoms have one additional electron.

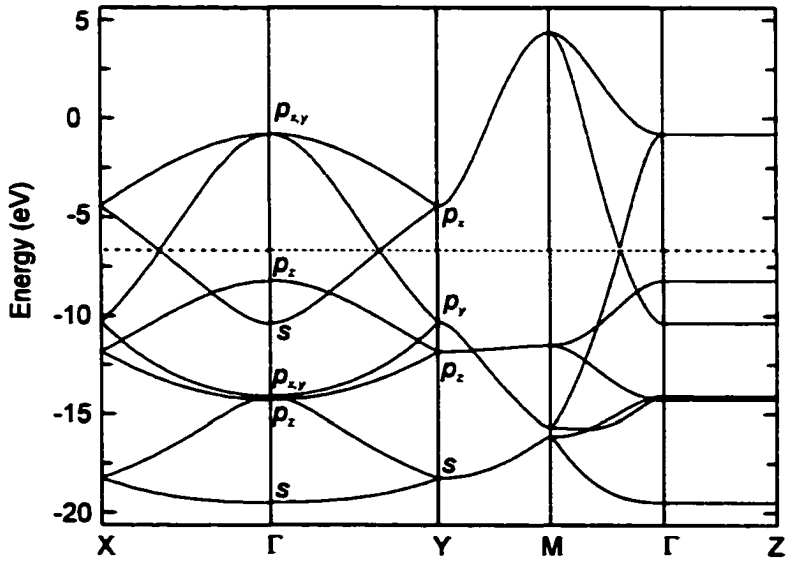

Figure 7. Band structure of the $(As2)^-$ layer of tetragonal $GdCuAs_2$ and orbital character of the states at Γ and Y.

From the EHTB calculations on GdCuAsP the displacements of the Cu and (As/P)2 atoms from their positions in the tetragonal structure do not change the total electronic energy. For this calculation, the unit cell was assumed to be tetragonal, but the Cu and (As/P)2 fractional coordinates were those in the real orthorhombic structure. In all calculations one P and one As atom were introduced into the As2 and CuP1 layers, respectively. When the structure is orthorhombicly distorted, with the Cu and (As/P)2 atoms being at their real displaced positions, the total electronic energy for GdCuAsP (-352.80 eV per unit formula) becomes even slightly larger than that for the hypothetical tetragonal structure (-352.81 eV). It must be remembered that the atomic arrangement of the tetragonal GdCuAsP structure is based on that of the orthorhombic one and in the real tetragonal phase, if it can be obtained at all, the atomic parameters can be somewhat different and the electronic energy of this tetragonal structure can therefore be even smaller. It is thus clear that the electronic energy is not lowered through a second-order Peierls distortion, but it is also clear that the orthorhombic structure is more stable, and that this stability originates with introduction of P atoms.

Size Effect in $RECuAs_{2-x}P_x$

As alluded to above, the size of the P atoms could be related to the distortion from the tetragonal to orthorhombic structures in $SmCuAs_{2-x}P_x$, $GdCuAs_{2-x}P_x$, $HoCuAs_{2-x}P_x$ and $ErCuAs_{2-x}P_x$; the smaller P atoms tend to stabilize the $GdCuAs_{1.15}P_{0.85}$-type structures. Since the vibrational mode B_{1g} responsible for the *P4/nmm* → *Pmmn* distortion is associated with the (As/P)2 and Cu nets, it is natural to confine our attention to these two nets. To go beyond a qualitative structural description of the transitions and to have a quantitative criterion for analyzing stability of the tetragonal $REMX_2$

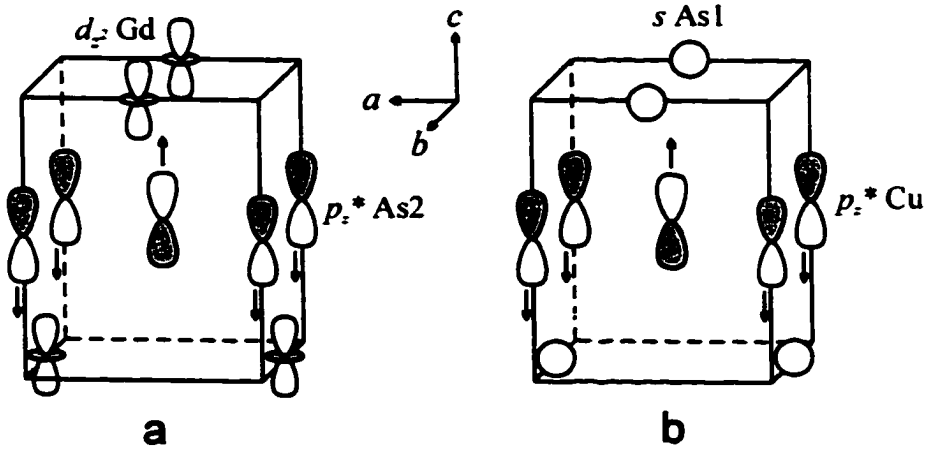

Figure 8. Allowed interactions through the B_{1g} normal mode (a) of the As2 atoms between the Gd d_{z^2} and As2 p_z* orbitals, (b) of the Cu atoms between the As1 *s* and Cu p_z* orbitals at Γ.

structures, we introduce a ***relative interatomic distance*** for the *M* and *X* nets. A relative interatomic distance is the ratio between the *X-X* or *M-M* interatomic distances projected onto the *ab* plane and the element diameters*.

In tetragonal $GdCuAs_2$ and other rare-earth copper arsenides the Cu net is structurally the same as the As2 layer. The element radii of the As and Cu atoms are close: 1.245 Å and 1.278 Å, respectively. So, the relative interatomic distances *r/d* in the horizontal As2 and Cu layer are similar in the tetragonal $GdCuAs_2$ phase ($r_{As\text{-}As}/d_{As}$ = 1.111 and $r_{Cu\text{-}Cu}/d_{Cu}$ = 1.082). When smaller P atoms (radius is 1.105 Å for the white modification) are introduced in the As2 square net, the relative interatomic distance for P becomes significantly larger than those for As and Cu and, accordingly, the P atom environment is unfavorable (in GdCuAsP r_{As}/d_{As} = 1.090, $r_{Cu\text{-}Cu}/d_{Cu}$ = 1.062 and $r_{P\text{-}P}/d_P$ = 1.228).

There are two ways, consistent with the B_{1g} normal mode, to increase packing and more effectively bind the P atoms in the structure. One would be to move the (As/P)2 out of the horizontal plane at $z = 0$ (normal mode B_{1g} in Fig. 8a) and closer to the Gd atoms, but leave the copper atoms in the original positions. The relative interatomic distance for Cu atoms would not change and they would dictate the unit cell dimensions in the *ab* plane. Although there is no experimental proof, it is reasonable to conclude that this kind of structural adaptation would have small or no effect on the *a, b* parameters but would decrease the *c* parameter. The second possibility is to keep the As/P atoms in the plane but to move Cu atoms out of the horizontal plane at $z = ½$ (normal mode B_{1g} in Fig. 8b) thereby decreasing the relative Cu-Cu interatomic distance projected on ***this plane*** in order to match the smaller relative (As/P)2-(As/P)2 interatomic distance in the plane at $z = 0$. In the second case the *a* and/or *b* parameters would decrease upon the *P4/nmm* → *Pmmn* transition. This type of structural adaptation is believed to occur in the $RECuAs_{2-x}P_x$ series as judged from the larger shifts of the Cu atoms in the orthorhombic arsenophosphides and from the lattice parameters of the two samarium phases with close As/P ratios across the transition point: $SmCuAs_{1.22}P_{0.78}$, *P4/nmm*, $a = b = 3.8863(8)$, $c = 9.919(2)$ Å and $SmCuAs_{1.11}P_{0.89}$, *Pmmn*, $a = 3.8659(8)$, $b = 3.8816(8)$, $c = 9.913(2)$ Å[9]. In both cases due to the B_{1g} normal mode the C_{4z} axis is lost and the *P4/nmm* symmetry is reduced to *Pmmn*.

EHTB calculations of the total electronic energy for the undistorted and distorted $(As/P)2^-$ and $(Cu(As/P)1)^{2-}$ layers in GdCuAsP support the orthorhombic distortion due to the B_{1g} shifts of the Cu atoms. The (As/P)2 and Cu displacements are both energetically unfavorable ($\Delta E_{el}>0$), but the B_{1g}

*We use the element radii / diameters for Cu, As and P since four of their nearest neighbors are atoms of the same type. Besides, the charges on Cu, As and P in the Cu and As/P layers are small, as determined from the analysis of the atomic orbital population for GdCuAsP.

shifts of the (As/P)2 atoms ($z_{As/P}$ = 0.00005) are more energetically unfavorable (ΔE_{el} = 0.05eV) than those of the Cu atoms (z_{Cu} = 0.49989) in the $(Cu(As/P)1)^{2-}$ units (ΔE_{el} = 0.03eV). Thus, from the experimental and theoretical data it can be concluded that in the orthorhombic *RE*$CuAs_{2-x}P_x$ phases it is the Cu layer that changes to be compatible with the more compact As/P layer and undergoes the distortion.

Since the electronic factors do not drive the *P4/nmm* → *Pmmn* transition, geometric factors with associated Madelung energies are most probably important in the distortion. A role of the latter factors can be traced through a volume decrease upon the transition that leads to a better packing and larger Madelung energy stabilization. Although indirectly, a volume decrease can be inferred from changes of the unit cell volume in the *RE*$CuAs_{2-x}P_x$ series. As seen in Fig. 9, there is a step down in the slope of the unit cell volume upon the *P4/nmm* → *Pmmn* transition in $SmCuAs_{2-x}P_x$ and $ErCuAs_{2-x}P_x$. This cannot be said about $GdCuAs_{2-x}P_x$ since there is only one data point for the tetragonal phase.

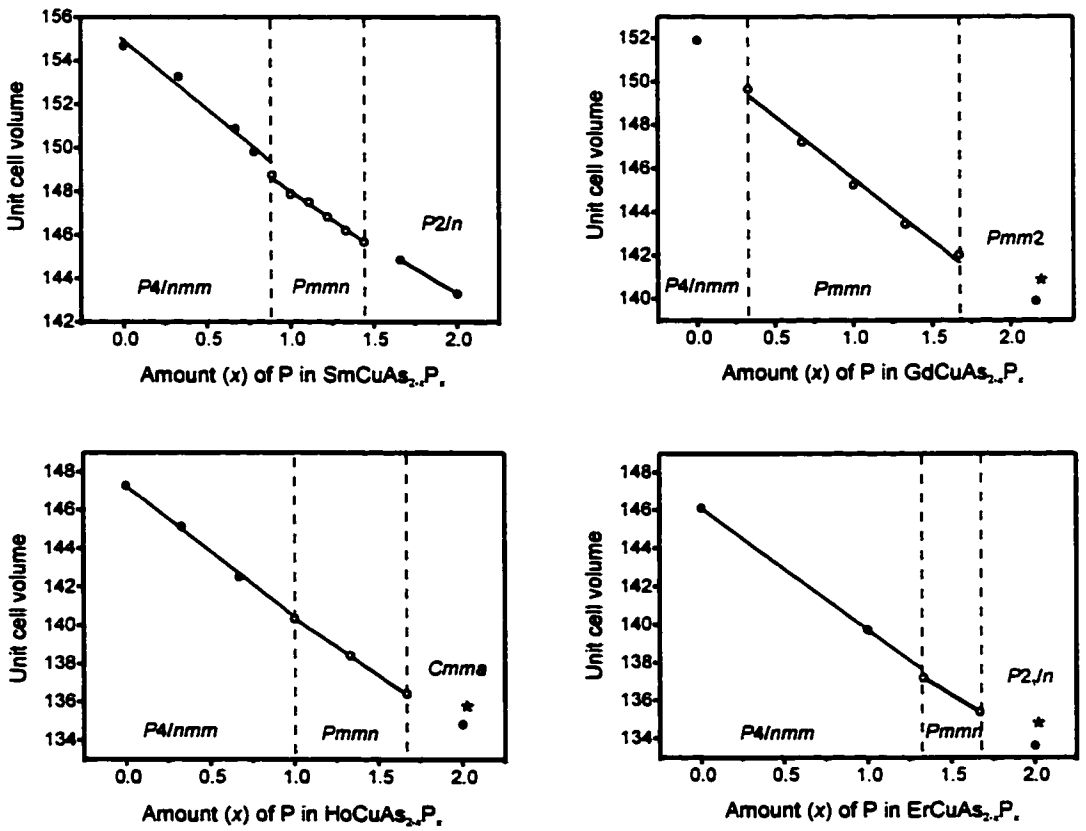

Figure 9. Unit cell volume versus phosphorus amount in the *RE*$CuAs_{2-x}P_x$ series. Dashed lines show the experimentally established regions for the orthorhombic arsenophosphides (open circles). Discontinuity in the unit cell volume curves during the *P4/nmm* → *Pmmn* distortions is artificially produced (not real) to illustrate the steps in the slopes. *$\frac{1}{2}V_{unit\ cell}$. For the Gd series the compositions of the phosphide is $GdCuP_{2.16}$.

In the $HoCuAs_{2-x}P_x$ series there is a change in the slope upon the distortion. These steps in $SmCuAs_{2-x}P_x$ and $ErCuAs_{2-x}P_x$ indicate clearly that an increase in packing is the structural response to the smaller P atoms.

To compare the Madelung energies of the tetragonal and distorted orthorhombic GdCuAsP structures we used a simple ionic picture based on an electron count in GdCuAsP. The Gd atoms have no short metal-metal bonds and therefore may be counted as Gd^{3+} in agreement with the results of the magnetic susceptibility measurements for $GdCuAs_2$ and $GdCuP_{2.20}$[6]. The (As/P)1 atoms have no close anion neighbors and can be assumed $(As/P)^{3-}$. The shortest Cu-Gd and Cu-Cu distances are 3.1986-3.1995 and 2.7211 Å in the real $GdCuAs_{1.15}P_{0.85}$ structure[6]. The copper distances are typical for Cu^+ (d^{10}) as usually found in pnictide and chalcogenide systems. Based on the above oxidation state assignments the electronic structure can be described as $(Gd^{3+})(Cu^+)((As/P)1^{3-})((As/P)2^-)$. Although this formula does not represent the real charge distribution in the unit cell, it is suitable for an analysis of the sign of the change in Madelung energy (ΔE_{ion}). Calculations show that E_{ion} for the orthorhombic structure (-85.87eV per unit cell) is slightly lower than E_{ion} for the hypothetical tetragonal structure (-85.80eV). It is obvious that the energetic gain upon the *P4/nmm* → *Pmmn* transition is, as it should be for a second-order transition considered in this way, rather small, but this energetic stabilization, originating with the introduction of the smaller P atoms, leads to the orthorhombic distortion in GdCuAsP.

Reverse *Pmmn* → *P4/nmm* Transition

The *P4/nmm* → *Pmmn* distortions in the $RECuAs_{2-x}P_x$ series are structural adaptations to small P atoms. The B_{1g} normal mode of the Cu1 atoms provides tighter environment for the P2 atoms through making the unit cell parameters smaller in the *ab* plane. Another way to bind the P atoms tightly in the structure would be to have some additional atoms around the (As/P)2 layer and in the tetragonal antiprisms made of the (As/P)2 and *RE* atoms. Two obvious requirements that have to be met in this case are the size of the additional atoms and the size of the void, which depends on the rare-earth element. Provided that no new element is introduced into the structure, only copper atoms are most likely to go into the voids. The rare-earth atoms are too large and phosphorus or arsenic is unlikely be in that place due to the repulsion between the negatively charged P or As atoms. Among the studied the $RECuAs_{2-x}P_x$ series (*RE* = Sm, Gd, Ho and Er), the samarium copper arsenophosphides have the largest voids and, therefore, could take some extra copper into their structures. Indeed, we were successful to introduce additional Cu atoms into the structure of a samarium arsenophosphide and restabilize the tetragonal structure through the reverse *Pmmn* → *P4/nmm* transition[9].

$SmCuAs_{0.67}P_{1.33}$ adopts the orthorhombic structure (*Pmmn*), while $SmCu_{1.1}As_{0.67}P_{1.33}$ and $SmCu_{1.2}As_{0.67}P_{1.33}$ are both tetragonal (*P4/nmm*).

The concept of the relative interatomic distance was helpful in understanding stability of some $SmCuAs_{2-x}P_x$ phases. The relative interatomic distances in the tetragonal samarium arsenophosphides $SmCuAs_{2-x}P_x$ with $0 < x < 0.78$ were found to be too large for these phases to remain tetragonal[9] (the borderline in *r/d* between the tetragonal and orthorhombic phases is discussed below). Additional Cu atoms were assumed in their structures and they were believed to stabilize these tetragonal structures. X-ray diffraction experiments performed on crystals from the $SmCuAs_{1.67}P_{0.33}$ sample proved small excess of Cu in their tetragonal structure (see the structure of $SmCu_{1.05}As_{1.67}P_{0.33}$ in Fig. 10). As expected, the additional copper atoms are around the (As/P)2 layer.

Role of the *M* and *X* Elements in $REMX_2$

In $RECuAs_{2-x}P_x$ the *P4/nmm* → *Pmmn* distortions occur when the relative interatomic distances in the (As/P) layer become smaller than those in the Cu layer. If this size argument is correct, then a similar trend would be observed for other rare-earth transition metal pnictides. Here, we consider known rare-earth copper or silver phosphides, arsenides and antimonides. The antimonides and copper arsenides have the tetragonal $HfCuSi_2$ structure while other phases adopt distorted variants of the $HfCuSi_2$ structure. For the analysis we use lattice parameters and compositions for $REAgSb_2$ from[11,18], for $RECuSb_2$ from[19], for $RECuAs_2$ and $RECu_{1+x}As_2$ from[11,20], for $REAgAs_2$ from[12], for $RECuAs_{2-x}P_x$ and $RECuP_2$ from[6,8,9]. The formula $RECuP_2$ is used here for simplicity and does not represent the actual compositions of the different phosphides, e.g., $SmCu_{1.15}P_2$ [9], $GdCuP_{2.20}$ [6], $HoCuP_2$ and $ErCuP_2$ [8]. Furthermore, the phosphides have larger distortions in the P

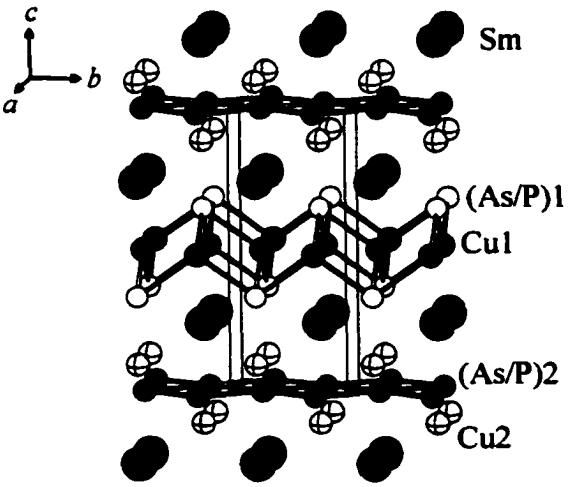

Figure 10. Structure of $SmCu_{1.05}As_{1.67}P_{0.33}$. Occupancy of the Cu2 site is 4.6(6)%.

layer compared to those in the (As/P) layers of orthorhombic RECuAs$_{2-x}$P$_x$ and their structural description is beyond the scope of this paper.

Fig. 11 shows the relative interatomic distances r_{x-x}/d_x in the X layer of the $REMX_2$ pnictides (RE = rare earth; M = Cu, Ag; X = P, As, Sb). For the orthorhombic structures these are the distances projected on the *ab* plane and for the pure phosphides they are the average projected distances. For the copper and silver antimonides the relative Sb-Sb interatomic distances are around 1.05 and the two plots nearly overlap, which means that the *a* and *b* parameters are determined by the size of the Sb atoms and that the Sb atoms are practically in contact. For the arsenide the RECuAs$_2$ and REAgAs$_2$ graphs are now well separated: the size of the Cu and Ag atoms starts to dictate unit cell dimensions in the *ab* plane.

As the relative X-X interatomic distances increase and become close to 1.13, the tetragonal structures undergo orthorhombic distortions. The reason for the change is that the X-X distance, which now depends on the M layer, is much larger than the diameter of the X atoms (i.e., relative X-X

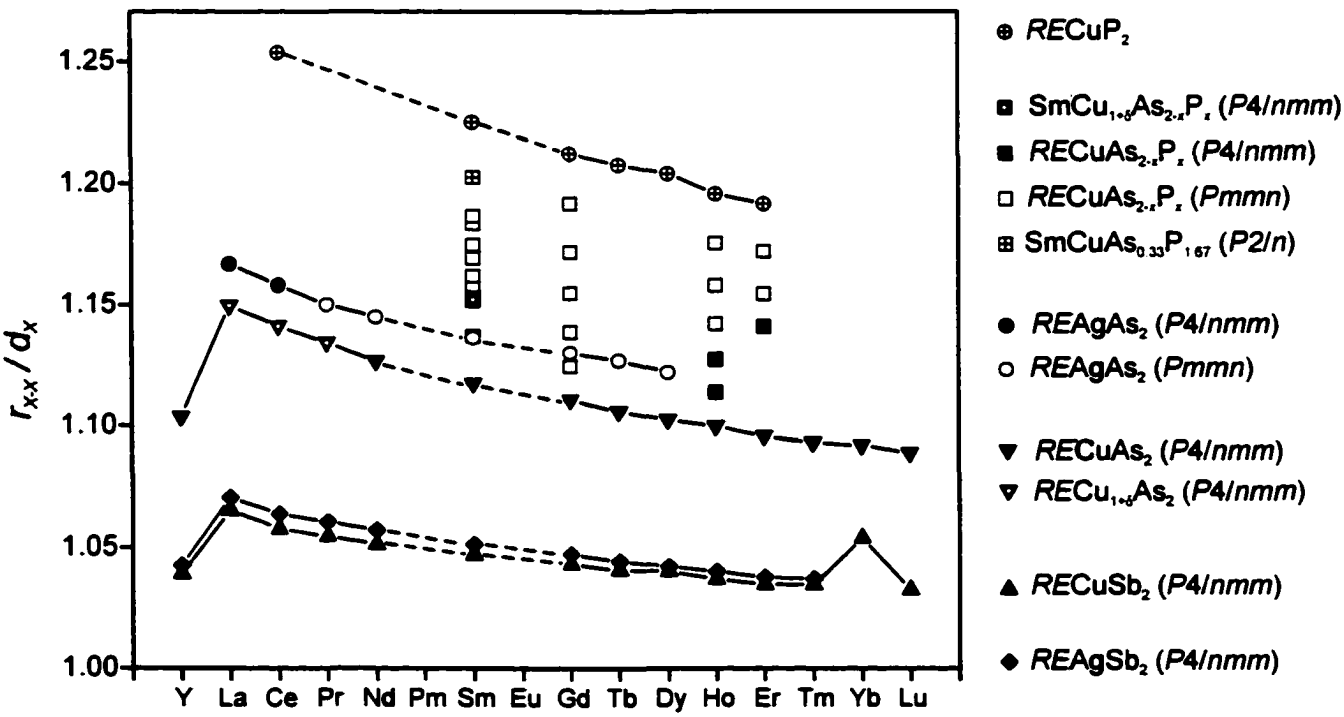

Figure 11. Relative interatomic distances r_{x-x}/d_x in $REMX_2$. r_{x-x}/d_x is the ratio between the average $X2$-$X2$ distance projected on the *ab* plane and the element diameter of X. For RECuAs$_{2-x}$P$_x$ the diameter d_x is the sum of the As and P radii weighted by the composition. The solid symbols denote the tetragonal HfCuSi$_2$-type structures, the open symbols represent the orthorhombic GdCuAs$_{1.15}$P$_{0.85}$-type structures, and the symbols with a cross represent the further distorted structures.

interatomic distances become larger), and the structures distort to adapt to the smaller *X* atoms. In *RE*CuAs$_{2-x}$P$_x$ full substitution of As atoms by P makes the *X* layer (As/P layer) even less dense and around $r_{x-x}/d_x = 1.20$, the orthorhombic structures undergo further distortions.

In Fig. 11 the tetragonal structures are represented by solid symbols, the orthorhombic structures by open ones and the structures of the phosphides by symbols with a cross. There is a separation between the tetragonal and orthorhombic structures and between the orthorhombic structures and the further distorted structures of the phosphides. Interestingly, the tetragonal copper arsenides of La, Ce and Pr, for which $r_{x-x}/d_x > 1.13$, have additional Cu atoms around the As layer[20]. Tetragonal *RE*CuAs$_2$ of the smaller rare-earth elements have not been reported to accommodate interstitial atoms[11,20]. It can be assumed that due to the large rare-earth atoms the relative As-As interatomic distances increase above the stability limit and the tetragonal structures of La, Ce and Pr can either distort to improve the packing or take in some additional atoms to more efficiently fill the space. The structures of La, Ce and Pr follow a second path (LaCu$_{1.23(1)}$As$_2$, CeCu$_{1.01(1)}$As$_2$ and PrCu$_{1.09(1)}$As$_2$) and preserve the tetragonal symmetry.

All known *RE*AgAs$_2$ structures except tetragonal LaAgAs$_2$ and CeAgAs$_2$ [12] are orthorhombicly distorted as expected from their r_{x-x}/d_x values. On the basis of the Cu interstitials in LaCu$_{1.23(1)}$As$_2$, CeCu$_{1.01(1)}$As$_2$ and PrCu$_{1.09(1)}$As and the r_{x-x}/d_x data, the LaAgAs$_2$ and CeAgAs$_2$ structures are likely to have additional Ag atoms around the As layer. Single crystal refinements are needed to test this argument. In the refined NdAgAs$_2$ structure the As2 displacements ($z = 0.9955(6)$) from the horizontal plane are larger than those of Cu ($z = 0.5001(5)$)[12]. It is likely that the B_{1g} normal mode of the As2 atoms, and thus rearrangement of the As layer, play the key role in the *P4/nmm* → *Pmmn* distortion of *RE*AgAs$_2$.

The *REMX*$_2$ structures undergo orthorhombic distortions to increase packing in the smaller *X* layer. However, in the distorted structures the relative *X*-*X* interatomic distances are still large and the *X* atoms are not in contact, although bringing them into closer proximity was the driving force for the symmetry-breaking transitions. These preserved large *X*-*X* separations show a complex interplay of electronic and geometric factors determining phase stability and, obviously, the orthorhombic structures are compromises in this interplay. So far, the lanthanide contraction was not considered. As judged from the slope of the lines in Fig. 11, its role is not important for *RE*AgSb$_2$ and *RE*CuSb$_2$. On the other hand, in the series with smaller *M* or *X* atoms the size of a rare earth starts to have an increased effect on the unit cell dimensions. The structural aspect of this increased influence can be seen in GdCuAs$_{2-x}$P$_x$, HoCuAs$_{2-x}$P$_x$ and ErCuAs$_{2-x}$P$_x$[6,8]. As the size of the rare-earth atom decreases,

distortions from the tetragonal to orthorhombic structures are shifted to higher phosphorus concentrations.

Recently, Seo and Corbett analyzed the factors causing the $SrIn_4$ phase to adopt the monoclinic $EuIn_4$ structure instead of the tetragonal $BaAl_4$-type[21]. The tetragonal $HfCuSi_2$ structure, in which the rare-earth copper or silver pnictides crystallize, can be derived from $BaAl_4$, or vice versa. Seo and Corbett showed that the geometric factors, not electronic ones, and the associated Madelung energy dictate the structures of $SrIn_4$ and $EuIn_4$. Monoclinic structures provide better packing for the Eu^{2+}, Sr^{2+} ions and the In_4^{2-} network, whereas the tetragonal structure is optimal for the larger Ba^{2+} ions. In $REMX_2$ we observe a similar size effect although distortions are different and less drastic.

Conclusions

Application of Landau theory to the *P4/nmm* → *Pmmn* distortions in the *RE*$CuAs_{2-x}P_x$ series showed that the transitions correspond to the one-dimensional irreducible representation B_{1g} and can be continuous. It was shown from group theoretical considerations that these symmetry-breaking transitions are not caused by Peierls instabilities of the square As/P nets: mixing of the crossing bands is not possible through the B_{1g} normal mode. Although second-order Peierls distortions of the tetragonal $HfCuSi_2$-type structures to the orthorhombic $GdCuAs_{1.15}P_{0.85}$-type structures are compatible with the B_{1g} vibration, there is no electronic energy gain upon the distortions, and thus this kind of instability is very unlikely to be a key factor in the transitions.

The *P4/nmm* → *Pmmn* distortions in *RE*$CuAs_{2-x}P_x$ and the structures of *RE*$AgAs_2$ are most likely to be the results of a subtle structural adaptation to the relative sizes of the given atoms. Introducing smaller P atoms in the As layer or replacing the Cu atoms by the larger Ag atoms create mismatches between sizes of the As/P and Cu or Ag layers. Now, better packing is achieved through the atomic rearrangements, mainly through the B_{1g} shifts of the Cu atoms in *RE*$CuAs_{2-x}P_x$ and As atoms in *RE*$AgAs_2$.

In $REMX_2$ a relative interatomic distance in the square net of a main group element *X* can be used to characterize the mismatch between the *X* and *M* layers. If tetragonal *RE*$CuSb_2$, *RE*$AgSb_2$ and *RE*$CuAs_2$ lie below the imaginary borderline, *RE*$AgAs_2$, *RE*$CuAs_{2-x}P_x$ and *RE*CuP_2 have larger relative *X*-*X* interatomic distance and undergo distortions.

Acknowledgement

This research was supported by the Office of the Basic Energy Sciences, Materials Sciences Division, US Department of Energy, DOE. The Ames Laboratory is operated for DOE by Iowa State University under contract No. W-7405-Eng-82.

References

(1) Hulliger, F.; Schmelczer, R.; Schwarzenbach, D. *J. Solid State Chem.* **1977**, *21*, 371-374.

(2) (a) Sfez, G.; Adolphe, C. *Bull. Soc. Fr. Mineral. Cristallogr.* **1972**, *95*, 553-557. (b) Ceolin, R.; Rodier, N.; Khodadad, P. *J. Less-Common Met.* **1977**, *53(1)*, 137-140

(3) Brechtel, E.; Cordier, G.; Schäfer, H. *Z. Naturforsch., B: Anorg. Chem., Org. Chem.* **1979**, *34B*, 251-255.

(4) Hulliger, F.; Schmelczer, R. *J. Solid State Chem.* **1978**, *26*, 389-396. (b) Wittmann, M.; Schmettow, W.; Sommer, D.; Bauhofer, W.; von Schnering, H. G. In *Solid Compounds of Transition Metals VI, International Conf.*: Stuttgart, 1979, p. 217

(5) Miller, G. J.; Li, F.; Franzen, H. F. *J. Am. Chem. Soc.* **1993**, *115*, 3739-3745.

(6) Mozharivskyj, Y.; Kaczorowski, D.; Franzen, H. F. *J. Solid State Chem.* **2000**, *155*, 259-272.

(7) Tremel, W.; Hoffmann, R. *J. Am. Chem. Soc.* **1987**, *109*, 124-140.

(8) Mozharivskyj, Y.; Kaczorowski, D.; Franzen, H. F. *Z. Anorg. Allg. Chem.* **2001**, *627*, 2163-2172.

(9) Mozharivskyj, Y.; Pecharsky, A. O.; Bud'ko, S. L.; Franzen, H. F. *submitted to Z. Anorg. Allg. Chem.*

(10) Bodnar, R. E.; Steinfink, H. *Inorg. Chem.* **1967**, *6*, 327-330.

(11) Brylak, M.; Möller, M. H.; Jeitschko, W. *J. Solid State Chem.* **1995**, *115*, 305-308.

(12) Demchyna, R. O.; Kuz'ma, Y. B.; Babizhetsky, V. S. *J. Alloys Compd.* **2001**, *315*, 158-163.

(13) Ren, J.; Liang, W.; Whangbo, M.-H., Crystal and Electronic Structure Analyser (CAESAR), North Carolina State University, Raleigh, NC, 1998.

(14) Alvarez, S. "Table of Parameters for Extended Hückel Calculations," Barcelona, 1987.

(15) Landau, L. D.; Lifshits, E. M. *Statistical Physics*; Pergamon Press: London, 1958; Vol. 5.

(16) Franzen, H. F. *Physical Chemistry of Solids*; World Scientific: Singapore, 1994.

(17) Franzen, H. F. *Chem. Mater.* **1990**, *2*, 486-491.

(18) Sologub, O.; Noël, H.; Leithe-Jasper, A.; Rogl, P.; Bodak, O. I. *J. Solid State Chem.* **1995**, *115*, 441-446.

(19) Sologub, O.; Hiebl, K.; Rogl, P.; Noël, H.; Bodak, O. *J. Alloys Compd.* **1994**, *210*, 153-157.

(20) Wang, M.; McDonald, R.; Mar, A. *J. Solid State Chem.* **1999**, *147*, 140-145.

(21) Seo, D.-K.; Corbett, J. D. *J. Am. Chem. Soc.* **2000**, *122*, 9621-9627.

CHAPTER 9. CONCLUSIONS

The structural changes in the *RE*CuAs$_{2-x}$P$_x$ phases (*RE* = Sm, Gd, Ho and Er, see Table) represent the complexity of interactions in the solid state. Each structure is a fine balance of the electronic, Coulomb and geometric factors that contribute to the Gibbs free energy. A change in intensive variables can break the balance and lead to a phase transition. It can be a difficult task to answer why a particular structure is formed during a transition, since there is no theoretical framework that handles all the above mentioned factors. However, it is usually possible to determine a factor that is dominant during the specific phase transition and determines the stability of the newly formed structure as compared to the old structure. The *RE*CuAs$_{2-x}$P$_x$ phases, because of the variation in the chemical content (As/P substitution), allow, with the aid of band structures, Madelung energies and Landau theory, a partial unraveling of the factors important in the symmetry-breaking transitions in the *RE*CuAs$_{2-x}$P$_x$ series.

1. Energetically Driven Distortions

1.1. P4/nmm → Pmmn Transitions

The tetragonal-to-orthorhombic transitions occur in all *RE*CuAs$_{2-x}$P$_x$ series studied. While the arsenides and arsenophosphides with small P concentrations crystallize with the HfCuSi$_2$-type structure (*P4/nmm* space group), the arsenophosphides with larger P amounts adopt the GdCuAs$_{1.15}$P$_{0.85}$-type structure (*Pmmn* space group). The *P4/nmm* → *Pmmn* transitions originate from the B_{1g} vibrational mode and are structural adaptations to smaller P atoms. These transitions provide tighter atomic packing and *better Coulomb interactions*.

Stability of the tetragonal *RE*CuAs$_{2-x}$P$_x$ and other *REMX*$_2$ phases with respect to the orthorhombic distortion can be characterized by a relative interatomic distance *r/d* in the As/P or *X* layer. *r/d* is the ratio between the average As/P-As/P or *X*2-*X*2 distance projected on the *ab* plane and the element diameter of As/P or *X*. While the tetragonal phases have small relative As/P-As/P or *X*-*X* interatomic distances, the orthorhombic phases have larger distances.

1.2. Distortions of the P Nets in the Phosphides

Full substitution of As atoms by P in *RE*CuAs$_{2-x}$P$_x$ results in further distortions of the originally tetragonal structures. The largest changes are observed in the P nets, and the new structures are different for each rare-earth (Table). Distortions of the P layers in SmCu$_{1.15}$P$_2$, GdCuP$_{2.20}$ and

$ErCuP_2$ are usefully thought of as Peierls-type distortions, i.e., they lower the *electronic (and total) energy* through opening band gaps and lead to more stable structures.

Table. Structural data of the $RECuAs_{2-x}P_x$ phases

Structure type	Space group	Supercell (tetr. cell as a basis)	Composition	Lattice parameters, Å		
				a	*b*	*c*
$HfCuSi_2$ or $CeCu_{1.10}As_2$ (stuffed $HfCuSi_2$)	*P4/nmm*	a_{tet}, b_{tet}, c_{tet}	$SmCu_{1+\delta}As_{2-x}P_x$ (x = 0-1.33)	3.8602-3.9458		9.853-9.964
			$GdCuAs_2$	3.9112		9.930
			$HoCuAs_{2-x}P_x$ (x = 0-0.67)	3.8204-3.8726		9.765-9.821
			$ErCuAs_{2-x}P_x$ (x = 0-1)	3.8623-3.7918		9.794-9.719
$GdCuAs_{1.15}P_{0.85}$ or $SmCu_{1.1}AsP$ (stuffed $GdCuAs_{1.15}P_{0.85}$)	*Pmmn*	$a_{ort} = a_{tet}$, $b_{ort} = b_{tet}$, $c_{ort} = c_{tet}$	$SmCu_{1+\delta}As_{2-x}P_x$ (x = 0.89-1.44)	3.830-3.868	3.850-3.882	9.880-9.913
			$GdCuAs_{2-x}P_x$ (x = 0.33-1.67)	3.793-3.883	3.812-3.890	9.822-9.908
			$HoCuAs_{2-x}P_x$ (x = 1-1.67)	3.740-3.788	3.761-3.803	9.699-9.741
			$ErCuAs_{2-x}P_x$ (x = 1.33-1.67)	3.731-3.755	3.748-3.768	9.683-9.697
$SmCuP_2$	*P2/n*	$a_{mon} = a_{tet}$, $b_{mon} = b_{tet}$, $c_{mon} = c_{tet}$	$SmCuAs_{2-x}P_x$ (x = 1.67-2) and $SmCuP_{2.3}$	3.812-3.836	3.8188-3.8429	9.806-9.827 γ=90.59-90.13°
$CeCu_{1.12}P_{1.97}$	*Cmmm*	$a_{ort} = (a_{tet}+b_{tet})$, $b_{ort} = 2c_{tet}$, $c_{ort} = (a_{tet} - b_{tet})$	$SmCu_{1-\delta}P_2$ (δ = 0.12-0.20)	5.433-5.453	19.47-19.51	5.433-5.439
$GdCuP_{2.20}$	*Pmm2*	$a_{ort} = (a_{tet} - b_{tet})$, $b_{ort} = (a_{tet} + b_{tet})$, $c_{ort} = c_{tet}$,	$GdCuP_{2.16}$-$GdCuP_{2.20}$	5.3747-5.3284	5.3830-5.3868	9.7375-9.7487
$HoCuP_2$	*Cmma*	$a_{ort} = (a_{tet} - b_{tet})$, $b_{ort} = (a_{tet} + b_{tet})$, $c_{ort} = c_{tet}$,	HoCuP2	5.2612	5.3088	9.655
$ErCuP_2$	$P2_1/n$	$a_{mon} = a_{tet}$, $b_{mon} = 2c_{tet}$, $c_{mon} = -b_{tet}$	$ErCuP_2$	3.725	19.276 β=90.46°	3.724

2. Role of the Entropy Factor

2.1. Configurational Contribution

The importance of the entropy contribution to the Gibbs free energy and thus its effect on atomic arrangement in the structure can be easily traced in the *RE*CuAs$_{2-x}$P$_x$ arsenophosphides. A configurational contribution to the entropy is crucial in stabilizing the mixed occupancy in the arsenophosphides. While geometric and electronic factors favor separation of the As and P atoms over two different crystallographic sites, *configurational entropy* stabilizes the As/P mixing on these two sites.

2.2. High Temperatures

As discussed in Chapter 1, the entropy factor becomes dominant at high temperatures. Since in a symmetry-breaking transition the high-symmetry structures have larger entropies than the low-symmetry structures, raising the temperature will always stabilize the high-symmetry structure, provided the high-symmetry structure does not undergo further transformation at high temperature and this temperature can be reached during the experiment. While performing the high-temperature X-ray powder diffraction on the GdCuP$_{2.16}$ phase (*Pmm*2 space group), we observed large changes in one of the lattice parameters at 600 and 700°C, that indicate a tendency toward a structural transformation at still higher temperatures. However, due to the experimental limitations we could not reach temperatures higher than 700°C.

3. Landau Theory and Symmetry-Breaking Transitions in *RE*CuAs$_{2-x}$P$_x$

The progress in the research on the *RE*CuAs$_{2-x}$P$_x$ series was dependent upon the ability of Landau theory to predict, explain and dismiss structural models and transitions. The *Pmmn* space group (arising from the B_{1g} vibrational mode) in all mixed arsenophosphides and the existence of these mixed arsenophosphides followed from the analysis of GdCuAs$_2$ and GdCuP$_2$, using Landau theory. The continued failure to obtain the high-symmetry structure (*P*4/*nmm*) and the low symmetry structure (*Pnmm*) coexisting at the same temperature led to the conclusion, later experimentally proven, that the tetragonal structures of the SmCu$_{1+\delta}$As$_{2-x}$P$_x$ arsenophosphides are stabilized by additional Cu atoms. On the other hand, the coexistence of the two structures with the *P*2/*n* and *Cmmm* symmetries at the SmCu$_{1.1}$P$_2$ and SmCu$_{1.16}$P$_2$ samples indicated that the structural change from the SmCuP$_2$ structure (*P*2/*n*) to the SmCu$_{1.15}$P$_2$ structure (*Cmmm*) is first-order and that this transition does not occur continuously upon introducing Cu atoms into the SmCuP$_2$ structure.

Although Landau theory cannot explain the energetic factors important in a symmetry-breaking transition, it can provide knowledge about the transition (nature, symmetry, irreducible representation of the transition) which, when combined with other theoretical techniques, can lead to unraveling of these factors. Landau theory coupled with the consideration of band structure and Coulomb interaction was successful in determining the forces that drive the $P4/nmm \rightarrow Pmmn$ transitions. Detailed analysis revealed that these tetragonal-to-orthorhombic deformations do not result from the Peierls-type instability of the square As/P nets, but are governed by the atomic sizes and Coulomb interaction.

APPENDIX A. MODULATED CRYSTAL STRUCTURE AND ELECTRONIC PROPERTIES OF SEMICONDUCTOR $Cu_{47}Si_{91}P_{144}$

A paper published in Zeitschrift für anorganische und allgemeine Chemie
Z. Anorg. Allg. Chem. **2000**, *626*, 2153

Yurij Mozharivskyj[a], Olaf Lang[b] and Hugo F. Franzen[a]
[a] *Department of Chemistry and Ames Laboratory of US DOE, Spedding Hall, Iowa State University, Ames, Iowa 50011, USA*
[b] *Institut für Anorganische Chemie und Analytische Chemie, Universität Mainz, Duesberg Weg 14-16, 55099 Mainz, Germany*

Abstract

Crystals of the copper silicon phosphide were synthesized by the iodine gas transport technique. The x-ray single crystal methods revealed a big superstructure with the lattice parameters $a=b=44.510$ and $c=20.772$Å and a basic tetragonal substructure with $a=3.7092$ and $c=5.1930$Å. Analysis of the intensities showed that the superstructure has a ½,½,½ tetragonal substructure with $a=22.255$ and $c=10.386$Å. This ½,½,½ substructure ($Cu_{47}Si_{91}P_{144}$) and the basic tetragonal structure ($Cu_{0.71}Si_{1.29}P_2$) were solved by the direct methods and refined in the $I\bar{4}m2$ space group. The phosphide is a semiconductor with a small energy gap of 0.0269(1)eV. The electrical properties are considered in terms of Anderson localization. The density of states was calculated using the extended Hückel tight binding method.

Keywords: silicon copper phosphide; modulated superstructure; semiconductor; Anderson localization; band structure.

1. Introduction

In 1961 two new ternary phosphides $CuSi_2P_3$ and $CuGe_2P_3$ which crystallized with the zinc blende (sphalerite) structure ($F\bar{4}3m$) were reported [1]. Both compounds had Cu and Si or Cu and Ge statistically mixed in ratio 1:2 and could be described with the general formula $A^IB^{IV}{}_2C^V{}_3$. The $A^IB^{IV}{}_2C^V{}_3$ phases have 4 electrons per atom with each atom tetrahedrally coordinated and, based upon electron counting, they should be semiconductors as are $A^{II}B^{VI}$ or $A^{III}B^V$ compounds [1]. Further

investigations of $CuGe_2P_3$ [2,3] were focused on its thermal lattice expansion and elastic behavior. The resistivity measurements proved $CuGe_2P_3$ to be a semiconductor with an energy gap of 0.90(5)eV [4]. The $CuSi_2P_3$ phosphide was not so well studied. Only the solubility of silicon in $CuSi_2P_3$ and a high melting point (1451K) for $CuSi_2P_3$ were reported [5]. The $CuSi_2P_3$ phosphide was considered to be a semiconductor as is $CuGe_2P_3$, but the energy gap was not determined. Also, a new silicon-rich phase, $CuSi_4P_3$, was obtained by a modified Bridgmann method melt growth technique and the thermal lattice expansion of this compound was measured between 299 and 784K [5]. The crystal structures of all phosphides were assumed to be cubic zinc blende and no further research on the atomic distribution of Cu, P and Ge or Si was performed. If in $CuSi_2P_3$ [1] the Cu and Si atoms are considered to occupy one site, in $CuSi_4P_3$ [5], which has the same zinc blende structure, the Cu and P atoms must now statistically share a common position or at least two different mixtures Cu+Si and Si+P on two different sites must exist. In the compound with a statistical mixture of site occupation at high temperatures, there is always a possibility of partial or complete ordering which would result in the superstructure or modulated structure at low temperatures. Should such a process occur in $CuSi_2P_3$, this would lead to separation of Cu and Si atoms on different sites.

The structure of nickel silicon phosphide presents an interesting case. A composition $Ni_{1.68}Si_{0.88}P_3$ [6] was reported for one of the seven ternary phases in the Ni-Si-P system [7]. Further studies of the same structure were done by the authors [8] who, using the same single crystal data set, were able to refine the structure with the two compositions $Ni_{1.282(4)}Si_{1.284(5)}P_3$ and $NiSi_2P_3$ to the very low R-factors 0.023 and 0.021, respectively. Using EDAX results and oxidation numbers (ON) they chose the composition $NiSi_2P_3$ to be the correct one. If an ON of –3 is assumed for phosphorus as the most electronegative element in $Ni_{1.282(4)}Si_{1.284(5)}P_3$, +4 for silicon, the nickel atoms are assigned an unusually high oxidation state of +3.88. However, this counting scheme yields a good result for $NiSi_2P_3$: -3 for P, +4 for Si and +1 for Ni. As was shown later [9], the conventional counting scheme, when applied to the intermetallic compounds, may lead to wrong conclusions. In the nickel silicon phosphide the *d*-orbitals of Ni are a little lower in energy than the *p*-orbitals of P and considerably lower than the *p*-orbitals of Si [9]. The *d*-band of Ni must be completely full and assigning the ON of +3.88 to the nickel atoms in $Ni_{1.282(4)}Si_{1.284(5)}P_3$ is unreasonable. Therefore, oxidation numbers are not always efficient in making the choice of a composition. Other methods need to be employed instead.

The low energy of the *3d*-orbitals accounts for the partial substitution of P by Co in $Hf_5Co_{1+x}P_{3-x}$ [10, 11]. The Co atoms, like the P atoms, act as a Lewis base, while the Hf atoms with high lying *5d*-orbitals can be considered as a Lewis acid, which provides electrons to Co and P. As a result the Co *d*-band is completely full and the Co atoms can be assigned a formal charge of -1. An

opposite substitution process is found in Hf_2NiP [12]. In the original HfNi compound half of the Ni atom sites are now occupied by P atoms. The introduction of the more electronegative phosphorus removes electrons from the Hf *5d*-orbitals, but the Ni *3d*-orbitals remains well below the Fermi level.

In this light the investigation of the crystal structure and electronic properties of $CuSi_2P_3$ was a fascinating task.

2. Experimental Part

2.1. Preparation

The powders of Cu (Alfa, 99.5%), Si (Alfa, 99.9%) and P(Alfa, 99%) in the ratio 1:2:3 with a total mass of 1g were intimately mixed and pressed in a glove box under an argon atmosphere. The sample was then sealed with 45mg of iodine in an evacuated silica tube (200mm length and 12mm inner diameter). The ampoule was placed for 10 days in the two-zone furnace (800–900°C) with the sample being in the cold end. Then the ampoule was furnace cooled and opened in the air. In the hot zone of the tube there were some crystals with a graphite-like luster of a practically spherical form.

2.2. X-ray Structure Determination

Suitability of crystals for the structure analysis was tested by the Laue method. A crystal in the form of a sphere (diameter 0.06mm) with sharp diffraction spots was chosen for a further investigation. The diffraction pattern of that crystal, as well as others, was very rich, indicating a possible complexity of the structure. The four-fold axis and four mirror planes along it were located by the Laue technique, the results were consistent with the Laue group 4/mmm along this direction. A very detailed analysis of the diffraction pattern revealed that the four-fold axis and mirror planes were pseudo-symmetry elements. While the strong and medium reflections fit perfectly into these symmetry elements, there were differences among the intensities of very weak "symmetry equivalent" reflections. A rotation photograph presented another surprise: the compound had a big superstructure. The strong reflections corresponded to a cell with a=5.22Å and the weak reflections gave a 12-fold larger periodicity with a=62.64Å. There was also some periodicity among the weak superstructure reflections. They could be divided into two groups, some were more intense with 6-fold multiplication of the subcell, while others, corresponding to 12-fold multiplication, were less intense. The superstructure could be considered to be a commensurate modulated structure along the a direction.

The intensity data set was collected at the SIEMENS SMART diffractometer with a two dimensional CCD detector. The reflections could be indexed in the tetragonal unit cell with a=

44.510 and c=20.772Å. The relation $a\sqrt{2}$ (a=44.510Å) with the previously found a value of 62.64Å indicated that the rotation photograph has been taken along the *ab* face diagonal. If only the strong and medium reflections of the data set were considered, the unit cell was found to be tetragonal with a= 3.7092 and c=5.1930 Å, but not cubic face-centered as originally thought. Some single crystals were ground and their x-ray diffraction pattern was recorded in a Guinier camera. Splittings of the peaks at 49° and 59° indicated that the structure is tetragonal (Fig.1). The lattice parameters were derived by the least squares procedure using Si as an internal standard and they had the values a=3.7076(7) and c=5.196(2) Å for the small tetragonal cell.

The weak superstructure reflections from the collected data set could be divided into two groups, as before, one set weaker and the other stronger. The stronger superstructure reflections gave a cell with a=b=22.255 and c=10.386Å, while weaker superstructure reflections doubled this cell to a=b=44.510 and c=20.772Å. For the sake of clarity in further discussion the cell with a=b=22.255 and c=10.386Å will be referred to as a ½,½,½ supercell, the cell with a=b=44.510 and c=20.772Å as a complete supercell or simply supercell and the smallest cell with a=b=3.7092 and c=5.1930Å as a subcell.

The subcell structure could be directly solved and easily refined in the tetragonal symmetry (Table 1a, 2, 3) using SHELXTL program package [13], the only anomaly was an unusually large extinction coefficient (0.51). The structure refinement to R_I = 0.0198 resulted in the $Cu_{0.71}Si_{1.29}P_2$ composition.

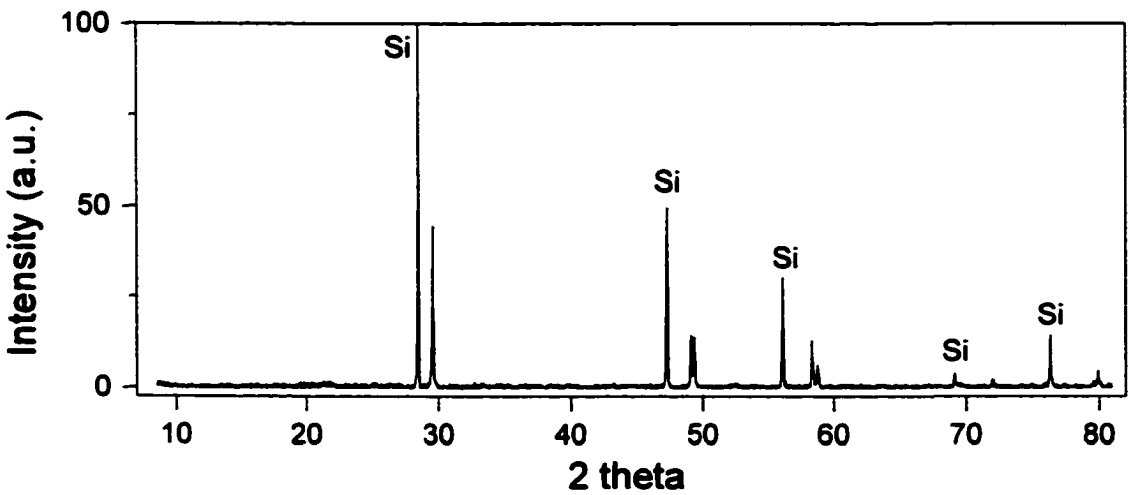

Figure 1. Guinier powder pattern (laser scanned and reproduced as diffractogram) with silicon as an internal standard. Super structure reflections are not clearly seen here because of the small amount of the crystal used.

Table 1. Crystal Data and Structure Refinements (T=293(2) K, MoK_α - Radiation, 2θ Range for the Data Collection was 2.58 to 57.24°, the Refinement Method was Full-Matrix Least-Squares on F^2)

	a	b
Empirical formula	$Cu_{0.71}Si_{1.29}P_2$ subcell	$Cu_{47}Si_{91}P_{144}$ ½,½,½ supercell
Space group	$I\bar{4}m2$ (No.119)	$I\bar{4}m2$ (No.119)
Unit cell dimensions	a = 3.7092(5) Å	a = 22.255(5) Å
	c = 5.1930(10) Å	c = 10.386(4) Å
Z	1	1
Density (calculated)	3.331 g/cm^3	3.235 g/cm^3
Index ranges	-4<=h<=4, -4<=k<=4, 6<=l<=5	-29<=h<=28, -26<=k<=29, -13<=l<=11
Reflections collected	225 [$R\sigma$ = 0.0289]	16290 [$R\sigma$ = 0.0648]
Absorption correction	empirical from ψ-scan	empirical from ψ-scan
Independent reflections	56 [*Rint* = 0.0560]	3218 [*Rint* = 0.1056]
Reflections with $I>2\sigma(I)$	56	575
Completeness to max 2θ	100.0 %	95.9 %
Data / restraints / par.	56 / 0 / 7	3218 / 0 / 96
Goodness-of-fit on F^2	1.177	0.803
Final R indices [$I>2\sigma(I)$]	R_1 = 0.0198, wR_2 = 0.0445	R_1 = 0.0564, wR_2 = 0.1989
R indices (all data)	R_1 = 0.0198, wR_2 = 0.0445	R_1 = 0.2094, wR_2 = 0.2674
Extinction coefficient	0.51(11)	0.00033(2)
Largest diff. peak and hole	0.226 and -0.581 e./Å^3	0.654 and -0.569 e./Å^3

Rint = $\Sigma|Fo^2-Fo^2mean|/\Sigma Fo^2$
$R\sigma = \Sigma\sigma Fo^2/\Sigma Fo^2$
$R_1 = \Sigma||Fo|-|Fc||/\Sigma|Fo|$
$R_w = (\Sigma w\times(Fo^2-Fc^2)^2 / \Sigma w\times(Fo^2)^2)^{1/2}$, $w = 1/(\sigma^2(Fo^2)+(a\times P)^2+b\times P)$
GooF = $(\Sigma w\times(Fo^2-Fc^2)^2 / (n-p))^{1/2}$ *with* $w = 1/(\sigma^2(Fo^2)+(a\times P)^2+b\times P)$, *n-number of observed reflections, p-number of parameters refined*

The analysis of the superstructure reflections for the ½,½,½ supercell indicated that their intensities corresponded well to the tetragonal cell, on the other hand, the superstructure reflections for the complete supercell could not be fit into a tetragonal cell. The presence of the weak superstructure reflections has complicated a space group choice, several space groups have been tested for the ½,½,½ supercell but only one ($I\bar{4}m2$) yielded a structure solution by the direct method and has given a reasonable structure (Table 1b, 4, 5) with a composition $Cu_{47}Si_{91}P_{144}$.

From the Laue photograph and the diffractometer intensity data no symmetry elements, except $\bar{1}$ due to centrosymmetric nature of the reciprocal space, could be found for the complete

supercell with $a=b=44.510$ and $c=20.772$Å and that left only the two space groups P1 and $P\bar{1}$ for consideration. The number of atoms in the asymmetric unit of the centrosymmetric case would exceed 1100, and in the non-centrosymmetric case it would be doubled. So far, we have not been able to refine that number of atoms successfully. Another difficulty was that the reflections for the complete superstructure were close to the very strong subcell reflections and their intensities were increased by overlap with these subcell reflections. Probably, a refinement technique, utilizing a modulated approach instead of the conventional one, would be more successful here.

To test the correctness of the ½,½,½ superstructure, the subcell reflections (h,k,l are multiplicands of 6, 6 and 2 simultaneously) were removed from the reflection array and the structure was refined to R_I=0.0946 with 3121 superstructure reflections only. The composition has changed a little from $Cu_{47}Si_{91}P_{144}$ to $Cu_{51}Si_{90}P_{144}$ but there were no significant shifts (more than 3 standard deviation) in the atomic positions. The refinement results supported our structural model for the ½,½,½ supercell.

Since during the single crystal growth the composition of the crystals obtained may deviate from the starting composition, a compound with a statistical mixture of Cu and P instead of Cu and Si as in $Cu_{47}Si_{91}P_{144}$, would also be possible for the product of the gas transport reaction. After the Si

Table 2. Atomic Coordinates and Anisotropic Displacement Parameters for $Cu_{0.71}Si_{1.29}P_2$.

Atom	Wyckoff symbol	x	y	z	U^{11}	U^{22}	U^{33}	U_{eq}, Å^2
Si*	2c	0	1/2	1/4	0.011(1)	0.011(1)	0.012(1)	0.011(1)
P	2a	0	0	0	0.009(1)	0.009(1)	0.009(1)	0.009(1)

* - 64.4% Si and 35.6(5)%Cu

The anisotropic displacement factor exponent takes the form: $-2\pi^2 [h^2 a^{*2} U^{11} + ... + 2 h k a^* b^* U^{12}]$; $U^{23} = U^{13} = U^{12} = 0$.

U_{eq} is defined as one third of the trace of the orthogonalized U^{ij} tensor.

Table 3. Interatomic Distances and Bond Angles in $Cu_{0.71}Si_{1.29}P_2$.

Atom	Atom	Distance, Å
Si	4P	2.2638(3)
P	4Si	2.2638(3)
Bond		**Angle**
P – Si – P		109.200(6)
P – Si – P		110.015(13)
Si – P – Si		109.200(6)
Cu – P – Si		110.015(13)

and P atoms were exchanged, the structure was refined with the same reflection data set to the formula $Cu_{42}P_{86}Si_{144}$. The *R*-factors ($R_1 = 0.0574$, $wR_2 = 0.2607$) and atomic positions were very close to those of $Cu_{47}Si_{91}P_{144}$, but the possibility of $Cu_{42}P_{86}Si_{144}$ was excluded by the energy dispersive analysis of x-rays.

The phosphide was assigned a final composition $Cu_{47}Si_{91}P_{144}$, which corresponds to the ½,½,½ supercell, the largest successfully refined structural model. Although the real composition of the compound, *i.e.* of the supercell with $a=b=44.510$ and $c=20.772$Å may deviate somewhat from $Cu_{47}Si_{91}P_{144}$, this formula is taken to represent the phosphide.

Table 4. Atomic Coordinates and Equivalent Isotropic Displacement Parameters for $Cu_{47}Si_{91}P_{144}$.

Atom	Wyckoff symbol	Occupancy, %	x	y	z	U_{eq}, Å^2
Si(1)	16j	87.8Si/12.2(6)Cu	0.9174(2)	0.6669(3)	0.8746(5)	0.011(2)
Si(2)	16j	31.9Si/68.1(7)Cu	0.9170(1)	0.8332(2)	0.8745(4)	0.020(1)
Si(3)	16j	84.7Si/15.3(7)Cu	0.8335(3)	0.9171(2)	0.6261(5)	0.012(2)
Si(4)	16j	42.2Si/57.8(5)Cu	0.7497(2)	0.6667(2)	0.8785(4)	0.011(1)
Si(5)	16j	83(1)Si	0.7482(4)	0.8330(6)	0.8672(7)	0.021(2)
Si(6)	16j	32.7Si/67.3(7)Cu	0.5840(1)	0.8334(2)	0.8749(4)	0.020(1)
Si(7)	8i	52.6Si/47.4(9)Cu	0.9183(3)	0	0.3740(7)	0.015(2)
Si(8)	8i	100	0.9137(4)	0	0.8742(11)	0.014(3)
Si(9)	8i	51.1Si/48.9(6)Cu	0.7527(3)	0	0.8790(6)	0.012(2)
Si(10)	8i	64(1)Si	0.7454(7)	0	0.3666(14)	0.011(4)
Si(11)	8i	48Si/52(1)Cu	0.5848(3)	0	0.3740(7)	0.019(2)
Si(12)	8i	100	0.5800(4)	0	0.8743(12)	0.015(3)
P(1)	16j	100	0.9165(3)	0.9171(3)	0.7503(8)	0.016(2)
P(2)	16j	100	0.9162(2)	0.7495(3)	0.7495(5)	0.014(2)
P(3)	16j	100	0.8343(3)	0.6681(3)	0.9998(4)	0.016(1)
P(4)	16j	100	0.7501(3)	0.9169(2)	0.7500(6)	0.016(2)
P(5)	8i	100	0.8348(5)	0	0.0031(8)	0.016(2)
P(6)	8i	100	0.8318(4)	0	0.4961(8)	0.014(2)
P(7)	8i	100	0.6685(4)	0	0.5023(8)	0.013(2)
P(8)	8i	100	0.6652(4)	0	0.9974(8)	0.017(2)
P(9)	8h	100	0.9162(3)	0.4162(3)	3/4	0.018(2)
P(10)	8h	100	0.7506(3)	0.2506(3)	3/4	0.019(2)
P(11)	8h	100	0.4168(3)	0.9168(3)	3/4	0.017(3)
P(12)	8g	100	0.8320(3)	0.8320(3)	0	0.014(2)
P(13)	8g	100	0.6648(3)	0.6648(3)	0	0.013(2)
P(14)	4f	100	0	1/2	0.9959(13)	0.015(3)
P(15)	2b	100	0	0	1/2	0.015(4)
P(16)	2a	100	0	0	0	0.014(4)

Table 5. Interatomic Distances in $Cu_{47}Si_{91}P_{144}$.

Atom	Atom	Distance, Å	Atom	Atom	Distance, Å
Si(1) -	P(2)	2.252(9)	Si(6) -	P(7)	2.263(6)
	P(9)	2.258(8)		P(11)	2.264(7)
	P(3)	2.260(7)		P(4)	2.265(8)
	P(8)	2.269(7)		P(3)	2.280(6)
Si(2) -	P(5)	2.243(6)	Si(7) -	P(15)	2.241(7)
	P(1)	2.268(8)		2P(1)	2.263(8)
	P(2)	2.272(8)		P(6)	2.305(11)
	P(12)	2.297(6)	Si(8) -	P(5)	2.208(14)
Si(3) -	P(13)	2.245(7)		2P(1)	2.250(10)
	P(1)	2.253(9)		P(16)	2.322(10)
	P(4)	2.259(10)	Si(9) -	P(5)	2.236(11)
	P(6)	2.287(7)		2P(4)	2.284(7)
Si(4) -	P(3)	2.265(7)		P(8)	2.303(11)
	P(13)	2.272(6)	Si(10) -	P(7)	2.217(16)
	P(2)	2.273(7)		2P(2)	2.223(9)
	P(10)	2.274(7)		P(6)	2.346(18)
Si(5) -	P(4)	2.224(12)	Si(11) -	2P(9)	2.266(7)
	P(10)	2.229(12)		P(14)	2.273(10)
	P(3)	2.257(9)		P(7)	2.290(11)
	P(12)	2.319(10)	Si(12) -	P(14)	2.234(14)
				2P(11)	2.259(10)
				P(8)	2.287(15)

2.3. Semiquantitative Microprobe Analyses

Semiquantitative microprobe energy dispersive analysis of x-rays (EDAX) was performed in a Philips PSEM 500 scanning electron microscope equipped with a KEVEX energy dispersive spectroscopy detector. Data acquisition was performed with an accelerating voltage of 20 kV and a 1 min accumulation time. The analysis of three crystals revealed copper, silicon and phosphorus in an approximate ratio 1:2:3.

2.4. Resistance Measurements

Single crystal conductivity was measured with a computer automated setup by the standard DC two probe technique. Electrode connections to the crystals were made with the use of 50 μm silver wires and indium solder. Samples were cooled in a He flow cryostat. The temperature was measured between 285K and 12K with a LakeShore DT 470 silicon diode temperature sensor located

close to the crystal. No indication of thermal hysteresis was observed, and the sample showed a good temperature equilibrium throughout the measurement cycle. The steps at the resistivity curve (Fig.2) are due to the changes in the sensitivity ranges of the used equipment.

3. Results and Discussion

3.1. Electrical Conductivity and Electronic Structure

The $Cu_{47}Si_{91}P_{144}$ phosphide is a semiconductor with a band gap of 0.0269(1)eV if only one type of carrier is important in the charge transfer in the crystal. If we assume that the compound has a completely filled valence band and empty conduction band, the valence shell of the atoms must be closed (octet rule) and there must be 4 electrons per atom. If a compound consists of three elements A^I, B^{IV} and C^V (where numbers indicate the number of electrons donated to the valence band or to make bonds) and A^I, B^{IV} or A^I, C^V are statistically mixed, there are only two possibilities for the compound to be a semiconductor. One is $A^IB^{IV}{}_2C^V{}_3$ [1], and the other is $A^IC^V{}_3B^{IV}{}_4$ or $A^IB^{IV}{}_4C^V{}_3$ which is realized in $CuSi_4P_3$ [5]. In applying the formulas $A^IB^{IV}{}_2C^V{}_3$ and $A^IB^{IV}{}_4C^V{}_3$ to the copper silicon phosphides we assume that the Cu d-band is fully occupied (d^{10}) and the copper atoms give only one electron to "produce bonds". This approach is based on the orbital energies (Table 6) [14] and, as will be shown later, is consistent with band structure calculations.

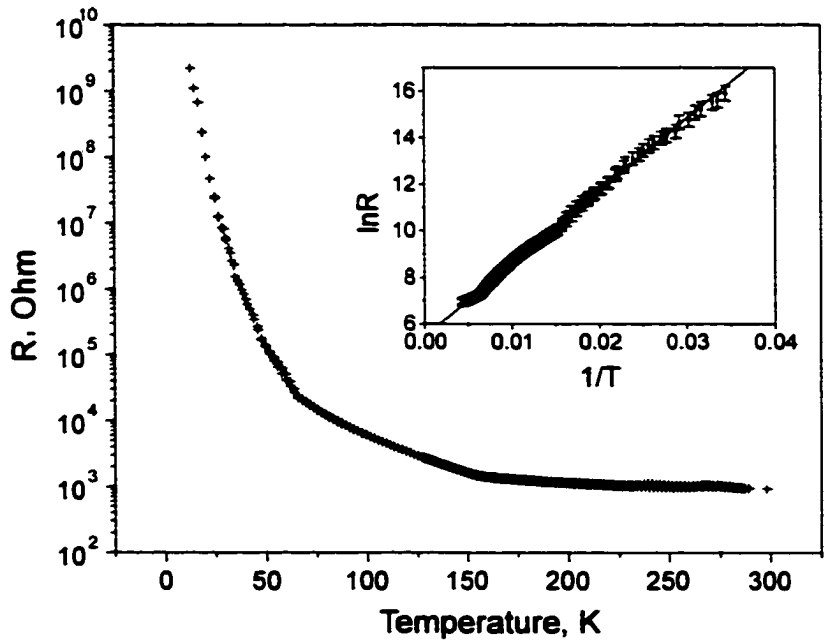

Figure 2. Electrical resistance of a single crystal of the copper silicon phosphide.

Table 6. Parameters for the Extended Hückel Tight-Binding Calculations

Atom	Orbital	H_{ii}, eV	ξ_1	c_1[a]	ξ_2	c_2[a]
P	3s	-18.6	1.75	1.00		
P	3p	-14.0	1.30	1.00		
Si	3s	-17.3	1.383	1.00		
Si	3p	-9.20	1.383	1.00		
Cu	4s	-11.4	2.20	1.00		
Cu	4p	-6.06	2.20	1.00		
Cu	3d	-14.0	5.95	0.5933	2.30	0.5744

[a] coefficients used in the double-zeta Slater-type orbitals

In our case the x-ray structure refinements have yielded the two solutions: $Cu_{47}Si_{91}P_{144}$ ($Cu_{0.98}Si_{1.90}P_3$) and $Cu_{42}P_{86}Si_{144}$ ($Cu_{1.17}P_{2.39}Si_4$), both of which deviate from the ideal compositions $CuSi_2P_3$ and CuP_3Si_4. The EDAX results supported only the $Cu_{47}Si_{91}P_{144}$ composition in which the ratio Cu:Si:P is close to the experimentally observed one 1:2:3. The deviation from the $Cu_{48}Si_{96}P_{144}$ ($CuSi_2P_3$) composition gives a lower electron count than expected: (47x1+91x4+144x5)/288=3.93. Thus, the valence band is not completely filled but the compound is a semiconductor with the small energy gap. Deficiency of electrons and small energy gap are characteristics of p-type extrinsic semiconductors: *e.g.* Si with the group III impurities such as B (0.044eV), Al (0.069eV) and Ga (0.073eV) [15]. In this type of semiconductor the concentration of the second element is very low, in our case none of the elements can be considered as an impurity.

On the other hand, we could assume that x-ray single crystal refinement did not give the exact formula of the compound and the real composition was the ideal one $Cu_{48}Si_{96}P_{144}$ ($CuSi_2P_3$). Now the compound is a $A^IB^{IV}{}_2C^V{}_3$ type semiconductor with a completely filled valence band. The energy gap in that case would be similar to that of $CuGe_2P_3$ (0.90eV) [4] or would lie between the values of the *III-V* compounds and pure Si (1.12eV) [15]. However, the *III-V* semiconductors have relatively large energy gaps as compared to the energy gap (ΔE) of $Cu_{47}Si_{91}P_{144}$: InAs 0.35eV, InP 1.3eV, GaAs 1.4eV and GaP 2.2eV [16]. The ternary $A^{II}B^{IV}C^V{}_2$ and $A^IB^{III}C^{VI}{}_2$ compounds, which are the extensions of the series with four electrons per atom, also have rather large ΔEs: $CdCuAs_2$ 0.55eV, $CdSnP_2$ 1.15eV, $CuAlS_2$ 3.5eV [15]. Therefore, the assumption of the ideal composition and exact electron count is unacceptable either.

In disordered structures with a non-periodic potential the electrons can be localized (Anderson localization [17]). Atomic orbitals in such crystals are divided into two types: those in the middle of the band extend through the solid as in a normal crystal, and those close to the top and

bottom of the band are localized in the vicinity of a particular atom. The region of localized states in the band will depend on the degree of disorder; in an extreme case all the states may become localized [18]. A boundary between the localized and extended states is a mobility edge. If there are enough electrons, the Fermi level may be above the mobility edge and electrons at the Fermi level are then in localized states, and cannot conduct current through the solid [19]. It has been suggested that the Anderson mechanism is mainly responsible for metal-insulator transitions in some oxides, such as $La_{1-x}Sr_xCoO_3$ and $La_{1-x}Sr_xVO_3$ [20], and for anomalies in resistivity of $KCu_{7.68}S_4$ [21]. The $KCu_{7.68}S_4$ sulfide is a semiconductor above 200K and a normal metallic conductor at lower temperatures. At high temperatures the vacancies on Cu sites are distributed randomly, the potential is non-periodic and the states at the top of the band, where the Fermi level lies, are localized. At the low temperatures the vacancies are ordered. As a result, a superstructure with a periodic potential is formed, all the states are delocalized and the compound is a metal.

In $Cu_{47}Si_{91}P_{144}$ the statistical mixture of Cu and Si and the deficient Si sites would produce a non-periodic potential, which would lead to localization of the states at the bottom and top of the band. Due to the deficiency of electrons the Fermi level would fall into the conduction band and if it would lie above the mobility edge, the compound would be a semiconductor. Since the localized states differ slightly in energy, the activation energy is very small. That model would explain the experimentally observed small energy gap and would be consistent with the x-ray structural results.

3.2. Band Structure Calculations

Band structure calculations were performed by the extended Hückel tight binding (EHTB) method [22] and the atomic parameters [14], employed for these calculations, are summarized in Table 6. When dealing with statistically mixed sites, one has to choose a bigger cell to separate the mixed atoms. One of the consequences for $Cu_{47}Si_{91}P_{144}$ would be a very large number of atoms in the unit cell and a long computational time. Therefore, the subcell with a=b=3.7092 and c=5.1930Å was chosen and the composition was assumed to be ideal $CuSi_2P_3$. On the basis of this subcell and its atomic positions a six-times larger cell was generated which would allow to have Cu and Si on different sites and to build the three-dimensional lattice. While there are a couple of possible arrangements of Cu and Si atoms in this cell, we analyzed two extreme cases since the other could be viewed as a combination of these two. Densities of states (DOS) for both models were practically the same and showed a band gap. Therefore, only one model and the corresponding DOS curves are presented in Fig.3 and 4. The number of electrons per atom was taken 3.93 to have the right position of the Fermi level which corresponded to the $Cu_{47}Si_{91}P_{144}$ composition. The Cu *3d* orbital

contribution lies well below the Fermi level in a narrow energy region of about 3eV, and its average energy is in the middle of the Si *p*-band and is a little higher than the center of the P *p*-block. The Cu 3d block is completely full and that supports our electron counting scheme, used above to figure out the compositions of the copper silicon phosphorus semiconductors: $A^{I}B^{IV}{}_{2}C^{V}{}_{3}$ and $A^{I}B^{IV}{}_{4}C^{V}{}_{3}$.

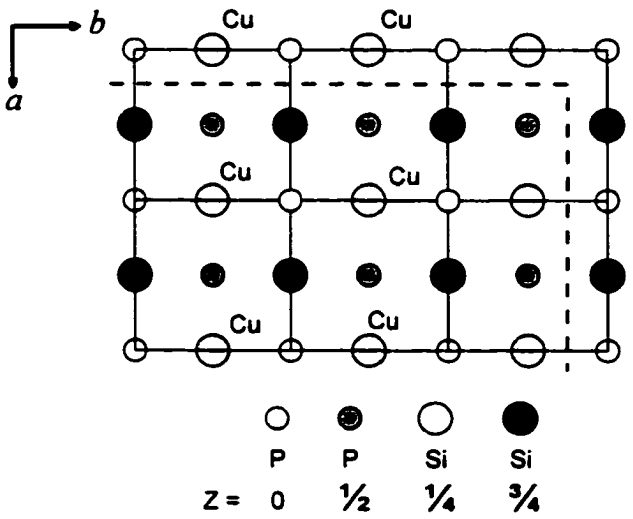

Figure 3. Model used for extended Hückel tight binding calculations. The dashed line present the asymmetric unit. Copper are shown, all other atoms are phosphorus and silicon.

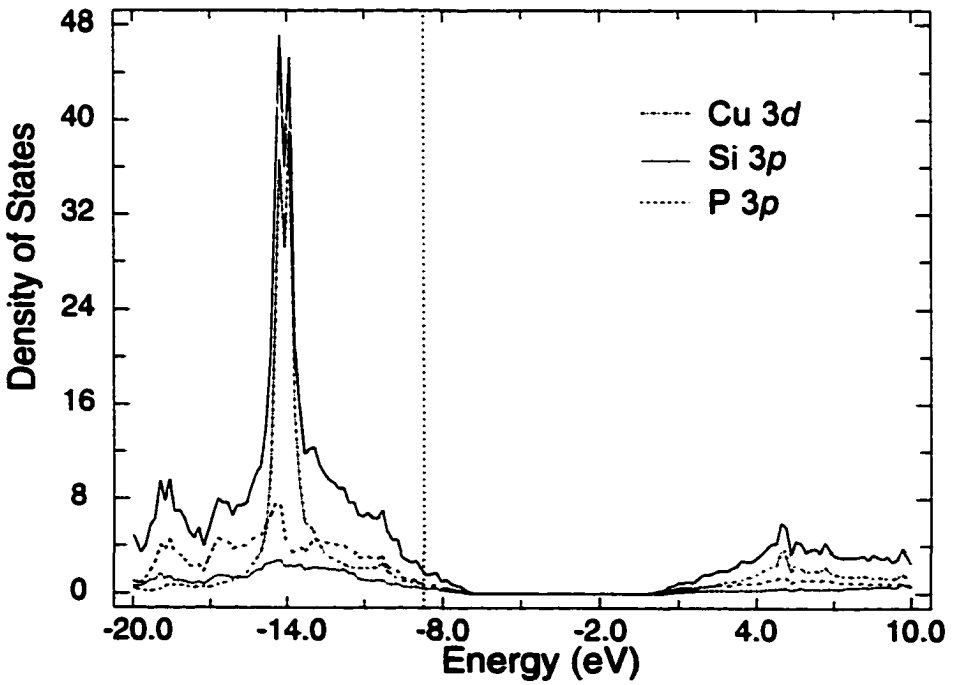

Figure 4. Projected density of states. The solid line refers to the total DOS.

The Fermi level with 3.93 electrons per atom is located at the upper part of the valence band close to the energy gap. The Si, P *p*-orbitals and Cu *d*-orbitals contribute mostly to the states at the top. Since, the structure $Cu_{47}Si_{91}P_{144}$ has Cu/Si statistical mixtures and deficiencies on the Si sites, the potential on these sites is unlikely to be periodic and the upper states are likely to be localized (Anderson model), resulting in a semiconductor behavior with a small energy gap.

3.3. Structure Description

We start the structural analysis from the subcell and then we will consider the changes in the subcell which give rise to the superstructure. Our superstructure exploration will be limited only to the refined ½,½,½ superstructure $Cu_{47}Si_{91}P_{144}$.

The $Cu_{0.71}Si_{1.29}P_2$ (Fig.5) subcell adopts a tetragonally distorted variant of the zinc blende structure. A small difference between the *a,b* and *c* parameters, as mentioned before, reduces the symmetry from cubic face-centered to tetragonal body-centered. The Cu and Si atoms statistically occupy the Zn site while the P atoms are on the S site of zinc blende. Each atom (Table 3) has four neighbors at the distance of 2.2683(3) Å and the angle between bonds is close to the ideal tetrahedral angle 109.5°. The subcell structure is the average superstructure, which can be treated as commensurate modulated. The "modulated" approach simplifies the description by introducing two kinds of modulation: displacive and compositional, which are handy tools in dealing with both commensurate and incommensurate modulated structures [23].

To determine what causes the $Cu_{47}Si_{91}P_{144}$ superstructure (Fig.6), we must consider both compositional and displacive perturbation. The displacive modulation can be characterized by the

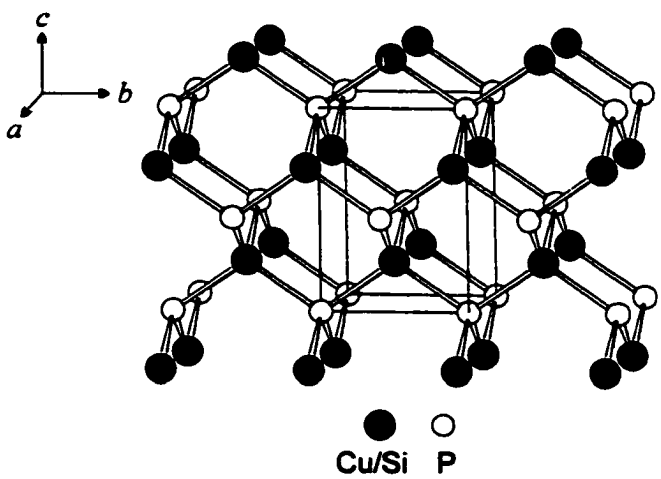

Figure 5. Structure of the subcell that represents the average atomic distribution of the supercell.

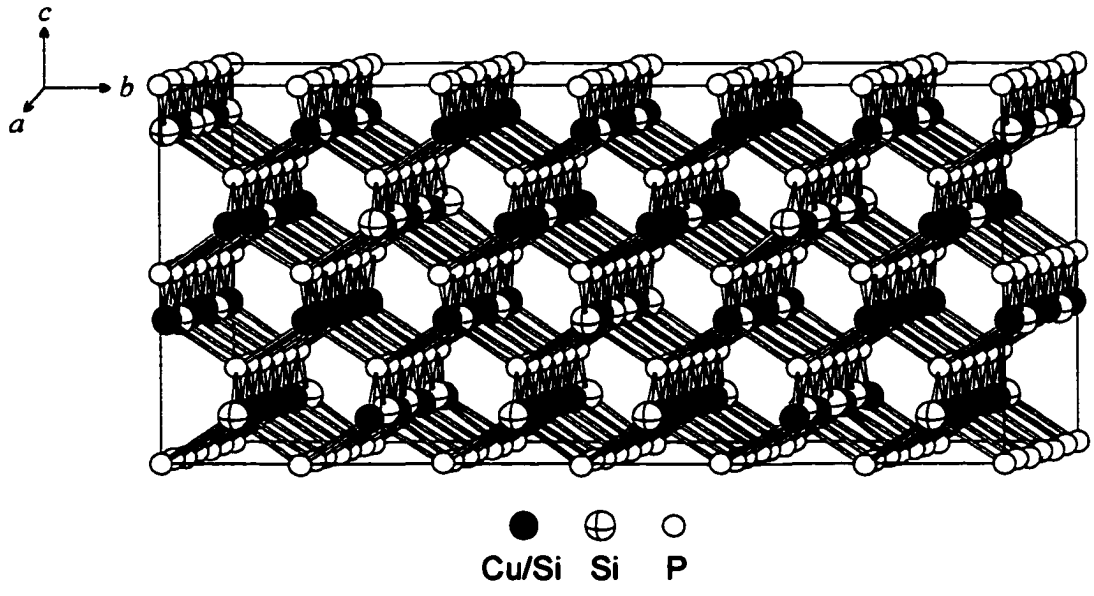

Figure 6. Structure of the ½, ½, ½ supercell.

Table 7. Coordinates of the Atoms in the ½,½,½ Superstructure without a Displacive Modulation

Atom	x	y	z
Cu/Si	0.0833*l*	0.0833*m*	0.1250*n*
P	0.0833*l*	0.0833*m*	0.2500*n*

l, *m* and *n* are integers

magnitude of the atom displacement from its position in the average structure (subcell). If there were no displacive modulation, the *x*, *y* and *z* parameters in the superstructure would have values presented in Table 7. The experimental values are very close to the calculated ones, so the displacement is not crucial in producing the superstructure.

There is only one Si/Cu (64.4% Si and 35.6%Cu) position in the subcell, but there are 8 mixed sites and four Si sites in the ½,½,½ supercell. The separation between the Si and Cu atoms in $Cu_{47}Si_{91}P_{144}$ produces pure silicon sites and a further differentiation between Cu and Si atoms is observed among the 8 mixed sites. The mixed Cu/Si sites can be divided into 5 groups according to the similarity of their site compositions and isotropic displacement parameters: Si1 and Si3, Si2 and Si6, Si7 and Si9, Si4, Si11. While the similarities among these Cu/Si sites reflect the underlying substructure, the differences show the compositional perturbation, which leads to the superstructure. The compositional modulation for the ½,½,½ supercell is presented schematically in Fig.7 where only the front layer in the *ac* plane is shown. Probably further separation of the Si and Cu atoms in the ½,½,½ supercell gives the complete superstructure. Two of the four pure silicon sites, which are

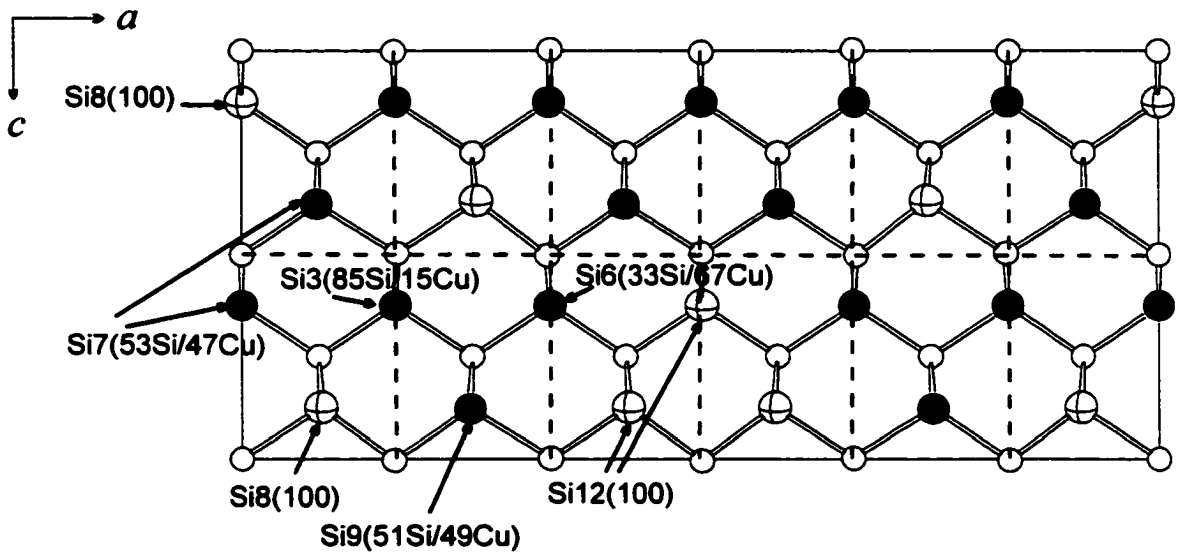

Figure 7. The modulation process as a change in composition of the Cu/Si sites in the ½, ½, ½ super structure. The dashed lines show the small subcells and the numbers in the parantheses are the site occupancies in percents.

partially occupied in $Cu_{47}Si_{91}P_{144}$, may also undergo splitting in the supercell, *e.g.* into fully occupied and empty positions. Compositional modulation is very common, specially among oxides. An example is an incommensurately modulated structure of $Nb_2Zr_{x-2}O_{2x+1}$ where the oxygen atom substructure does not have the same periodicity along the *a* direction as does the average metal atom substructure [24,25]. The compositional modulation with resulted superstructures is encountered in the solid solutions. The "infinite series " of modulated phases with the anion deficient α-UO_3-structure is reported within the composition range from pure Ta_2O_5 to $Ta_{22}W_4O_{67}$ [26, 27].

Since there are more crystallographically different point positions in the $Cu_{47}Si_{91}P_{144}$ superstructure, there are more interatomic distances for Si/Cu and P atoms as compared to the $Cu_{0.71}Si_{1.29}P_2$ subcell, but all of them are close to each other and are also close to the interatomic distances in $Cu_{0.71}Si_{1.29}P_2$. These similarities are due to the small displacive modulation in the superstructure.

The $CuGe_2P_3$ [1] and $NiSi_2P_3$ [8] structures are close to that of $Cu_{47}Si_{91}P_{144}$. In all structures the atoms are tetrahedrally coordinated, the Cu, Ni, Ge and Si atoms have only P neighbors and vice versa. In $NiSi_2P_3$ there is a full separation of Ni and Si atoms, which resulted in the orthorombic variant (a=3.505(1), b=11.071(3) and c=5.307(1)Å [8]) of the zinc blende structure. The $CuGe_2P_3$ phosphide (a=5.37Å[1]) still retains the original zinc blende atomic motive with Cu and Ge atoms statistically mixed on the Zn site. The average Ni-P distance of 2.209Å in $NiSi_2P_3$ is close to the

average for Si-P of 2.251Å in the same structure. In $Cu_{47}Si_{91}P_{144}$ there is no distinct separation between Cu-P and Si-P bonds, the average Cu/Si-P distances of 2.265Å is a little larger than the corresponding distances in $NiSi_2P_3$ but it is a little shorter than Si-P ones of 2.271Å in orthorombic SiP [28].

3.4. Conclusions

The structure of the copper silicon phoshide was solved and refined at the level of the subcell (a=3.7092, c=5.1930Å) and ½,½,½ supercell (a=22.255, c=10.386Å). The composition $Cu_{47}Si_{91}P_{144}$ was assigned on the basis of the refined ½,½,½ supercell. It is has been shown that mainly the compositional modulation of the subcell leads to the formation of the ½,½,½ superstructure. Probably, yet further separation between Cu and Si atoms gives additional perturbation and produces the complete superstructure (a=b=44.510, c=20.772Å).

Since the number of electrons per atom is less than four, the Fermi level falls into the conduction band, but the compound is a semiconductor with a small energy gap of 0.0269eV. Electronic properties can be described by the Anderson localization of the states due to the non-periodic potential in the crystal.

Acknowledgements

Yurij Mozharivskyj is grateful to the DAAD (Deutscher Akademischer Austauschdienst) for a scholarship at Mainz University, Mainz, Germany. The research was also sponsored by the US Department of Energy through Ames Laboratory under contract No. W-7405-Eng-82.

References

[1] O. G. Folberth and H. Pfister, *Acta Crystallogr.* **1961**, *14*, 325.

[2] B. R. Pamplin and M. S. Omar, *Prog. Cryst. Growth Charact.* **1984**, *10*, 183.

[3] J. E. MacDonald, G. A. Saunders, M. S. Omar and B. R. Pamplin, *J. Phys. Status Solidi (a)*, **1985**, *89*, K137.

[4] L. I. Berger, V. I. Sokolova and V. M. Letrov, *Tr. Vsev. Nauch.-Issled. Inst. Khim. Reak. Osobo Chist. Khim. Veshchestv.* **1967**, *30*, 406.

[5] G. Bhikshamaian, S. V. Suryanarayana and M. S. Omar, *J. Mat. Sci. Lett.* **1988**, *7*, 1074.

[6] O. N. Il'nits'kaya, P. Yu. Zavalij, Yu. B. Kuz'ma, *Dopov. Akad. Nauk Ukr.RSR, Ser.B*, **1989**, *38*.

[7] O. N. Il'nits'kaya and Yu. B. Kuz'ma, *Zh. Neorg. Khim.* **1992**, *37*, 734.

[8] J. Wallinda and W. Jeitschko, *J. Solid State Chem.* **1995**, *114*, 476.

[9] K.-S. Lee, H.-J. Koo, D. Dai, J. Ren and M.-H. Whangboo, *Inorg. Chem.* **1999**, *38(2)*, 340.

[10] H. Kleinke, H. F. Franzen, *J. Alloys Compd.* **1996**, *238*, 68.

[11] H. Kleinke, H. F. Franzen, *J. Alloys Compd.* **1997**, *255*, 110.

[12] H. Kleinke and H. F. Franzen, *Angew. Chem. Int. Ed. Engl.* **1997**, *36 No.5*, 513.

[13] *SHELXTL*, Bkuker Analytical X-Ray System, Madison, USA 1997.

[14] S. Alvarez, *Table of Parameters for Extended Hückel Calculations*, Barcelona 1987.

[15] R. A. Smith, *Semiconductors*, Cambridge University Press 1978.

[16] O. Madelung, *Physics of III-V Compounds*, Wiley, New York, 1964.

[17] P. W. Anderson, *Phys. Rev.* **109**, 1492 (1958).

[18] B. Kramer, in: *Springer Proceedings in Physics*, Vol.28, T.Ando and H.Fukuyama, Springer-Verlag, Berlin - New York 1988, p.84.

[19] P. A. Cox, *The Electronic Structure and Chemistry of Solids*, Oxford University Press 1987.

[20] C. N. Rao and P.G anguly, in: *Localization and Metal – Insulator Transition*, H.Fritzschke and D.Adler, Plenum Press, New York - London 1985, p.53.

[21] K.-S. Lee, D.-K.S eo, M.-H. Whangbo, H. Li, R. Mackay, and S.-J. Hwu, *J. Solid State Chem.* **1997**, *134*, 5.

[22] J. Ren, W. Liang and M.-H.W hangbo, *Crystal and Electronic Structure Analyser (CAESAR)*, North Carolina State University, Raleigh, NC, 1998.

[23] R.L. Withers, S. Schimd and J.G. Thompson, *Prog. Solid State Chem.* **1998**, *26 No.1.*

[24] J.G. Thompson, R.L. Withers, J. Sellar, P.J. Barlow and B.G. Hyde, *J. Solid State Chem.* **1990**, *88*, 465.

[25] K. Fütterer, S. Schimd, J.G. Thompson, R.L. Withers, Nishizawa and S. Kishimoto, *Acta Crystallogr., Sect. B*, **1995**, *51*, 688.

[26] R.S. Roth and J.L. Waring, *J. Res. NBS, Sect. A*, **1970**, *74*, 485.

[27] R.S. Roth, J.L. Waringand H.S. Parker, *J. Solid State Chem.* **1970**, *2*, 445.

[28] T. Wadsten, *Chem. Scr.* **1975**, *8*, 63.

APPENDIX B. HIGH-TEMPERATURE MODIFICATION OF Y_5Sb_3 AND ITS TERNARY ANALOGUE $Y_5Ni_xSb_{3-x}$

A paper published in Journal of Alloys and Compounds
J. Alloys Comp. 319 (2001) 100

Yurij Mozharivskyj and Hugo F. Franzen
Department of Chemistry and Ames Laboratory of US DOE, Spedding Hall, Iowa State University, Ames, Iowa 50011, USA

Abstract

The high-temperature modification of Y_5Sb_3 has been discovered: the Yb_5Sb_3 structure type, *Pnma* space group, a = 11.867(1), b = 9.2247(9) and c = 8.0977(8) Å. It has been estimated that the first-order structural transition from the low-temperature form (Mn_5Si_3 type) to the high-temperature form is above 1265°C but below 1400°C. Antimony atoms on one of the two sites can be partially substituted by Ni atoms, which results in a $Y_5Ni_xSb_{3-x}$ formula with $0 \leq x < 1$. The high-temperature structure was refined for a $Y_5Ni_{0.38}Sb_{2.62}$ crystal, obtained by annealing a sample in an induction furnace for 2 hours at 1265°C. All high-temperature nickel-containing phases $Y_5Ni_xSb_{3-x}$ with the ordered Yb_5Sb_3 structure undergo a decomposition to low-temperature Y_5Sb_3 (Mn_5Si_3 type) and a nickel-containing phase, when annealed at 800°C. Extended Hückel tight-binding calculations show that substitution of Sb by Ni is unfavorable with respect to the Y-Sb bonding. The structure of $Y_5Ni_xSb_{3-x}$ is stabilized by the configurational entropy, resulting from a statistical mixture of Sb and Ni atoms on one site. Choice of an Sb site to be occupied by Ni is dictated by bonding maximization in the substituted structure. The high-temperature Y_5Sb_3 and $Y_5Ni_{0.38}Sb_{2.62}$ phases are weak Pauli paramagnets.

Keywords: high-temperature modification of yttrium antimonide, partial substitution of antimony by nickel, crystal structure, bonding, Pauli paramagntes.

Introduction

During recent years, a number of early late-transition metal and rare-earth late-transition metal pnictides with interesting structural properties has been discovered [1-12]. One of the features

of the metal rich pnictides is trigonal prisms of the earlier transition metal or *f*-elements centered by a late transition metal: Zr_6Co in Zr_6CoAs_2 [4], Hf_6Ni in $Hf_6Ni_{1-x}Sb_{2+x}$ [5] and RE_6M in RE_5M_2X (*RE* = Y, Gd-Lu, *M* = Ni, Pd and *X* = Sb, Bi [9-12]). Mulliken overlap population (MOP) indicates that in these ternary compounds such mixed-metal bonds can be as strong as in the binary mixed metal compounds [12]. Also the strength of the interaction between the atoms of an early transition metal or an *f*-element is comparable to those in the pure elements [5, 12]. In RE_5M_2X tetrahedral clusters of a rare earth with bonding even stronger than in the corresponding rare-earth metal can be isolated [12].

Another interesting bonding and structural feature of some pnictides is partial substitution of a main group element by a late transition metal and vice versa, e.g., $Hf_6Ni_{1-x}Sb_{2-x}$ with x = 0-0.3 [5] and $Hf_5Co_{1-x}P_{3-x}$ with x = 0-0.5 [7]. In $Hf_5Co_{1-x}P_{3-x}$ the low energy of the *3d*-orbitals, relative to the energy of the Hf *5d*-orbitals, accounts for the partial substitution of P by Co. The Co atoms, like the P atoms, act as a Lewis base, while the Hf atoms with high lying *5d*-orbitals act as a Lewis acid, providing electrons to Co and P. An opposite substitution process is found in $Hf_6Ni_{1-x}Sb_{2-x}$. In the compound Hf_6NiSb_2, Ni and Sb atoms are in the Y trigonal prisms. The introduction of antimony with low lying *5s*- and *5p*-orbitals removes electrons from the Hf *5d*-orbitals, but the Ni *3d*-orbitals remains well below the Fermi level and the formal charge on the Ni atoms does not change a lot.

Many of the early late-transition metal pnictides have been obtained at relatively high temperatures, typically over 1400°C [3-8]. The effect of high temperatures on the formation of the ternary phases was discussed by Franzen and Köckerling for the M'_yM_zX phosphides and sulfides [13], in which the *M'* and *M* atoms are statistically distributed over some or all metal sites, e.g., $Nb_{4.31}Ta_{6.69}S_4$ [14] and $Zr_{6.45}Nb_{4.55}P_4$ [15]). The M'_yM_zX phases are stable with respect to disproportionation only at high temperatures, demonstrating that they are entropically stabilized materials. However, there is another fine-tuning step in the stabilization of the observed ternaries, namely the distributed fractional site occupancy (DFSO) stabilization. This step in the formation of a DFSO ternary from the conceptual random solid solution ternary consists of distributing the metal atoms on the metal sites such that the metal-metal bonding is maximized in a manner consistent with maintenance of a substantial portion of the configurational entropy.

Considering the variety of binary rare-earth rich phases and existence of the early-transition metal rich ternary phases, one can expect new ternary compounds to exist in the rare-earth rich regions. Utilizing ideas about the stabilizing effects of statistical mixtures at high temperatures, we prepared a sample with the initial composition Y_5NiSb_3 by arc melting and annealed it for 2 hours at 1265°C. The structure solution, based on the single crystal data, resulted in the $Y_5Ni_{0.38}Sb_{2.62}$ composition and prompted us to further investigate phases with this structure. In the present paper we

consider the crystal structure, bonding and magnetic properties of the antimonides $Y_5Ni_xSb_{3-x}$ with $0 \leq x < 1$.

Experimental

2.1. Syntheses and X-ray Structure Analysis

The starting materials were Y (99.99%, Metals Development, Ames Laboratory), Ni (99.95%, Johnson Matthey GmbH) and antimony (99.999%, Johnson Matthey GmbH). The first prepared sample was the one with the initial composition Y_5NiSb_3 and with a total weight of 1g (2mg of Sb were added to compensate for losses during the melting). It was arc melted in an argon atmosphere, then turned over and remelted to achieve homogeneity. The sample was wrapped in tantalum foil, placed into a tungsten crucible and heated in an induction furnace at 1265°C for 2 hours under the dynamic vacuum of $5x10^{-6}$ torr. Small, air stable crystals of metallic luster in the form of square plates were obtained. Some crystals were selected and their quality was checked by the Laue method. The crystal that yielded the sharpest diffraction spots was chosen for data collection on a SIEMENS SMART diffractometer with a two-dimensional CCD detector (Table 1). From analysis of the intensities the space group *Pnma* was chosen and the structure was solved and refined in this space group to $R_1 = 0.0509$, using the SHELXTL program [16] (Table 2, 3). All atomic coordinates were put into the standard setting by the STRUCTURE TIDY program [17]. During the refinement process the isotropic displacement parameter for the Sb2 atoms was high, introducing a statistical mixture with Ni atoms on this site resulted in a reasonable U_{eq} value and lower R factors (0.0509 instead of 0.0608). The Hamilton test [18] indicates that a full Sb occupancy on the Sb2 site can be rejected at a lower than 0.005 level.

After the structure was solved and refined to $Y_5Ni_{0.38}Sb_{2.62}$, four $Y_5Ni_xSb_{3-x}$ samples with x = 0, 0.38, 0.6 and 1.0 were prepared to determine homogeneity and temperature stability ranges. In each case an extra 2mg of Sb were added and the samples were arc melted. The powder patterns of the cast samples were recorded with a Guinier camera (FR 552, ENRAF-NONIUS, Cu$K\alpha_1$) under vacuum with silicon as an internal standard. Y_5Sb_3, $Y_5Ni_{0.38}Sb_{2.62}$ and $Y_5Ni_{0.60}Sb_{2.40}$ were single-phase samples to X-rays and exhibited only lines corresponding to the Yb_5Sb_3 type, while Y_5NiSb_2 had extra lines of a second unidentified phase. The Guinier patterns were laser scanned to obtain peak positions and the lattice parameters (Table 4) were determined by the least-squares procedure using the CSD program package [19]. It was concluded that the homogeneity range for the high-temperature $Y_5Ni_xSb_{3-x}$ phase extends from $x = 0$ to at least $x = 0.6$, but it does not reach $x = 1.0$ (Y_5NiSb_2 composition). The four samples were sealed in evacuated silica tubes and annealed for 10 days at 800°C. The powder patterns of the annealed samples had strong lines of the low-temperature modification of Y_5Sb_3 (the Mn_5Si_3

Table 1. Crystal Data and Structure Refinements for a $Y_5Ni_{0.38}Sb_{2.62}$ Single Crystal, Obtained by the Annealing at 1265°C

Empirical formula	$Y_5Ni_{0.38}Sb_{2.62}$
Space group	*Pnma*
Unit cell dimensions, Å	a = 11.963(2) b = 9.1330(18) c = 8.0500(16)
Volume, Å^3	879.5(3)
Z	4
Density (calculated)	5.935 g/cm^3
Temperature during collection	20(2)°C
Wavelength	0.71073 Å
Diffractometer	Siemens SMART
2θ range	6.10 to 58.18°
Index ranges	$-16 \le h \le 16$, $-11 \le k \le 12$, $-9 \le l \le 10$
Reflections collected	5475
Abs. correction / Program	Empirical / SADABS
Independent reflections	1150 [R(int) = 0.1579]
Completeness to max 2θ	91.5 %
Refinement method	Full-matrix least-squares on F^2
Data / restraints / parameters	1150 / 0 / 44
Goodness-of-fit on F^2	1.054
Final R indices [$I > 2\sigma(I)$]	$R_1 = 0.0509$, $wR_2 = 0.1186$
R indices (all data)	$R_1 = 0.0702$, $wR_2 = 0.1270$
Largest diff. peak and hole	2.464 and -2.634 e./ Å^3

$Rint = \Sigma|Fo^2-Fo^2mean|/\Sigma Fo^2$.
$R_1 = \Sigma||Fo|-|Fc||/\Sigma|Fo|$.
$R_w = (\Sigma w\times(Fo^2-Fc^2)^2 / \Sigma w\times(Fo^2)^2)^{1/2}$, $w = 1/(\sigma^2(Fo^2)+(a\times P)^2+b\times P)$.
$GoF = (\Sigma w\times(Fo^2-Fc^2)^2 / (n-p))^{1/2}$ with $w = 1/(\sigma^2(Fo^2)+(a\times P)^2+b\times P)$, n is the number of observed reflections, p is number of parameters refined.

Table 2. Atomic Coordinates and Equivalent Isotropic Displacement Parameters (U_{eq}, Å^2) for $Y_5Ni_{0.38}Sb_{2.62}$

Atoms		x	y	z	U_{eq}
Y(1)	4*c*	0.2192(1)	¼	0.8324(2)	0.019(1)
Y(2)	4*c*	0.0025(1)	¼	0.5325(2)	0.016(1)
Y(3)	4*c*	0.02941(1)	¼	0.3575(2)	0.021(1)
Y(4)	8*d*	0.0681(1)	0.0490(2)	0.1866(2)	0.022(1)
Sb(1)	8*d*	0.3275(1)	0.0100(1)	0.0695(1)	0.015(1)
Sb(2) / Ni*	4*c*	0.4804(1)	¼	0.5881(2)	0.016(1)

* 62.0(5)%Sb + 38.0(5)%Ni.
U_{eq} is defined as one third of the trace of the orthogonalized U^{ij} tensor.

Table 3. Anisotropic Displacement Parameters ($Å^2$) for $Y_5Ni_{0.38}Sb_{2.62}$

Atoms	U^{11}	U^{22}	U^{33}	U^{23}	U^{13}	U^{12}
Y(1)	0.023(1)	0.020(1)	0.014(1)	0	-0.006(1)	0
Y(2)	0.012(1)	0.017(1)	0.018(1)	0	0.000(1)	0
Y(3)	0.015(1)	0.022(1)	0.025(1)	0	0.005(1)	0
Y(4)	0.014(1)	0.036(1)	0.015(1)	-0.002(1)	0.001(1)	0.000(1)
Sb(1)	0.013(1)	0.018(1)	0.014(1)	0.002(1)	0.001(1)	0.000(1)
Sb(2) / Ni	0.017(1)	0.018(1)	0.014(1)	0	-0.003(1)	0

The anisotropic displacement factor exponent takes the form: $-2\pi^2[h^2 a^{*2} U^{11} + ... + 2 h k a^* b^* U^{12}]$.

Table 4. Lattice Parameters for the Cast $Y_5Ni_xSb_{3-x}$ Phases

Composition	a, Å	b, Å	c, Å	V, $Å^3$
Y_5Sb_3	11.867(1)	9.2247(9)	8.0977(8)	886.4(1)
$Y_5Ni_{0.38}Sb_{2.62}$	11.889(2)	9.209(2)	8.077(1)	884.3(3)
$Y_5Ni_{0.60}Sb_{2.40}$	11.903(3)	9.191(3)	8.053(2)	881.0(4)
Y_5NiSb_2	11.950(5)	9.177(7)	8.038(4)	878.5(9)

type) and weak additional lines of a nickel-containing phase, which we did not identify.

To estimate the transition temperature for Y_5Sb_3 the cast Y_5Sb_3 sample was wrapped in tantalum foil, put into a tungsten crucible and annealed in the induction furnace for 2 hours at 1265°C, then rapidly cooled by radiative heat loss. The Guinier pattern of the resulting sample had lines of the two modifications of Y_5Sb_3: both the low-temperature one (the Mn_5Si_3 type) and the high-temperature one (the Yb_5Sb_3 type), with the low-temperature form being dominant.

The "A_5Pn_3" (A = Ca, Sr, Ba, Sm, Eu, Yb, Pn = Sb, Bi) pnictides, formerly described as the binary Yb_5Sb_3-type compounds, have been shown to be, in reality, hydrogen-stabilized A_5Pn_3H phases [20]. Annealing at 1100°C for 2 hours under the dynamic vacuum dehydrogenates the samples and results in the formation of the hexagonal A_5Pn_3 phases (the Mn_5Si_3 type) [20]. The condition of our experiment (1265°C, 2 hours and dynamic vacuum) excludes the hydrogen contamination of the $Y_5Ni_{0.38}Sb_{2.62}$ structure and the high-temperature form of Y_5Sb_3. But to rule out the possibility that incomplete dehydrogenization at 1265°C resulted in the putative high-temperature Y_5Sb_3 and $Y_5Ni_{0.38}Sb_{2.62}$ phases being hydrogen stabilized, the small amounts (about 200mg) of the cast Y_5Sb_3 and $Y_5Ni_{0.38}Sb_{2.62}$ samples were wrapped in the cleaned tantalum foil, put into a tungsten crucible and annealed in the induction furnace at 1400°C for 5 hours under the dynamic vacuum of about $5x10^{-6}$ torr. The powder patterns of the treated samples contained only lines of the orthorhombic phases (the Yb_5Sb_3 type) and no lines of the hexagonal form of Y_5Sb_3. It can be undoubtedly concluded that

hydrogen is not a factor (although small traces of it may still be present) determining the stability of the orthorhombic high-temperature Y_5Sb_3 and $Y_5Ni_{0.38}Sb_{2.62}$. Also, the annealing at 1400°C narrowed the transition temperature regions to the 1265-1400°C for Y_5Sb_3 and to 800-1400°C for $Y_5Ni_{0.38}Sb_{2.62}$ and further investigation is needed to determine their more precise values. The high-temperature modification of Y_5Sb_3 is kinetically stable with respect to changes at room temperature. The Guinier pattern of Y_5Sb_3, previously annealed at 1400°C, then finely ground and kept in the open air for two days, did not show any structural transformation, oxidation or decomposition.
The orthorhombic $Y_5Ni_{0.38}Sb_{2.62}$ phase was obtained back when the sample, previously annealed at 800°C, was heated in the induction furnace at 1400°C for 5 hours .

The two structure types Yb_5Sb_3 [21] and Y_5Bi_3 [22] are very similar and can be easily confused. The single crystal solution of $Y_5Ni_{0.38}Sb_{2.62}$ indicated the Yb_5Sb_3 type, also the Guinier patterns of the high-temperature Y_5Sb_3 form fit ideally into this structure type.

2.2. Band Structure Calculations

Band structure calculations were performed by the extended Hückel tight binding (EHTB) method [23]. We analyzed three models with the Sb atoms, partially substituted by the Ni atoms. In model *I* ($Y_5Ni_{0.25}Sb_{2.75}$) only one Sb2 atom in the unit cell was substituted by a Ni atom, in model *II* ($Y_5Ni_{0.5}Sb_{2.5}$) two Sb2 atoms were substituted. Model *III* is a hypothetical one, in which only one Sb1 atom is replaced by Ni and the Sb2 site is solely occupied by Sb. The lattice and atomic parameters of the refined $Y_5Ni_{0.38}Sb_{2.62}$ phase were used for these three models.

We also calculated the densities of states (DOS) and crystal orbital overlap populations (COOP) for the high-temperature modification of Y_5Sb_3, using the lattice parameters derived from the Guinier powder pattern (Table 4) and the atomic parameters from Yb_5Sb_3 [21]. The atomic parameters of Yb_5Sb_3 [21] are close to those of the refined $Y_5Ni_{0.38}Sb_{2.62}$ structure and were chosen for the calculations since these parameters result in a little larger atomic distances between Sb2 and neighboring Y atoms. Larger interatomic distances with Sb2 can be expected since Sb (r_{Sb} = 1.45 Å) is larger than Ni (r_{Ni} = 1.25 Å) and no Ni atoms are present in the structure.

The atomic orbital energies and coefficients for the Slater-type orbitals were taken from [24]. The parameters for Y and Ni were refined by the alternating charge iteration technique for the three models and Y_5Sb_3, while the Sb parameters were kept constant. Table 5 gives only the refined orbital parameters for model *I*, the parameters of model *II* and *III* and Y_5Sb_3 are very close to those of model *I* and are not presented here.

Table 5. Parameters for the Extended Hückel Tight-Binding Calculations for Model I[a]

Atom	Orbital	H_{ii}, eV	ξ_1	c_1[b]	ξ_2	c_2[b]
Y	5s	-7.54	1.39	1.00		
Y	5p	-4.74	1.39	1.00		
Y	4d	-7.52	4.33	0.5657	1.06	0.6575
Ni	4s	-7.22	1.825	1.00		
Ni	4p	-3.65	1.125	1.00		
Ni	3d	-10.39	5.75	0.5683	2.00	0.6292
Sb	5s	-18.80	2.323	1.00		
Sb	5p	-11.70	1.999	1.00		

[a] One Sb2 atom is substituted by a Ni atom. The composition is $Y_5Ni_{0.25}Sb_{2.75}$.
[b] Coefficients used in the double-zeta Slater-type orbitals.

2.3. Magnetic Measurements

Temperature dependent measurements of the magnetic susceptibilities of bulk samples of orthorhombic Yb_5Sb_3 and $Y_5Ni_{0.38}Sb_{2.62}$, annealed at 1400°C, were performed at 3 Tesla at temperatures between 6 K and 300 K, using a Quantum Design SQUID magnetometer.

3. Discussion

3.2. Temperature Stability of Y_5Sb_3 and $Y_5Ni_xSb_{3-x}$ Phases

The changes the $Y_5Ni_xSb_{3-x}$ phases undergo with changing temperature and the experimental evidences for those changes were described above. The results are summarized in what follows. The cast samples of Y_5Sb_3 and $Y_5Ni_xSb_{3-x}$, formed by very rapid cooling of the liquid mixtures after arc melting, were obtained as the high-temperature forms. Also $Y_5Ni_{0.38}Sb_{2.62}$, treated at 1400°C for 5 hours, has the Yb_5Sb_3 structure. After annealing the samples at 800°C for 10 days all have the Mn_5Si_3 type structure, and no lines corresponding to the high-temperature structure of the Yb_5Sb_3 type are observed. Therefore, at high-temperatures Y_5Sb_3 and $Y_5Ni_xSb_{3-x}$ adopt the Yb_5Sb_3 structure, while at low temperatures Y_5Sb_3 crystallizes in the Mn_5Si_3 structure. The nickel-containing $Y_5Ni_xSb_{3-x}$ phases with the Yb_5Sb_3 structure are stable only at high temperatures, at 800°C they fully decompose. For Y_5Sb_3 the transformation temperature is estimated to be above 1265°C but below 1400°C.

From the two-phase nature of the Y_5Sb_3 sample, annealed at 1265°C, it can be concluded that the transformation from the low-temperature form (the Mn_5Si_3 type) to the high-temperature form (the Yb_5Sb_3 type) and vice versa is a first-order transition. In a second-order transition the two phases cannot coexist simultaneously, since the thermodynamic potential of either state beyond the transition

point does not correspond to an equilibrium state, i.e. to a minimum in the internal energy [25]. In our case the two modifications of Y_5Sb_3 coexisted at some transition temperature, which indicates the transition to be first-order. Also a structural analysis of the symmetries of the two Y_5Sb_3 forms indicates a first-order transition.

3.2. Structure Description

The refined $Y_5Ni_{0.38}Sb_{2.62}$ structure is presented at Fig. 1. An approach somewhat different from that previously used [21] will be given here to elucidate the structural features that are found among other pnictides. The Y1-3 atoms, located on the mirror planes, form in the *ac* plane 3.6.3.6 layers, which are superimposed along the *b* direction. Such stacking produces trigonal Y1-3 channels, which share edges in the *ac* plane, and hexagonal channels which share edges with other hexagonal channels and sides with the trigonal channels. The trigonal prisms (constituting parts of the channels) are centered by Sb1 atoms. The hexagonal channels are filled with Y4 and Sb2/Ni atoms, forming an array along the *b* direction (Fig. 2). Trigonal prismatic coordination of the VA element is one of the structural features that is common to a number of ternary pnictides: e.g., Zr_6P in $Zr_9Co_2P_4$ and $Zr_9Ni_2P_4$ [3], Zr_6As in Zr_6CoAs_2 [4], Hf_6Sb in $Hf_6Ni_{1-x}Sb_{2+x}$ [5] and Hf_6P in $Hf_5Co_{1+x}P_{3-x}$ [6, 7]. The $Y_5Ni_{0.38}Sb_{2.62}$ structure is no exception to this general occurrence.

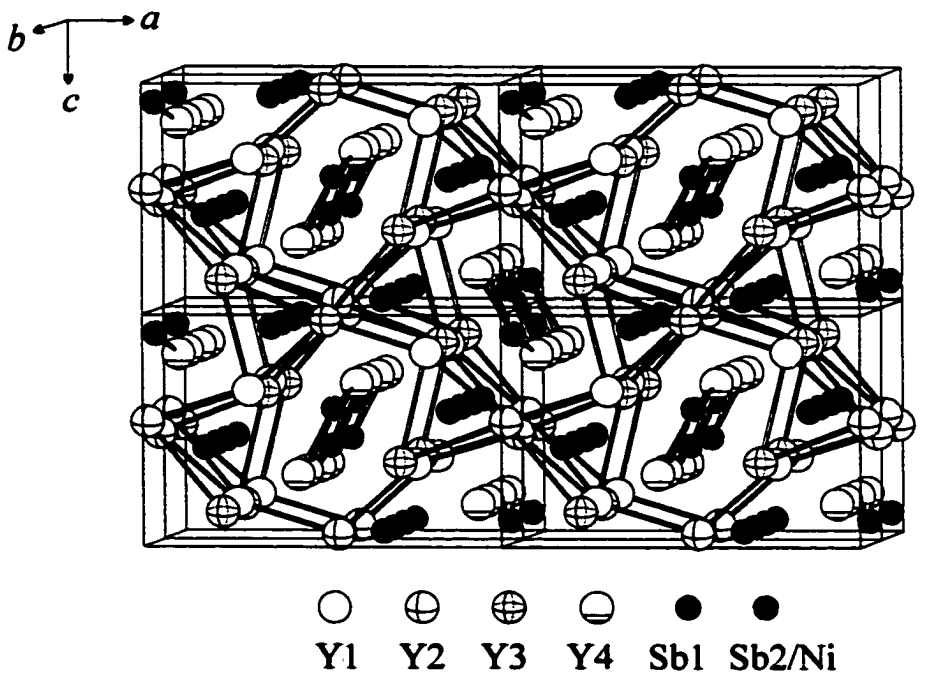

Figure 1. Structure of $Y_5Ni_{0.38}Sb_{2.62}$.

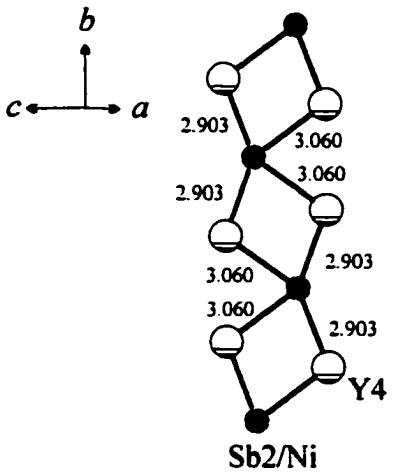

Figure 2. Chain of the Y4 and Sb2/Ni atoms inside the hexagonal channels.

The hexagonal channels are also structural units typical for pnictides and chalcogenides, but these channels are normally of a more regular form. In $Hf_5Co_{1+x}P_{3-x}$ [6, 7], $Hf_5Ni_{1+x}P_3$ [26] and $Sc_5Ni_2Te_2$ [27] they are fused to a double channel, in Hf_2NiP [8] the whole structure is built from face-sharing hexagonal channels, in $Y_5M_2Te_2$ (M = Fe, Co, Ni) [28] they form layers. In these above mentioned structures the channels are filled with late-transition metal and metalloid atoms, or just with late-transition metal atoms in the form of a zigzag line. In $Y_5Ni_xSb_{3-x}$, however, the channels are filled with Y and Sb/Ni atoms in the form of the double Y line, bridged by the Sb/Ni atoms (Fig. 2).

Some of bonds in the $Y_5Ni_{0.38}Sb_{2.62}$ structure are given in Table 6. The Y – Sb1 distances are close to the sum of metallic radii of Y and Sb (r_Y+r_{Sb}=1.776+1.45=3.226Å) and are not discussed here. On the other hand, the Y – Sb2/Ni distances of 2.901 – 3.065 Å, while they are rather short for a Y-Sb bond, are typical for a Y-Ni bond. This is a result of the structural adaptation to the smaller substituting atoms: shorter distances will result in larger Y-Ni orbital overlap and strong bonding that will compensate for the lost Y-Sb interactions.

In the known ternary pnictides with similar structural characteristics, statistical mixing of a metalloid and a transition metal occurs in the trigonal prisms ($Hf_6Ni_{1-x}Sb_{2+x}$ [5]) or in the pentagonal prisms ($Hf_5Co_{1+x}P_{3-x}$ [6, 7]), but not in the hexagonal channels. In $Y_5Ni_xSb_{3-x}$, however, the Ni atoms are found on the Sb2 site in the hexagonal channels, not on the Sb1 sites inside the trigonal prisms, although there are no size restrictions for Ni, since the Ni atoms are smaller than the Sb atoms. Interestingly, the substitution of Sb2 by Ni does not go to the completion, which is obvious from the two-phase nature of the cast Y_5NiSb_2 sample. The preference of Ni for the Sb2 site and the constraints on the substitution are discussed below in terms of bonding maximization.

3.2. Electronic Structure and Bonding

According to their composition and structural patterns the high-temperature $Y_5Ni_xSb_{3-x}$ phases must be metallic. Band calculations were performed to gain more insight into bond strengths and electron distribution. Fig. 3 shows the total and projected densities of states (DOS and PDOS) for Y_5Sb_3 (the Yb_5Sb_3 type) and $Y_5Ni_{0.25}Sb_{2.75}$ (model *I*). The characters of the DOS and PDOS curves for models *II* and *III* are similar to those of model *I* and they are not presented here. As is typical for metal rich antimonides, the Fermi level occurs at the low-energy part of the conduction band composed, in this case, mainly of the Y *d*-orbitals. The only significant difference between the DOS

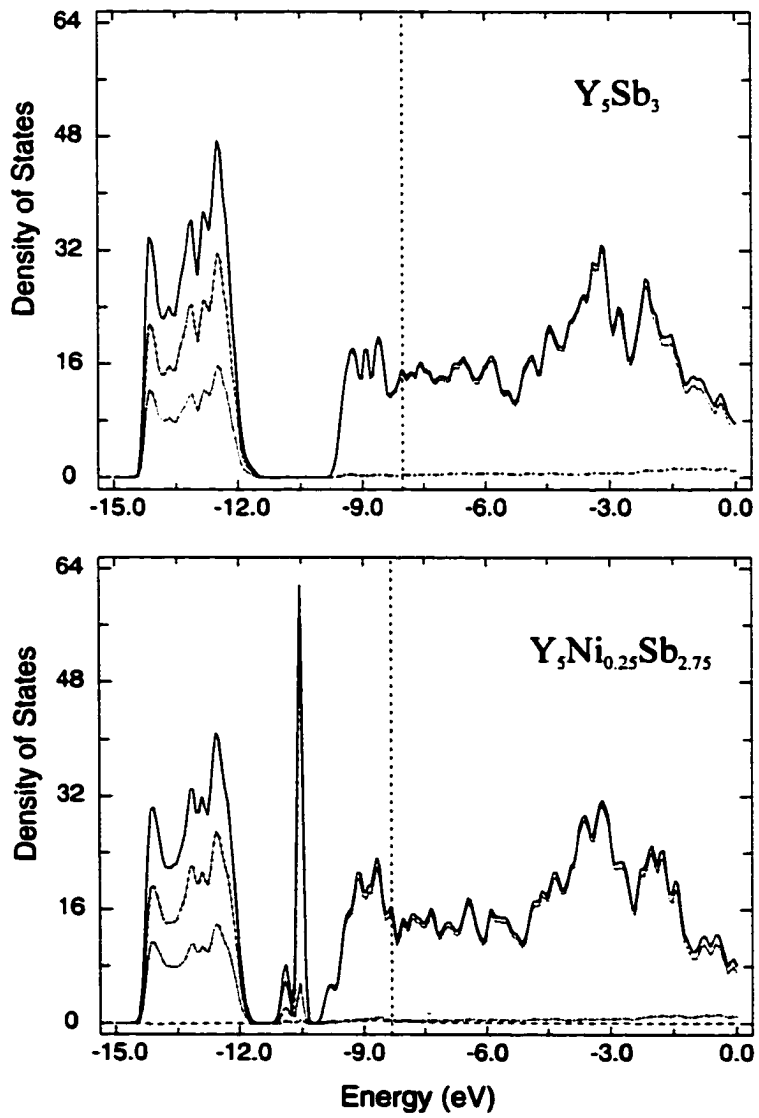

Figure 3. Total and projected densities of states for Y_5Sb_3 (Yb_5Sb_3 type) and $Y_5Ni_{0.25}Sb_{2.75}$ (model I). Vertical line represents energy of the Fermi level. Solid line is total DOS, dotted line is Y contribution, dashed line is Ni contribution and dash-dot line shows Sb contribution.

curves of Y_5Sb_3 and $Y_5Ni_{0.25}Sb_{2.75}$ is the presence, in the latter case, of the sharp peak from the localized 3*d*-orbitals of Ni. The bonding contributions from *s* and *p* orbitals of Sb, with some mixture of Y orbitals, lie around –13.5eV and –20eV (out of the presented energy window). The presence of the Ni and Sb states above –10eV indicates the interaction of Sb and Ni orbitals with Y orbitals, and this interaction gives the flat PDOS curves at the region.

Analysis of distances and bond strengths is essential in understanding a crystal structure. In a complex structure like that of $Y_5Ni_xSb_{3-x}$ each atom has a number of nearest neighbors, some of the neighbors may not have strong bonding to the central atom despite the short separation. It is an example of the matrix effect: a separation, fixed by the geometric factors, is more important than the near-neighbor interaction. Table 6 shows the bond distances and Mulliken overlap populations for models *I*, *II* and *III*. The matrix effect is present for the Y sublattice, e.g. the Y4-Y4 bond of 3.671(3)Å is much stronger (MOP = 0.321) than the shorter Y1-Y2 bonds of 3.542(2), 3.559(2)Å (MOP = 0.144, 0.157) in model *I*. The strength of the Y-Sb interactions depends on the atomic separation without exceptions.

Analysis of the average Y-Y, Sb-Y and Ni-Y MOP's for models *I* and *II* reveal that the substitution of Sb by Ni atoms increases the Y-Y bonding, has practically no effect on the Y-Ni interaction and weakens the Sb-Y bonding (Table 6). Another aspect of the Sb/Ni exchange is that relatively strong Sb-Y bonds are substituted for weaker Ni-Y bonds. Thus, the substitution of Sb by Ni is unfavorable with respect to the Sb-Y bonding, and that explains, in part, why the substitution does not go to $x = 1$ in $Y_5Ni_xSb_{3-x}$.

One of the common structural features in the pnictides, discussed above, is a trigonal prismatic coordination of a late-transition metal by an early-transition or an *f*-element. Also, substitution of a metalloid atom by a transition metal occurs on the metalloid site inside the trigonal prisms in some pnictides. In the case of $Y_5Ni_xSb_{3-x}$ the Sb2 atoms in the hexagonal channels, not the Sb1 atoms in the trigonal prisms, are substituted by the Ni atoms, although there is no size constraint for the Ni atoms, which would dictate the choice. Comparison of the average MOP's for model *I* and *III* shows a relatively small increase in the Y-Y (from 0.188 to 0.189) and Sb-Y (from 0.338 to 0.346) bonding, and a large drop in the Ni-Y bonding (from 0.156 to 0.112). To maximize the Ni-Y overlap and bonding the Ni-Y distances in model *III* have to be smaller, which would change the other interatomic distances, mainly the Y-Y ones. Such rearrangement would influence the strong Y-Y interaction and would tend to destabilized the structure.

Crystal orbital overlap populations (COOP) were calculated to gain more insight into the different bonds. The COOP curves of the Y-Y, Ni-Y and Sb-Y interactions for Y_5Sb_3 (Yb_5Sb_3 type)

Table 6. Interatomic Distances and MOPs per Atomic Pair (Number of Equivalent Bonds is given in Brackets)

Bond	Distance	MOP, model 1[a]	MOP, model 2[b]	MOP, model 3[c]
Y1 - Y2	3.542(2)	0.144(x4)	0.152(x4)	0.144(x4)
Y1 - Y2	3.559(2)	0.157(x4)	0.165(x4)	0.156(x4)
Y1 – Y3	3.927(2)	0.092(x4)	0.099(x4)	0.101(x4)
Y1 - Y4	3.843(2)	0.176(x8)	0.184(x8)	0.164(x8)
Y1 – Y4	3.913(2)	0.107(x8)	0.117(x8)	0.105(x8)
Y2 – Y3	3.762(2)	0.201(x4)	0.186(x4)	0.236(x4)
Y2 – Y3	4.009(2)	0.123(x4)	0.122(x4)	0.142(x4)
Y2 – Y4	3.426(2)	0.285(x8)	0.278(x8)	0.313(x8)
Y2 - Y4	3.645(2)	0.131(x8)	0.143(x8)	0.124(x8)
Y3 – Y4	3.545(2)	0.259(x8)	0.251(x8)	0.289(x8)
Y3 - Y4	3.774(2)	0.194(x8)	0.208(x8)	0.175(x8)
Y4 – Y4	3.534(3)	0.235(x4)	0.272(x4)	0.164(x4)
Y4 – Y4	3.671(3)	0.321(x4)	0.329(x4)	0.310(x4)
Average MOP		*0.188*	*0.194*	*0.189*
Sb1 - Y2	3.1406(14)	0.373(x8)	0.367(x8)	0.375(x7) / 0.130(x1)
Sb1 - Y2	3.1409(13)	0.366(x8)	0.367(x8)	0.361(x7) / 0.117(x1)
Sb1 - Y1	3.182(1)	0.362(x8)	0.359(x8)	0.365(x7) / 0.125(x1)
Sb1 – Y3	3.216(2)	0.339(x8)	0.336(x8)	0.343(x7) / 0.120(x1)
Sb1 - Y1	3.230(1)	0.337(x8)	0.341(x8)	0.331(x7) / 0.122(x1)
Sb1 – Y4	3.262(2)	0.326(x8)	0.328(x8)	0.323(x7) / 0.125(x1)
Sb1 – Y3	3.266(1)	0.305(x8)	0.307(x8)	0.302(x7) / 0.104(x1)
Sb1 – Y4	3.369(2)	0.238(x8)	0.237(x8)	0.241(x7) / 0.093(x1)
Sb1 - Y4	3.503(2)	0.206(x8)	0.205(x8)	0.204(x7) / 0.069(x1)
Sb2 / Ni – Y3	2.901(2)	0.457(x3) / 0.155(x1)	0.455(x2) / 0.157(x2)	0.457(x4)
Sb2 / Ni – Y4	2.903(2)	0.445(x6) / 0.174(x2)	0.445(x4) / 0.173(x4)	0.449(x8)
Sb2/ Ni - Y1	2.927(2)	0.436(x3) / 0.168(x1)	0.431(x2) / 0.165(x2)	0.442(x4)
Sb2 / Ni – Y4	3.060(2)	0.373(x6) / 0.140(x2)	0.369(x4) / 0.140(x4)	0.371(x8)
Sb2 / Ni – Y2	3.065(2)	0.341(x3) / 0.141(x2)	0.344(x2) / 0.140(x2)	0.344(x4)
Average MOP Sb – Y / Ni - Y		*0.370 / 0.156*	*0.331 / 0.155*	*0.346 / 0.112*

[a] Composition is $Y_5Ni_{0.25}Sb_{2.75}$. One Sb2 atom is substituted by a Ni atom.
[b] Composition is $Y_5Ni_{0.50}Sb_{2.50}$. Two Sb2 atoms are substituted by Ni atoms.
[c] Composition is $Y_5Ni_{0.25}Sb_{2.75}$. One Sb1 atom is substituted by a Ni atom. Hypothetical model.

and $Y_5Ni_{0.25}Sb_{2.75}$ (model *I*) are shown in Fig. 4. The Y-Y overlap is bonding, the Sb-Y one is slightly antibonding for the two phases at the Fermi level. The Ni-Y interactions are weakly bonding around the Fermi level, above –7.5eV they become antibonding (Fig. 4b). The character of the Y-Sb and Ni-

Y interactions of $Y_5Ni_{0.25}Sb_{2.75}$ reflects the above-discussed changes in the MOP's upon substitution of Sb by Ni: introducing more Ni atoms and therefore more electrons into $Y_5Ni_xSb_{3-x}$ would decrease the Sb-Y bonding more than it would increase the Ni-Y bonding.

The substitution has a little effect on the Y-Y bonding and on the charge on the Y atoms. At first glance it may seem that introducing the less electronegative Ni atoms with more valence electrons (10 instead of 5) would result in a more reduced state of the Y atoms and stronger Y-Y bonding. However, the Ni *d*-orbitals lie below the Y orbitals, and they act as a Lewis base (acceptor of electrons) as do the Sb *s*- and *p*-orbitals. This leads to a small changes in the Y-Y interactions.

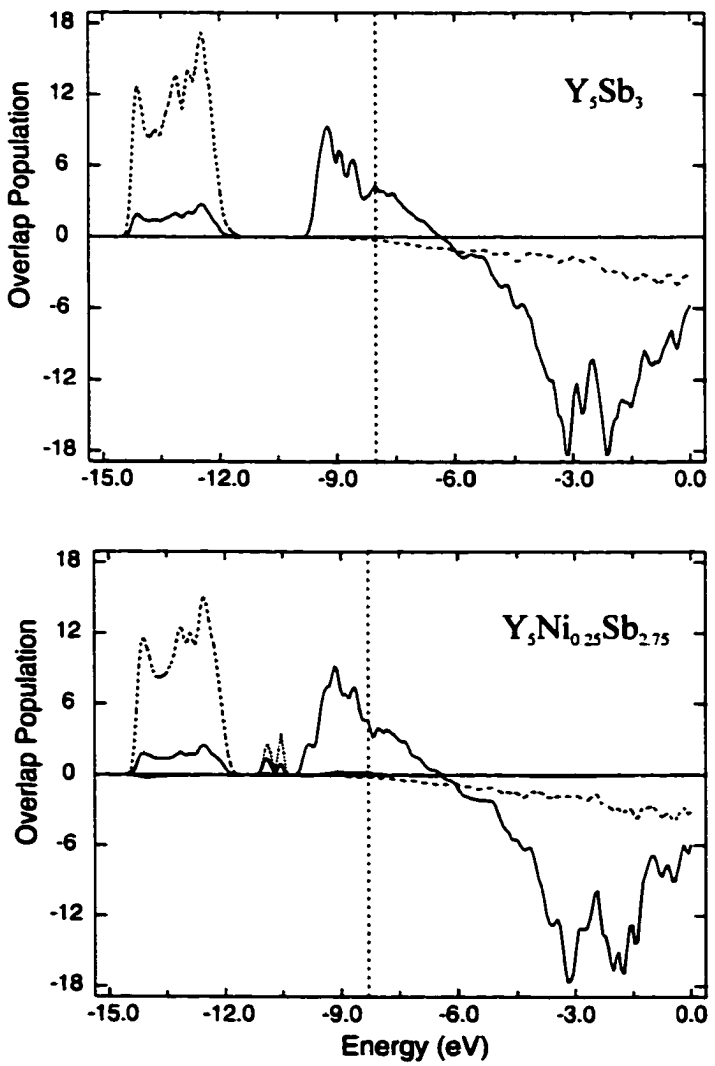

Figure 4. COOP curves for Y_5Sb_3 (Yb_5Sb_3 type) and $Y_5Ni_{0.25}Sb_{2.75}$ (model I). Interactions in the upper part are bonding (+), in the lower part antibonding (-). Solid line is Y-Y interactions, dashed line is Sb-Y and dotted is Ni-Y interactions.

Since the substitution of Sb2 by Ni in $Y_5Ni_xSb_{3-x}$ is not favorable with the respect to the Sb-Y bonding, the question may be asked why does the Sb/Ni mixture exist at all? The answer comes from the entropy part in the Gibbs free energy. According to the statistical mechanics the entropy for the completely random solid solution in the $Y_5Ni_{0.38}Sb_{2.62}$ structure would be:

$$\Delta S/R = -4(x_{Ni}\ln x_{Ni} + x_{Sb}\ln x_{Sb}) = 2.66,$$

which yields a stabilizing contribution of 2.66x1538x8.314 = 34,013 J/mol (34.0 kJ/mol) to the Gibbs free energy at 1538K (1265°C), the temperature of the annealing. The maximum entropy at the given temperature would be for $x_{Ni} = x_{Sb} = 0.5$, i.e. for the Sb2 site to be half occupied by the Sb atoms and half by Ni atoms. This fact, in addition to the bonding-based arguments, can explain why the substitution does not extend to the Y_5NiSb_2 composition.

From the formula for the Gibbs free energy it follows that high temperatures increase the stability of the $Y_5Ni_xSb_{3-x}$ phases, while the lower ones result in the reduced stability that will lead to decomposition below some temperature. The experimental temperature-dependent stability of the $Y_5Ni_xSb_{3-x}$ phases with a statistical Sb/Ni mixture is consistent with these conclusions. It must be understood that although the configurational entropy contribution is temperature dependent and important in the transition, it is only one of the many factors that determine the stability. The high-temperature Y_5Sb_3 phase has no configurational entropy contribution from the Sb/Ni mixture, but it still undergoes the transition due to the other factors.

The entropy is not site specific. The statistical Sb/Ni mixture with $x_{Ni} = 0.19$ and $x_{Sb} = 0.81$ on the Sb1 site, which gives the same $Y_5Ni_{0.38}Sb_{2.62}$ composition, would produce even a larger contribution (49.7 kJ/mol) to the free energy than the mixture on the Sb2 site does (34.0 kJ/mol). The conceptual step in the formation of $Y_5Ni_{0.38}Sb_{2.62}$, or other $Y_5Ni_xSb_{3-x}$ phase, from the conceptual random Sb/Ni solution, consists of distributing the Ni atoms on the Sb atoms site in the way that Sb-Y and Ni-Y bonding is maximized in a manner consistent with maintenance of a substantial part of the configurational entropy. The substitution of the Sb2 atoms by Ni atoms in model *I* increases the Ni-Y bonding to a greater extent and at the same time decreases the Sb-Y bonding less than the substitution of the Sb1 site in the model *III*.

3.3. Magnetic Properties

Due to the postulated metallic character of the $Y_5Ni_xSb_{3-x}$ series, these antimonides are expected to show Pauli paramagnetism. Since the magnetic susceptibility of a Pauli paramagnet is proportional to the density of states at the Fermi level [29], the magnetic moments of $Y_5Ni_xSb_{3-x}$ will depend on the character of the DOS's and the position of the Fermi level (number of electrons). The

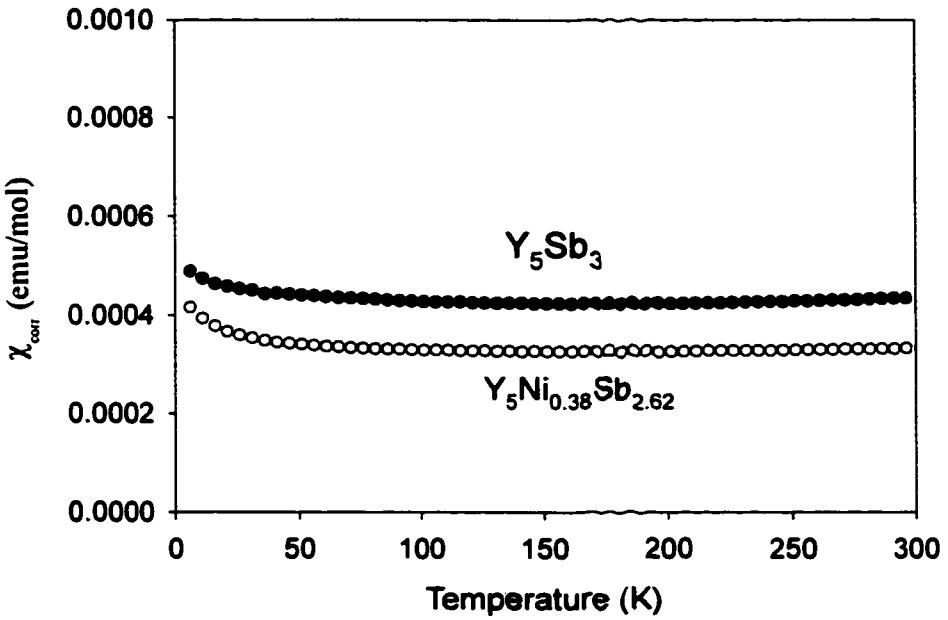

Figure 5. Temperature dependence of the magnetic susceptibility for Y_5Sb_3 and $Y_5Ni_{0.38}Sb_{2.62}$ at 3 Tesla.

density of states for Y_5Sb_3 and $Y_5Ni_{0.25}Sb_{2.75}$ are similar at the Fermi level. Increase in the Ni content from 0.25 to 0.38 in $Y_5Ni_{0.38}Sb_{2.62}$ will shift the Fermi level to higher energy states where there occurs a local minimum, which would result in a lower susceptibility. The experimental measurements of the susceptibilities for orthorhombic high-temperature Y_5Sb_3 and $Y_5Ni_{0.38}Sb_{2.62}$ confirm these considerations (Fig. 5).

Acknowledgement

This research was supported by the Office of the Basic Energy Sciences, Materials Sciences Division, US Department of Energy, DOE.The Ames Laboratory is opperated for DOE by Iowa State University under contract No. W-7405-Eng-82.

References

[1] V. A. Brushkov, Y. F. Lomnitskaya, Y. B. Kuz'ma, Sov. Phys. Crystallogr. 33(2) (1988) 199.

[2] Y. F. Lomnitskaya, Y. B. Kuz'ma, Inorg. Mater. 16(6) (1980) 705 (translated from Izvest. Akad. Nauk SSR).

[3] H. Kleinke, H. F. Franzen, Inorg. Chem. 35 (1996) 5272.

[4] H. Kleinke, J. Alloys Compd. 252 (1997) L29.

[5] H. Kleinke, J. Alloys Compd. 270 (1998) 136.

[6] H. Kleinke, H. F. Franzen, J. Alloys Compd. 238 (1996) 68.

[7] H. Kleinke, H. F. Franzen, J. Alloys Compd. 255 (1997) 110.

[8] H. Kleinke, H. F. Franzen, Angew. Chem., Int. Ed. Engl. 36(5) (1997) 513.

[9] Y. Mozharivskyj, Y. B. Kuz'ma, J. Alloys Compd. 236 (1996) 203.

[10] Y. Mozharivskyj, Y. B. Kuz'ma, Metally, 4 (1999) 139.

[11] S. I. Mikhalenko, Y. Mozharivskyj, Y. B. Kuz'ma, Dopov. Nats. Akad. Nauk Ukr. 10, (1998) 108.

[12] Y. Mozharivskyj, H. F. Franzen, J. Solid State Chem. 152 (2000) 478.

[13] H. F. Franzen, M. Köckerling, Prog. in Solid State Chem. 23(4) (1995) 265.

[14] X. Yao, H. F Franzen, J. Solid State Chem. 86 (1990) 88.

[15] G. A. Marking, H. F. Franzen, Chem. of Mat. 5 (1993) 678.

[16] SHELXTL, Bruker Analytical X-Ray Systems, Madison, USA, 1997.

[17] E. Parthé, K. Cenzual, R. E Gladyshevskyi, STRUCTURE TIDY, J. Alloys Compd. 197(2) (1993) 291.

[18] W. C. Hamilton, Acta Crystallogr. 18, (1965) 502.

[19] L. G. Akselrud, Y. M. Grin, V. K. Pecharsky, P. Y. Zavalij, CSD - universal program package for single crystal and powder data treatment, Proc.12th European Crystallographic Meet., Academy of Sciences, Moscow, USSR, August 28-29, 1989, Kristallographiya, Suppl., 155 (1989) 2.

[20] E. A. Leon-Escamilla, J. D. Corbett, J. Alloys Compd. 265 (1998) 104.

[21] G. D. Brunton, H. Steinfink, Inorg. Chem. 10 (10) (1971) 2301.

[22] Yu. Wang, E. J . Gabe, L. D. Calvert, J.B.Taylor, Acta Crystallogr. 32B (1976) 1440.

[23] J. Ren, W. Liang, M.-H. Whangbo, Crystal and Electronic Structure Analyser (CAESAR), North Carolina State University, Raleigh, NC, 1998.

[24] S. Alvarez, Table of Parameters for Extended Hückel Calculations, Barcelona 1987.

[25] L. D. Landau, E. M. Lifshitz, Statistical Physics, Addison-Wesley, Reading, Massachusetts, USA, 1958, p. 434.

[26] H. Kleinke, H. F. Franzen, Chem. Mater. 9(4) (1997) 1030-1035.

[27] P. A. Maggard, J. D. Corbett, Inorg. Chem. 38 (1999) 1945.

[28] P. A. Maggard, J. D. Corbett, J. Am. Chem. Soc. 122 (200) 10740.

[29] C. Kittel, Introduction to Solid State Physics, 7th Edition, New York, John Wiley and Sons, Inc., 1996.

APPENDIX C. CRYSTAL STRUCTURE AND BONDING IN THE RARE-EARTH RICH TERNARY PNICTIDES RE_5M_2X (RE = Y, Gd, Tb, Dy, Ho, Er, Tm, Lu; M = Ni, Pd; X = Sb, Bi)

A paper published in Journal of Solid State Chemistry
J. Solid State Chem. **152**, 478 (2000)

Yurij Mozharivskyj and Hugo F. Franzen
Department of Chemistry and Ames Laboratory of US DOE, Spedding Hall, Iowa State University, Ames, Iowa 50011, USA

Abstract

Eleven new rare-earth antimonides and bismuthides RE_5M_2X (see Table 1) have been synthesized and characterized by X-ray powder methods. The compounds are isostructural to the previously reported pnictides RE_5M_2X and adopt the Mo_5B_2Si structure (*I4/mcm* space group, an ordered variant of Cr_5B_3). Atomic and thermal parameters have been refined for Ho_5Ni_2Sb and Ho_5Ni_2Bi. Extended Hückel tight binding calculations performed on Y_5Ni_2Sb show strong Y-Ni, Y-Sb and Y-Y interactions.

1. Introduction

Investigation of ternary rare-earth transition metal antimonides and bismuthides has been growing over the last two decades. The interest in this field is prompted by the search for new magnetic materials (1-4), and by attempts to synthesize new compounds and to understand their chemistry (5). Exchanging a rare-earth element allows tracking steric factors in the structures (4, 6). An increase in atomic radii normally leads to a larger unit cell but it may also result in the change of the structure type: *RE*NiSb (*RE*=La, Ce, Pr, Nd, Sm) crystallize with ZrBeSi structure, while the antimonides of the heavy rare-earths (Gd-Lu) adopt the MgAgAs structure (4). On the other hand, substitution of a transition metal results in subtle electronic effects (7, 8) that determine the structure and homogeneity ranges for the structure. Varying composition results not only in different structures but also leads to different spatial arrangements of building units: compounds with a high amount of antimony adopt one- or two-dimensional structures (1-3, 5, 9-11) whereas antimonides richer in a

rare-earth or transition metal are normally three-dimensional (2, 4, 6, 12, 13). Crystal structures of the bismuthides (8, 14) are similar to those of the antimonides, but there are few known compounds.

The studies in the rare-earth transition metal antimonide and bismuthide systems have been mainly focused on the region with relatively high (over 30 at.%) amounts of antimony or bismuth. Considering the variety of binary rare-earth rich phases, one can expect new compounds to exist in the rare-earth rich regions. Recently synthesized pnictides RE_5M_2X (RE = Y, Gd-Lu except Yb, M = Ni, Pd, X = Sb, Bi) (13, 15, 16) extended the number of the known rare-earth rich phases, which were, until recently, limited to those of the RE_5CuBi_3-type (17). A larger content of a rare-earth and the presence of a late transition metal, as opposed to a metalloid, in the RE_5M_2X phases dictates increased metal-metal interaction.

Combination of the early transition metal or *f*-elements with late transition metals could be considered as a Lewis-acid-base reaction and could lead to the formation of the strong intermetallic bonds. The extra stability of such polar interactions was first noted by Brewer and Wengert (18) who proposed that for a fourth group element, such as zirconium, the maximum in stability should be with iridium or platinum. For a third group metal, such as yttrium, the maximum interaction would be expected at platinum. The significance of these bonds can be seen in the surrounding of the atoms and structural motif of the early-late transition metal compounds. In the late-transition metal poor phases, such as Hf_5MTe_3 (19), Zr_6MTe_2 (20), $Zr_9Ni_2P_4$ (21) and $Ta_9M_2S_6$ (22), these bonds take precedence over the interactions between the late transition metal (M) and main group element. Mixed-metal features in pnictides and chalcogenides are largely trigonal prisms of the earlier transition metal or f-elements centered by a late transition metal: Zr_6Co in Zr_6CoAs_2 (23), Hf_6Ni in $Hf_6Ni_{1-x}Sb_{2-x}$ (24), Sc_6Ni in $Sc_5Ni_2Te_2$ (25), Ta_6M (M = Fe, Co, Ni) in $Ta_9M_2S_6$ (22) and RE_6M in RE_5M_2X (13, 15, 16). Mulliken overlap population (MOP) indicates that in the ternary compounds with a main group element such mixed-metal bonds can be as strong as in the binary mixed metal compounds (26). Also the strength of the interaction between early transition metal atoms is comparable to those in the pure elements (24). As a result separate clusters or one-, two- and three-dimensional frames of the early-transition metals can be formed, depending on the number of metal-based electrons. In Ta_2S and Ta_6S (27) the Ta atoms form chains of the fused pentagonal antiprisms, in $Hf_5Co_{1+x}P_{3-x}$ (28, 29) the Hf atoms constitute double hexagonal channels, and in Hf_2NiP (30) the Hf atoms form 2D zigzag nets with weak bonding between them.

In the present paper we consider the metal-metal bonding in the rare-earth rich ternary pnictides, extending the ideas of the interaction from the early-late transition metal compounds to the phases with rare-earth metals (*f*-elements) and nickel or palladium.

2. Experimental

2.1. Syntheses

The starting materials were ingots of *RE* elements (with purity not less than 99.8%), antimony (99.99%, Johnson Matthey GmbH), bismuth (99.999%, ChemPur), nickel (99.99%, ChemPur) and palladium (99.9%, Merck KGaA). The mixtures of the components with the initial compositions RE_5M_2X and with a total weight of 1g were arc-melted in an argon atmosphere, then turned over and remelted to reach the homogeneity. The samples were sealed in evacuated silica tubes and annealed at 800°C for 10 days and then furnace cooled.

2.2. Structure Analysis

The data for the new pnictides RE_5M_2X (see Table 1) were collected using Siemens D5000 ($CuK_{\alpha 1}$ radiation) and Scintag ($CuK_{\alpha 1}$ and $CuK_{\alpha 2}$ radiation, cooled solid state detector) powder diffractometers. The patterns revealed the new phases to be isostructural with the known RE_5M_2X compounds. The CSD (31) program package was used to describe the peak profiles and determine their 2θ-angle values, and the lattice parameters were derived by the least squares procedure (Table 1).

The structures of Ho_5Ni_2Sb and Ho_5Ni_2Bi were refined by the Rietveld method (Fig. 1, program FullProf (32)). The final R - factors as well as the details relevant to the data collections and refinements are compiled in Table 2. The atomic and isotropic thermal parameters are given in Table 3, the interatomic distances are presented in Table 4.

During the refinement of erbium nickel bismuthide (15) a large temperature factor was observed for the Ni atoms. During the final steps of the refinement the occupancy factor for Ni was allowed to deviate from unity which led to the Ni deficiency ($Er_5Ni_{1.72(4)}Bi$) and to a lower *R*-value. On the basis of this finding for the Er compound, partial occupancies were assigned to the other rare-earth nickel bismuthides (15), but the refinement of Ho_5Ni_2Sb and Ho_5Ni_2Bi (this work) did not yield a Ni deficiency for these compounds. For Ho_5Ni_2Sb and Ho_5Ni_2Bi the temperature factors of the Ni atoms were even lower than for the other elements, which was a convincing argument for the Ni position being fully occupied. So, only $Er_5Ni_{1.72(4)}Bi$ was found to occur with a Ni deficiency (Table 1), all other pnictides were assumed to have the ideal composition RE_5M_2X. However, this assumption does not rule out a Ni deficiency in other compounds and a possible deviation from the composition RE_5M_2X must be checked for each pnictide individually, when needed.

Small differences between the lattice parameters for Ho_5Ni_2Sb and Ho_5Ni_2Bi, previously reported (13, 15) and obtained by the Rietveld method, are due to variations in the sample preparation, treatment and equipment, used.

Table 1. Lattice Parameters of the RE_5M_2X Pnictides

Compound	a, Å	c, Å	c/a	V, Å^3	Reference
Y_5Ni_2Sb	7.662(3)	13.502(9)	1.762	792.7	(13)
Gd_5Ni_2Sb	7.698(3)	13.403(9)	1.741	794.3	this work
Tb_5Ni_2Sb	7.641(2)	13.266(5)	1.736	774.5	(13)
Dy_5Ni_2Sb	7.593(2)	13.258(5)	1.746	764.4	(13)
Ho_5Ni_2Sb*	7.563(1)	13.250(3)	1.752	757.9	(13)
Er_5Ni_2Sb	7.531(2)	13.178(7)	1.750	747.4	(13)
Tm_5Ni_2Sb	7.459(3)	13.252(9)	1.777	737.3	this work
Lu_5Ni_2Sb	7.429(2)	13.190(8)	1.775	728.0	(13)
Y_5Ni_2Bi	7.673(2)	13.566(5)	1.768	798.7	(15)
Gd_5Ni_2Bi	7.756(2)	13.537(6)	1.745	814.3	(15)
Tb_5Ni_2Bi	7.693(2)	13.445(6)	1.748	796.0	(15)
Dy_5Ni_2Bi	7.651(4)	13.450(9)	1.758	787.3	(15)
Ho_5Ni_2Bi*	7.624(4)	13.420(6)	1.760	780.0	(15)
$Er_5Ni_{1.72(4)}Bi$	7.5813(9)	13.395(2)	1.767	769.8	(15)
Tm_5Ni_2Bi	7.522(4)	13.411(8)	1.783	758.8	(15)
Lu_5Ni_2Bi	7.429(2)	13.415(9)	1.806	740.3	(15)
Y_5Pd_2Sb	7.733(1)	13.582(5)	1.756	812.2	(16)
Gd_5Pd_2Sb	7.812(3)	13.645(7)	1.747	832.7	this work
Tb_5Pd_2Sb	7.730(2)	13.508(5)	1.747	807.1	(16)
Dy_5Pd_2Sb	7.715(2)	13.507(4)	1.750	804.0	(16)
Ho_5Pd_2Sb	7.6795(7)	13.476(8)	1.755	794.7	(16)
Er_5Pd_2Sb	7.641(4)	13.465(9)	1.762	786.2	(16)
Tm_5Pd_2Sb	7.585(2)	13.457(6)	1.774	774.2	(16)
Lu_5Pd_2Sb	7.5531(8)	13.345(2)	1.767	761.3	(16)
Y_5Pd_2Bi	7.779(1)	13.699(5)	1.761	829.0	this work
Gd_5Pd_2Bi	7.864(2)	13.644(4)	1.735	843.8	this work
Tb_5Pd_2Bi	7.820(1)	13.585(2)	1.737	830.8	this work
Dy_5Pd_2Bi	7.770(2)	13.558(5)	1.745	818.5	this work
Ho_5Pd_2Bi	7.719(1)	13.563(5)	1.757	808.1	this work
Er_5Pd_2Bi	7.695(1)	13.527(4)	1.758	801.0	this work
Tm_5Pd_2Bi	7.652(1)	13.474(4)	1.761	788.9	this work
Lu_5Pd_2Bi	7.586(2)	13.440(6)	1.772	773.4	this work

* lattice parameters from the Rietveld refinement (this work) are given in Table 2

Table 2. Collection and Refinement Data for Ho_5Ni_2Sb and Ho_5Ni_2Bi

	Ho_5Ni_2Sb	Ho_5Ni_2Bi
Space group (Pearson symbol)	*I4/mcm* (*tI*32)	*I4/mcm* (*tI*32)
Lattice parameters, Å	a = 7.5793(3) c = 13.2864(6)	a = 7.6140(3) c = 13.4435(6)
Diffractometer	Scintag	Scintag
Wavelenght	Cu$K_{\alpha 1}$ and Cu$K_{\alpha 2}$	Cu$K_{\alpha 1}$ and Cu$K_{\alpha 2}$
2θ and step	20°-90°, 0.02°	20°-90°, 0.02°
Reflections	188	192
Fitted parameters	19	15
$R_P = \Sigma \lvert y_{oi}-y_{ci} \rvert / \Sigma \lvert y_{oi} \rvert$	0.0636	0.0652
$R_{wP}=(\Sigma w_i(y_{oi}-y_{ci})^2/ \Sigma w_i(y_{oi})^2)^{1/2}$	0.0811	0.0856
$R_I = \Sigma \lvert I_o-I_c \rvert / \Sigma \lvert I_o \rvert$	0.0680	0.0348
$R_F = \Sigma \lvert F_o-F_c \rvert / \Sigma \lvert F_o \rvert$	0.0770	0.0318

$w_i = (y_{oi})^{-1/2}$.

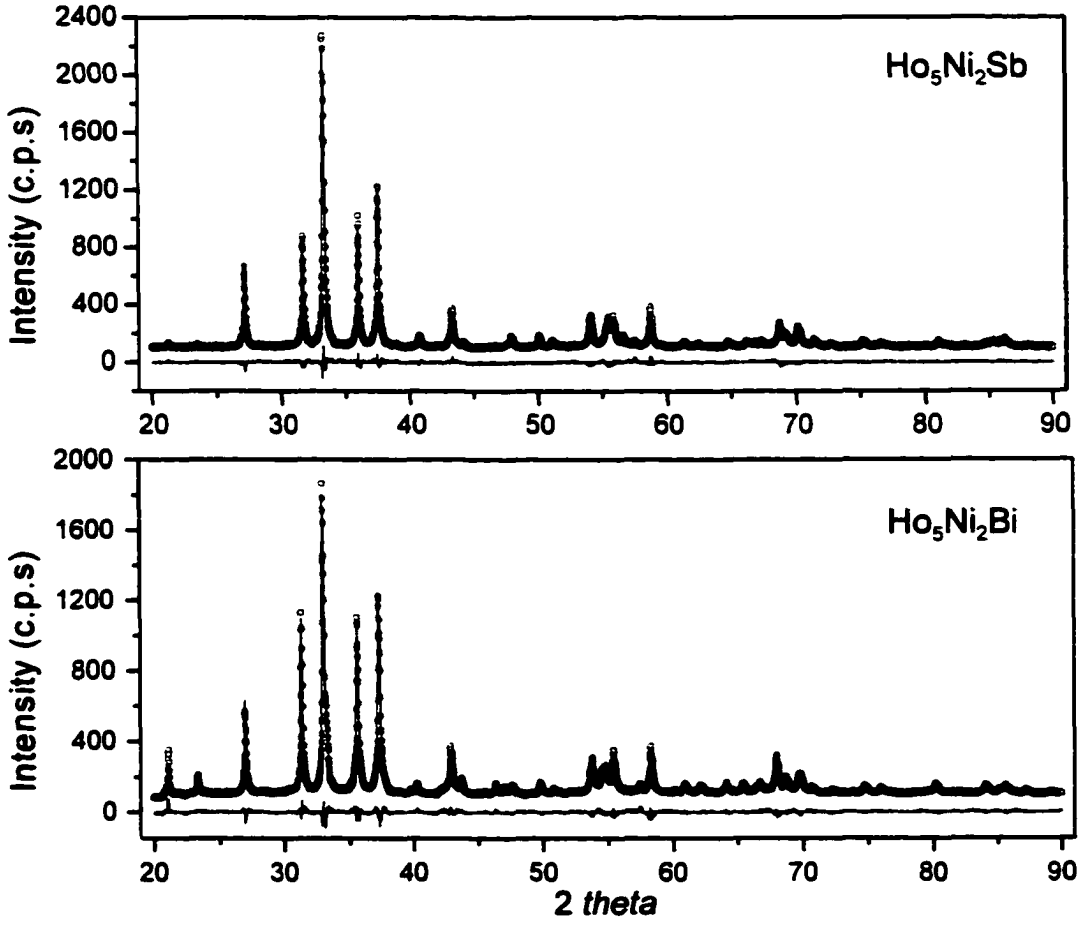

Figure 1. Observed (circles) and calculated (solid line) profiles and difference between them for Ho_5Ni_2Sb and Ho_5Ni_2Bi.

Table 3. Atomic and Isotropic Thermal (*B*iso, Å^2) Parameters for Ho_5Ni_2Sb and Ho_5Ni_2Bi (Space Group *I*4/*mcm*, Mo_5B_2Si-Type Structure)

		Ho_5Ni_2Sb				Ho_5Ni_2Bi			
Atom		*x*	*y*	*z*	*B*iso	*x*	*y*	*z*	*B*iso
Ho1	4*c*	0	0	0	2.71(13)	0	0	0	1.47(13)
Ho2	16*l*	0.1579(2)	*x*+½	0.1388(1)	3.03(6)	0.1555(2)	*x*+½	0.1372(1)	1.22(4)
Ni	8*h*	0.3675(6)	*x*+½	0	2.29(14)	0.3706(6)	*x*+½	0	0.58(14)
X	4*a*	0	0	¼	2.66(14)	0	0	¼	0.80(7)

Table 4. Interatomic Distances (Å) in Ho_5Ni_2Sb and Ho_5Ni_2Bi

Atoms	Ho_5Ni_2Sb	Ho_5Ni_2Bi	Atoms	Ho_5Ni_2Sb	Ho_5Ni_2Bi
Ho1 - 4Ni	2.961(4)	2.989(4)	Ho2 - 1Ho2	3.689(2)	3.690(3)
2*X*	3.3216(6)	3.3609(6)	2Ho2	3.802(2)	3.847(2)
8Ho2	3.400(1)	3.419(1)			
			Ni - 1Ni	2.842(6)	2.786(6)
Ho2 - 2Ni	2.879(4)	2.854(4)	4Ho2	2.879(4)	2.854(4)
1Ni	2.906(4)	2.962(4)	2Ho2	2.906(4)	2.962(4)
2*X*	3.215(1)	3.253(1)	2Ho1	2.961(4)	2.989(4)
1Ho2	3.386(2)	3.348(2)			
2Ho1	3.400(1)	3.419(1)	*X* - 8Ho2	3.215(1)	3.253(1)
1Ho2	3.553(2)	3.652(2)	2Ho1	3.3216(6)	3.3609(6)

X = Sb or Bi

2.3. Band Structure Calculations

Band structure calculations were performed by the extended Hückel tight binding (EHTB) method (33). To simplify calculations the antimonide Y_5Ni_2Sb, which does not require using f-orbitals, was chosen for an electronic structure characterization. Y_5Ni_2Sb, instead of Ho_5Ni_2Sb, is also the preferred choice because there are no well-tabulated atomic data for holmium for extended Hückel calculations. Atomic coordinates in Y_5Ni_2Sb were assumed to be the same as in refined Ho_5Ni_2Sb (Table 3). This assumption can be justified by similarity in the atomic coordinates of Ho_5Ni_2Sb and previously reported Gd_5Ni_2Sb (13) and by the fact that yttrium is close both crystallographically and chemically to the Gd-Lu lanthanoids.

The orbital energies and coefficients for the Slater-type orbitals were taken from (34). Then the parameters of Y and Ni were refined by the alternating charge iteration technique, while the Sb parameters were kept constant (Table 5).

Table 5. Parameters for the Extended Hückel Tight-Binding Calculations

Atom	Orbital	H_{ii}, eV	ξ_1	c_1[a]	ξ_2	c_2[a]
Y	5s	-6.82	1.39	1.00		
Y	5p	-4.30	1.39	1.00		
Y	4d	-6.56	4.33	0.5657	1.06	0.6575
Ni	4s	-6.83	1.825	1.00		
Ni	4p	-3.35	1.125	1.00		
Ni	3d	-9.76	5.75	0.5683	2.00	0.6292
Sb	5s	-18.80	2.323	1.00		
Sb	5p	-11.70	1.999	1.00		

[a] coefficients used in the double-zeta Slater-type orbitals

3. Results and Discussion

3.1. Structure Description

The RE_5M_2X compounds (Fig. 2) crystallize with the Mo_5B_2Si-type (35, 36) structure that is an ordered version of Cr_5B_3 in which the boron atoms occupy the two point positions 4(a) and 8(h). Distribution of the *M* and *X* atoms in RE_5M_2X (also the B and Si atoms in Mo_5B_2Si) on the boron sites in Cr_5B_3 obeys the stoichiometry as well as the size factor (13). More detailed structural description of the compounds depends on whether the electronic properties or the structural relationship to other compounds is to be emphasized. Traditionally, structures have been described in terms of coordination polyhedra (37,38). These polyhedra may be then oriented in various ways and connected via corners, edges, or faces. This approach allows visualization of coordination spheres and rationalizes bonding between the central atom and its close neighbors. Another concept describes crystal structures in terms of stacked layers, focusing on the atom connectivity. In this light, the structure of Ho_5Ni_2Sb (Fig. 2) can be built from Ho2 $3^2.4.3.4$ networks, known as an Archimedean tiling. There are four such layers per unit cell, two of them (***A***) are rotated at 45° to the other two (***B***) (Fig. 2), and their stacking order along the *c* direction is ***AABBAA***. Separation between the same tilings in Ho_5Ni_2Sb is 3.689Å, the distance between the different tilings is only 2.954Å. Superimposing the same two $3^2.4.3.4$ networks (***A*** or ***B***) produces voids in the shape of trigonal and tetragonal prisms, while combination of two different networks ***A+B*** forms tetrahedra and tetragonal antiprisms (Archimedian cubes). Small Ni atoms center the small trigonal prisms, larger Sb atoms center the tetragonal antiprisms and the Ho1 atoms are in the tetragonal prisms (Fig. 3). Now, the structure can be alternatively viewed as the stacking of two slabs in the *c* direction, one (*I*) being made of filled face-sharing trigonal and tetragonal prisms, the other (*II*) of empty tetrahedra and filled edge-sharing tetragonal antiprisms.

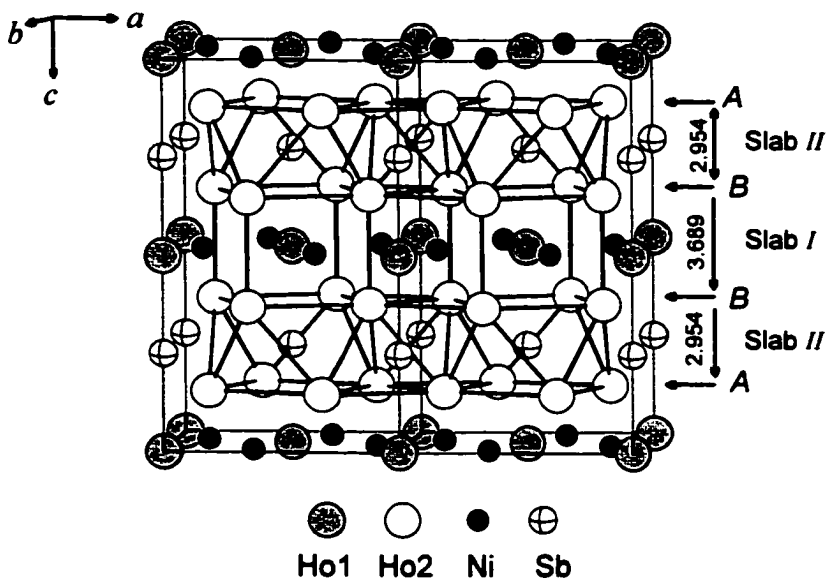

Figure 2. Structure of Ho_5Ni_2Sb wit emphases on the building slabs *I* and *II* and on the distances between $3^2.4.3.4$ Ho nets.

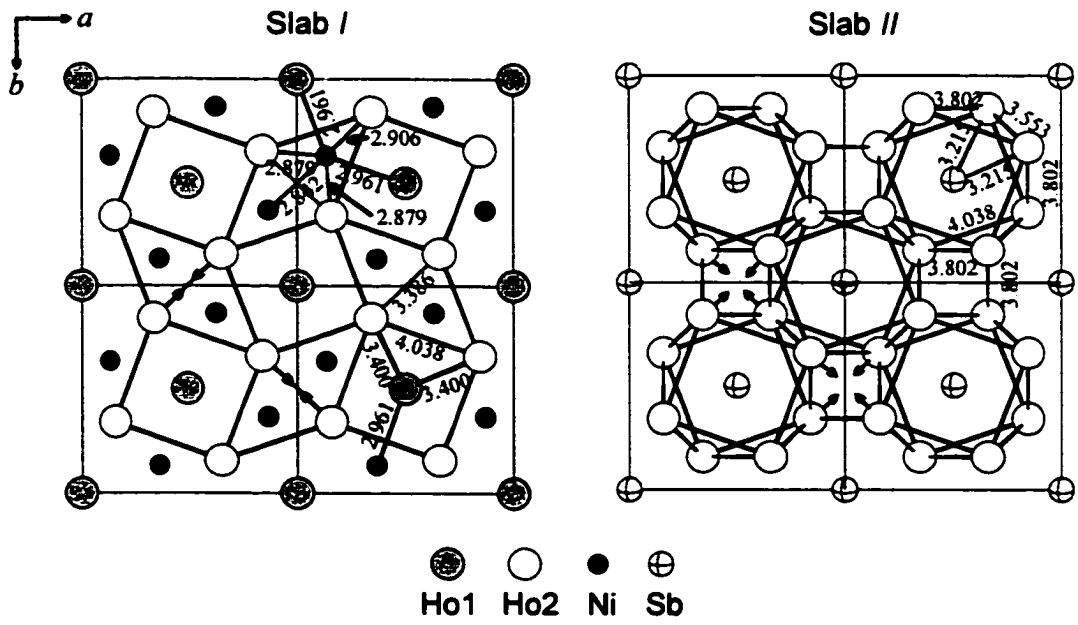

Figure 3. Projections of slabs *I* and *II* onto the *ab* plane. The arrows show the contractions of the Ho2-Ho2 bonds upon substitution of Sb by Bi.

Inserting Ni atoms in the small trigonal prisms of slab *I* results in Ho-Ni distances (Fig. 3 and Table 4) which are shorter than the sum of the metallic radii $r_{Ho}+r_{Ni}=1.743+1.246=2.989$Å. Antimony or bismuth atoms, located in large tetragonal antiprisms of slab *II*, do not interact strongly with eight

Ho neighbors at distances of 3.215Å and 3.253Å. There is variety of Ho-Ho distances in the structure, but only one Ho2-Ho2 bond in the $3^2.4.3.4$ network is of particular interest. These two atoms are shared by two base-fused triangles in the $3^2.4.3.4$ tiling and they belong to two different tetragonal antiprisms in slabs *II* (Fig. 3). This interatomic distance is quite short (3.386Å) in Ho_5Ni_2Sb but it is even shorter (3.348Å) in the larger Ho_5Ni_2Bi. The same trend is observed for the Ni-Ni interactions and one of Ni-Ho2 bonds. This is opposite to what one would expect from the substitution of Sb atoms by larger Bi atoms. Thus, a more detailed analysis of the structure is instructive.

Introducing Bi atoms in place of Sb atoms in the tetragonal antiprisms results in a larger volume and larger distances between the atoms forming the antiprism. Inflating the volume shortens the distances between Ho2 atoms, which belong to the neighboring antiprisms and form a base of the triangles in $3^2.4.3.4$ network. Shorter bases result in the shorter Ni-Ho2 distances and Ni atoms from the face-sharing trigonal prisms come closer. Other distances undergo a small increase in Ho_5Ni_2Bi as expected.

Table 1 presents lattice parameters for RE_5M_2X and Fig. 4 shows changes in unit cell volumes versus atomic number. The Pd compounds have larger ***a*** and ***c*** constants than the corresponding Ni compounds. The volume of all pnictides decreases gradually with the atomic number of the rare-earth and the plots reflect the well-known lanthanide contraction. We were not able to synthesize similar compounds with the lighter rare-earths or with ytterbium. The absence of Yb compounds in the series might be explained by its mixed valence and larger atomic radius.

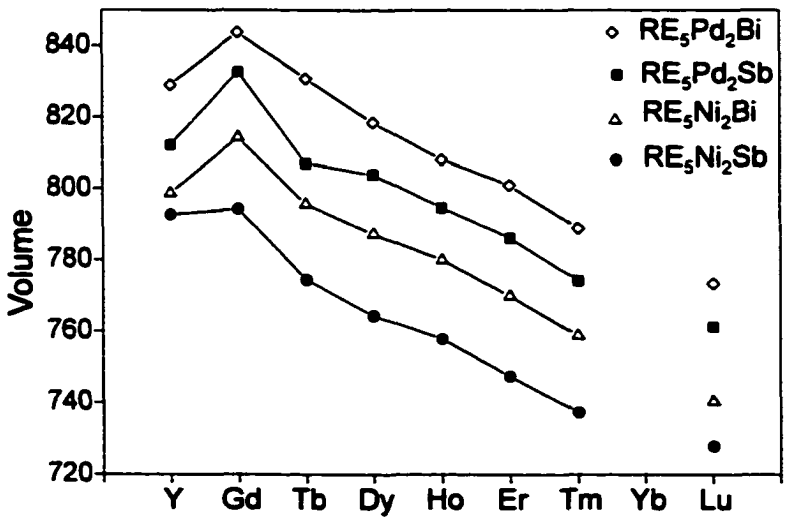

Figure 4. Unit cell volume ($Å^3$) versus atomic number for RE_5M_2X

3.2. Electronic Structure and Bonding

According to the composition and the structural pattern, RE_5M_2X must be metallic and the valence electrons must be delocalized. Band calculations were performed to gain more insight into bond strength and electron distribution. Figure 5 shows the total and projected densities of states (PDOS) for Y_5Ni_2Sb. As is typical for electron poor compounds, the Fermi level resides at the low-energy part of the conduction band composed in this case mostly of Y orbitals, with some contribution from Ni orbitals. The bonding contributions from *s* and *p* orbitals of Sb (the most electronegative element) with some mixture of Y orbitals lie at lower energies –13eV and –20eV (out of the presented energy window) separated by gaps from the conduction band. The sharp peak at -10eV corresponds mainly to contribution of *3d* Ni orbitals, which are quite localized. The existence of an Y contribution at this region shows covalent mixing of the Y orbitals with the Ni orbitals. On the other hand, the Ni orbitals, mainly *s*-type, interact with the Y orbitals, giving a flat PDOS curve at –9 to –5eV. The main contribution in this region comes from the Y *d* orbitals that produce most of the states in the vicinity of the Fermi level. According to the calculations Y_5Ni_2Sb and other RE_5M_2X phases should be good metallic conductors.

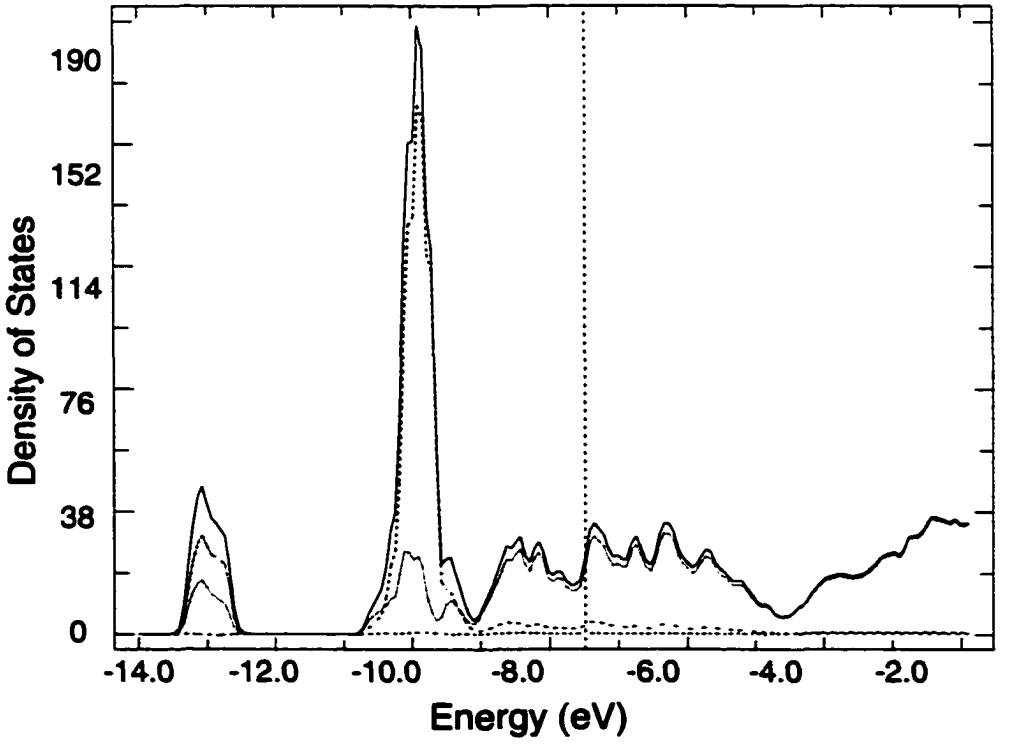

Figure 5. Total and projected densities of states for Y_5Ni_2Sb.Vertical line represents energy of the Fermi level. Solid line is total DOS, dotted line is Y contribution, dashed line is Ni contribution, and dash-dot line shows Sb contribution.

A complex structure like this presents a variety of distances and bond strengths. Comparisons of the interatomic distances with overlap populations allow one to see where matrix effects, separations fixed by geometric factors, may be more important than bonding in near-neighbor contacts. In cases of matrix effects an application of the empirical Pauling bond-order equation $D(n)=D(1)-0.6\log n$ (39), which assigns an order n to a bond of distance $D(n)$, is usually quite misleading and calculation of Mulliken overlap populations is preferred. For this purpose, pairwise overlap populations for Y-Y, Y-Ni and Y-Sb interactions along with the distances in increasing magnitude are listed in Table 6. The corresponding distances from Ho_5Ni_2Sb are given in the last column to simplify the association of the bonds in Y_5Ni_2Sb with the atomic arrangement in the structure. In general, there is parallel between the electron densities and bond lengths, but some significant deviations assist in highlighting important bonding details. For two Y2-Y2 bonds of 3.423Å and 3.856Å the MOPs are large: 0.374 and 0.246, even when compared to the average MOP of 0.277 in the yttrium metal with the average Y-Y distance of 3.6016Å. These four Y2 atoms form distorted tetrahedra in slab *II* (Fig.3), located between the tetragonal antiprisms consisting of Y2 atoms and centered by Sb atoms. The electron density of the bonds inside the tetrahedra is fairly high, which may seem to be rather unusual at the first instant, since these atoms are bound to relatively electronegative Sb atoms. But the Y2 pairs have the Sb neighbors only on one side, on the other side there are other Y2 pairs. The energy of these Y2 states is not as high as in the case with Sb on both sides, and more electrons are located in them. This agrees well with the previously discussed tendency of the early transition metals for strong metal-metal interactions, resulting in separate clusters as well as frameworks. Contrarily, a Y2-Y2 pair of 3.605Å, which bridges two edge-sharing tetragonal antiprisms in slab *II*, have a small MOP of 0.189, which indicates a lower electron concentration and weaker bonding. Now, this is not surprising, since this bond is more isolated from the Y2 neighbors and is between two Sb atoms. The fourth Y2-Y2 bond of 3.749Å reflects the interaction between two yttrium $3^2.4.3.4$ tilings of the same kind, ***A*** or ***B***, and it is fairly strong (MOP=0.222). There is also bonding between crystallographically different yttrium atoms, which arises from the centering of the Y2 tetragonal prisms by Y1atoms. Despite being short (3.442Å) the Y1-Y2 bonds are not the strongest among the Y-Y interactions. The natural assumption is that this distance is moderately to heavily influenced by matrix effects. The analysis of the Y-Y bonds shows that the description of the Y2 (Ho2) host structure, based only on geometrical factors, does not reflect strong bonding interactions and is mainly presented to visualize the structural relationship and make the description easier.

Table 6. Interatomic Distances and MOPs per Atomic Pair for Y_5Ni_2Sb (a = 7.662Å and c = 13.502Å, Atomic Coordinates from Ho_5Ni_2Sb) and Corresponding Distances in Ho_5Ni_2Sb

Bond	No.	Distance in Y_5Ni_2Sb	MOP in Y_5Ni_2Sb	Distance in Ho_5Ni_2Sb
Y1 - Y2	32×	3.442	0.232	3.400
Y1 - Ni	16×	2.993	0.123	2.961
Y1- Sb	8×	3.375	0.248	3.322
Y2 - Y2	8×	3.423	0.374	3.386
Y2 - Y2	8×	3.605	0.189	3.553
Y2 – Y2	8×	3.749	0.222	3.689
Y2 – Y2	16×	3.856	0.246	3.802
Y2 - Ni	32×	2.916	0.128	2.879
Y2 - Ni	16×	2.944	0.128	2.906
Y2 - Sb	32×	3.254	0.304	3.215
Ni - Ni	4×	2.873	-0.066	2.842
Ni - Y2	32×	2.916	0.128	2.879
Ni - Y2	16×	2.944	0.128	2.906
Ni – Y1	16×	2.993	0.123	2.961
Sb – Y2	32×	3.254	0.304	3.215
Sb – Y1	8×	3.375	0.248	3.322

There are three kinds of Y-Ni bonds, all of them come from slab *I* and result from the centering of the trigonal Y2 prisms by Ni atoms. The shortest Y2-Ni bond of 2.916Å has a electron density (MOP=0.128) similar to that of the largest Y1-Ni bond of 2.993Å (MOP=0.123). These Y-Ni interactions are somewhat weaker than the Y-Ni interactions in binary YNi (MOPs are 0.147 to 0.184 for distances 2.897 to 2.992Å). As mentioned above, trigonal prisms with a central late transition metal are characteristic features of the metal-rich pnictides and chalcogenides and the compounds RE_5M_2X are of no exception here. The $Y(2)_6Ni$ prisms joined with the $Y(2)_6Y(1)$ tetragonal prisms shape one part (slab *I*) of the structure, where strong metal-metal bonds seem to play the key role.

The second part (slab *II*) of the structure, composed of Y2 and Sb, has strong Y-Sb bonding and MOP of 0.304 reflects these interactions with interatomic distances of 3.254Å. There are also interactions of Sb atoms with eclipsed Y1 atoms from the neighboring slabs *I*, but as expected from the bond distances, these interactions are weaker. Except for the bonding in the Y2 tetrahedra, there are no strong dimensionally preferred interactions. This is different from what is often encountered in

the early-late transition metal chalcogenides and pnictides, e.g., $Sc_5Ni_2Te_2$ contains channels of Sc atoms, filled with Ni atoms (25).

Crystal orbital overlap populations (COOP) were also calculated to gain more insight into different interatomic bonds. The COOP curves of the Y-Y, Y-Ni and Y-Sb interactions are shown in Fig.6. The overlap between Y and Sb orbitals is strongly bonding at -13eV and -20eV (out of the given energy window) and becomes slightly antibonding at the Fermi level, the Y-Ni and Y-Y interactions are bonding until -4.8eV. The Y-Y and Y-Ni bonds contribute significantly to the region at the Fermi level and become even more bonding at the higher energy, around -7eV. Over -5eV both interactions are antibonding, especially the Y-Y overlap falls steeply into negative region. Theoretically, introducing more electrons would increase the Y-Ni and Y-Y bonding, while the Y-Sb interactions would remain almost unchanged. The bonding would be optimized for valence electron count of 55 electrons with the bonding-antibonding transition of the Y-Ni and Y-Y states at around -4.8eV. The valence electron number of 55 per formula unit would correspond to the phases of the same composition with *VIB* elements, the phases with intermediate electron counts from 40 (number of valence electrons per formula unit in RE_5M_2X) to 55 would have *IVB* and *VB* elements instead of rare-earths. However, our attempts to synthesize isostructural E_5M_2X compounds, where E = Zr, Hf, Nb, Ta, Mo, W and M = Ni or Co, were unsuccessful.

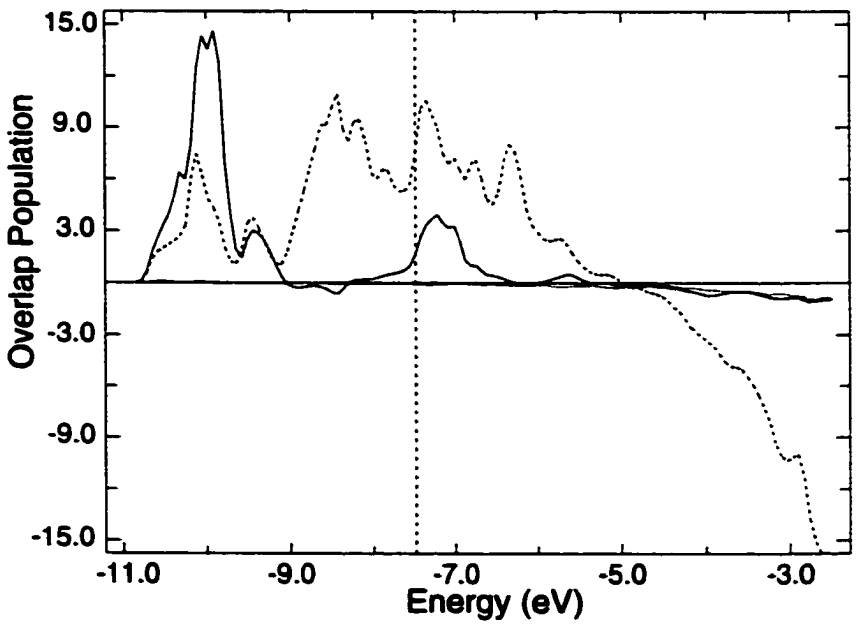

Figure 6. COOP curves for Y_5Ni_2Sb. Interactions in the upper part are bonding (+), in the lower part antibonding (-). Solid line is Y-Ni interactions, dashed line is Y-Y, and dotted line is Y-Sb interactions.

If the number of electrons is reduced, the Fermi level falls into the slightly antibonding region of the Y-Ni states, which is unfavorable and besides, reduces the total binding energy of the structure. This observation might explain, why we could not obtain holmium antimonides with chromium, manganese, iron and cobalt.

Acknowledgements

This research was supported by the Office of the Basic Energy Sciences, Materials Sciences Division, US Department of Energy, DOE. The Ames Laboratory is operated for DOE by Iowa State University under contract No. W-7405-Eng-82.

Special thanks to Alexandra O. Pecharsky for collecting powder diffraction data for the Rietveld refinement.

References

1. O. Sologub, K. Hiebl, and P. Rogl, *J. Alloys Compd.* **210**, 153 (1994).
2. O. Sologub, K. Hiebl, P. Rogl, and O. I. Bodak, *J. Alloys Compd.* **227**, 40 (1995).
3. O. Sologub, M. Vybornov, P. Rogl, and K. Hiebl, *J. Solid State Chem.* **122**, 266 (1996).
4. K. Hartjes and W. Jeitschko, *J. Alloys Compd.* **226**, 81 (1995).
5. M. J. Fergunson, R. W. Hushagen, and A. Mar, *J. Alloys Compd.* **249**, 191 (1997).
6. V. K. Pecharsky, Yu. V. Pankevich, and O. I. Bodak, *Sov. Phys.-Crystallogr.* **28**, 97 (1983).
7. P. Wollesen, W. Jeitschko, M. Brylak, and L. Dietrich, *J. Alloys Compd.* **245**, L5 (1996).
8. W. K. Hoffman and W. Jeitschko, *J. Less-Common Met.* **138**, 313 (1988).
9. G. Bolloré, M. J. Fergunson, R. W. Hushagen, and Arthur Mar, *Chem. Mater.* **7**, 2229 (1995).
10. M. Brylak and W. Jeitschko, *Z. Naturforsch. B:Chem. Sci.* **50**, 899 (1995).
11. R. A. Gordon, F. J. DiSalvo, and R. Pöttgen, *J. Alloys Compd.* **228**, 16 (1995).
12. A. E. Dwight, *Acta Crys*tallogr., *Sect. B: Struct. Crystallogr. Cryst. Chem.* **B33**, 1579 (1977).
13. Y. Mozharivskyj and Y. B. Kuz'ma, *J. Alloys Compd.* **236**, 203 (1996).
14. A. E. Dwight, *Proceedings of the Rare Earth Research Conference, 11th, Michigan, 1974*, **2**, 642 (1974).
15. Y. Mozharivskyj and Y. B. Kuz'ma, *Metally*, **4**, 139 (1999).
16. S. I. Mykhalenko, Y. Mozharivskyj, and Y. B. Kuz'ma, *Dopov. Nats. Akad. Nauk Ukr.* **10**, 108 (1998).
17. D. Hohnke and E. Parthe, *J. Less-Common Met.* **17**, 291 (1969).
18. L. Brewer and P. R. Wengert, *Metall. Trams.* **4**, 2674 (1973).

19. R. L. Abdon and T. Hughbanks, *J. Am. Chem. Soc.* **117**, 10035(1995).
20. C. Wang and T. Hughbanks, *Inorg. Chem.* **35**, 6987 (1996).
21. H. Kleinke and H. F. Franzen, *Inorg. Chem.* **35**, 5272 (1996).
22. B. Harbrecht and H. F. Franzen, *J. Less-Common Met.* **113**, 349 (1985).
23. H. Kleinke, *J. Alloys Compd.* **252**, L29 (1997).
24. H. Kleinke, *J. Alloys Compd.* **270**, 136 (1998).
25. P. A. Mggard and J. D. Corbett, *Inorg. Chem.* **38**, 1945 (1999).
26. M. Wang, R. McDonald, and A.Mar, *Inorg. Chem.* **38**, 3435 (1999).
27. M. Koeckerling and H. F. Franzen, *Croatica Chem. Acta*, **68**(4), 709 (1995).
28. H. Kleinke and H. F. Franzen, *J. Alloys Compd.* **38**, 68 (1996).
29. H. Kleinke and H. F. Franzen, *J. Alloys Compd.* **255**, 110 (1997).
30. H. Kleinke and H. F. Franzen, *Angew. Chem., Int. Ed. Engl.* **36(5)**, 513 (1997).
31. L. G. Akselrud, Y. M. Grin, V. K. Pecharsky, and P. Y. Zavalij, "CSD - universal program package for single crystal and powder data treatment", *Proc.12th European Crystallographic Meet., Moscow, August 20-28, 1989*, Academy of Sciences, Moscow, USSR, *Kristallographiya, Suppl.* **155**, 2 (1989).
32. J. Rodriguez-Carvajal, "FullProf", Version 3.5, 1997.
33. J. Ren, W. Liang and M.-H. Whangbo, "Crystal and Electronic Structure Analyzer (CAESAR)", North Carolina State University, Raleigh, NC, 1998.
34. S. Alvarez, "Table of Parameters for Extended Hückel Calculations", Barcelona, 1987.
35. H. Nowotny, E. Dimakopoulou, and H. Kudielka, *Monatsh. Chem.* **88**, 180 (1957).
36. B. Aronsson, *Acta Chem. Scand.* **12**, 31 (1958).
37. E. I. Gladyshevski and Yu. N. Grin', *Kristallografiya*, **26**, 1204 (1981).
38. Y. B. Kuz'ma, "Kristallochimiya Boridov", in Russian, Vyshcha Shkola, Lvov, Ukraine, 1983.
39. L. Pauling, "The Chemical Bond", Cornell Univ. Press, Ithaca, NY, 1967.

APPENDIX D. CRYSTAL STRUCTURE OF RARE-EARTH RICH PLATINIUM PNICTIDES RE_5Pt_2X (RE = Y, Gd, Tb, Dy, Ho, Er, Tm, Lu; X = Sb, Bi) AND MAGNETIC PROTERTIES OF Er_5Pt_2Bi

A paper published in Journal of Alloys and Compounds
J. Alloys Comp. 327 (2000) 78

Yurij Mozharivskyj and Hugo F. Franzen
Department of Chemistry and Ames Laboratory of US DOE, Spedding Hall, Iowa State University, Ames, Iowa 50011, USA

Abstract

Fifteen new rare-earth antimonides and bismuthides RE_5Pt_2X (see Table 1) have been synthesized and characterized by X-ray powder methods. The compounds are isostructural to previously reported RE_5M_2X pnictides and adopt the Mo_5B_2Si structure (*I4/mcm* space group, an ordered variant of Cr_5B_3). The RE_5M_2X series now includes 47 antimonides and bismuthides with M = Ni, Pd, Pt and the heavy rare earths except for ytterbium. Atomic and thermal parameters have been refined and the magnetic susceptibility was measured for Er_5Pt_2Bi.

Introduction

Recently, we have reported on the crystal structure and bonding of the rare-earth rich ternary pnictides RE_5M_2X (RE = Y, Gd, Tb, Dy, Ho, Er, Tm, Lu; M = Ni, Pd; X = Sb, Bi) (1). Calculation of crystal orbital overlap populations (COOP) for Y_5Ni_2Sb showed bonding Y-Y, Y-Ni and non-bonding Y-Sb interactions at and above the Fermi level (-7.5eV). Over -4.8eV both bonding Y-Y and Y-Ni interactions become antibonding, especially the Y-Y overlap population falls steeply into a negative region [1]. Theoretically, introducing more electrons up to -4.8eV would increase the total Y-Ni and Y-Y overlap population and, thus, the Y-Ni and Y-Y bonding, while the Y-Sb interactions would remain almost unchanged. The bonding would be optimized for a valence electron count of 55 electrons per unit formula with the bonding-antibonding transition of the Y-Ni and Y-Y states at around -4.8eV. The valence electron number of 55 per formula unit would correspond to the phases of the same composition with *VIB* elements, the phases with intermediate electron counts from 40 (number of valence electrons per formula unit in RE_5M_2X) to 55 would have *IVB* and *VB* elements

instead of rare earths. However, all attempts to synthesize isostructural E_5M_2X antimonides and bismuthides, where E = Zr, Hf, Nb, Ta, Mo, W and M = Ni or Co, were unsuccessful. Planned substitution of rare-earth atoms by E atoms only inside the tetragonal prism (4*c* position) did not give desired RE_4EM_2X phases.

On the other hand, substitution of Ni and Pd atoms by Pt atoms would not change the valence electron count. The states of the 5*d* Pt orbitals would be shifted to higher energies but still they would be below the Fermi level. The character of DOS and COOP curves for RE_5Pt_2X would be similar to those for nickel- and palladium-containing phases. Thus it was concluded that isostructural phases with platinum were possible and later they were indeed experimentally obtained. The structure was refined and a magnetic susceptibility was measured for Er_5Pt_2Bi.

2. Experimental Procedures

2.1. Synthesis

The starting materials were ingots of RE elements (with purity not less than 99.8%), antimony (99.99%, Johnson Matthey GmbH), bismuth (99.999%, ChemPur), and platinum (99.9%, Metals Development, Ames Laboratory). The mixtures of the components with the initial compositions RE_5Pt_2X and with a total weight of 0.5g were arc-melted in an argon atmosphere, then turned over and remelted to reach homogeneity. The samples were sealed in evacuated silica tubes and annealed at 800°C for 10 days and then furnace cooled.

2.2. X-Ray Analysis

The powder diffraction data of the new pnictides RE_5Pt_2X (see Table 1) were recorded with a Guinier camera (FR 552, ENRAF-NONIUS, Cu$K\alpha_1$) with silicon as an internal standard. The patterns revealed the new phases to be isostructural with the known RE_5M_2X compounds. The Guinier patterns were laser scanned to obtain peak positions, and the lattice parameters (Table 1) were determined by the least-squares procedure using the CSD program package [2].

For structure refinement the data for Er_5Pt_2Bi were collected at a Scintag powder diffractometer (Cu$K_{\alpha 1}$ and Cu$K_{\alpha 2}$ radiation, cooled solid state detector). The atomic and isotropic thermal parameters were refined by the Rietveld method (Fig. 1, program FullProf [3]). The final R - factors as well as the details relevant to the data collections and refinements are compiled in Table 2. The atomic and isotropic thermal parameters are given in Table 3, the interatomic distances are presented in Table 4.

Table 1. Lattice Parameters of the RE_5Pt_2X Pnictides

Compound	a, Å	c, Å	c/a	V, Å^3
Y_5Pt_2Sb	7.675(3)	13.575(9)	1.769(1)	799.6(7)
Gd_5Pt_2Sb	7.801(2)	13.556(5)	1.7377(8)	825.0(4)
Tb_5Pt_2Sb	7.748(3)	13.463(9)	1.738(1)	808.2(7)
Dy_5Pt_2Sb	7.686(3)	13.420(9)	1.746(1)	792.8(7)
Ho_5Pt_2Sb	7.681(3)	13.365(9)	1.740(1)	788.5(7)
Er_5Pt_2Sb	7.666(3)	13.391(8)	1.747(1)	787.0(6)
Tm_5Pt_2Sb	7.584(3)	13.394(9)	1.766(1)	770.4(7)
Lu_5Pt_2Sb	7.519(3)	13.326(7)	1.772(1)	753.4(6)
Y_5Pt_2Bi	7.735(4)	13.661(5)	1.766(1)	817.3(6)
Gd_5Pt_2Bi	7.851(2)	13.687(7)	1.743(1)	843.6(5)
Tb_5Pt_2Bi	7.783(3)	13.599(9)	1.747(1)	823.8(7)
Dy_5Pt_2Bi	7.744(2)	13.557(9)	1.751(1)	813.0(6)
Ho_5Pt_2Bi	7.710(2)	13.576(8)	1.761(1)	807.0(6)
Er_5Pt_2Bi	7.6982(8)	13.561(3)	1.7616(4)	803.7(2)
Tm_5Pt_2Bi	7.642(2)	13.491(8)	1.765(1)	787.9(5)

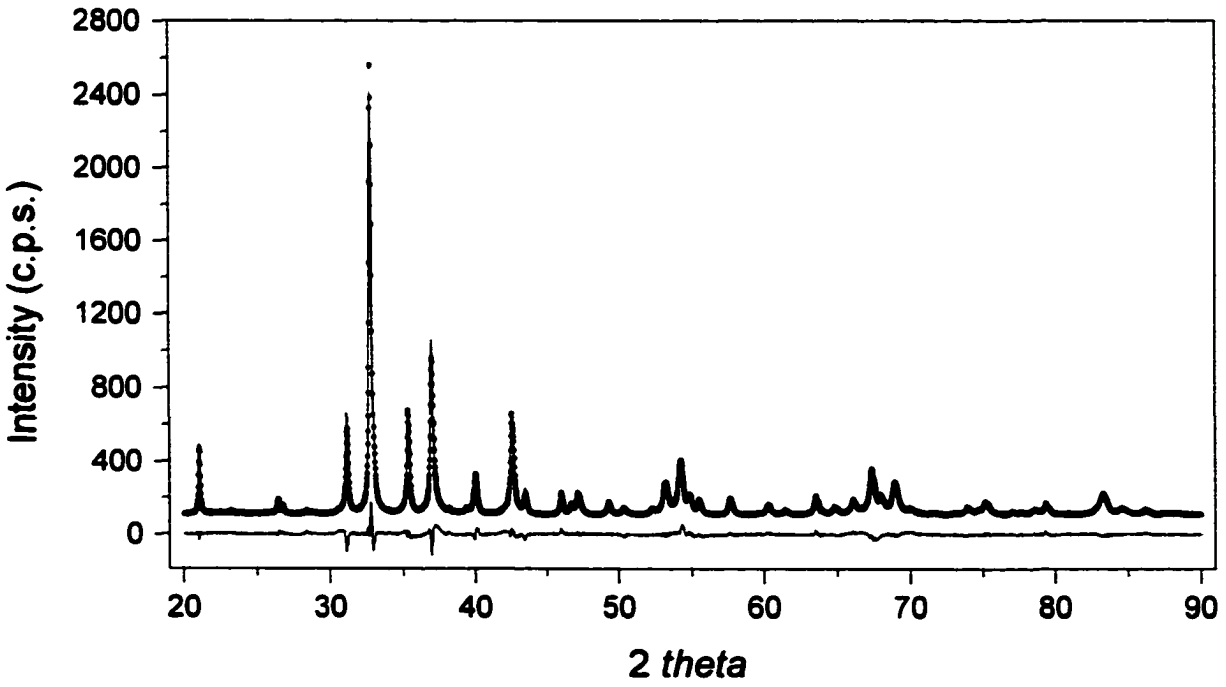

Figure 1. Experimental (circles) and calculated (solid line) profiles and difference between them for Er_5Ni_2Bi.

Table 2. Collection and Refinement Data for Er_5Pt_2Bi

Space group (Pearson symbol)	*I4/mcm* (*tI*32)
Lattice parameters, Å	a = 7.7012(3)
	c = 13.5599(4)
Diffractometer	Scintag
Wavelength	Cu$K_{\alpha 1}$ and Cu$K_{\alpha 2}$
2θ and step	20°-90°, 0.02°
Reflections	194
Fitted parameters	15
$R_P = \Sigma \lvert y_{oi}-y_{ci} \rvert / \Sigma \lvert y_{oi} \rvert$	0.118
$R_{wP}=(\Sigma w_i(y_{oi}-y_{ci})^2 / \Sigma w_i(y_{oi})^2)^{1/2}$	0.129
$R_I = \Sigma \lvert I_o-I_c \rvert / \Sigma \lvert I_o \rvert$	0.0496
$R_F = \Sigma \lvert F_o-F_c \rvert / \Sigma \lvert F_o \rvert$	0.0388

$w_i = (y_{oi})^{-1/2}$.

Table 3. Atomic and Isotropic Thermal (B_{iso}, Å^2) Parameters for Er_5Pt_2Bi (*I4/mcm* space group, Mo_5B_2Si-type structure)

Atom		x	y	z	B_{iso}
Er1	4*c*	0	0	0	2.13(11)
Er2	16*l*	0.15581(16)	x+½	0.13793(9)	1.47(5)
Pt	8*h*	0.36124(18)	x+½	0	1.31(5)
Bi	4*a*	0	0	¼	1.63(7)

Table 4. Interatomic Distances (Å) in Er_5Pt_2Bi

Atoms		Atoms	
Er1 – 4Pt	2.980(1)	Er2 – 1Er2	3.741(2)
2Bi	3.3900(4)	2Er2	3.873(2)
8Er2	3.459(1)		
		Pt – 2Er2	2.916(2)
Er2 – 1Pt	2.916(2)	4Er2	2.943(2)
2Pt	2.943(2)	2Er1	2.980(1)
2Bi	3.283(1)	1Pt	3.023(2)
1Er2	3.394(2)		
2Er1	3.459(1)	Bi – 8Er2	3.283(1)
1Er2	3.667(2)	2Er1	3.3900(4)

2.3. Magnetic Measurements

Magnetic measurements for a bulk Er_5Pt_2Bi sample, annealed at 800°C, were performed in the temperature range 1.7-350 K and in applied magnetic fields up to 55 kOe, using a Quantum Design MPMS-5 SQUID magnetometer.

3. Results and Discussion

3.1. Structure Description

The RE_5Pt_2X compounds crystallize with the Mo_5B_2Si-type [4, 5] structure that is an ordered version of Cr_5B_3. Detailed description of the structure can be found in references [1] and [6]. Here we will give only a short outline of the refined Er_5Pt_2Bi structure (Fig. 2). There are two types of Er2 3^2434 layers that are rotated by 45° with respect to each other and they alternate along the *c* direction. Stacking of these layers produces trigonal (occupied by Pt) and tetragonal (occupied by Er1) prisms, tetragonal antiprisms (filled with Bi) and empty tetrahedra. The Er-Er and Er-Bi interatomic distances are close to the sum of metallic radii, somewhat short distances are observed for Er-Pt interactions (the sum of the metallic radii $r_{Er} + r_{Pt} = 1.734 + 1.373 = 3.107$ Å). These distance observations were found in the previously reported refined structures of Ho_5Ni_2Sb and Ho_5Ni_2Bi [1].

Table 1 presents lattice parameters for RE_5Pt_2X and Fig. 3 shows changes in unit cell volumes versus atomic number. The bismuthides have larger *a* and *c* constants than the corresponding antimonides. The volume of all pnictides decreases gradually with the atomic number of the rare-

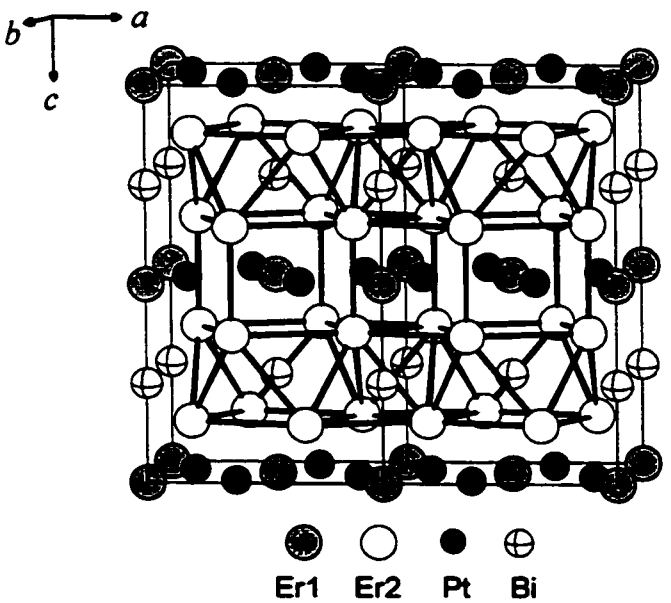

Figure 2. Structure of Er_5Ni_2Bi with emphases on the $3^2.4.3.4$ Er nets.

earth and the plots reflect the well-known lanthanide contraction. We could not synthesize similar compounds with the lighter rare earths or with ytterbium. Also Lu_5Pt_2Bi could not be prepared in the course of our experiments. The absence of Yb compounds in the series might be explained by its mixed valence and larger atomic radius. An interesting feature can be seen on the plot (Fig. 3): the unit cell volume curves have steeper slopes after erbium. So far, we have no explanation for this unusual behavior.

Calculation of the Mulliken overlap population (MOP) for Y_5Ni_2Sb (1) indicated strong Y-Y and Y-Ni interactions, which is typical for the metal rich compounds. On the basis of similarity in the structures and interatomic distances of Y_5Ni_2Sb and RE_5Pt_2X we can assume the same type of interaction in RE_5Pt_2X.

3.2. Magnetic Properties of Er_5Pt_2Bi

The temperature dependence of the inverse molar magnetic susceptibility of Er_5Pt_2Bi is presented in Fig. 4. The susceptibility above 50 K follows the Curie-Weiss (CW) law, with the CW parameters being θ_p = -6.7(7) K and μ_{eff} = 9.8(1) μ_B. It is worth noting that the experimental value of the effective magnetic moment is close to the value expected for a free Er^{3+} ion with the $4f^{11}$ electronic configuration ($g\sqrt{J(J+1)} = 9.59$). This observation supports a localized character of the *f* electrons and shows that their role in the bond formation is rather small.

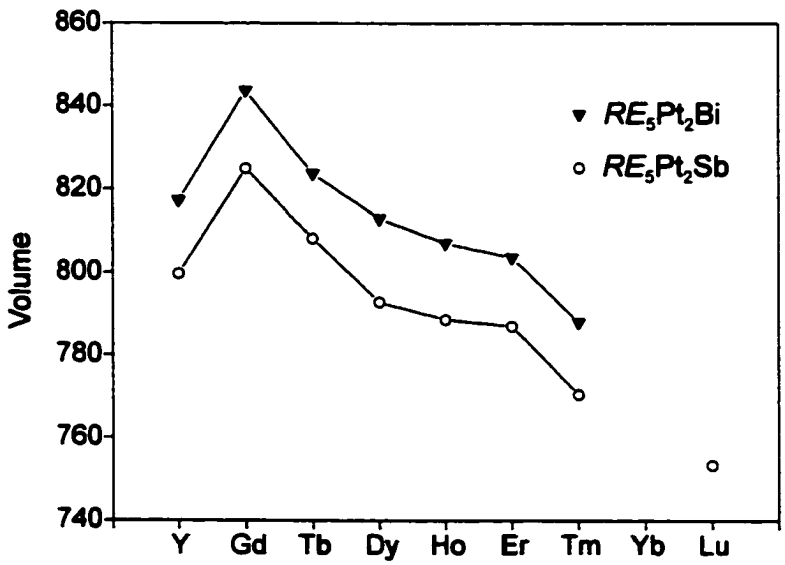

Figure 3. Unit cell volume (Å^3) versus atomic number for RE_5Pt_2X.

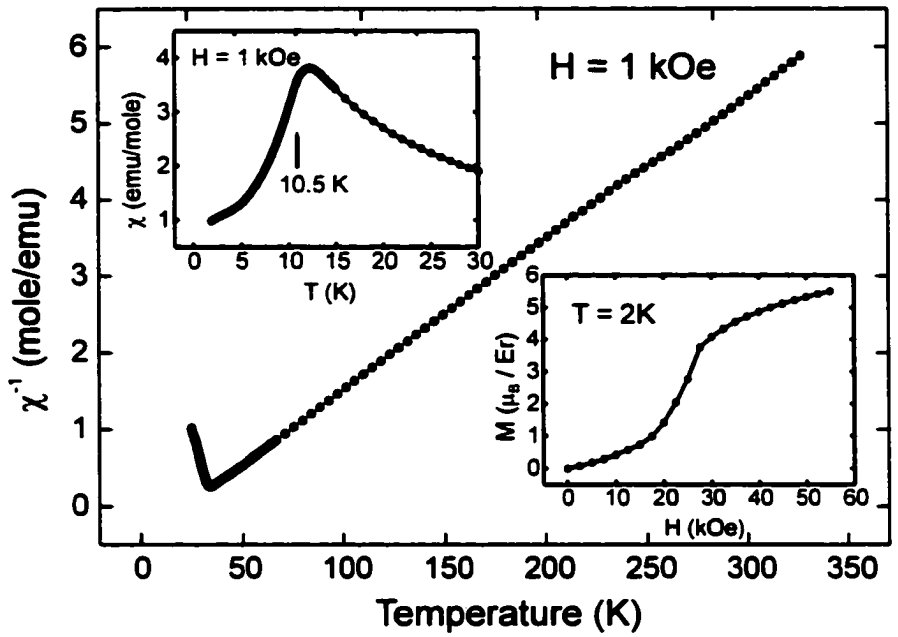

Figure 4. Magnetic data for Er_5Ni_2Bi.

As is apparent from the upper inset to Fig. 4, showing the behavior of $\chi(T)$ at low temperatures, Er_5Pt_2Bi orders antiferromagnetically at 10.5 K. An antiferromagnetic nature of the ground state in the compound is studied by a characteristic field variation of the magnetization (see the lower insert to Fig. 4), which exhibits a metamagnetic-like transition at about 25 kOe. At 2 K the magnetization of Er_5Pt_2Bi shows a tendency to saturation in high fields and the erbium magnetic moment at 2 K in 55 kOe amounts to 5.5 μ_B, which is smaller than the moment expected for Er^{3+} ($gJ = 9$).

Acknowledgements

This research was supported by the Office of the Basic Energy Sciences, Materials Sciences Division, US Department of Energy, DOE. The Ames Laboratory is operated for DOE by Iowa State University under contract No. W-7405-Eng-82.

Special thanks to Dr. Alexandra O. Pecharsky for collecting powder diffraction data and Sergej Bud'ko for performing magnetic measurements.

References

[1] Yu. Mozharivskyj, F. H. Franzen, J. Solid State Chem. 152 (2000) 478.

[2] L. G. Akselrud, Y. M. Grin, V. K. Pecharsky, P.Yu. Zavalij, CSD - universal program package for single crystal and powder data treatment, Proc.12th European Crystallographic Meet., Moscow, August 20-28, 1989, Academy of Sciences, Moscow, USSR, Kristallographiya, Suppl. 155 (1989) 2.

[3] J. Rodriguez-Carvajal, FullProf, Version 3.5, 1997.

[4] H. Nowotny, E. Dimakopoulou, H. Kudielka, Monatsh. Chem. 88 (1957) 180.

[5] B. Aronsson, Acta Chem. Scand. 12 (1958) 31.

[6] Y. Mozharivskyj, Yu B. Kuz'ma, J. Alloys Compd. 236 (1996) 203.

ACKNOWLEDGEMENTS

The people who helped me and contributed to my research are acknowledged at the end of the chapters. Specially, I would like to express my deep gratitude and respect to professor Hugo Fritz Franzen, my adviser, for his wise guidance and support, all the knowledge and understanding of chemistry he gave me, the enjoyable time I had with him, and for the nice working atmosphere he created in his group. Also, I want to thank Gordon J. Miller and Vitalij K. Pecharsky for fruitful collaborations, and all the professors who taught me, and the Department of Chemistry for accepting me to the graduate program and providing me with the assistantship.

My thanks go also to James Anderegg and Shirley Standley for helping me with all the working and organizational issues I had during my dissertations; to all former and present members of professors Franzen's, Corbett's and Miller's groups for training me, discussing my research and just having a good time with me.

I would like to thank my parents, who supported me through my college years and provided me with the understanding of what is important in life, and my wife Oksana who was here with me all these years and made my stay in Ames pleasant.

This research was supported by Ames Laboratory of the U.S. Department of Energy.

The United State Government has assigned the DOE Report number IS-T 1929 to this thesis.